

Analog Radio-over-Fiber for 5G/6G Millimeter-Wave Communications

Citation for published version (APA):

Pérez Santacruz, J. (2022). *Analog Radio-over-Fiber for 5G/6G Millimeter-Wave Communications*. [Phd Thesis 1 (Research TU/e / Graduation TU/e), Electrical Engineering]. Eindhoven University of Technology.

Document status and date:

Published: 28/10/2022

Document Version:

Publisher's PDF, also known as Version of Record (includes final page, issue and volume numbers)

Please check the document version of this publication:

- A submitted manuscript is the version of the article upon submission and before peer-review. There can be important differences between the submitted version and the official published version of record. People interested in the research are advised to contact the author for the final version of the publication, or visit the DOI to the publisher's website.
- The final author version and the galley proof are versions of the publication after peer review.
- The final published version features the final layout of the paper including the volume, issue and page numbers.

[Link to publication](#)

General rights

Copyright and moral rights for the publications made accessible in the public portal are retained by the authors and/or other copyright owners and it is a condition of accessing publications that users recognise and abide by the legal requirements associated with these rights.

- Users may download and print one copy of any publication from the public portal for the purpose of private study or research.
- You may not further distribute the material or use it for any profit-making activity or commercial gain
- You may freely distribute the URL identifying the publication in the public portal.

If the publication is distributed under the terms of Article 25fa of the Dutch Copyright Act, indicated by the "Taverne" license above, please follow below link for the End User Agreement:

www.tue.nl/taverne

Take down policy

If you believe that this document breaches copyright please contact us at:

openaccess@tue.nl

providing details and we will investigate your claim.

Analog Radio-over-Fiber for 5G/6G Millimeter-Wave Communications

PROEFSCHRIFT

ter verkrijging van de graad van doctor aan de
Technische Universiteit Eindhoven, op gezag van
de rector magnificus prof.dr.ir. F.P.T. Baaijens,
voor een commissie aangewezen door het College
voor Promoties, in het openbaar te verdedigen
op vrijdag 28 oktober 2022 om 11:00 uur

door

Javier Pérez Santacruz

geboren te Málaga, Spanje

Dit proefschrift is goedgekeurd door de promotoren en de samenstelling van de promotiecommissie is als volgt:

voorzitter:	prof.dr.ir. A. B. Smolders
promotor:	prof.dr.ir. I. Tafur Monroy
co-promotor:	dr. S. Rommel
co-promotor:	dr. A. Jurado-Navas (Universidad de Málaga)
leden:	prof.dr.ir. D. M. W. Leenaerts
	prof.dr. J. Capmany (Universitat Politècnica de València)
	prof.dr.ir. J. P. M. G. Linnartz
	dr. R. Puerta (Ericsson)

Het onderzoek of ontwerp dat in dit proefschrift wordt beschreven is uitgevoerd in overeenstemming met de TU/e Gedragscode Wetenschapsbeoefening.

A catalogue record is available from the Eindhoven University of Technology Library.

ISBN: 978-90-386-5564-2

NUR: 959

Title: Analog Radio-over-Fiber for 5G/6G Millimeter-Wave Communications

Author: Javier Pérez Santacruz

Eindhoven University of Technology, 2022

Keywords: Millimeter-wave wireless communications, ARoF, optical beamforming, waveforms, OFDM, phase noise, beam steering, systems on-chip, 5G, 6G, fronthaul, and full-optoelectronic heterodyne links.

Copyright © 2022 by Javier Pérez Santacruz

All rights reserved. No part of this publication may be reproduced, stored in a retrieval system, or transmitted in any form or any means without prior written consent of the author.

Typeset using L^AT_EX, printed in the Netherlands.

“Not all those who wander are lost.”

J.R.R. TOLKIEN

“Caminante, no hay camino, se hace camino al andar.”

ANTONIO MACHADO

Summary

The ongoing deployment of the fifth-generation (5G) of mobile networks and its anticipated successor 6G aim to fulfill the requirements associated with the increasing mobile data traffic volumes. Since the sub-7 GHz spectrum bands are congested, the exploitation of millimeter-wave (mm-wave) signals is considered as the evident next step to keep up with the upcoming demands. However, as mm-wave signals suffer from high free-space path loss (FSPL) and atmospheric absorption, the coverage radius of mm-wave cells is limited to ≈ 200 m. Therefore, the number of mm-wave cells or remote antenna units (RAUs) will be larger to cover the same area, compared to sub-7 GHz mobile networks. Then, analog radio-over-fiber (ARoF) arises as an excellent solution to transport radio frequency (RF) signals in the fronthaul link since it allows to reduce the complexity of mm-wave cell equipment and its control.

In this thesis, first, the fundamentals of ARoF as fronthaul link for mm-wave 5G/6G signals are explained. Then, the main performance limiting factors of ARoF systems, such as high FSPL, phase noise, and dynamic range, are introduced. Considering these limiting factors, the key aspects to deploy a scalable and robust mm-wave 5G/6G fronthaul based on ARoF are defined. These key aspects are as follows: (i) waveform selection and signal processing; (ii) phase noise mitigation in 5G/6G ARoF systems; (iii) ARoF system-level implementation and channel optimization; and (iv) beamforming for mm-wave ARoF fronthaul. Next, a detailed investigation on the question of waveform selection and digital signal processing (DSP) methods for ARoF fronthaul links is discussed. The considered main waveform candidates for 5G/6G communications are explained and qualitatively compared. In order to consider performance impairments of a realistic scenario, these waveforms are also experimentally evaluated in laboratory setup conditions, and, accordingly, an analysis and a comparison are provided. Furthermore, performing probabilistic amplitude shaping (PAS) technique over orthogonal frequency-division multiplexing (OFDM) subcarriers is analyzed and proposed as a suitable modulation scheme to optimize the channel capacity use in ARoF systems.

Concerning phase noise mitigation, this work experimentally evaluates 5G New

Radio (5G NR) signals under different phase noise conditions in a mm-wave ARoF setup. The results of this experiment show a significant degradation in the received OFDM signals for relatively high phase noise levels. Hence, novel and efficient algorithms to mitigate phase noise in OFDM signals are introduced and validated experimentally. Regarding the ARoF system-level implementation, a novel bidirectional ARoF fronthaul scheme is designed to comply with mm-wave 5G standards. The novelty of this bidirectional scheme lies in the reuse of the mm-wave carrier for both directions and the usage of multicore optical fibers (MCFs), reducing the overall complexity, volume, cost, and power consumption of the system. Then, the aforementioned scheme is experimentally validated by successfully transmitting different types of 5G NR signals. In addition, a PAS-OFDM scheme is assessed in the proposed bidirectional transmission setup. The obtained results show a substantial improvement in the use of the channel capacity with respect to the traditional bit-loading technique, confirming PAS-OFDM as a suitable solution for 5G/6G mm-wave fronthaul links.

Finally, this thesis considers the limitations of increased FSPL for the propagation of mm-wave by studying techniques to adaptively track users and reduce interference in mm-wave wireless links. In particular, beamforming is one of the preferred solutions to alleviate the severe FSPL in mm-wave 5G small cell coverage scenarios. In comparison with the traditional approach of beamforming with RF electronics, optical beamforming stands out as an alternative solution due to its small footprint, large bandwidth, and low loss. For this reason, this part of the thesis focuses on the characterization and experimental validation of an optical beamforming chip implementing a 4x4 Blass matrix. In parallel, an exhaustive measurement campaign is carried out on an outdoor mm-wave experiment based on ARoF fronthaul. This outdoor setup uses electrical beamforming with phased array antennas, harnessing the maturity of this beamforming approach. In summary, the research results of this thesis represent a notable step towards a scalable and robust mm-wave 5G/6G fronthaul based on ARoF by providing and experimentally validating efficient solutions to mitigate the main limiting factors in ARoF systems.

The organization of this thesis is structured in chapters covering the research questions mentioned above, including published articles, complemented by chapters introducing to the overall field, a summary of main contributions, some conclusions, and suggestions for further work. The presented work was performed partly with the ‘5G System Technological Enhancements Provided by Fiber Wireless Deployments (5G STEP FWD)’ project, which has received funding from the European Union’s Horizon 2020 research and innovation programme.

Contents

Summary	vii
1 Introduction	1
1.1 Motivation	2
1.1.1 mm-wave 5G/6G communications	4
1.1.2 Analog radio-over-fiber for the mm-wave 5G/6G fronthaul	6
1.2 Contributions and structure of the dissertation	7
2 Millimeter-wave analog radio-over-fiber wireless links	11
2.1 mm-wave ARoF signal generation	12
2.1.1 Optical two-tone mm-wave signal generation	12
2.1.2 Optical data modulation	15
2.2 Signal propagation effects in optical fiber	17
2.2.1 Chromatic dispersion	18
2.2.2 Non-linear propagation effects	20
2.3 mm-wave ARoF signal detection	21
2.4 mm-wave wireless channel	23
2.5 mm-wave signal detection and downconversion	26
2.6 Components with non-linear response in mm-wave ARoF wireless systems	29
2.7 Summary of mm-wave ARoF wireless impairments	30
3 Waveforms and digital signal processing for mm-wave ARoF systems	33
3.1 Waveforms for mm-wave ARoF 5G/6G communications	34
3.1.1 Waveform KPIs in mm-wave ARoF wireless systems	35
3.1.2 Waveform comparison in mm-wave ARoF wireless systems	37
3.2 Probabilistic amplitude shaping in mm-wave ARoF wireless systems	37
P1: Candidate Waveforms for ARoF in Beyond 5G	43
P2: Experimental Assessment of Modulation Formats for Beyond 5G mm-Wave ARoF Systems	61

P3: Probabilistic Amplitude Shaping to Enhance ARoF Fronthaul Capacity for Mm-Wave 5G/6G Systems	69
4 Phase noise in OFDM mm-wave ARoF systems	77
4.1 Transmission channel model with phase noise	78
4.2 Phase noise impact on OFDM signals	80
4.3 Algorithms to mitigate phase noise in OFDM signals	83
4.4 Experimental analysis of phase noise on OFDM mm-wave ARoF systems	87
4.5 State-of-the-art of phase noise compensation in mm-wave ARoF systems	88
P4: Analysis and Compensation of Phase Noise in Mm-Wave OFDM ARoF Systems for Beyond 5G	91
P5: Experimental Study of the Phase Noise in K-band ARoF systems for Low Complexity 5G receivers	103
P6: Experimental ARoF System Based on OPLL Mm-Wave Generation for Beyond 5G	111
P7: Optical Phase-Locked Loop Phase Noise in 5G Mm-Wave OFDM ARoF Systems	117
P8: Probabilistically Shaped OFDM for Gradual Capacity Adaptation in 5G ARoF Systems	129
5 Optimized mm-wave 5G/6G deployment based on ARoF	135
5.1 Fronthaul architectures for mm-wave 5G/6G networks	136
5.2 Bidirectional ARoF experimental demonstration for mm-wave 5G scenarios	140
5.3 Performance optimization in mm-wave ARoF systems	142
P9: Bidirectional mm-Wave ARoF Fronthaul over Multicore Fiber for 5G and Beyond	143
P10: Bidirectional ARoF Fronthaul over Multicore Fiber for Beyond 5G Mm-Wave Communications	149
6 Beamforming for mm-wave mobile communications	159
6.1 Beamforming approaches	160
6.2 ARoF fronthaul architecture with beamforming implementation . .	162
6.3 Experimental demonstrations of mm-wave fronthaul with beamforming	165
P11: Incoherent Optical Beamformer for ARoF Fronthaul in Mm-wave 5G/6G Networks	167
P12: Experimental outdoor IFoF fronthaul with adaptive analog beamforming for mm-wave 5G/6G networks	179

7	Conclusions and future outlook	193
7.1	Summary and conclusions	193
7.2	Future outlook and recommendations	195
	Bibliography	201
	List of Acronyms	217
	List of Publications	223
	Curriculum Vitae	225

Introduction

Throughout history, humans have evolved and improved the techniques for transmitting information through different media. Newspapers, television, telegraph, or smoke signals are some examples of methods to transmit information [1]. More specifically, telecommunication technologies play and have played a key role in the evolution of humanity [2]. In the mid-20th century, the information age began with the development of the transistor, allowing the digitization of information [3]. In this way, the information can be transmitted in an efficient, replicable, and secure manner through the network. As a result, globalization accelerated dramatically, inducing some of the fastest technological and economic growths in human history [2].

In the 1980s, mobile communications commenced with the deployment of its first generation (1G). However, 1G services were only accessible to a few niche markets [4]. With the next generations of mobile networks, 2G, 3G, and 4G or Long-Term Evolution (LTE), mobile services became more accessible and thus contributed to a significant impact on society, culture, economy, environment, and industry [5], [6]. For example, in 2018, over 3.6 billion mobile devices connected to the LTE network were registered worldwide, following the exponential growth of the last decade [7]. That drastic yearly increase in the number of devices connected to the mobile network furthers the rapid growth of mobile data traffic [7]. For this reason, it is crucial to constantly update and enhance the mobile network, with 5G the generation currently being deployed and 6G the future generation yet to be standardized.

Figure 1.1(a) shows the global evolution and prediction of mobile data traffic in terms of exabytes per month [8]. Moreover, Fig. 1.1(a) distinguishes between the data traffic of 5G and previous generations. Observing Fig. 1.1(a), it can be noticed that the current 5G data traffic is small compared to other mobile technologies. Nevertheless, 5G data traffic exhibits an exponential growth trend over

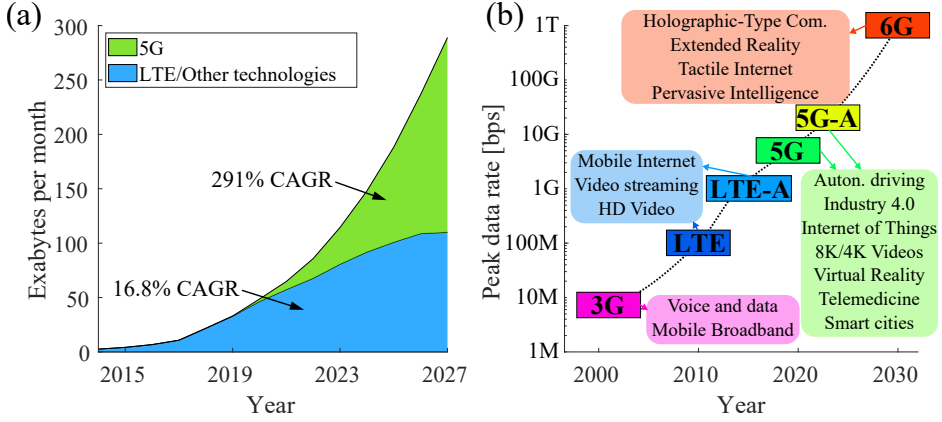


Figure 1.1: Overview of mobile network evolution: (a) global mobile data traffic prediction in terms of exabytes per month (data obtained from [8]); (b) mobile technology evolution over the years. LTE-A: LTE-Advanced; 5G-A: 5G-Advanced; HD: high-definition.

the upcoming five years while the rest of mobile technologies present a logarithmic trend [8], highlighting the extreme importance of 5G in fulfilling mobile traffic demands in the coming decade. In addition, the slope of the mentioned mobile traffic trends can be quantified with the compound annual growth rate (CAGR) [9]. The CAGR values of Fig. 1.1(a) are calculated from 2019 to 2027, where the overall traffic CAGR is 31.3%.

As mentioned above, the mobile network must adapt to the mobile traffic requirements. Figure 1.1(b) illustrates the evolution of the mobile networks in terms of peak data rate from 2000 to 2030 [10], [11]. Peak data rate is the highest data rate under ideal conditions for a single user and is traditionally considered the most symbolic parameter for comparing different mobile generations [10]. Analyzing Fig. 1.1(b) from approximately 2014, it can be seen that the peak data rate evolution of the mobile network has a similar trend to the mobile data traffic. However, as discussed above, the mobile traffic trend in the upcoming years offers a dramatic exponential growth which imposes an important enhancement for the future mobile generations (5G and 6G) compared to their predecessors. Besides, the overall data traffic of mobile networks scales with the number of users within the cell and with the reduction of the cell radius. Therefore, concerning 5G/6G, new technologies and paradigms must be investigated to satisfy the needs and demands in the mobile network.

1.1 Motivation

The emergence of new applications and services, such as 4K/8K video streaming, augmented reality, autonomous driving, or vehicular communications, demands

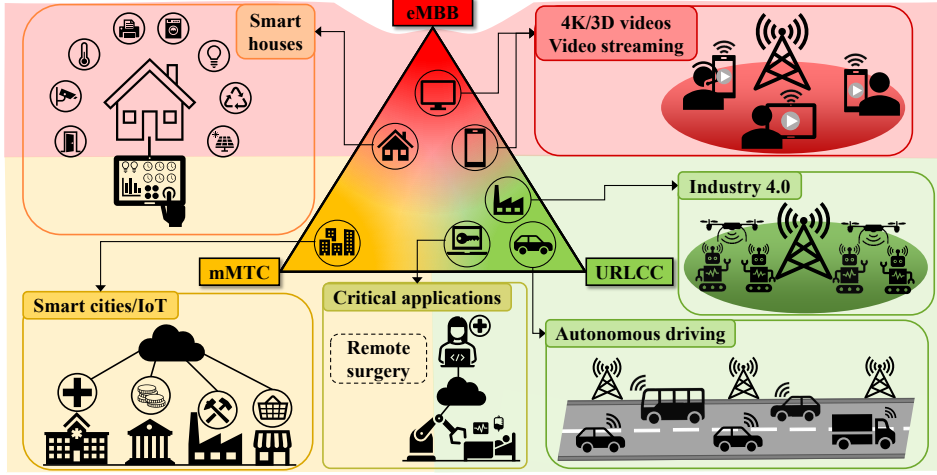


Figure 1.2: 5G applications use cases for the three different categories of traffic types: 4K/3D videos, video streaming, industry 4.0, autonomous driving, critical applications such as remote surgery, smart cities, IoT, and smart houses.

great versatility from the mobile network due to the different types of requirements that these applications and services demand. In particular, mobile augmented reality (MAR) applications demand exigent requirements in terms of latency and data capacity, which current mobile networks cannot support [12]. Hence, in 5G NR technology, three types of categories are considered to classify the different applications and services according to their requirements. These three categories are as follows [13]: enhanced mobile broadband (eMBB) whose primary target is the data rate; massive machine-type communications (mMTC) aim to ensure robust communications for a large number of low-power connected devices; and ultra-reliable and low latency communications (URLLCs) focus on guaranteeing communications where high reliability and low latency are essential.

Figure 1.2 shows various applications and use cases for the three different categories mentioned above: eMBB enables 4K/3D video downloads; mMTC allows Internet of Things (IoT) and smart cities; and URLLC paves way for industry 4.0, autonomous driving, and critical applications. However, there are some applications that do not belong exactly to a specific category and thus demand hybrid requirements. This is the case of smart houses where data rate and the number of connected devices are the primary objectives. Video streaming use cases also have hybrid requirements where data rate, low latency, and reliability are the main requirements. Given the high variety of applications and services that 5G brings, a heterogeneous system is the obvious architecture solution to efficiently integrate the aforementioned applications in future mobile networks [14].

Nonetheless, the management of the control plane in heterogeneous networks is

notoriously more complex than in conventional networks [15]. As a consequence, network slicing and software-defined networking (SDN) arise as great solutions because they allow optimizing the physical resources depending on the current stage and demands of the mobile network [16]. SDN and network slicing are capable of integrating the future heterogeneous mobile network in an efficient manner [15], [16]. However, the implementation of these technologies alone is not sufficient to guarantee the demanding data rates that some 5G/6G applications require. In fact, the performance improvements of SDN and network slicing are limited by the features of the deployed hardware. Therefore, to achieve a substantial improvement in the mobile network, the physical layer must also be upgraded. Focusing on the data rate requirements of eMBB, Shannon's formula should be considered [17]:

$$C[\text{bps}] = W \cdot \log_2 \left(1 + \frac{S}{N} \right), \quad (1.1)$$

where C is the channel capacity, W is the channel bandwidth, and S/N is the signal-to-noise ratio (SNR). According to Shannon's formula, the way to increase the capacity consists of incrementing W and/or SNR. SNR offers a logarithmic increase in the capacity, while W has a linear impact on the capacity. Furthermore, augmenting the SNR usually implies a higher transmitted power, which is not always feasible due to safety matters and power limitations in the physical devices. Therefore, increasing W results in a more attractive approach to boost the channel capacity.

Since the low-frequency spectrum is highly congested [18], exploiting high-frequency bands is considered the evident approach to increase the data rate in mobile networks since large bandwidths are available to use. In such manner, peak data rates of 10 Gbps or even 1 Tbps can be reached fulfilling the mobile data traffic demands (Fig. 1.1(a)) [10]. However, working at high-frequency bands implies several challenges that must be investigated and addressed to perform robust communications.

1.1.1 mm-wave 5G/6G communications

Nowadays, 5G is the mobile technology solution to satisfy the current and upcoming mobile traffic needs. The initial 5G deployment focuses on the exploitation of the sub-7 GHz bands. Nonetheless, the sub-7 GHz bands are congested, enabling scarce bandwidth to be used. Therefore, moving to higher frequency bands is crucial to use larger bandwidth guaranteeing the fulfillment of the mobile data demand, with the millimeter-wave (mm-wave) domain being the next operational band to exploit. The 3rd Generation Partnership Project (3GPP) defines two frequency ranges (FRs) for 5G networks [19]: FR1 (0.41 – 7.125 GHz) and FR2 (24.25 – 52.6 GHz).

Figure 1.3 shows the 5G spectrum allocation defined by the 3GPP standard. In addition, and according to the Institute of Electrical and Electronics Engineers

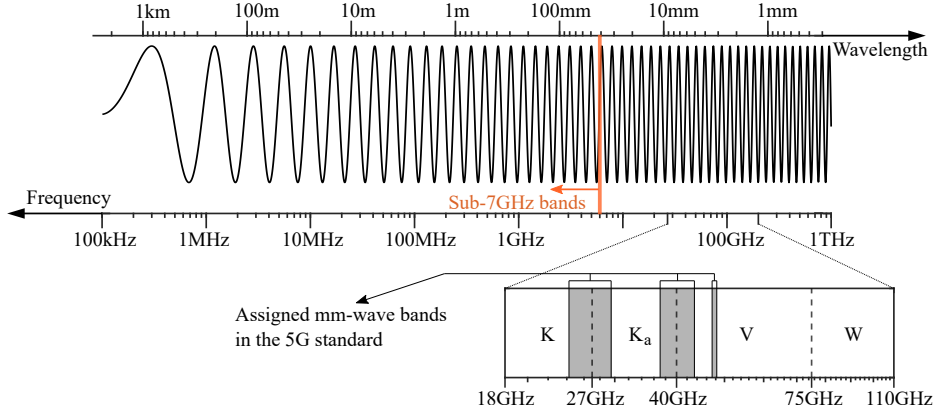


Figure 1.3: Electromagnetic spectrum allocation of 5G in the 3GPP standard.

(IEEE), the mm-wave domain is partitioned into different bands [20] (see Fig. 1.3): K-band (18 – 27 GHz), K_a -band (27 GHz to 40 GHz), V-band (40 – 75 GHz), and W-band (75 – 110 GHz). Furthermore, 3GPP 5G standard specifies several mm-wave subbands to operate (see Table 1.1) [19], which are identified in Fig. 1.3 with a gray colour.

However, compared to lower frequency bands, the usage of mm-wave frequencies involves in several transmission impairments, as high free-space path loss (FSPL), material penetration losses, and atmospheric attenuation, which drastically diminish the received signal power in the end-user. This fact implies that the coverage radius of the mm-wave cells or remote antenna units (RAUs) is limited to approximately 200 m [21]. Thereby, the number of mm-wave RAUs will be an order of magnitude larger than the current sub-7 GHz mobile network. Hence, investigation on current and new types of mobile network architectures to implement low-complexity RAUs is highly required in order to deploy a scalable

Table 1.1: 5G NR operating bands in FR2 defined by 3GPP.

Operating band	Frequency range for UL and DL
n257	26.5 – 29.5 GHz
n258	24.25 – 27.5 GHz
n259	39.5 – 43.5 GHz
n260	37 – 40 GHz
n261	27.5 – 28.35 GHz
n262	47.2 – 48.2 GHz

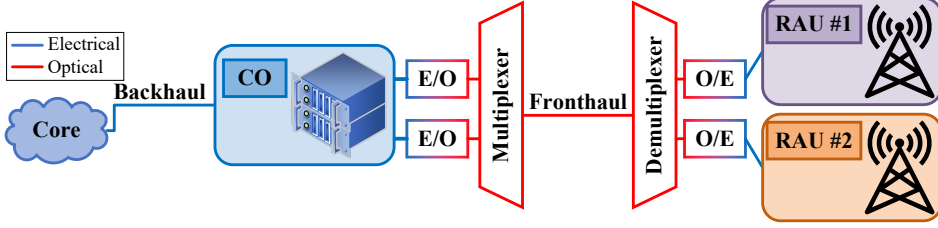


Figure 1.4: C-RAN mobile network architecture. E: electrical; O: optical.

mm-wave 5G/6G network. Accordingly, new technologies, solutions, and methods must be investigated and implemented to mitigate the impairments related to the mm-wave spectrum usage.

1.1.2 Analog radio-over-fiber for the mm-wave 5G/6G fronthaul

In mobile communications, the traditional radio access network (RAN) is based on the interconnection through the backhaul between the core network and base stations that are placed in different locations. This mobile architecture is named distributed RAN (D-RAN). On the contrary, centralized RAN (C-RAN) includes the central office (CO) as an extra node in the mobile network. The CO serves as intermediate point between the base stations and the core network, allowing for centralized monitoring [22]. Also, some of the functions performed at the base station migrate to the CO site, increasing the centralization operation and reducing base stations to RAUs. C-RAN was first introduced by China Mobile Research Institute in 2010 [23]. Compared to D-RAN, C-RAN is a preferred solution as network ownership, operation, maintenance, and energy consumption are reduced [22], [24]. However, C-RAN adds a new link to the mobile network denoted as fronthaul. The deployment of fronthaul links is mostly realized with optical fibers since it allows long-distance communications with low attenuation [25]. The typical distance of fronthaul links varies between 10 km and 20 km [26]. Figure 1.4 shows the C-RAN architecture in mobile network scenarios.

Common public radio interface (CPRI) is the first selected technology to cover the fronthaul in pre-5G networks [27]. CPRI implements digital radio-over-fiber (DRoF) to transport 5G New Radio (5G NR) signals through the fronthaul [27]. For performing this, DRoF requires the digitization of the analog (5G NR) signals by using serializers and deserializer at CO and RAU sites. For this serialization process, a set of analog-to-digital and digital-to-analog converters (ADCs, DACs) are needed. In the CPRI fronthaul, the baseband processing is performed in the CO. Nonetheless, as DRoF serially transports the bits, that represent the analog samples of the 5G NR signals, in the optical fiber, the optical spectral efficiency is

low [28]. Thereby, since the exploitation of the mm-wave bands will allow the utilization of larger bandwidth spectrum compared to the current sub-7 GHz network, CPRI-based fronthaul can suffer from bottlenecks [27]. Consequently, alternative solutions, such as next generation fronthaul interface (NGFI) and enhanced CPRI (eCPRI), aim to mitigate the bottleneck in the fronthaul by re-distributing some baseband functionalities to the RAU [27]. However, this re-distribution of functionalities leads to an augmentation in RAU complexity that is not suitable for a scalable mm-wave RAU deployment. Furthermore, the utilization of larger bandwidths in DRoF-based fronthaul technologies imposes higher sampling rates on the used ADCs and DACs, further reducing scalability and increasing cost and power consumption [29].

Thus, analog radio-over-fiber (ARoF) arises as an excellent solution to implement the mm-wave fronthaul for the following reasons:

- ARoF offers high bandwidth efficiency because the RF signal is directly modulated into the optical domain [28]. As consequence, the bottleneck issue of the fronthaul is mitigated by utilizing ARoF.
- ARoF does not require a digitization procedure. Hence, ARoF dispenses with ADCs and DACs in the RAU, enabling low-complexity mm-wave cells [27], [30].
- ARoF can be used to transport 5G NR signals modulated on a mm-wave carrier through the optical fronthaul [31]. In this manner, a frequency source and the upconversion process are not required in the RAU, further reducing the complexity of the RAU.
- Since ARoF allows low-complexity RAUs in the fronthaul, a scalable and efficient mobile network deployment based on C-RAN can be accomplished, bringing the advantages of using a C-RAN architecture, such as reduced power consumption and low latency [24].

However, in contrast to DRoF, the transmitted signal deteriorates more in the ARoF link due to the following impairments: non-linear effects in optical fiber transmission; signal distortion in the E/O and O/E conversions [28]; increased phase noise due to the generation and transportation of mm-wave signals in the optical domain [32]; chromatic dispersion due to optical fiber propagation [33]; and a reduction of the dynamic range. Therefore, to deploy a robust and scalable mm-wave fronthaul based on ARoF, the impact of the mentioned impairments must be mitigated by introducing of new technologies and solutions.

1.2 Contributions and structure of the dissertation

The work presented in this dissertation was carried out within the framework of the ‘5G System Technological Enhancements Provided by Fiber Wireless Deployments

(5G STEP FWD)’ project, which has received funding from the Horizon 2020 research and innovation program of the European Union [34]. The mission of 5G STEP FWD consists of evolving the current passive optical network (PON) to support the growing data demand of 5G. With the PON evolution as the goal, 5G STEP FWD points to two main approaches: the study and analysis of the network physical layer from both device and system level perspectives; and the examination and evaluation of network layer applications such as network slicing, SDN, or network function virtualization (NFV). In particular, the scope of the author’s project is the investigation of technologies for enabling the transmission of mm-wave signals over optical networks.

The objective of this work is to cover the main key aspects and research questions (RQs) related to the implementation and deployment of a robust and scalable mm-wave 5G/6G fronthaul based on ARoF. Hence, this dissertation is organized into different chapters whose goal is a better understanding of these key aspects and comprehensive answers to the research questions. These chapters are complemented with published articles. A summary of the chapters of this dissertation and their corresponding research question(s) can be found below:

- **Chapter 2** explains the fundamentals of the building blocks involved in mm-wave ARoF wireless links. The challenges, impairments and, different techniques used in each of these blocks are presented, described, and addressed. Moreover, the main advantages and disadvantages of mm-wave ARoF wireless channels are listed and discussed. **Chapter 2** sets the foundation for the other chapters of this dissertation.
- In **Chapter 3**, first, the main modulation format candidates in mm-wave ARoF systems are presented and explained. Next, a thorough comparison between these modulation formats is performed both in qualitative and experimental terms. In **P1**, a qualitative comparison is realized by using a set of key performance indicators (KPIs) as figures of merit. Then, an experimental comparison among the modulation format candidates through a mm-wave ARoF setup is carried out in **P2**. Moreover, the fundamentals of probabilistic amplitude shaping (PAS) technique are explained. Finally, the capability of PAS to improve the channel capacity in mm-wave ARoF systems is introduced and discussed in **P3**.

RQ-1: What are the main limitations and challenges for transmitting waveform signals through a mm-wave ARoF wireless link for 5G/6G communications?

RQ-2: What are the most efficient waveforms and modulation schemes for mm-wave ARoF combined channel in 5G/6G scenarios?

RQ-3: What communication performance can be achieved for the main waveform candidates for 5G in an experimental mm-wave ARoF wireless setup?

- In **Chapter 4**, the fundamentals of phase noise, including its origin and model, are explained and, the different types of impairments in orthogonal frequency-division multiplexing (OFDM) signals due to phase noise are presented. Consequently, several digital signal processing (DSP) approaches to reduce the impact of phase noise in OFDM signals are explained in **P4**, **P5**, **P6**, and **P7** and compared in this chapter. In order to quantify the impact of phase noise in a realistic scenario, the studied DSP approaches are evaluated on different experimental mm-wave ARoF setups and the respective results are shown in **P4**, **P5**, **P6**, and **P7**. In such setups, two techniques, with different phase noise characteristics, are employed to generate mm-wave signals in the optical domain. Furthermore, one of these setups is designed to gradually increase the final phase noise of the system and thus profoundly analyze the performance of the DSP algorithms under test. As the last point of **Chapter 4**, **P8** proposes and validates PAS-OFDM as an excellent solution to gradually adapt the bit rate depending on the phase noise conditions in an experimental mm-wave ARoF setup that is able to progressively increase the final phase noise of the system.

RQ-4: How can DSP techniques be improved to reduce the impact of phase noise in OFDM signals with 5G numerology in mm-wave ARoF systems? What are the advantages and disadvantages of using these techniques?

- In **Chapter 5**, first, the main technologies to implement the mm-wave 5G/6G fronthaul are presented and qualitatively compared. Later, focusing on the ARoF solution, a novel bidirectional mm-wave ARoF system adhering to the 5G standard is proposed and experimentally validated in **P9** and **P10**. Also, **P3** employs the proposed bidirectional mm-wave ARoF setup to estimate the benefits of employing PAS-OFDM in terms of channel capacity use in an experimental scenario. The experimental results of **P3** highlights PAS-OFDM as a promising modulation format technique for future mobile standardization since it enables to gradual reduce the impact of the major impairments in mm-wave ARoF wireless systems.

RQ-5: How to efficiently implement a bidirectional mm-wave ARoF wireless link following 5G standards in terms of cost and power consumption? What is the communication performance of transmitting 5G NR signals through this experimental bidirectional setup?

- The two main approaches to realize beamforming are analyzed and compared in **Chapter 6**: optical beamforming and electrical beamforming. The work presented in **P11** mainly focuses on the optical beamforming approach due to its potential benefits such as low cross-talk and losses. Besides, optical beamforming lacks exhaustive investigation, experimentation, and demonstration in the research field. More specifically, **P11** presents and thoroughly charac-

terizes a novel incoherent optical beamforming network (iOBFN) built on a photonic integrated circuit (PIC). Moreover, **P12** presents a comprehensive measurement campaign of an outdoor experimental setup where a radio-over-fiber (RoF) fronthaul link is evaluated. In **P12**, 64-element phased array antennas, located at the RAU and end-user, are used to perform a double beam angle sweep, enabling for assessments regarding RoF mm-wave communications in an outdoor scenario.

RQ-6: How to integrate optical/electrical beamforming solutions in the mm-wave ARoF fronthaul in a centralized and optimized manner?

RQ-7: How to fully characterize and validate PIC-based optical beamforming?

RQ-8: What are the benefits in terms of communication performance of using analog beamforming with phased array antennas in a mm-wave outdoor experiment based on ARoF?

- Finally, **Chapter 7** summarizes the contributions and conclusions of the presented work. Moreover, regarding the implementation of ARoF in the mm-wave 5G/6G fronthaul, future lines of research, opportunities, visions of the future, and challenges yet to be addressed are commented on and explained.

Millimeter-wave analog radio-over-fiber wireless links

In Chapter 1, the benefits of ARoF to deploy a scalable, robust, and efficient mm-wave fronthaul were introduced and explained. However, mm-wave ARoF wireless links brings with it several drawbacks that limit the final performance of the communication system. Thereby, current and new technologies must be investigated, analyzed, tested, and validated in ARoF scenarios to reduce the performance degradations due to such drawbacks. The goal of this chapter focuses on the description and explanation of all the components involved in mm-wave ARoF wireless systems.

Figure 2.1 shows the general scheme of a mm-wave ARoF wireless system. In this scheme, first, two optical tones carrier the data signal in the optical domain for mm-wave generation. This process can be divided into two parts: optical two-tone generation and data signal modulation onto an optical carrier. After this process, the resulting optical signal travels through an optical fiber. In a mobile network scenario based on C-RAN, the distance of the optical fiber corresponds to the distance between the CO and RAU (10 – 20 km) [26].

Next, the optical signal at the output of the optical fiber is detected by a heterodyne process and, consequently, the data signal is upconverted to the desired mm-wave frequency in the electrical domain carrying the modulation introduced on the optical carrier. After the corresponding RF filtering and amplification, the mm-wave signal is transmitted wirelessly. In the mm-wave wireless channel, the transmitted RF signal suffers from several phenomena whose properties depend on the channel conditions. More specifically, in mm-wave wireless transmissions, one of this phenomena is high FSPL, which is attached to high-frequency bands. As a consequence, the coverage area of mm-wave cells is approximately in the range of 10 m to 200 m [35]. Subsequently, the captured RF signal from the receiver

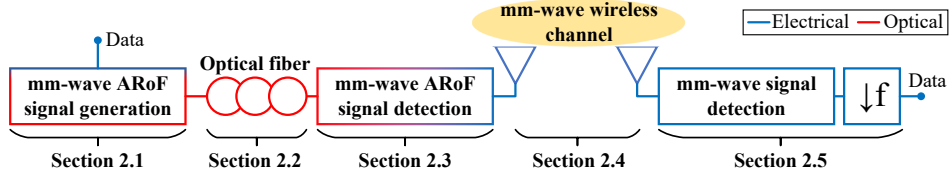


Figure 2.1: General scheme of a mm-wave AROF wireless system.

antenna needs to be downconverted and then sampled for digital post-processing. For that, a mm-wave signal detection block together with a downconversion process are needed to digitize the received signal.

In the next sections of this chapter, the fundamentals and drawbacks of the mentioned AROF blocks are individually explained through theoretical formulation and numerical examples oriented towards 5G/6G cases. In the following chapters of this dissertation, the aim is centred on the study, evaluation, and investigation of different technologies and solutions to alleviate the signal deterioration caused by a concrete drawback in mm-wave AROF wireless systems.

2.1 mm-wave AROF signal generation

As commented above, the mm-wave AROF signal generation block is composed of two procedures: optical two-tone generation with a separation of the target mm-wave frequency (f_{RF}); and the modulation of the data signal onto the previously generated optical two-tone signal. These two procedures can be realized in separated blocks or in an unified single block. The following two subsections present and describe different approaches to carry out these two procedures. Furthermore, the presented approaches are compared by using several KPIs, providing the best solution according to the system requirements.

2.1.1 Optical two-tone mm-wave signal generation

Figure 2.2 displays four different techniques to generate two optical tones with a certain frequency spacing. There are other technologies, that are not considered in this dissertation, to generate an optical two-tone signal, such as dual-wavelength laser source or mode-locked lasers (MLLs) [31], [36]. The simplest approach to generate two optical tones with a determined frequency separation is by running two independent lasers (see Fig. 2.2(c)). However, the frequency drift and phase mismatch between both lasers imply high phase noise and frequency instability [37]. As a consequence, the transmission of coherent modulations and the use of heterodyne receivers are not feasible in terms of performance when applying two free running lasers technique [38]. Subsequently, other technologies for generating optical two-tone signals arose as alternatives by reducing the final phase noise and

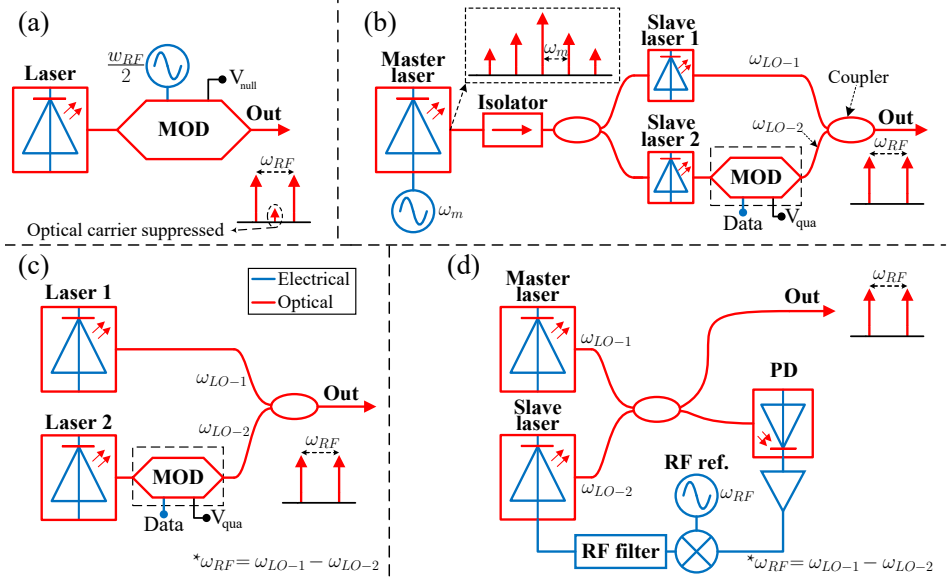


Figure 2.2: Techniques to generate two optical tones with a separation of the desired mm-wave frequency ($f_{RF} = \omega_{RF}/2\pi$): (a) external modulation technique; (b) optical-injection-locking (OIL) technique; (c) two free running lasers technique; (d) optical phase-locked loop (OPLL) technique. MOD: modulator.

frequency drift. Nonetheless, comparing to the two free running option, such technologies bring some disadvantages such as power output reduction or complexity increase. Table 2.1 compares the techniques displayed in Fig. 2.2 in terms of several KPIs: phase noise will be introduced in this chapter and more deeply in Chapter 4; power efficiency is directly related to the final output power and determines if optical amplification is needed; complexity refers to the necessary devices for performing the technique and the complications for stabilizing the system; and frequency range indicates the maximum frequency separation between the two generated tones. The four optical two-tone generation techniques illustrated in Fig. 2.2 are explained and detailed below:

- a) **External modulation:** this technique consists of modulating an RF carrier with half of the desired mm-wave frequency ($\omega_{RF}/2$) by using an external optical modulator. Hence, by utilizing the harmonics of second order, two optical tones are produced with a separation of the target frequency (ω_{RF}) [39]. The bias voltage applied to the optical modulator determines different type of outputs: single-sideband (SSB), double-sideband (DSB), or optical carrier suppression (OCS) [40]. According to [40], OCS is the best option in terms of sensitivity, spectral efficiency, and power penalty for data transmission over long-distances. Moreover, since the two tones are generated by a single opti-

Table 2.1: Qualitative comparison between different techniques for generating optical two-tone signals.

KPI/ Technique	External mod.	OIL	Two free run. lasers	OPLL
Phase noise	Very low	Low	Very high	Medium
Power efficiency	Low	Medium/High*	Very high	High
Frequency range	Ltd. by Mod. and RF source	High*	High	Ltd. by loop comps.
Complexity	Medium	Medium	Low	Medium

(*) → Higher harmonic orders of the OFCG signal can be selected, offering a wider frequency range at the cost of reducing the final output power.

cal source, the final phase noise mostly depends on the linewidth of the RF carrier if the two tones remain synchronized [32]. However, as the modulator must be set in the null point to realize OCS, the output optical power by using the external modulation technique is highly reduced. Therefore, external modulation solution requires, in most of the applications, an optical amplification stage. As last remark, the frequency range of this technique is limited by the bandwidths of the optical modulator and the RF source.

b) Optical-injection-locking (OIL): a basic OIL is formed by a master laser, isolator, and slave laser [41]. The purpose of the isolator is to prevent the coupling of both back reflections and slave laser emission to the master laser [41]. As a consequence of this injection process, the frequency of the slave laser approaches that of the master laser. Thus, the system keeps locked in a specific region. Nonetheless, this locked region is denominated as stability region which depends on the optical injection ratio and the frequency detuning [41]. In order to generate two optical tones with a certain frequency separation, OIL is combined with optical frequency comb generators (OFCGs) [42]. Then, two specific tones of OFCG can be selected by employing two slave lasers (see Fig. 2.2(b)). In this manner, since both slave lasers are locked to the tones of the master comb, the final phase noise of the system is low, but slightly higher than with the external modulation technique [43]. In addition, this injection procedure is efficient in terms of power consumption since it is based on the photon-photon interaction when external light is injected into the cavity of the slave lasers [44]. Regarding the frequency range characteristics, the OIL frequency tunability is mainly determined by the comb generator source, which is attached to an RF source, enabling the selection of any OFCG tone: $n \cdot \omega_m$, $n \in \mathbb{Z}$. Higher frequency tones of the OFCG signal offer lower power levels, as can be seen in the spectrum graph of Fig. 2.2(b). Therefore, selecting high-frequency tones for injection implies

a reduction of the final power of the OIL system represented in Fig. 2.2(b).

- c) **Two free running lasers:** this technique requires two independent lasers with different wavelengths and their outputs are combined by an optical coupler. Since there is not any intermediate process in the optical carrier combination, the optical power losses are minimal. Thereby, two free running lasers method stands out as the most efficient in terms of power in the comparison of Table 2.1 because it does not include additional optical components that reduce the input power in the PD. Furthermore, its complexity is reduced because RF components are not required. However, the final phase noise of the system is proportional to the combined linewidth of both lasers [41]. In addition, frequency drift is an important drawback in the two free running lasers technique [37]. Hence, the resulting phase noise and frequency drift of this technique are high for coherent transmissions [38], [45]. Nevertheless, the frequency range of two free running lasers technique is only limited by the lasers, enabling large frequency separations between both tones.
- d) **Optical phase-locked loop (OPLL):** OPLL can be considered as an advanced version of the two free running lasers method. The objective of OPLL consists of controlling the phase of one of the lasers to track that of the other. This phase tracking is carried out by a phase-locked loop [46], [47]. In this manner, respecting the two free running lasers technique, the phase noise is highly diminished [41]. Nonetheless, the frequency range properties of the OPLL system are limited by the components involved in the loop. In other words, the maximum frequency that this two-tone generation technique achieves is principally determined by the RF components and the PD.

As an important remark, the techniques of Figs. 2.2(b) and (c) contain a dotted black box where an optical modulator is inserted. This box indicates the possibility of modulating data into the optical domain at the two-tone generation procedure. In this way, a SSB signal is produced. For the remaining two-tone generation techniques, an optical signal modulation process is needed. The next subsection focuses on different techniques and approaches to modulate the data with the generated two optical tones.

2.1.2 Optical data modulation

One of the main approaches to transport mm-wave data signal through an optical fiber lies in generating two optical components: the optical data at a certain optical frequency and an optical tone at a different optical frequency. Then, after the optical heterodyne detection in the PD, the resulting data signal is converted to the frequency separation between the mentioned two optical components [48]. There are two main ways to generate these two optical components in the mm-wave range:

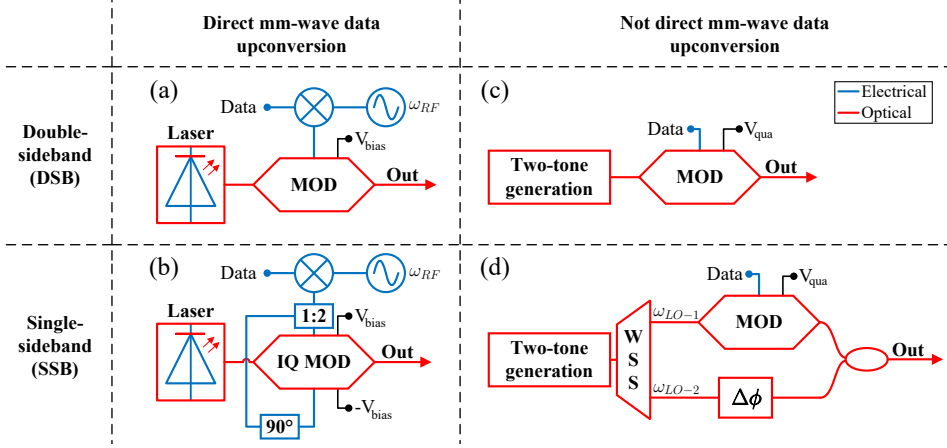


Figure 2.3: Different techniques for performing mm-wave AROF optical upconversion: DSB or SSB; and direct or not direct. MOD: modulator.

direct and not direct optical mm-wave upconversion. The not-direct optical mm-wave upconversion utilizes the two-tone generation blocks explained in the previous subsection. Figure 2.3 illustrates different techniques to realize an optical mm-wave upconversion of the data distinguishing between DSB and SSB configurations. The techniques of Figs. 2.3(a) and (b) are based on the optical upconversion by using modulators. Nonetheless, there are other optical upconversion techniques based on wavelength-conversion and non-linearity of photo-detectors, whose study is out of the scope of this dissertation [49].

Figures 2.3(a) and (b) show two optical upconversion techniques based on direct mm-wave signal modulation [50]. Both techniques require an RF mixer since the mm-wave upconversion is realized in the electrical domain. The main difference between schemes of Figs. 2.3(a) and (b) lies in the usage of an optical in-phase and quadrature (IQ) modulator. In this manner, schematics (a) and (b) of Fig. 2.3 generate optical DSB and SSB signals, respectively [51].

As mentioned above, the schemes of Figs. 2.3(c) and (d) employ the optical two-tone generation as initial block. Therefore, the bandwidth requirements of the optical modulator used for optical data modulation are more relaxed compared to the direct optical mm-wave upconversion methods. Scheme of Fig. 2.3(c) directly uses the two-tone signal for converting the data into the optical domain by using a single modulator. The simplicity of this method leads to a DSB optical signal at the output. At this point, and in order to generate a SSB signal with the optical two tones, a filtering process is required to separate these two tones. Scheme of Fig. 2.3(d) uses a wavelength selective switch (WSS) for this filtering process [52]. In Fig. 2.3(d), the upper branch is used to modulate the data signal while the lower branch includes an optical fiber cord to compensate the length mismatch

between both branches ($\Delta\phi$). In this way, the two tones do not lose coherence, avoiding phase noise degradation [32]. Finally, the modulated and unmodulated tones are combined with an optical coupler.

As an additional consideration, the data signal represented in each scheme of Fig. 2.3 can be both baseband or with a specific intermediate frequency (IF). When IF data is applied, an optical SSB can be obtained from the schemes of Figs. 2.3(a) and (c) by subsequently realizing a fine optical filtering [53]. In the next section, the relevance of transmitting a SSB signal, instead of a DSB one, through the optical fiber is highlighted.

2.2 Signal propagation effects in optical fiber

By 1964, with the first demonstration of fiber-based laser/amplifier, all the needed building blocks for developing optical communications had been realized [54]. Since that time, the potential of optical communications were and are being harnessed due to its extremely low attenuation, enabling reliable long-distance communications. Nowadays, optical fibers provide even lower losses values ≈ 0.15 dB/km [55]. In general, the main categories of optical fibers are the following [56], [57]: single-mode fiber (SMF), multi-mode fiber (MMF), few-mode fiber (FMF), multi-core fiber (MCF), and coupled-core fiber (CCF). Since SMF degrades the transmitted signal less and requires less complexity, SMFs are mostly used in long-haul networks [56]. However, SMFs lead to impairments that can be described with its transfer function [25]:

$$H_{SMF}(\omega) = e^{L[-\alpha + j\beta'(\omega)]}, \quad (2.1)$$

where α refers to the attenuation coefficient, L is the optical fiber length in m, and β' corresponds to the phase constant in rad/m. The attenuation coefficient α is commonly expressed in dB/km and its typical value is around 0.185 dB/km at 1550 nm in standard SMF (SSMF) [55]. In addition, since the signal bandwidth is very low compared to the optical carrier, it can be assumed that α behaves linear with respect to the frequency. Nonetheless, in Eq. (2.1), β' changes with the frequency, and it can be expressed as [25]:

$$\beta'(\omega) = \beta(\omega) + \frac{k_0 \bar{n}_2}{A_{eff}} P, \quad (2.2)$$

where $\beta(\omega)$ indicates the part of $\beta'(\omega)$ that depends on ω , k_0 is the free-space wavenumber in rad/m, \bar{n}_2 corresponds to the non-linear index coefficient in m^2/W , A_{eff} is the effective mode area in m^2 , and P refers to the optical power in W. The first component of Eq. (2.2) indicates the frequency dependence of the index of refraction coefficient \bar{n} and can be expanded by using a Taylor series around the optical carrier frequency ω_{LO} as follows [25], [58]:

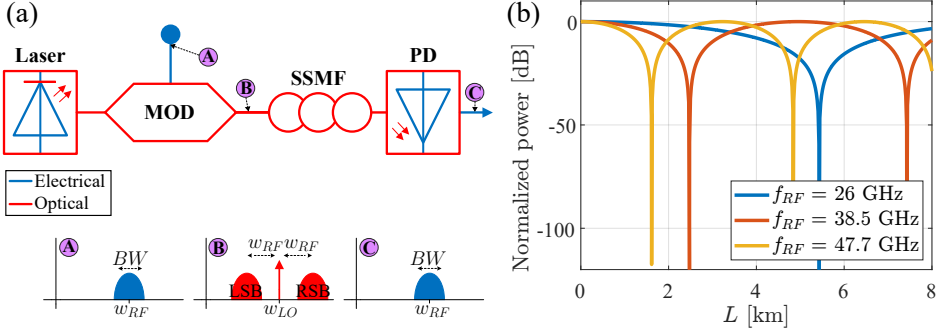


Figure 2.4: RF induced power fading in the optical fiber: (a) basic schematic for modulating an RF signal into the optical domain; (b) graph that represents the induced power fading effect by chromatic dispersion of the optical fiber as a function of the optical fiber length for different f_{RF} frequencies. LSB: left sideband; RSB: right sideband.

$$\beta(\omega) = \bar{n} \frac{\omega}{c} \approx \beta_0 + \beta_1(\Delta\omega) + \frac{1}{2}\beta_2(\Delta\omega)^2 + \frac{1}{6}\beta_3(\Delta\omega)^3, \quad (2.3)$$

where c is the speed light in the vacuum in m/s, $\Delta\omega = \omega - \omega_{LO}$, and $\beta_m = (d^m \beta / d\omega^m)$. From Eq. (2.2), two phenomena that occur in the optical fiber can be deduced: chromatic dispersion and non-linear refraction (non-linear effect). These two phenomena are explained in the following subsections. There other phenomena in the optical fiber such as polarization mode dispersion (PMD) or dispersion slope which are out of the scope of this dissertation [59], [60].

2.2.1 Chromatic dispersion

It is well known that the chromatic dispersion (D) results from the summation of the material dispersion (D_M) and the waveguide dispersion (D_W) [25], [61]. Additionally, from Eq. (2.3), the chromatic dispersion is directly related to β_2 with the following equation:

$$D = \frac{-\beta_2 \omega_{LO}^2}{2\pi c}. \quad (2.4)$$

According to the International System of Units (SI), the unit of the chromatic dispersion D is in s/m², although it is mostly expressed in ps/(nm · km). For SSMFs, 17 ps/(nm · km) of chromatic dispersion is a typical value at 1550 nm [55].

Figure 2.4(a) shows a basic schematic of transporting an RF signal over an optical fiber [62]. In addition, spectra at different points of the schematic are also represented in Fig. 2.4(a). In this schematic, an optical carrier with a specific angular frequency ω_{LO} is generated in the laser. Next, the RF signal is modulated with an optical modulator, producing a DSB signal in the optical domain (see inner plot of Fig. 2.4(a) labelled as (B)). Then, the resulted DSB signal travels along an

optical fiber and, thus, different phase rotations are originated in each band due to the chromatic dispersion effect of the optical fiber. Finally, the optical signal at the output of the SSMF beats in a PD, retrieving by heterodyne detection the introduced RF signal whose power is multiplied by a constant that depends on the phase mismatch of the two optical sidebands. This phenomenon is called RF power fading induced by chromatic dispersion and its power constant C_{PF} can be expressed as follows [63], [64]:

$$C_{PF} = \cos^2(\theta_{LSB} - \theta_{RSB}) = \cos^2(\pi cLD(\frac{\omega_{RF}}{\omega_{LO}})^2), \quad (2.5)$$

where θ_{LSB} and θ_{RSB} are the phase rotations induced by the chromatic dispersion of the fiber in the left and right sidebands, respectively. Observing Eq. (2.5), it can be noticed that C_{PF} presents nulls when the argument of the cosine is equal to $\pi/2 + n\pi$, with n being an integer number (\mathbb{Z}). These nulls depends on the carrier frequency of the RF signal (ω_{RF}) and the chromatic dispersion D and length L of the optical fiber. Fixing D and ω_{RF} , the distances of the optical fiber that produce nulls due to the chromatic dispersion can be calculated as:

$$L_{PF,k} = \frac{0.5 + k}{cD} \cdot \left(\frac{\omega_{LO}}{\omega_{RF}}\right)^2, \quad k \in \mathbb{Z}. \quad (2.6)$$

Figure 2.4(b) illustrates the effect of the power fading induced by chromatic dispersion, applying Eq. (2.5). In this example, the chromatic dispersion is 17 ps/(nm · km) at 1550 nm of wavelength and the power fading factor is calculated for three different frequencies. These three frequencies are the center points of the mm-wave 5G bands n258, n260, and n262, respectively (see Table 1.1). Furthermore, the optical fiber distances with power fading nulls coincide with Eq. (2.6). There are three main approaches to mitigate the RF power fading produced by the chromatic dispersion: compensate the phase mismatch after or in between the optical fiber [64]; suppressing one of the optical carriers in case of using an IF data signal and optical two-tone generation; or suppressing one of the optical sidebands by optical filtering or using IQ modulators to get a SSB signal [65]. Therefore, by employing the SSB schemes of Fig. 2.3, the power fading induced by chromatic dispersion is suppressed. Besides, SSB optical transmission is also a preferred option in terms of power efficiency.

It is worth mentioning that there are other effects produced in the transmitted pulses due to chromatic dispersion of the optical fiber [25], [66]–[68]: pulse broadening, chirping, and signal beating. Nevertheless, since the values of the distance and chromatic dispersion of the optical fiber are usually known, these chromatic dispersion effects can be efficiently compensated with, for instance, dispersion compensation fibers (DCFs), photonic crystal fibers (PCFs), or digital filters [69], [70].

2.2.2 Non-linear propagation effects

The second component of Eq. (2.2) depends on the power of the optical field. This fact leads to a non-linear phase shift (ϕ_{NL}) provoked by two phenomena [25]: self-phase modulation (SPM) and cross-phase modulation (XPM). Both phenomena are proportional to the total input power P_{in} [25]. The final ϕ_{NL} value is the result of the summation of both phenomenon phase shifts [71]:

$$\phi_{NL} = \phi_{SPM} + \phi_{XPM}. \quad (2.7)$$

SPM leads to frequency chirping and broadening of optical pulses [25], [72]. In this case, the frequency chirp is proportional to the derivative in time of the input power ($\frac{\partial P_{in}(t)}{\partial t}$) [25]. Therefore, an optical input signal, whose power substantially fluctuates, is affected by a high range of ϕ_{SPM} random values, complicating its post-compensation process. The expression of ϕ_{SPM} can be described as follows [25]:

$$\phi_{SPM}(t) = \gamma P_{in}(t) L_{eff}, \quad (2.8)$$

where $L_{eff} = [1 - \exp(-\alpha L)]/\alpha$ and $\gamma = k_0 \bar{n}_2 / A_{eff}$. The non-linear coefficient γ has a value of $1.3 \text{ W}^{-1} \cdot \text{km}^{-1}$ in SSF [73]. SPM results negligible for low optical input powers. However, if $L = 20 \text{ km}$, $\alpha = 0.2 \text{ dB/km}$, and $\gamma = 1.3 \text{ W}^{-1} \cdot \text{km}^{-1}$, when P_{in} reaches $\approx 6 \text{ mW}$, ϕ_{SPM} is considered significant ($\phi_{SPM} > 0.1$) and it cannot be easily compensated since it is not linear [25].

XPM is considered when more than one channel is transmitted simultaneously in the optical fiber. Hence, XPM must be taken into account in wavelength-division multiplexing (WDM) systems. Thereby, for WDM realization, the final non-linear phase shift of a channel with index n is described by the following equation [25], [74]:

$$\phi_{NL}^n(t) = \phi_{SPM}^n(t) + \phi_{XPM}^n(t) = \gamma L_{eff} \left(P_{in}^n(t) + 2 \sum_{m \neq n} P_{in}^m(t) \right). \quad (2.9)$$

It can be noticed from Eq. (2.9) that the value of ϕ_{NL}^n in a specific time depends on the introduced input power (P_{in}) of all the channels, making the complexity of the post-compensation process proportional to the number of channels.

Additionally, stimulated Brillouin scattering (SBS) is one of the main non-linear effects, affecting narrow-linewidth optical carriers [75]. In SMFs, SBS occurs in the backward direction with a certain frequency shift [25]. The power of this undesired backscattered wave is proportional to the input power [76]. Hence, the backscattered wave beats with the input signal, generating an acoustic wave [76]. As a consequence, the beating term intensifies the amplitude of the acoustic wave, which augments the amplitude of the backscattered wave, causing a positive feedback loop [25]. The SBS threshold (SBST) delimits the maximum input power where the backscattered wave increases rapidly due to this positive feedback loop

phenomenon. The SBST depends on the optical fiber length. For SSMFs with $L = 20$ km, the SBST is approximately 8 mW [76].

On the other hand, stimulated Raman scattering (SRS) is another non-linear effect in the optical fiber that is generally not a relevant impairment in optical single channel communications due to its high power threshold (≈ 500 mW) [25]. However, SRS is considered a concern in WDM systems because Raman amplification is used in these systems [25], [77]. Finally, there are other non-linear effects in the optical fiber, such as four-wave mixing, although, the interest of these non-linear effects is minor in the study cases of this dissertation [25], [78].

2.3 mm-wave ARoF signal detection

There are two main categories of coherent optical detection [45]: homodyne and heterodyne. The homodyne receiver employs the same wavelength used in the transmitter while the heterodyne one uses a different wavelength. In the classical approach, homodyne and heterodyne detections refer to add an optical local oscillator (LO) at the receiver side. For the optical mm-wave transportation, an optical two-tone generation is needed at the transmitter, dispensing with the optical LO at the receiver. Therefore, optical mm-wave transportation is intrinsically related to heterodyne detection and only requires a PD in the receiver [79].

Considering the two-tone generation block explained in subsection 2.1.1, two optical carriers are generated with different wavelengths. Then, regarding the SSB case of Fig. 2.3, one of these tones is used for the optical data modulation described in subsection 2.1.2. The data signal formulation in the electrical domain can be expressed with the following equation:

$$s(t) = A_s(t)e^{j(\omega_{IF}t + \varphi_s(t))}, \quad (2.10)$$

where A_s and φ_s refer to the amplitude and phase of the data signal, respectively. In Eq. (2.10), ω_{IF} corresponds to the employed IF frequency. In the baseband case of the data signal, ω_{IF} is equal to 0. After optical modulation of the data signal, one tone is unmodulated and the other is modulated with $s(t)$. As a result, there are three optical signals: the two optical tones and a modulated DSB signal in case of IF data. These optical signals can be expressed as follows [79], [80]:

$$E_{LO-1}(t) = \sqrt{P_1} e^{-j(\omega_{LO-1}t + \varphi_1(t))} \quad (2.11)$$

$$E_{LO-2}(t) = \sqrt{P_2} e^{-j(\omega_{LO-2}t + \varphi_2(t))} \quad (2.12)$$

$$E_s(t) = \sqrt{P_s} A(t) e^{-j((\omega_{LO-2} \pm \omega_{IF})t + \varphi_2(t) + \varphi_s(t))}, \quad (2.13)$$

where $\sqrt{P_1}$, $\sqrt{P_2}$, and $\sqrt{P_s}$ refer to the optical amplitude of the first tone, second tone, and the optical data signals, respectively. In Eqs. (2.11) and (2.12), φ_1 and φ_2 correspond to the phase of each optical tone and these phases evolve during

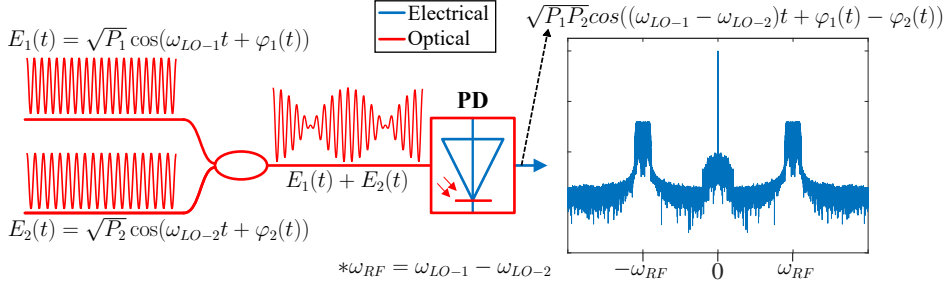


Figure 2.5: Representation of the mm-wave AROF signal detection process [79].

time. Examining Eq. (2.13), it can be noticed that the optical tone of Eq. (2.12) has been employed for the optical data modulation. Being the difference of ω_{LO-1} and ω_{LO-2} the desired RF frequency (ω_{RF}), the data signal is converted to ω_{RF} when the optical tone of Eq. (2.11) and the optical data signal of Eq. (2.13) beat in the PD. The resulting beating of these two optical signals in the PD can be formulated as follows [79]:

$$\begin{aligned}
 E_{PD}(t) &\propto |E_{LO-1}(t) + E_s(t)|^2 \propto \\
 &\propto \text{DC} + \sqrt{P_s P_2} A(t) \cos\left[\underbrace{[\omega_{LO-1} - \omega_{LO-2}]t}_{\omega_{RF}} + \underbrace{[(\varphi_1(t) - \varphi_2(t)) + \varphi_s(t)]}_{\varphi_l(t)}\right].
 \end{aligned} \tag{2.14}$$

In Eq. (2.14), the terms produced by the beating of Eq. (2.12) with Eq. (2.11) and Eq. (2.12) with Eq. (2.13) are not considered for simplicity. Examining Eq. (2.14), it can be noted that two sideband signals, located at $\omega_{RF} - \omega_{IF}$ and $\omega_{RF} + \omega_{IF}$, are generated after the PD. If the data signal is converted into the optical domain with an IQ modulator (see Figure 2.3), a SSB data signal is produced in the output of the PD at $\omega_{RF} + \omega_{IF}$ or $\omega_{RF} - \omega_{IF}$ [81]. Therefore, after the heterodyne process, the modulated data signal into the optical domain is upconverted to $\omega_{RF} + \omega_{IF}$ and/or $\omega_{RF} - \omega_{IF}$. Moreover, from Eq. (2.14), it can be observed that the phase of the data signal φ_s is combined with the result of the subtraction between the phase of the two optical tones ($\varphi_1(t) - \varphi_2(t) = \varphi_l(t)$). In other words, the phase of the data signal is affected by the phase noise caused by the incoherence of the optical tones ($\varphi_l(t)$). In the case of incoherent data signal, the phase noise $\varphi_l(t)$ does not affect the communication performance, since incoherent modulation format does not use the phase to code the information. However, in coherent modulation communications, the phase noise $\varphi_l(t)$ can significantly affect the communication performance and the selection of a proper two-tone signal generation technique is crucial (see Table 2.1).

Furthermore, a direct current (DC) component is reflected in Eq. (2.14). In addition, there are other higher frequency components that can be mathematically deduced from the beating of Eq. (2.11) with Eq. (2.13) such as $2\omega_{LO-1}$ and $2(\omega_{LO-2} \pm \omega_{IF})$. Nevertheless, these frequency components cannot be physically generated at the output of the PD because of their extremely high frequencies [82], [83].

It is worth mentioning that low frequency components at ω_{IF} and $2\omega_{IF}$ are also generated when the modulated optical tone of Eq. (2.12) and the optical data signal of Eq. (2.13) beat in the PD. Nonetheless, these frequency components do not belong to the desired RF frequency. Also, it is relevant to mention that the beating of Eq. (2.12) with Eq. (2.11) produced in the PD generates a frequency term at ω_{RF} , close to the band of interest. With proper RF filtering, this RF carrier at ω_{RF} and the remaining undesired frequency components can be filtered.

Figure 2.5 shows a representation of the heterodyne signal detection process to transport and generate a mm-wave carrier at angular frequency of ω_{RF} . In the spectrum plot of Fig. 2.5, it is assumed that one of the optical carriers (E_1 or E_2) is used to modulate the data signal in the optical domain. Moreover, observing the out-of-bands (OOBs) of the produced RF data signal in Fig. 2.5, it can be seen that this RF signal contains phase noise ($\varphi_I(t)$). The DC component is also represented in the spectrum graph of Fig. 2.5. After the ARoF signal detection, the obtained mm-wave signal is filtered and boosted. Thus, the resulting signal is ready to be transmitted in the mm-wave wireless channel.

2.4 mm-wave wireless channel

After the mm-wave ARoF signal detection, the obtained electrical signal might require amplification and filtering processes. Then, the resulting mm-wave signal is ready to be transmitted through the wireless channel. As commented in Section 1.1, compared to lower frequency bands, the usage of mm-wave signals leads to certain impairments. These impairments are the following:

- The received signal power suffers from a severe reduction due to the intrinsically high FSPL associated with high-frequency carriers [21]. This increase in FSPL can be compensated for by enhancing the gain of the antennas used in the wireless communication.
- Atmospheric attenuation, rain-induced fading, and foliage attenuation are higher in the mm-wave domain than in the sub-7 GHz bands, further limiting the power budget [21].
- Material penetration losses are substantially higher in mm-wave frequencies than in lower frequency bands, increasing the probability of a complete blockage in the line-of-sight (LOS) path [21], [35].

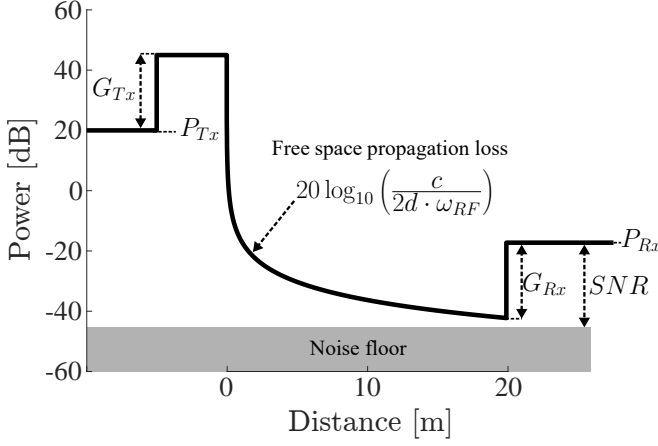


Figure 2.6: Representation of the power budget in a wireless scenario according to Friis' equation at 27.5 GHz of center frequency. The noise floor level depends on the employed devices in the communication system.

All the impairments listed above imply a high reduction of the communication power budget. Friis' equation allows to coarsely estimate the power budget of a wireless link as follows [84]:

$$P_{Rx}[dB] = P_{Tx}[dB] + G_{Tx}[dBi] + G_{Rx}[dBi] - FSPL[dB] \quad (2.15)$$

$$FSPL[dB] = 20 \log_{10}(d) + 20 \log_{10}(f_{RF}) - 147.55, \quad (2.16)$$

where P_{Rx} and P_{Tx} are the received and transmitted power, respectively. Moreover, G_{Tx} and G_{Rx} are the antenna gains in dBi. Inspecting the FSPL term of Eq. (2.16), it can be deduced that the received power P_{Rx} is inversely proportional to the carrier frequency f_{RF} . Since P_{Tx} is limited by safety matters, mm-wave amplifier output power, and efficiency limits, the alternative way to compensate for the increased FSPL due to the usage of higher frequencies consists of improving the antenna gain and beam steering capability in both the transmitter and receiver sides. Chapter 6 focuses on the implementation of beamforming solutions in mm-wave AROF wireless systems. Furthermore, it is worth mentioning that the other limiting power factors, such as the material penetration losses or atmospheric attenuation, are not included in the Friis' equation.

Figure 2.6 shows an illustration of Eq. (2.15). In Fig. 2.6, it can be observed that the transmitted power to the wireless channel depends on P_{Tx} and G_{Tx} . Then, at distance 0 m, there is a power step proportional to $-20 \log_{10}(f_{RF}) + 147.55$. After this step, the power logarithmically decays with the distance d according to $-20 \log_{10}(d)$. In the receiver side, the SNR is defined by the ratio between the received power P_{RX} and the noise floor level. It is important to highlight that amplification processes in the transmitter and receiver sides are not considered in

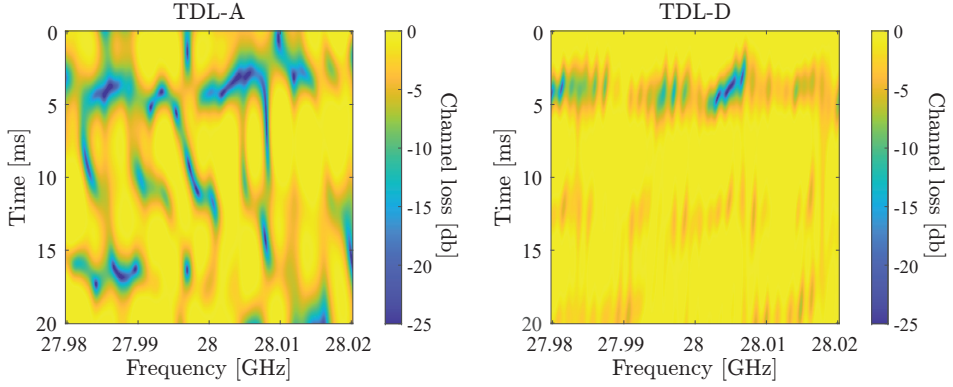


Figure 2.7: Power spectrum of the mm-wave channel loss in dB as a function of the time and frequency for two different TDL models [86]: TDL-A and TDL-D simulating NLOS and LOS communications, respectively.

the representation of Fig. 2.6. The application of these amplifications processes alters the final SNR, depending on the noise figure (NF) and gains of the employed amplifiers [85].

It is important to mention that phase noise increases as the carrier frequency does [87]. Therefore, compared to their frequency band predecessors, phase noise can be a more limiting performance factor in mm-wave scenarios. In addition, as in lower frequency bands, mm-wave signals suffers from other phenomena in the wireless channel, such as Doppler effect and power fading caused by multipath [88], [89]. The methods to mitigate the signal deterioration due to theses phenomena are well known and studied [90], [91].

3GPP defines a wireless channel model in [86] for frequencies from 0.5 GHz to 100 GHz. Therefore, K-band, K_a-band, and V-band are included in this model. The work of this dissertation is more focused on the first two mm-wave bands (K-band and K_a-band). In the standard of [86], different scenarios are specified, such as indoor office, urban micro (UMi)-street canyon or urban macro (UMa). Moreover, different tapped delay line (TDL) profiles are defined depending on the wireless channel characteristics.

For a realistic mm-wave mobile network scenario, the parameters to configure a model regarding the 3GPP standard of [86] can be the following: UMi is the selected scenario; the carrier frequency is set to 28 GHz (center frequency of n257 band, see Table 1.1); the user velocity is 3 km/h (table 7.6.4.2-5 of [86]); and the delay spread is established to 66 ns (table 7.7.3-2 of [86]). With the mentioned configuration parameters, the graphs of Fig. 2.7 are obtained by using the 5G toolbox of Matlab. The graphs of Fig. 2.7 show the frequency spectrum of the wireless channel loss in dB evolving during time. Furthermore, Fig. 2.7 represents two different TDL profiles: TDL-A with non-line-of-sight (NLOS) communication

and TDL-D with LOS communication.

Comparing the two graphs of Fig. 2.7, it can be noticed that the power fading, caused by the multipath phenomenon, is more severe in the TDL-A case. This fact is because the power fading levels in the frequency domain are inversely proportional to the power ratio between the first and second dominant rays. TDL-A describes a NLOS link and, thus, the power ratio between these two rays is lower. Also, it is important to mention that the frequency separation between consecutive power fade in the spectrum is inversely proportional to the delay spread of the channel. Another consideration, regarding the graphs of Fig. 2.7, is that the wireless channel is a linear time-invariant (LTI) system. This LTI property is mainly caused by the movement of the user and the rest of the components involved in the wireless scenario.

2.5 mm-wave signal detection and downconversion

After the transmission through the wireless channel, the data at a certain mm-wave frequency is retrieved in the received side. RF receivers are classically classified into two categories: coherent and incoherent. Coherent RF receivers are capable of demodulating IQ signals while incoherent ones only extract the amplitude of the received signal. In addition, depending on the downconversion strategy, RF receivers are categorized into homodyne and heterodyne systems. In homodyne receivers, the frequency of the LO is the same as the carrier of the received signal. In the case of heterodyne detection, the LO frequency is different from the received RF carrier.

The objective of this section is to explain the different techniques to recover the transmitted data through the mm-wave AROF wireless channel. For achieving this, the first step is to capture the transmitted signal from the wireless channel by utilizing either an antenna or an antenna array (AA) designed to operate at the specific mm-wave frequency. After the antenna or AA, filtering and amplification blocks are required. In this way, the mm-wave signal can be appropriately obtained. Then, the following step focuses on downconverting and demodulating the mm-wave data. Nowadays, the conventional, low-complex, and efficient manner to demodulate and recover the transmitted data through a channel consists of digitizing the received analog signal and demodulating the digitized signal in the DSP. Thus, the data can be properly recovered.

In general, there are three main approaches to digitize a mm-wave analog signal: sampling at the mm-wave, IF, or baseband domains. In the cases of sampling at the mm-wave and IF domains, the sampled signal is downconverted to the baseband domain in the DSP. There is a trade-off between complexity of the analog receiver and the sampling rate requirements of the employed ADCs. For instance, sampling the signal in the mm-wave domain dispenses with most of the analog components involved in the receiver while the ADC requirements are highly exigent [92]. In the opposite case, sampling in the baseband domain relaxes the ADC requirements

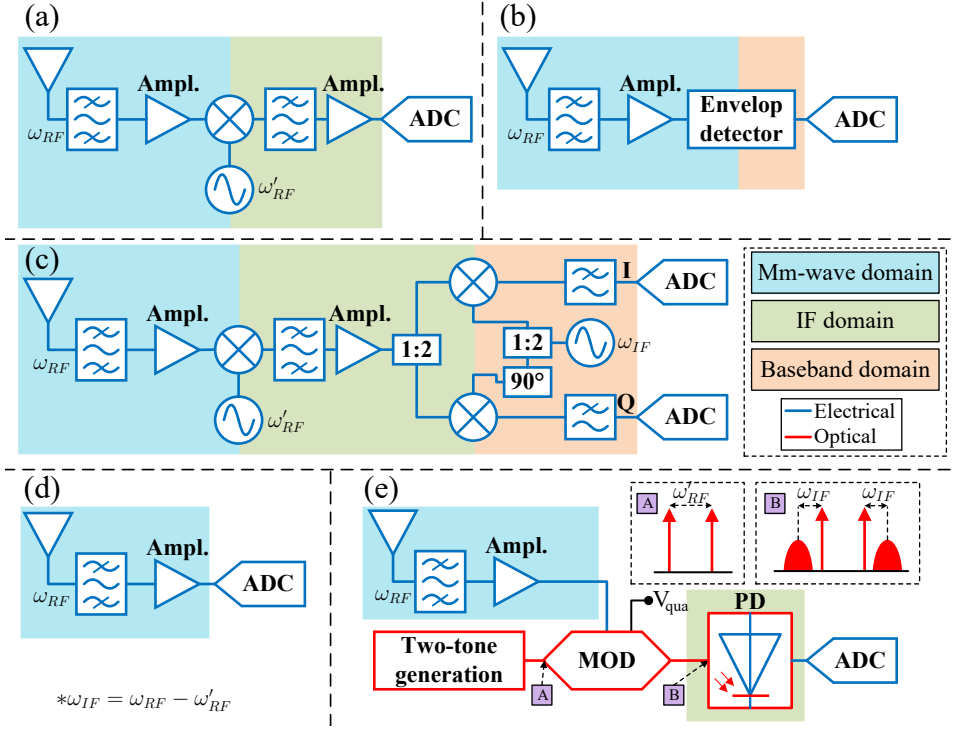


Figure 2.8: Schemes to detect and downconvert the mm-wave wireless signal: (a) digital-IF receiver; (b) receiver based envelope detection for baseband downconversion; (c) superheterodyne receiver with baseband digitization; (d) receiver based on direct mm-wave digitization (all software); (e) IF photonic downconversion receiver based on an optical modulator.

while the needed analog receiver system is more complex [93]. Figure 2.8 depicts different receiver schemes to detect and digitize the wireless mm-wave signal:

- a) **Digital-IF receiver** (Fig. 2.8(a)): this receiver utilizes an intermediate downconversion in the analog domain by employing a LO with a frequency ω'_{RF} different from the frequency ω_{RF} of the received signal [94]. After the mixing process, the signal is downconverted to an IF ($\omega_{IF} = \omega_{RF} - \omega'_{RF}$). Thus, the IF signal is sampled by an ADC and converted to the baseband domain in the DSP.
- b) **Receiver based envelope detection** (Fig. 2.8(b)): the use of RF envelope detectors is an alternative RF downconversion to RF mixers [95]. In this manner, a vector signal generator (VSG) to produce the LO carrier is not required, reducing the cost, volume, and energy consumption of the receiver. The RF envelope downconversion employs the square-law detection

for converting the mm-wave signal to the baseband domain. The drawback of this receiver is that the square-law detection implies signal-signal beat interference (SSBI) [96]. SSBI impedes directly recovering the data phase. DSP solutions, such as the Kramers-Kronig receiver, enable the phase recovery after the envelope detection [96]. Another way to transmit coherent modulation formats by using the receiver based envelope detection consists of downconverting the mm-wave signal to the IF domain. However, for achieving this, an RF carrier with an IF separation from the data must be combined with the data in the envelope process [97].

- c) **Superheterodyne receiver** (Fig. 2.8(c)): the architecture of the superheterodyne receiver employs two LOs [93], [98]. The first LO is utilized for converting the mm-wave signal to the IF domain. The resulting IF signal is mixed with the second LO. To recover the in-phase and quadrature signals a 90° RF phase shifter and 1:2 RF power splitter are employed. Therefore, with these two RF components, two RF carriers with a phase difference of 90° are obtained from the second LO. Then, by employing these two RF carriers, IQ signals can be independently sampled with two ADCs. The superheterodyne receiver requires many RF components to sample the received mm-wave signal. Nevertheless, this architecture highly reduces the requirements of the ADCs and the downconversion in DSP is not needed.
- d) **All software receiver** (Fig. 2.8(d)): the contrast solution to the superheterodyne architecture is the all software receiver [92]. In this architecture, the needed RF devices are those to detect the mm-wave wireless signal: antenna or AA, filter, and amplifiers. The downconversion process is realized in the DSP. In this manner, the analog complexity is highly reduced compared to the rest of the receiver architectures. However, since the sampling of the signal is performed in the mm-wave domain, the sampling rate of the employed ADC must comply with the following condition [99]: $f_s \geq 2f_{RF} + BW$, where BW is the bandwidth of the signal. Thereby, for mm-wave signals, the all software receiver is not a convenient solution due to the demanding ADC specifications and the cost attached to it.
- e) **Photonic downconversion** (Fig. 2.8(e)): photonic downconversion is an alternative manner to traditional RF approaches [100], [101]. The scheme of Fig. 2.8(e) shows one of the multiple ways to downconvert the received mm-wave signal by using photonic components. In this scheme, the optical two-tone signal generation block, explained in subsection 2.1.1, is combined with an optical modulator to convert the RF signal to the optical domain. In this case, the separation of the two tones is ω'_{RF} in order to sample the signal in the IF domain. Thus, the resulting optical spectrum after the optical modulator has an equivalent shape as the inner plot, labelled as B, of Fig. 2.8(e). Subsequently, the beating process in the PD enables to convert the received signal to the IF domain.

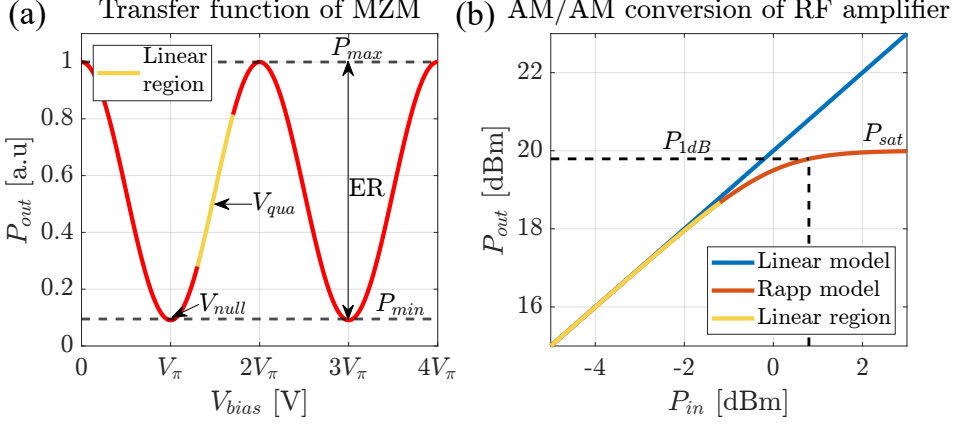


Figure 2.9: Transfer functions of two non-linear components involved in ARoF systems: (a) MZM; (b) RF amplifier. ER: extinction ratio.

In the scientific papers of this dissertation, all the experimental setups employ the digital-IF receiver of Fig. 2.8(a) since it offers an adequate trade-off between hardware and DSP complexity for mm-wave wireless communications.

2.6 Components with non-linear response in mm-wave ARoF wireless systems

In Section 2.2, it was remarked that the optical fiber produces linear and non-linear effects in the transmitted signal. In addition, there are other non-linear components in mm-wave ARoF wireless systems. Concretely, two of the most relevant ones in ARoF systems are: Mach-Zehnder modulators (MZMs) and RF amplifiers. The transfer function of a MZM with symmetric coupler and opposite driving voltages is given by the following equation [102]:

$$H_{MZM} = \frac{E_{out}}{E_{in}} = \cos\left(\frac{\Phi[V(t)]}{2}\right) \cdot \cos(\omega_{LO}t), \quad (2.17)$$

where $V(t)$ is the applied driving voltage, E_{in} , and E_{out} are the input and output electromagnetic fields of the MZM, respectively. Furthermore, in Eq. (2.17), $\Phi[V(t)]$ is the optical carrier phase difference in the different branches of the MZM and it expressed as:

$$\Phi[V(t)] = \pi \frac{V(t)}{V_\pi}, \quad (2.18)$$

where V_π is the half-wave voltage of the MZM. It is important to mention that the extinction ratio (ER) impairment of MZMs is not included in Eq. (2.17). ER

indicates the ratio between the maximum and minimum powers that the MZM provides (P_{max} and P_{min}). Hence, a finite ER implies that the minimum power given by the MZM is not totally null [103]. Therefore, ER leads to a degradation of the final SNR since it indirectly increases the overall noise floor level of the system.

Figure 2.9(a) shows the power form of Eq. (2.17), highlighting the linear region and the ER of the MZM. With the objective to operate in the quadrature point of the MZM, the biased voltage V_{bias} must be set to the value: $V_{qua} = 0.5V_{\pi} + nV_{\pi}$, $n \in \mathbb{Z}$. As it can be noticed, the MZM function, represented in Fig. 2.9(a), is more linear in the points close to V_{qua} and becomes less linear in the points close to nV_{π} . Therefore, there is a trade-off between non-linear degradation of the signal and obtaining the maximum SNR by covering the full operation power range of the MZM.

RF amplifiers also feature a non-linear transfer function. The Rapp model describes the amplitude/amplitude (AM/AM) conversion of an RF amplifier [104]. Power saturation (P_{sat}) and 1 dB compression power (P_{1dB}) are two important power parameters to characterize the behavior of RF amplifiers. The AM/AM conversion of a particular RF amplifier is represented in Fig. 2.9(b), by using the linear and Rapp models. In this figure, the input and output powers (P_{in} , P_{out}) of the RF amplifier are plotted in dBm. The linear model of the AM/AM conversion for an RF amplifier is also illustrated in Fig. 2.9(b). By comparing the linear and Rapp models in Fig. 2.9(b), the linear operation region of the RF amplifier can be delimited. Hence, as in the MZM case, there is a trade-off between non-linear degradation of the signal and the power level or SNR at the output of the RF amplifier.

Peak-to-average power ratio (PAPR) is one of the drawbacks related to multi-carrier waveforms, such as OFDM [105]. A waveform signal with high PAPR suffers from severe non-linear degradation when it passes through non-linear components. Therefore, waveform signals with high PAPR are sensitive to non-linear distortion in ARoF components such as MZMs and RF amplifiers [106], [107].

2.7 Summary of mm-wave ARoF wireless impairments

In previous sections of this chapter, the fundamentals and impairments of the different blocks that compound a mm-wave wireless ARoF system are individually described and explained. Nonetheless, there are general impairments that affect any communication system such as the additive white Gaussian noise (AWGN) or dynamic range. Therefore, as a summary of Chapter 2, the main impairments of mm-wave ARoF wireless systems are compiled and listed below:

- **Non-linearity:** non-linear effects occur in ARoF components such as MZMs, optical fiber, RF amplifiers, DACs, or ADCs. In most cases, the non-linear

effect is intensified or starts to be significant when the introduced input power to the non-linear component overcomes a certain limit, as in the optical fiber case. In long-distance communications, both in the optical and wireless domain, the required transmission power is high and, hence, non-linear regions of some devices can be reached. As a consequence, the transmitted signal suffers from non-linear degradation that requires complex techniques to compensate for it [108].

- **AWGN noise:** in many communications systems, AWGN noise is a limiting factor that reduces the overall capacity [17]. ARoF components, such as PDs, lasers, or optical amplifiers, add noise to the transmitted signal. Moreover, as commented in Section 2.4, mm-wave signals suffer from high attenuation in the wireless channel, limiting the power budget of the system. Therefore, for overcoming this high attenuation, RF amplification is required. However, RF amplification augments the noise floor [85]. Thereby, in mm-wave ARoF wireless scenarios, the noise floor is increased along the system, remarking as a limiting factor to increase the data rate.
- **Dynamic range:** the combination of the noise floor together with the non-linear region establishes a specific power area where the signal is not fully covered by noise and not degraded by non-linear effects. This area corresponds to the dynamic range (see Fig. 2.10). In mm-wave ARoF wireless scenarios, the components involved in the system squeeze the power margin between the non-linear region and noise floor, severely diminishing the dynamic range. This fact leads to a reduction of the SNR. In addition, signals with high PAPR, such the 5G standardized OFDM signal, compress even more the dynamic range area. A direct way to increase the SNR consists of approaching close or even reaching the non-linear region at the price of increasing the complexity in the receiver by compensating the non-linear degradation in the received signal.
- **Phase noise:** the phase noise level of RF oscillators is proportional to the carrier frequency [87]. Hence, signal degradation due to phase noise is higher in mm-wave channels than in sub-7 GHz channels. Furthermore, for the optical mm-wave transport, the optical two-tone generation methods explained in subsection 2.1.1 are more likely to have higher phase noise levels than conventional RF oscillators due to the incoherence between the two tones [32]. For some two-tone signal generation approaches, such as the OPLL technique of Fig. 2.2(d), the resulting phase noise of the produced mm-wave carrier, after the PD beating, is larger than in the employed RF oscillators [47]. Therefore, phase noise is a critical limiting factor in mm-wave ARoF systems.

According to the mm-wave ARoF impairments mentioned above, the following chapters of this dissertation aim to reduce their effect: Chapter 3 compares qualitatively and experimentally the main modulation format candidates in mm-wave

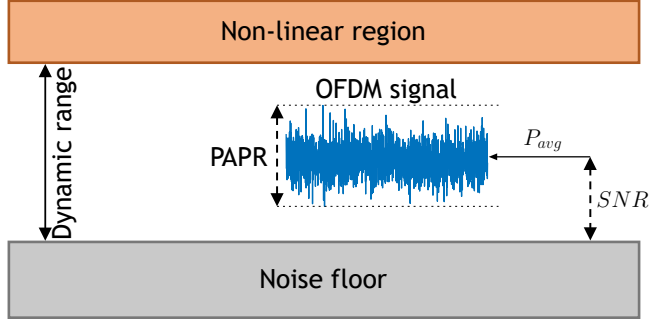


Figure 2.10: Dynamic range representation in mm-wave ARoF wireless systems with OFDM transmission case. P_{avg} : average power.

ARoF wireless systems, facilitating the waveform selection that adapts better to the channel conditions; Chapter 4 is focused on the study, analysis, and compensation of phase noise in mm-wave ARoF systems oriented towards 5G/6G communications; Chapter 5 targets a robust and optimized system level implementation for mm-wave ARoF wireless solutions, taking into account the aforementioned impairments; Chapter 6 focuses on amending the power limitation in mm-wave ARoF wireless systems by investigating two different beamforming approaches in these systems.

Waveforms and digital signal processing for mm-wave ARoF systems

The contribution of this chapter attempts to answer the research questions **RQ-1**, **RQ-2**, and **RQ-3**. For that, several KPIs, that are related to the type of transmitted waveform through the mm-wave ARoF wireless channel, are defined. Hence, the main waveform candidates for 5G/6G communications are qualitatively compared by using these defined KPIs as figures of merit [109], [110]. This qualitative comparison allows identifying the most suitable waveform candidates for a given scenario, paving the path to further determined the best waveform(s). Nonetheless, a qualitative comparison is not conclusive enough to determine the best waveform(s) for the mm-wave ARoF channel. Therefore, a comparison of the 5G/6G waveform candidates in an experimental setup provides more compelling results than a qualitative comparison. Thus, first, in Section 3.1, the main waveform candidates for 5G/6G systems are explained. Second, and in the same section, it is defined several KPIs that serve as figures of merit for estimating the suitability of the waveforms under evaluation for transmission in mm-wave ARoF wireless systems. Next, it is described the experimental setup used to perform the quantitative comparison between the waveforms under evaluation. Finally, the experimental results are analyzed and studied, providing conclusions related to the waveform candidates that best suit mm-wave ARoF wireless systems.

Section 3.2 studies the feasibility of applying PAS solutions to mm-wave ARoF systems. PAS algorithms have been thoroughly studied, analyzed, and evaluated in long-distance optical fiber communications, exhibiting improved capacity over traditional uniform M-QAM modulations and modulation schemes such as the bit-loading technique. This improved capacity through the use of PAS solutions is

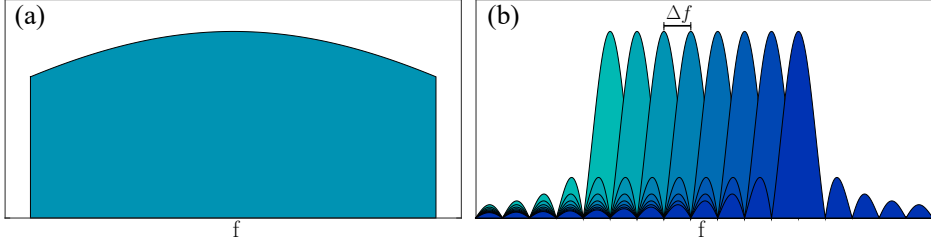


Figure 3.1: Spectrum representation of: (a) single-carrier (SC) waveform; (b) and a multi-carrier (MC) waveform. $\Delta f \rightarrow$ frequency spacing between subcarriers.

because PAS enables fine adaptation of the waveform to the channel conditions by modifying the probabilistic distribution of the M-QAM constellation, as detailed in [111], [112]. Thereby, the implementation of PAS algorithms on mm-wave ARoF channels is a potential candidate to enhance communication performance. In particular, in that Section 3.2, PAS is performed on the M-QAM data subcarriers of OFDM signals (PAS-OFDM). For a proper study and analysis, Section 3.2 also explains the theoretical fundamentals of PAS and the benefits of PAS-OFDM to alleviate signal degradation caused by the impairments of mm-wave ARoF wireless systems. Additionally, Section 3.2 proposes a novel soft PAS demapping algorithm that allows the reduction of the final bit error rate (BER) by harnessing the redundancy included in the PAS blocks.

3.1 Waveforms for mm-wave ARoF 5G/6G communications

Typically, waveforms can be divided into two main categories: single-carrier (SC) and multi-carrier (MC) waveforms. The main difference between these two categories is the physical dimension in which data is modulated: SC waveforms modulate the data in the time domain while MC waveforms in the frequency domain. Due to this fact, SC and MC waveforms offer different characteristics. For instance, the spectrum shape of SC and MC waveforms have different properties, as can be seen in Fig. 3.1.

Another distinction between SC and MC waveforms lies in the shape of the time domain signal. MC waveform signals typically exhibit a higher PAPR than SC waveform signals. This high PAPR matter is one of the main drawbacks of MC waveforms, as commented in the previous chapter. On the other hand, MC waveforms are more robust to multipath effect than SC waveforms because of their frequency properties. There are other features that characterize waveforms, such as phase noise robustness, complexity, or spectral efficiency. These features are discussed in the next subsection.

Thus, and starting with SC waveforms, there are not many candidates for 5G/6G communications as they are not able to allocate resources in the frequency domain [113]. On the contrary, MC waveforms are capable of multiplexing resources in time and frequency domains due to their frequency properties. In LTE, OFDM allows allocation of resource blocks (RBs) in time and frequency domains [114]. This resource allocation feature offers an easy and optimized way to distribute resources among different users in a mobile cell [115]. One of the most widely employed and researched SC waveforms in the mobile communication literature is the denominated single-carrier quadrature amplitude modulation (SC-QAM).

Concerning the MC waveforms, the main candidates in the next 5G/6G standards are [109], [110], [116]: orthogonal frequency-division multiplexing (OFDM), filter bank multi-carrier (FBMC), universal filtered multi-carrier (UFMC), and generalized frequency division multiplexing (GFDM). There are other waveforms that are not pure SC or MC modulation formats. These waveforms can be defined as hybrid SC/MC modulation formats and offer combined properties of SC and MC signals. Two popular hybrid SC/MC waveforms are: single-carrier frequency-division multiplexing (SC-FDM) (standardized waveform for uplink communication in LTE and 5G [19]) and multi-band carrierless amplitude and phase modulation (Multi-CAP) [117]. One of the main contributions of **P1** concerns the explanation and description of the aforementioned 5G/6G waveform candidates, comparing their functionality schemes.

3.1.1 Waveform KPIs in mm-wave ARoF wireless systems

The KPIs, which serve as figures of merit to determine the most suitable waveform in a specific mm-wave ARoF wireless scenario, can be clustered into three categories: KPIs for general wireless systems, KPIs for mm-wave wireless communications, and KPIs in ARoF systems. **P1** enumerates and explains the main KPIs of mm-wave ARoF wireless systems according to these three categories. In particular, the PAPR of the waveform under test is considered one of the most relevant KPIs in general wireless communications. As discussed in Chapter 2, the importance of the PAPR is due to the non-linear effects produced in widely used generic devices, such as RF amplifiers, DACs, or ADCs, when the input signals have a high PAPR value.

PAPR is one of the most challenging impairments in the standardized OFDM waveform [105], [118]. The PAPR value in OFDM signals is directly proportional to the number of subcarriers (N_{SC}) or, in other words, to the length of the inverse discrete Fourier transform (IDFT) [119]. Figure 3.2(a) shows the cumulative distribution function (CDF) of the PAPR of OFDM signals with different numbers of subcarriers (N_{SC}). These PAPR CDF results have been obtained by Monte Carlo simulations. By observing Fig. 3.2(a), the dependence of the PAPR value on the number of subcarriers can be clearly seen. The resulting bandwidth of an OFDM

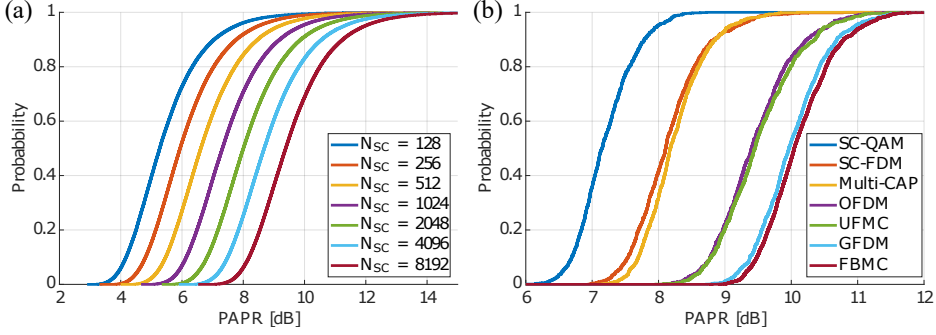


Figure 3.2: PAPR comparison for different 5G/6G waveform candidates: (a) PAPR CDF of OFDM signals for different numbers of subcarriers (N_{SC}); (b) PAPR comparison for the main waveform candidates in 5G/6G systems ($N_{SC} = 4096$).

signal can be roughly calculated as follows:

$$BW_{OFDM} = N_{SC} \cdot \Delta f, \quad (3.1)$$

where Δf is the frequency separation between subcarriers. In Eq. (3.1), all N_{SC} subcarriers are assumed to be active. By targeting a specific value of BW , N_{SC} is reduced if Δf is incremented. In this manner, the final PAPR of the resulting OFDM signal is diminished at the price of incrementing Δf . However, as the value of Δf decreases, channel estimation performance and robustness to multipath degrade because of the lower subcarrier resolution in the frequency domain [120], [121]. Therefore, there is a trade-off between channel estimation yields, multipath robustness, and PAPR.

Figure 3.2(b) depicts the PAPR CDF of the main 5G/6G waveforms mentioned above. The results in Fig. 3.2(b) have also been obtained with Monte Carlo simulations. The different waveform parameters of these simulations are set to have the same bandwidth, number of subcarriers (in the case of MC waveforms), and bit rate for all waveforms under test. In this way, a fair comparison of the PAPR behavior of such waveforms is realized. By inspecting Fig. 3.2(b), it is evident that MC waveforms (OFDM, UPMC, GFDM, and FBMC) exhibit larger PAPR values than SC-QAM. Methods to reduce PAPR can be applied to MC waveforms. Nonetheless, apart from additional complexity, the application of these PAPR reduction methods implies at least one of the following drawbacks: power increase, bandwidth expansion, or BER degradation [122]. Furthermore, for hybrid SC/MC waveforms, the PAPR values of SC-FDM and Multi-CAP are between the PAPR values of pure SC and MC waveforms. Hence, as mentioned above, hybrid SC/MC waveforms offer combined characteristics between pure SC and MC waveforms.

There are other KPIs, such as OOB emissions, spectral efficiency, or robustness to frequency-selective channels, that determine the suitability of a waveform

in mm-wave ARoF wireless systems. **P1** profoundly covers and exposes the main KPIs for a waveform in mm-wave ARoF wireless systems, marking the interconnection and relationship between the different KPIs.

3.1.2 Waveform comparison in mm-wave ARoF wireless systems

By using a set of KPIs, **P1** performs a qualitative comparison between the leading waveform candidates for mm-wave ARoF 5G/6G communications. In such a manner, depending on the ARoF and mm-wave wireless characteristics, the most suitable waveform can be decided by inspecting this qualitative comparison. Moreover, **P1** exposes the most used waveforms in ARoF experiments during the last ten years, highlighting OFDM and SC waveforms as the most popular in this research field.

The qualitative comparison of **P1** serves to give an overview to determine the most adequate waveform. However, a qualitative comparison lacks empirical arguments to clearly choose the best waveform in a determined channel scenario. Hence, an experimental comparison is able to provide more arguments to select the most suitable waveform or waveforms. **P2** carries out an experimental mm-wave ARoF wireless setup at 26 GHz of carrier frequency (n258 band, see Table 1.1). This experimental setup is performed on a 9 m wireless link where the transmitting and receiving antennas are aligned and remain static, having a LOS. In the experimental setup of **P2**, the aforementioned waveform candidates are compared with equivalent configuration parameters in order to achieve the same bandwidth, bit rate, subcarrier spacing, and number of subcarriers. Thereby, a fair comparison is made and the most suitable waveform(s) under test can be selected by inspecting the BER results. For the implemented mm-wave ARoF wireless case in the experimental setup of **P2**, SC-FDM and Multi-CAP stand out as the best waveforms in terms of BER because of their relative low PAPR levels (see Fig. 3.2(b)). The conclusions of **P2** point out that a re-evaluation of the used waveform must be accomplished in future 5G/6G standards for mm-wave ARoF wireless scenarios.

3.2 Probabilistic amplitude shaping in mm-wave ARoF wireless systems

The objective of PAS consists of altering the probabilistic distribution of a pulse-amplitude modulation (PAM) signal. In such a manner, the distribution of the signal can adapt to the channel conditions and, thus, optimize the communication performance [111]. In the literature of communication systems, constant composition distribution matching (CCDM) is the most investigated solution to perform PAS. However, CCDM approach is highly inefficient in terms of rate loss and energy-efficiency when short PAS blocklengths are required [123], [124]. In

URLLCs scenarios, for example, short blocklengths are highly necessary to avoid an increase in the overall latency due to the package encapsulation and decapsulation processes. In contrast to CCDF solution, other PAS algorithms, such as enumerative sphere shaping (ESS) or shell mapping (SM), are more energy-efficient for short blocklengths [123], [125]. In particular, the ESS approach of [125] is a suitable PAS solution because of its low computational complexity, low rate loss, and high energy efficiency [123].

The application of PAS to SC-QAM signals has been shown to provide an improved channel capacity utilization in optical fiber communications, compared to the classic uniform QAM approach [111], [112]. One of the reasons for this capacity improvement is that PAS-QAM signals are less sensitive than uniform QAM signals to non-linear degradations in the optical fiber [111]. Furthermore, PAS-QAM with fixed forward error correction (FEC) performs better in terms of performance and rate adaptability than other modulation scheme solutions, such as uniform QAM with variable FEC or time-division hybrid modulation (TDHM) with fixed FEC [111].

To perform PAS on uniform QAM signals, a probability distribution conversion must be applied in each dimension: in-phase and quadrature dimensions, specifically. In this manner, the distribution of the resulting QAM symbols is not uniform and, thus, low-power QAM symbols are more frequent than high-power ones. The Maxwell-Boltzmann distribution is one of the most common choices for this distribution conversion and its probability for a given QAM symbol x_i of the IQ constellation is expressed as follows [112]:

$$P_X^*(x_i) = \frac{1}{\sum_{j=1}^M e^{-\nu|x_j|^2}} e^{-\nu|x_i|^2}, \quad (3.2)$$

where M determines the modulation order of the QAM signal (M-QAM). Furthermore, the parameter ν of Eq. (3.2) is a scaling factor that determines the probability ratio between the low-power and the high-power QAM symbols. In other words, the value of ν intensifies the probability of low-power QAM symbols while reducing the probability of high-power QAM symbols. For ν equal to 0, the resulting distribution is uniform. Figure 3.3 shows the Maxwell-Boltzmann distribution of Eq. (3.2) for different values of ν in a 64-QAM constellation. As it can be observed in Fig. 3.3, the probability of the inner QAM symbols of the constellation is directly proportional to ν .

For SC waveform transmissions, the achievable information rate (AIR) is a good figure of merit for estimating the amount of information that can be recovered from an ideal bit-metric decoding (BMD) scheme [126]. In an AWGN channel, an AIR for this BMD scheme is the BMD rate (R_{BMD}). R_{BMD} can be estimated with the

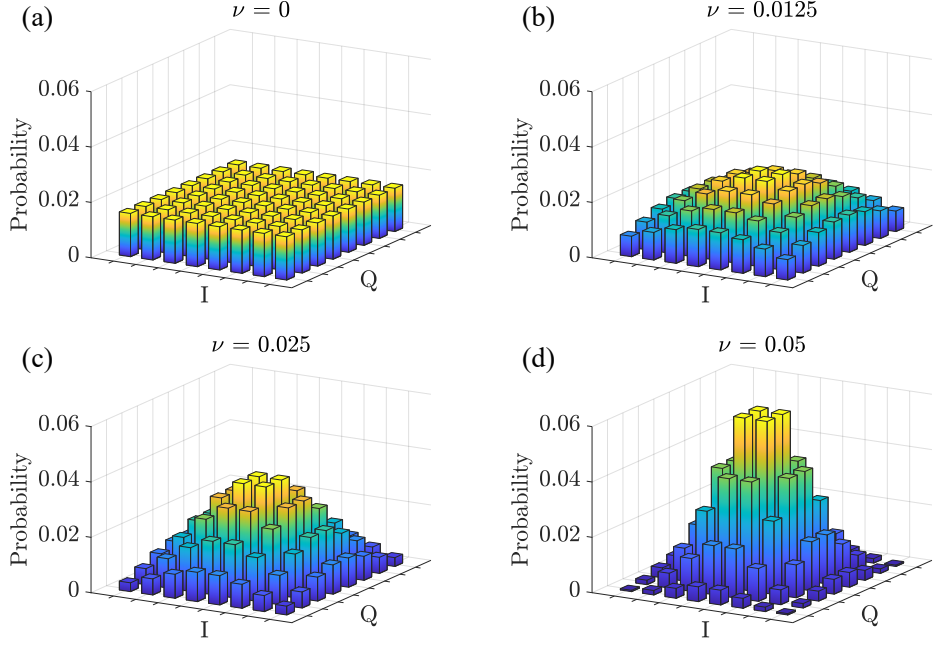


Figure 3.3: Maxwell–Boltzmann distribution in 64-QAM constellation for different values of ν .

following equation [112], [126]:

$$R_{\text{BMD}} \approx \frac{1}{N} \sum_{k=1}^N [-\log_2 P_X(x_k)] - \frac{1}{N} \sum_{k=1}^N \sum_{i=1}^s \left[\log_2 \left(1 + e^{(-1)^{b_{k,i}} \Lambda_{k,i}} \right) \right], \quad (3.3)$$

where s indicates the number of bits that each M-QAM symbol contains and b refers to the transmitted bit in the k -th M-QAM symbol in the i -th bit-level position. Also, $\Lambda_{k,i}$ is the log-likelihood ratio (LLR) of an AWGN channel and can be calculated as follows [112], [126]:

$$\Lambda_{k,i} = \log \frac{\sum_{x \in \chi_1^i} e^{-\frac{|y_k - x|^2}{2\sigma^2}} P_X(x)}{\sum_{x \in \chi_0^i} e^{-\frac{|y_k - x|^2}{2\sigma^2}} P_X(x)}, \quad (3.4)$$

where χ_1^i and χ_0^i denote the set of M-QAM symbol points where the i -th bit-level position is 1 or 0, respectively. The parameter σ of Eq. (3.4) determines the standard deviation of the AWGN noise while the parameter y refers to the received M-QAM symbol.

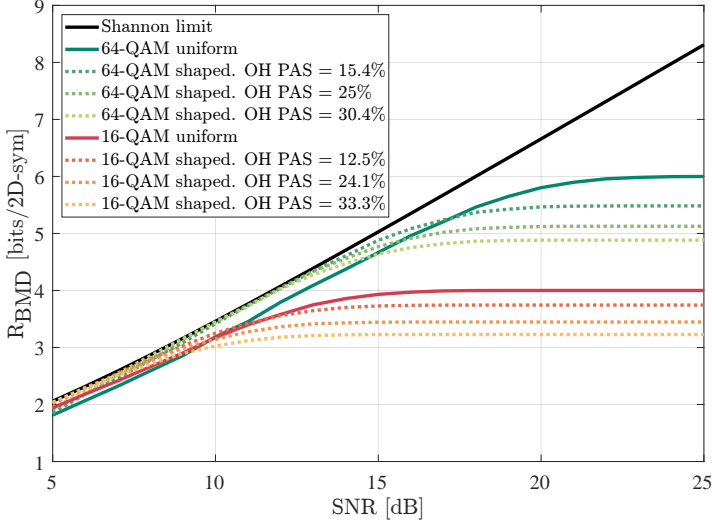


Figure 3.4: Bit-level AIR as a function of SNR in an AWGN channel for different M-QAM configurations: uniform (continuous lines) and PAS (dotted lines). OH: overhead.

Curves in Fig. 3.4 have been obtained with Monte Carlo simulations and by estimating R_{BMD} as Eq. (3.3) indicates. These Monte Carlo simulations emulate an AWGN channel where the SNR is gradually increased. In this simulation, different M-QAM configurations have been evaluated: 16-QAM/64-QAM uniform/shaped. Moreover, Shannon limit of Eq. (1.1) is also represented in the results of Fig. 3.4. By inspecting Fig. 3.4, it can be noticed that the shaped or PAS M-QAM configurations provide higher R_{BMD} , reducing the gap between channel capacity and Shannon limit. In addition, it is important to mention that PAS implementations allow a fine gradual adaptation of the final throughput depending of the channel conditions (SNR in AWGN channels). In other words, PAS offers a small throughput separation between consecutive modulation scheme configurations, allowing it to be finely matched to the current condition of the channel (see small steps between the different PAS configurations in Fig. 3.4).

By observing Fig. 3.4, it is shown that PAS-QAM signals provide more R_{BMD} than conventional uniform QAM solutions, especially for low SNR values. However, R_{BMD} cannot properly reflect the gain of using PAS in multi-carrier modulations such as OFDM. Furthermore, Eq. (3.3) is only valid for AWGN channels and is not adequate for non-linear channels as the ARoF link. Besides, the theoretical calculation of the bit-level AIR of PAS-OFDM signals in mm-wave ARoF wireless channels is highly complex. Hence, evaluation of different PAS-OFDM configurations in experimental mm-wave ARoF wireless testbeds is an alternative to appraise the possible improvements of using PAS-OFDM solutions.

P3 highlights the benefits of applying PAS in mm-wave ARoF wireless sys-

Table 3.1: Overview of experimental ARoF setups applying PAS algorithms for mm-wave 5G/6G communications. DM: distribution matching; IFoF: intermediate frequency-over-fiber; IM-DD: intensity-modulation and direct-detection.

Date	Operation frequency	System description	PAS algorithm	Modulation format	Ref
07/'19	Baseband	Optical long-haul setup	ESS vs CCDM (comparison)	64-QAM	[124]
07/'19	97 GHz	mm-wave ARoF wireless setup	DM (not specified)	PAS-OFDM	[126]
12/'19	Baseband	IM-DD setup	CCDM	PAS-OFDM	[127]
03/'20	60 GHz	IFoF wireless setup	CCDM	PAS-OFDM	[128]
06/'22	26 GHz (DL & UL)	mm-wave ARoF wireless for DL & IFoF wireless for UL	ESS	PAS-OFDM (5G)	P3






tems. More specifically, in **P3**, PAS-OFDM is identified as a promising modulation scheme as it enables to gradually mitigate the impact of three of the main impairments in mm-wave ARoF wireless systems: phase noise, non-linear effects, and reduced received power. Also, **P3** evaluates an ESS scheme applied to the M-QAM data subcarriers of OFDM signals which are transmitted through a bidirectional mm-wave ARoF wireless setup. This setup is thoroughly explained in **P10** (Chapter 5). The experimental results of **P3** exhibit a significant enhancement when the ESS scheme under test is employed, compared to the classic bit-loading scheme. Moreover, **P3** proposes a simple soft ESS demapping algorithm that allows to reduce the final BER by harnessing the PAS redundancy included in the ESS block.

Table 3.1 presents the state-of-the-art (SOTA) on ARoF experiments where PAS algorithms are evaluated. As it can be observed in Table 3.1, there is a research gap in experimental ARoF demonstrations oriented towards mm-wave 5G/6G fronthaul where PAS solutions are tested. **P3** fills this research gap by providing experimental results where the BER improvements by using PAS-OFDM can be quantified. Moreover, for the first time (to the best of the author's knowledge), **P3** evaluates an ESS scheme in an experimental mm-wave ARoF wireless setup following the 5G standard.

P1: Candidate Waveforms for ARoF in Beyond 5G

J. P. Santacruz, S. Rommel, U. Johannsen, A. Jurado-Navas, and I. Tafur Monroy, “Candidate Waveforms for ARoF in Beyond 5G,” *Applied Sciences*, vol. 10, no. 11, Jun. 2020. DOI: [10.3390/app10113891](https://doi.org/10.3390/app10113891)

Candidate Waveforms for ARoF in Beyond 5G

Javier Pérez Santacruz ^{1,*}, Simon Rommel ¹, Ulf Johannsen ², Antonio Jurado-Navas ³
and Idelfonso Tafur Monroy ¹

¹ Institute for Photonic Integration, Eindhoven University of Technology,

5600MB Eindhoven, The Netherlands; s.rommel@tue.nl (S.R.); i.tafur.monroy@tue.nl (I.T.M.)

² Centre for Wireless Technology, Eindhoven University of Technology, 5600MB Eindhoven, The Netherlands; u.johannsen@tue.nl

³ Department of Communications Engineering, University of Málaga, 29071 Málaga, Spain; navas@ic.uma.es

* Correspondence: j.perez.santacruz@tue.nl; Tel.: +34-681-230-250

Received: 7 May 2020; Accepted: 30 May 2020; Published: 4 June 2020



Abstract: 5G mobile networks aim to support a large variety of services with different and demanding requirements. To achieve this, analog radio over fiber (ARoF) fronthaul along with millimeter-wave (mmWave) cells is a strong candidate to be part of the 5G architecture. Very high throughput can be achieved by using mmWave signals due to the large available bandwidths, which combines well with the advantages of employing ARoF technology. Nevertheless, combined mmWave and ARoF systems face a particular challenge as the impacts of both channels—such as high free-space path loss, phase noise, chromatic dispersion, and other degrading effects—affect the signal without the possibility for intermediate restoration. The selection of the signal waveforms plays an important role in reducing these defects. In addition, waveforms are one of the keys in the physical layer available towards satisfying the requirements for 5G and beyond. In this manuscript, several key requirements are presented to determine the merit of candidate waveform formats to fulfill the 5G requirements in the mmWave ARoF architecture. An overview of the different suitable waveforms for this architecture is provided, discussing their advantages and disadvantages. Moreover, a comprehensive comparison in terms of different requirements is also presented in this paper.

Keywords: 5G; ARoF; mmWave; DSP; waveform; modulation; OFDM

1. Introduction

The increasing number of mobile devices demanding internet applications has motivated the exploration of diverse possibilities and methods for achieving a higher capacity of exchanging information with enhanced coverage potential [1]. Based on ITU-T FG-IMT-2020 [2], fifth-generation (5G) networks should provide 1000 times more wireless capacity than currently available, supporting internet connectivity with exceptionally low latency (<1 ms) to over 7 trillion wireless devices among 7 billion people. Considering the capacity associated with the anticipated small cells, it is expected that data rate requirements range between 100 Mbit/s and 1000 Mbit/s and beyond, with peaks up to 10 Gbit/s.

Accordingly, 5G millimeter-wave (mmWave) wireless channel bandwidths will be more than ten times greater than current 4G Long-Term Evolution (LTE) cellular channels [3,4] to deliver an unprecedented level of service to the end user. Since wavelength shrinks by an order of magnitude at mmWave when compared to today's 4G microwave frequencies, they will be affected by a severe free space path loss (FSPL) and a considerable attenuation that is caused by diffraction and material penetration, thus elevating the importance of line-of-sight (LOS) propagation, reflection, and scattering. Therefore, cell coverage areas in 5G, are approximately in the range of 10 to 200 m [5]. This fact implies an increase in the number of cells and nodes in current mobile networks.

Fiber optic networks with their immense capacities are set to be the most important connection type for front- and backhaul for such wireless networks, due to their high bit rates achieved and the long distances covered. While in current centralized radio access network (C-RAN) deployments fronthaul data is transported in digitized form, i.e., as in phase and quadrature (IQ) samples of the RF waveform, this is highly inefficient with regards to optical spectrum usage and the required data rates quickly become prohibitive as radio bandwidth and carrier frequencies grow. In this respect, analog radio over fiber (ARoF) technology, where the required RF waveform is transported in the optical network as an analog signal, paves the way as an efficient solution in terms of spectral efficiency compared to digital RoF (DRoF) [4,6]. Thus, ARoF efficiently leverages on the advantages of fiber optics, such as low attenuation and high bandwidths.

To support the integration of diversified data traffic types and integration of mobile front- and backhaul with other services in a shared network, emerging flexible, robust and high capacity passive optical networks (PONs) are considered for ARoF architectures [7]. In addition, wavelength division multiplexing (WDM) is already commonly used in aggregation and metro networks because it provides a graceful upgrade path to accessing the available optical spectrum, as well as having advantages in terms of scalability and network management. As the number of required channels growth, especially with dense 5G deployments, the number of available wavelengths must be increased to allow provisioning of sufficient capacity while minimizing waste of spectrum. In this respect, the separation among wavelengths must be reduced, resulting in ultra-dense WDM (UDWDM). In this regard, the EU-H2020 project-ITN 5G STEP FWD [8] proposes to transform the current PONs to UDWDM-PONs.

The combination with ARoF, i.e., ARoF over UDWDM-PONs, is a strong candidate to be part of the 5G front- and backhaul architecture. As an illustrative case, Figure 1 shows a feasible structure of mmWave cells over UDWDM-PONs for RoF systems. However, the reduction of wavelength spacing in UDWDM-PONs and the impairments inherent to working with mmWave signals may induce system performance degradations [9]. Furthermore, the use of ARoF fronthaul directly concatenates the optical and wireless channels, creating a hybrid channel of potentially larger complexity than the pure wireless channel observed with digitized fronthaul. A possible way to mitigate impairments and to address a more complex channel lies in implementing advanced waveform formats.

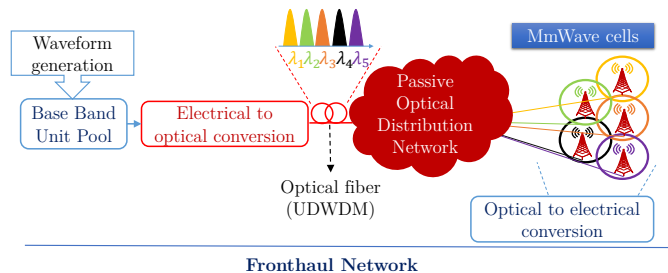


Figure 1. Radio over fiber (RoF) configuration for mmWave cells over ultra-dense wavelength division multiplexing-passive optical networks (UDWDM-PONs).

In terms of waveform, consider now LTE fourth-generation (4G) cellular networks, where orthogonal frequency-division multiplexing (OFDM) is the digital modulation technique adopted in the standards [10]. However, the spectral efficiency of OFDM is limited by the inclusion of a cyclic prefix (CP) and by its large side lobes, which require some null guard tones at the spectrum edges [11]. Furthermore, OFDM signals may suffer from large peak-to-average-power ratio (PAPR) values. Moreover, due to frequency deviations, the subcarriers will be no longer orthogonal, causing inter-carrier interference (ICI). Similar effects arise when the OFDM technique is affected by Doppler spread for the case of non-linear time-invariant (non-LTI) channels [12]. For those reasons, OFDM should be enhanced by using another alternative waveform format for next generation mobile

networks (5G and beyond). Thus, in this manuscript, we offer an analysis and comparison of different candidate waveform formats for future mobile networks.

This paper is organized as follows. Section 2 introduces the requirements for waveforms to be used in high-bandwidth mmWave signals and ARoF transport. Section 3 shows and describes potential heirs of OFDM for beyond 5G in mmWave over UDWDM-PONs. Section 4 displays the state-of-the-art (SoA) on waveforms in ARoF experiments. Section 5 compares the presented candidate waveforms based on the requirements detailed in Section 2. Finally, Section 6 provides some concluding remarks.

2. Requirements to Waveforms for Beyond 5G

In this section, different key requirements associated with waveform formats for mmWave transport over ARoF systems are reviewed. Three main scenarios are distinguished: (i) general wireless communications, (ii) mmWave wireless communications, and (iii) ARoF systems. As shown in Figure 2, any requirement considered through this paper is connected with one or several 5G requirements, and thus they jointly allow a good comparison of candidate waveforms for 5G and beyond.

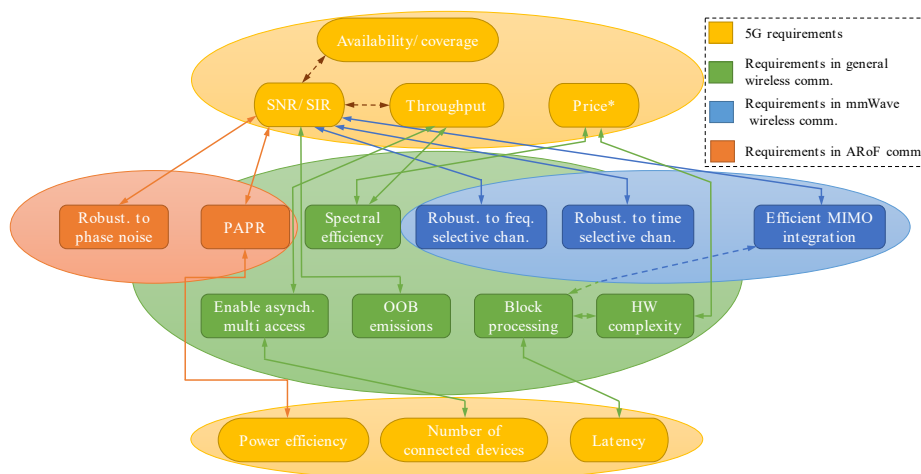


Figure 2. Relationships among requirements for candidate waveforms and 5G requirements. Three subsets of waveform requirements are defined: the ones for general wireless communications, the specific ones for mmWave wireless communications, and the ones for ARoF transport of high-bandwidth signals.

2.1. Requirements for General Wireless Communications

In terms of general requirements for wireless communications, a prospective waveform format should include the following features.

- **Peak-to-average power ratio:** PAPR indicates the relationship between the maximum peak and the average transmitted power of the signal. The worst impairment metrics associated to high PAPR in terms of communication are high power consumption and severe signal distortions. Note that energy efficiency is one of the most important requirements in 5G [13]. Signal distortions due to high power values are caused by nonlinearities in devices such as Mach–Zehnder modulators (MZMs) and power amplifiers, causing spectral regrowth and higher bit error rates (BER) [14]. Thus, a waveform format that produces high PAPR is not suitable for an energy efficient network.
- **Spectral efficiency:** Due to both licensing requirements and the spectrum scarcity resulting from the increasing transmission bandwidth requirement with demand for any time, anywhere, any situation communication this indicator is considered pivotal. The spectral efficiency is a very

important factor in a system because it is directly related to its bit rate achieved. According to the 5G requirements proposed in ITU-R M.2410-0 [13], the peak spectral efficient target is 30 bit/s/Hz and 15 bit/s/Hz for downlink and uplink respectively.

- **Block processing delay:** This requirement is seen relevant since it affects the final latency. A waveform format with high complexity suffers large block processing delays. Additionally, block processing delay is lower-bounded by symbol duration in many cases. The final latency of any communication can not be less than the block processing time. The latter can be reduced by employing techniques such as pipelining, efficient algorithms or by reducing symbol temporal period. One of the most challenging objectives in 5G is to reach communications with a maximum delay of 1 ms for the user plane [13].
- **Robustness to frequency-selective channels:** Multipath propagation is a phenomenon present in any wireless communication. It is caused by multiple reflections and refraction processes suffered by the transmitted signal, resulting in a received signal that is dispersed in time. Each path features its own delay and, accordingly, the temporal dispersion can induce to inter-symbol interference (ISI). Delay spread is a measure of the multipath profile of a mobile communications channel. As frequency fading can severely impact transmission, waveforms must be designed to be robust to this impairment.
- **Robustness to time-selective channels:** Most multipath channels are of time-varying nature. That nature arises as, for example, either transmitter the receiver are moving, and thus the location of reflectors in the transmission path, which gives rise to multipath, will change over time. Thus, if we repeatedly transmit pulses from a moving transmitter, we will observe changes in the amplitudes, delays, and the number of multipath components corresponding to each pulse. Regarding the 5G requirements proposed in ITU-R M.2410 [13], the 5G network should support a spectral efficiency of 0.45, 0.8, 1.12, and 1.5 bit/s/Hz for a mobility speed of 500, 120, 30, and 10 Km/h, respectively, and thus robustness to time-selective channels is key for candidate waveforms.
- **Out of band (OOB) emissions:** Linked to the spectral efficiency, this parameter is very significant as the radio spectrum is generally shared by different users, providers, and technologies. In order to efficiently support multiplexing of services, both in-band and out-of-band emissions must be kept to a minimum, so that services being transmitted on adjacent frequency channels do not interfere with one another. According to release 15 of 3GPP [15], the bandwidth is up to 400 MHz for carrier frequencies above 24 GHz. A portion of such a bandwidth (around 20%) is used as a guard band. Therefore, the OOB should be high enough to achieve a reduced interference between the adjacent channels and, thus, to obtain an adequate frequency multiplexing of services. For example, the OOB emission shall not exceed -5 dBm for bandwidths of 50, 100, 200 and 400 MHz in the OOB region of 0 to 5 MHz [15].
- **Enabling asynchronous multiple access:** Asynchronous multiple access is relevant as it allows to efficiently utilize resources. In frequency division duplex (FDD) and time division duplex (TDD) systems, asymmetric and dynamic allocation of both time and frequency resources is feasible for increasing bandwidths in order to accommodate the asymmetric traffic with higher efficiency [16]. Namely, waveform formats enabling asynchronous multiple access are connected with more efficient channel usage and corresponding higher total throughput.
- **Filter granularity:** This factor indicates the level in which the waveform is using the filtering stage. The filter granularity is directly related to latency and OOB emissions. As a direct consequence, long filters cause a high block processing delays and thus negatively impact achievable latency. On the contrary, other waveform formats implementing shorter filter lengths do not induce high latency because they filter by sub-band (wide filter bandwidth) [17]. Therefore, a trade-off between low OOB emissions and low latency is required. Thus, a very narrow filter granularity (subcarrier) implies very low OOB emissions. However, the filter length will be very long and, in consequence, the latency will increase.

- **Hardware (HW) complexity:** The importance of low hardware complexity is associated with both the final expense and the complexity of the system. As already mentioned in the introductory section, the number of cells will increase in the next generation of mobile networks. Therefore, the complexity and cost of the hardware in each cell is a key factor when determining the feasibility of a modulation format.

2.2. Requirements in MmWave Wireless Communications

MmWave signals are seriously affected by FSPL due to their inherent high frequencies. This fact plays an important role in determining the mmWave range. Furthermore, this type of signals are highly sensitive to attenuation. It turns out that atmospheric attenuation, rain-induced fading, snow, fog, foliage attenuation, and material penetration considerably adds more limitations to the maximum range of mmWave link [18]. Accordingly, mmWave signals reach shorter distances than the signals used in LTE. Fortunately, the reflected multipath components suffer a considerable attenuation so that their number is reduced [18]. Therefore, as the multipath effect in mmWave scenarios is less intense (except in special scenarios characterized by sand and/or dust atmosphere), it is more difficult to establish a non-line-of-sight (NLOS) communication [18]. Considering the limitation in distance that mmWave signals presents, a recommendable requirement for waveform formats is described below.

- **Efficient MIMO integration:** Multiple-input multiple-output (MIMO) systems are a suitable technique to overcome the aforementioned significant low attenuation of mmWave wireless communications. Massive MIMO is an extended solution to form very directive lobes in a certain direction. However, this technique demands high signal processing requirements to manage its associated beamforming matrix [19]. Therefore, a modulation format with efficient MIMO integration is required to reduce the complexity of the beamforming system.

2.3. Requirements in ARoF

ARoF combines optical and RF transmission. An example of a simple ARoF scheme is shown in Figure 3, where f_{RF} is the RF carrier frequency and f_L the optical carrier frequency. The characteristic of the spectrum form for each step of the ARoF system can also be observed in Figure 3. The appropriate requirements for this type of scheme are listed below.

- **Robustness to phase noise:** ARoF is limited by phase noise when phase modulations are used. In the optical part, one of the most prominent impairments of the optical fiber is the chromatic dispersion. This dispersion produces phase rotation and ISI. Furthermore, in the mmWave tone generation, phase noise is introduced. The impact of this phase noise depends on the used technique to produce the mmWave tones in the optical domain [20]. Therefore, high robustness to phase noise is a relevant requirement for a waveform format in an ARoF system.
- **Dynamic range (DR):** ARoF is restricted by dynamic range too. The DR determines the minimum and maximum amplitude of the signal received to recover the information correctly. Then, the maximum DR value is directly related to the highest signal peaks (PAPR). In the optical part, the noise floor is increased by relative intensity noise (RIN) from the laser, amplifier spontaneous emission (ASE) from the amplifiers, and thermal and shot noises from the photodiode [21]. In its part, each RF device adds noise that can be quantified by the noise figure. All these additive noise contributions increase the noise floor. On the other hand, a distortion region is created and increased by the non-linearity of the optical fiber and the RF amplifier [14]. This region is also incremented by the intermodulation products and spurious of the RF amplifiers and MZMs, respectively [22,23]. Thus, the distortion region and the noise floor, which suffer from ARoF systems, limit the DR extremely. Therefore, the DR of ARoF systems determines the type of waveform format that will be used and is related indirectly with the PAPR of the waveform.

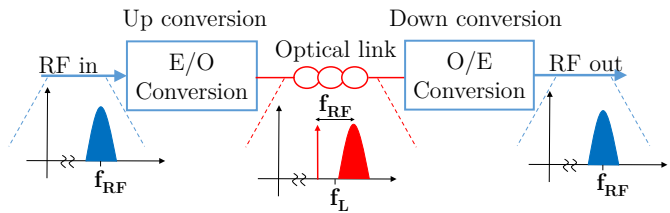


Figure 3. Simple analog radio over fiber (ARoF) scheme.

3. Candidate Modulation Formats for MmWave Over UDWDM-PONs

Waveform formats are mainly divided into two categories: multi-carrier and single carrier waveforms. Through this paper, we study different proposals belonging to any of both aforementioned groups. The transmitter structures for all the cases analyzed in this section are summarized in Table 1.

Table 1. Overview of the waveform schemes and their signal generation processes.

	Constellation mapping	Up-sampling	Filter	FFT	IFFT	Sum	CP	Windowing	Filter
OFDM	✓	-	-	-	size N	-	✓	+WOLA	bandpass (F-OFDM)
FBMC	OQAM	K factor per SR	per SR	-	size KN	and overlap	-	✓	-
UFMC (K SBs)	✓	-	-	-	K IFFTs size N (add zeros)	-	zero-guard (optional)	-	FL per SB and sum
GFDM	✓	per SR	per SR	-	-	✓	✓	+WOLA	-
MCAP	✓	per symb.	IQ FLs per SB	-	-	✓	-	-	-
SC-FDM	✓	-	-	size N	size $> N$ (add zeros)	-	✓	+WOLA	-
SC amp. only	PM	-	PS (↓ OOB)	-	-	-	-	-	-
SC amp. and phase	✓	-	PS (↓ OOB)	-	-	-	-	-	-

* SR → subcarrier. FL → filter. SB → sub-band. IQ → in-phase and quadrature. PM → pulse mapping. PS → pulse shapping.

3.1. Orthogonal Frequency Division Multiplexing (OFDM)

OFDM is a popular multi-carrier waveform format developed for RF systems and applied in LTE downlink. It can significantly increase the data rate in bandwidth-constrained channels with high spectral efficiency and allowing efficient MIMO integration. Furthermore, the robustness of OFDM to either phase noise as to time-selective channels depends on the spacing of its subcarriers [24]. Therefore, by using the scalable numerology and the subcarrier spacing, OFDM can be robust to almost any channel condition imposed by the scenario and by other requirements.

On the other hand, the basic OFDM suffers high OOB emissions so multiple techniques have been proposed to reduce them. These techniques are classified into two main categories: (1) windowed-OFDM and (2) filtered-OFDM [12]. The weight overlap and add based OFDM (WOLA-OFDM) is the windowed technique implemented in LTE [25]. This technique greatly reduces the OOB emissions without including high complexity. The WOLA-OFDM OOB emission level decreases with the length of CP since this length determines the length of the window. An asymmetric window may be used instead of well-known symmetric windows for reduction of the cyclic prefix by 30% [25] and, therefore, to reduce overhead. This technique suppresses OOB emission but makes the system more susceptible to channel induced ISI and ICI.

3.2. Filter Bank Multi-Carrier (FBMC)

FBMC is a multi-carrier waveform similar to OFDM that has been proposed in ITU-R M.2320 [16] as a promising waveform format for 5G. As the main feature, this waveform format does not include a CP. Therefore, its associated spectral efficiency is higher than that of OFDM. In addition, the half-Nyquist prototype filters mitigate ISI and the offset quadrature amplitude modulation (OQAM) removes ICI.

FBMC uses subcarrier filtering. Thanks to this feature, the filter length is long (high latency), the OOB emission are reduced, and the isolation between the subcarriers increases (high robustness to time-selective channels). However, a complex method is needed to estimate and compensate the channel. Therefore, MIMO integration with FBMC is more difficult. It is worth noting that FBMC can also employ scalable numerology.

3.3. Universal Filtered Multi-Carrier (UFMC)

UFMC is a type of sub-band filtering based on multi-carrier waveforms, combining the simplicity of OFDM with the advantages of FBMC. However, these advantages involve an increase in the complexity at the transmitter caused by the implementation of a filter and by applying a fast Fourier transform (FFT) for each sub-band, whereas at the receiver it requires doubling the size of the FFT. As a result, the total band composed of N subcarriers is divided into K sub-bands. Therefore, the UFMC transmitter performs the related K inverse FFTs (IFFTs) of size N separately, one per sub-band, by introducing zeros in the subcarriers not belonging to the sub-band. Each resulting signal is then filtered according to its frequency band and added to the other outputs [17].

On the other hand, the UFMC receiver recovers the signal through a size $2N$ FFT by adding zeros on the edge. Due to the size of the FFT, the use of CPs is avoided to correctly recover the signal, and thus a very high spectral efficiency can be achieved. However, this fact causes an additive noise increase in the receiver, thus obtaining a worse performance compared to OFDM [17].

3.4. Generalized Frequency Division Multiplexing (GFDM)

Like FBMC, GFDM is a multi-carrier waveform based on subcarrier filtering, where every subcarrier is shaped by a circular filter. The total number of mapped QAM symbols is arranged into K subcarriers and M subsymbols. Therefore, the total number of data symbols is $N = MK$ [26]. Next, every subcarrier is upsampled, filtered, and shifted to its carrier frequency. Then, these subcarrier signals are added, with a CP included at the end of each resulting block of subsymbols to avoid ISI [27]. Unlike OFDM, CPs are added per block (set of subsymbols) and not per symbol. Therefore, GFDM spectral efficiency is higher compared to OFDM [27], although with a high latency due to processing large blocks at a time.

As GFDM is not orthogonal, additional techniques must be implemented to properly recover the signal. There exist two main techniques: (1) interference cancellation scheme [28], and (2) OQAM [29], the latter with less complexity. Such techniques make GFDM receivers more complex. Moreover, GFDM is weaker than OFDM in terms of carrier frequency offset (CFO) [26].

3.5. Multi-Band Carrierless Amplitude and Phase Modulation (Multi-CAP)

Carrierless amplitude and phase modulation (CAP) is a multilevel and multidimensional modulation seen as a particular implementation of single carrier QAM using filters with orthogonal response. This absence of a carrier leads to less expensive and simpler transceivers compared to single carrier QAM, although increasing features in terms of spectral efficiency and performance [30,31].

As a representative feature, CAP is characterized by a low PAPR and simple implementation. However, CAP is proven to be very sensitive to frequency-selective channels and, to overcome this impairment, it requires a very complex equalizer and, consequently, suffers from inefficient MIMO integration. In this respect, a variant of CAP dividing the signal into different sub-bands, multi-CAP,

is proposed [30], where signal power and modulation order can be adapted to the concrete channel condition associated to each sub-band.

3.6. Single Carrier Frequency Division Multiplexing (SC-FDM)

The Single Carrier Frequency Division Multiplexing (SC-FDM) technique combines the advantages of OFDM, frequency-domain spread multi-carrier code-division multiple access (CDMA), and the conventional single-carrier direct-sequence CDMA (DS-SS-CDMA). Moreover, interleaved frequency division multiple access (IFDMA) scheme in SC-FDM systems does not exhibit PAPR problems, while localized frequency division multiple access (LFDMA) implementation slightly conflicts in terms of PAPR. For these cases, we can maximize as much as possible that aforementioned figure of merit to achieve the best possible performance in the system.

In fact, SC-FDM and not OFDM is the waveform preferred in the LTE uplink due to its low PAPR and, in this respect, the energy consumption of the mobile station is hugely reduced. SC-FDM is not a pure single carrier waveform. Its features are halfway in between the features of pure single carrier waveforms and multi-carrier waveforms. Therefore, SC-FDM presents better performance than multi-carrier waveforms in terms of PAPR, but PAPR is higher than that of pure single carrier waveforms [24]. Like basic OFDM, SC-FDM has high OOB emissions. The WOLA technique is further applied in SC-FDM in order to reduce the level of secondary lobes affecting adjacent bands.

3.7. Single Carrier Amplitude Only

Referring to single carrier waveforms that solely modulate the signal by amplitude, this type of waveform is characterized by its simplicity and robustness to phase noise. As weak points, they show very low spectral efficiency and high OOB emissions. As a representative implementation of single carrier amplitude only, widely employed in optical systems, we can mention on-off keying (OOK). Pulse with modulation (PWM) and pulse position modulation (PPM) are other types of single carrier amplitude modulation that encode each symbol with different pulse width and pulse position, respectively. OOK, PWM, and PPM provide very low spectral efficiency. To achieve a higher value, several techniques were proposed. One of these consists of adding several levels of amplitude to the resulting modulated symbols. In this way, pulse amplitude modulation (PAM), multilevel-PWM (M-PWM) and vector weight multilevel PPM (vw-MPPM) [32] arise.

Finally, an effort to reduce the huge OOB emissions inherent to pure single carrier waveforms is to generate Gaussian pulses instead of rectangular pulses. Furthermore, the average power is reduced with this mechanism and so, the PAPR magnitude.

3.8. Single Carrier Amplitude and Phase

This solution supposes higher order modulation than the waveforms explained above. Its main features are the same as for a single carrier waveform. The modulation formats employed are based on amplitude and phase. Therefore, high spectral efficiency can be achieved. However, these systems are, in general, weaker to phase noise.

One of the most popular amplitude and phase modulation formats is QAM. Based on it, amplitude and phase shift keying (APSK) was proposed and, as QAM, it is considered a combination of amplitude shift keying (ASK) and phase shift keying (PSK), but without being restricted to quadrature constellations. Namely, APSK is more flexible than QAM and, thus, there are many APSK constellation designs for different channels [12] with remarkable importance for those focused on achieving a channel capacity very close to the Shannon limit.

4. SoA of Waveforms Used in ARoF

Next, in this section, we review the use of waveform formats in ARoF research and experiment. The attention of ARoF research has been devoted to merging radio frequency and optical fiber technologies, aiming to increase the capacity and mobility of the access network. In the first attempts,

ARoF setups employed single carrier waveforms for their simplicity and robustness. Waveforms such as OOK and single carrier QAM were used in [33–38], respectively. However, they are not optimal for wireless communications due to their limited spectral efficiency and the scarcity of spectrum in the wireless channel.

Once OFDM was proposed for 4G, experiments involving ARoF also started employing it, and nowadays this waveform is still widely used since it is included in the standard for the current mobile network and for the first release of 5G [15]. ARoF setups with OFDM are found in [3,39–43] as illustrative examples. However, OFDM presents several issues as already discussed above and, for that reason, advanced multi-carrier waveforms have emerged recently such as FBMC, UFMF, GFDM and multi-CAP, which can be prominent candidates beyond 5G. Accordingly, these waveforms are now used in ARoF experiments: FBMC in [44,45]; GFDM in [46–49]; and multi-CAP in [50–52], to name but a few.

In Figure 4 we have compiled the recent usage trend of the different waveforms considered here in ARoF experiments of the last ten years. In this respect, ARoF set-ups have been organized in terms of wired/wireless experiments, real-time or offline signal processing, and featuring carriers below or above 6 GHz. Remarkably, as indicated in Figure 4, OFDM and single carrier waveforms are the most employed waveform formats for the considered period of the last ten years. Nevertheless, advanced multi-carrier waveforms are acquiring increasing relevance to mitigate ISI and multipath impairments.

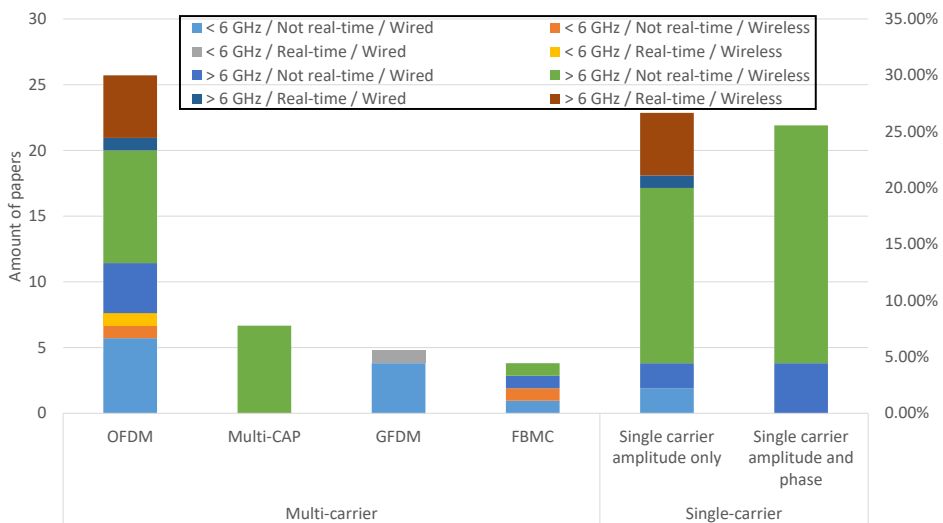


Figure 4. Overview about the state-of-the-art (SoA) on the waveform formats in ARoF experiments corresponding to the last ten years.

The aim of some of these experiments is to emulate the behavior of a mmWave cell over an ARoF system for 5G. To correctly emulate such a case, it is necessary to use carrier frequencies above 6 GHz, including the wireless link and implement real-time signal processing (brown label). However, from Figure 4 we observe that only OFDM and single carrier modulation formats have been used under these conditions. Therefore, for the rest of the waveform formats, research under such complete conditions, especially including real-time signal processing and the inclusion of the mmWave wireless transmission, is required to fill this gap.

On a further note, the future 5G will work with bands below and above 6 GHz for wireless transmission. Therefore, performance evaluations for the identified candidate waveforms in these

bands are required and a comprehensive comparison thereof is of great value in identifying the best candidates for beyond 5G. In this respect, these performance evaluations should include real-time signal processing to judge on their complexity and feasibility in as system context, as well as include actual wireless transmission to evaluate them under realistic channel conditions.

5. Comparison of Candidate Waveforms

Table 2 summarizes the different waveform formats analyzed throughout this paper in terms of the requirements discussed in Section 2. Thus, for each of those waveforms, different requirements are compared and analyzed in further detail.

- **Filter granularity:** Both GFDM and FBMC need longer filter lengths as they perform it by subcarrier (narrow filter bandwidth). On the other hand, F-OFDM, UPMC, and multi-CAP use shorter filter length because its granularities are per sub-band (wide filter bandwidth) [17]. Filter granularity can only be associated with multi-carrier waveforms (full band, sub-band, and subcarrier). Therefore, GFDM and FBMC present higher latency than the rest of multi-carrier waveforms.
- **PAPR:** From Table 2, we can observe that pure multi-carrier waveforms (OFDM, FBMC, UPMC, and GFDM) are associated with high values of PAPR. On the contrary, single-carrier waveforms present very low PAPR. It is worth noting that multi-CAP and SC-FDM both provide a low PAPR because they are not pure multi-carrier waveforms. On the other hand, any multi-carrier waveform can reduce its PAPR through different techniques. Nevertheless, they all increase the complexity in the system and, furthermore, include at least one of the following impairments [53]; power increase, bandwidth expansion, or BER degradation. For this reason, these techniques are not frequently considered as desirable.
- **Spectral efficiency:** This indicator is very important in order to achieve the bit rate requirements for 5G and beyond. High spectral efficiency is reached with a multi-carrier waveform and it increases by augmenting the modulation order. Single-carrier waveforms on the other hand provide lower spectral efficiency due to their limitations in the spectral domain. Comparing the spectral efficiency among the multi-carrier waveforms, FBMC, GFDM, and UPMC are the best because of their CP structure. In particular, FBMC and UPMC do not use CP while GFDM requires low CP overhead.
- **Block processing delay:** GFDM and FBMC present large block processing delays, as, among other reasons, its filter lengths are long, as mentioned previously. On the other hand, the block processing for the single-carrier waveforms is low because of their simplicity. Moreover, it is important to highlight that the final delay is intrinsically related to the symbol duration and thus, the latency is proportional to the subcarrier spacing in the case of FFT-based modulation formats.
- **Robustness to phase noise:** Single-carrier amplitude only is the best option as it does not use phase modulation. Robustness to phase noise is a pivotal point for low-cost base stations as very sophisticated and expensive devices are necessary to reduce the phase noise in hardware [24]. Pure single-carrier waveforms are inherently robust to phase noise, and they are better than the multi-carrier waveforms in this aspect [24]. However, we have to consider that this type of robustness is proportional to spacing among the subcarriers in the multi-carrier waveforms as mentioned in Section 3.
- **Robustness to frequency-selective channels:** Multi-carrier waveforms are better than single-carrier waveforms for this factor because frequency-selective fading will affect only a few subcarriers and not the entire band. That is, with adaptive bit loading, the impact of frequency-selectivity can be normalized.
- **Robustness to time-selective channels:** Single-carrier waveforms present better behavior than multi-carrier waveforms since the ICI inherently affects the multi-carrier waveforms [24]. Furthermore, as explained in Section 3, this robustness is proportional to the spacing among the subcarriers in the multi-carrier waveforms. GFDM, in particular, is the worst option due

to it needs long symbol duration, and therefore the changes of the channel strongly affect the GFDM symbol. On the other hand, and for the case of multi-carrier waveforms, FBMC is the best solution since the much better frequency-domain localization for the transmit filter than any other multi-carrier waveform. Therefore, the ICI can be efficiently removed for each subcarrier [17].

- OOB emissions: Because of their configuration, the OOB emissions of multi-carrier waveforms are much lower than those of single-carrier waveforms. At this point, OOB emissions can be reduced via filtering or pulse shaping. The characteristic of these techniques strongly influence the final OOB emissions. FBMC provides the lowest OOB emissions due to its filtering by subcarrier.
- Efficient MIMO integration: This factor has a strong relationship with the channel equalization implemented in the system. In addition, it is an indicative of the complexity of MIMO systems. All pure multi-carrier waveforms present highly efficient MIMO integration because they do not use complex channel estimation. Specifically, they use frequency-domain channel estimation through equally spaced pilots. FBMC and GFDM are exceptions in this case, as they require more complex channel equalization. Namely, FBMC needs to eliminate the imaginary interference in each scattered pilot [54], while GFDM requires a channel estimation in each subsymbol. On the other hand, single-carrier waveforms need more complex channel estimation to compensate. A popular estimation technique for this type of waveform is the adaptive decision feedback equalizer (DFE). It is a complex estimation and that is why the single-carrier waveforms are less efficient in terms of MIMO integration.
- Enable asynchronous multiple access: Pure multi-carrier waveforms do not allow to implement asynchronous multiple access in the system. This is due to the use of slots distributed in frequency, not in time. Consequently, this was one of the main reasons why SC-FDM was selected to be the waveform in the uplink for LTE.
- HW complexity: To implement the waveform in a field-programmable gate array (FPGA), the complexity of the system will determine the needed number of slice registers, look-up tables (LUTs) and random access memory (RAM) blocks [27]. According to Table 1, the single-carrier waveforms present a lower HW complexity as they need a smaller number of operations in order to process the transmitted and received signal. On the other side, GFDM, UPMC, and FBMC are the most complex waveforms due to the additional procedures that they add.

Table 2. Comparison between different waveform formats for mmWave ARoF.

Requirement\Waveform	OFDM	FBMC	UPMC	GFDM	MCAP	SC-FDM	SC amp. Only	SC amp. and Phase
Filter granularity	FB	SR	SB	SR	SB	-	-	-
PAPR	H	H	H	H	L	L	VL	VL
Spectral efficiency	H	VH	VH	VH	M/H	H	M/L	M/H
Block processing delay	M	H	M	H	M/L	M	L	L
Robust. to phase noise	M	M	M	M/H	M/H	M/H	H	M/H
Robust. to freq.-selec. chan.	H	H	H	H	M/H	M/H	M	M
Robust. to time-selec. chan.	M	M/H	M	M/L	M	M/H	H	H
OOB emissions	L	VL	VL	L	L	L	M/H	M
Efficient MIMO integration	H	M	H	M	L	M	L	L
Enable async. multi. access	No	No	No	No	Yes	Yes	Yes	Yes
HW complexity	M	H	H	H	M/L	M/H	L	L

* FB → full-band. SR → subcarrier. SB → sub-band. V → very. H → high. M → medium. L → low.

Observing Table 2, we can conclude that it is difficult to decide which waveform can be more suitable as they offer different advantages and disadvantages. In fact, any of those waveforms are well-appropriated for a particular type of service or channel due to their capacity to adapt to a subgroup of specific requirements. Indeed, according to IMT-2020, there are three foreseen categories of traffic types in 5G and beyond. These have different characteristics and use cases [55]: enhanced mobile broadband (eMBB) mainly requires high bit rate, massive machine-type communications (mMTC) will

support a huge quantity of devices with low power requirements, and ultra-reliable and low latency communications (URLLC) are targeted at mission critical communications where both low latency and superior reliability must be guaranteed. Thus, the optimal solution would be to select a suitable waveform format for each scenario for both uplink and downlink. It is necessary to highlight that an additional requirement is crucial in the uplink, resulting from the fact that the user performs a multicast transmission to the base station. Thus, to enable asynchronous multiple access is a primordial requisite for the uplink and hence, waveforms allowing asynchronous multiple access are very recommendable in the uplink.

For eMBB, the main requirement is the bit rate. Therefore, the spectral efficiency of the selected waveform should be very high and it should be robust to the ARoF system to achieve high modulation orders. In this sense, FBMC and UPMC are the two selected candidates since their characteristics are better adapted to those requirements. Nevertheless, FBMC implies a complex MIMO scheme due to its method to estimate and compensate the channel. In its part, UPMC allows an easier MIMO system to accomplish high antenna gain and, in consequence, high signal-to-noise ratio (SNR). Therefore, UPMC is one of the best candidates to be the heir of OFDM in the eMBB downlink. Concerning the uplink, the waveforms that allow asynchronous multiple access and high spectral efficiency are multi-CAP and SC-FDM. Indeed, multi-CAP can further achieve a higher bit rate because it can adapt the modulation order depending on the SNR in each sub-band [31]. Thus, multi-CAP could be the heir of the SC-FDM for the uplink in eMBB.

Following the mMTC requirements, the used waveform should support a huge number of devices. These devices transmit reduced amount of information as indicators of the system. Therefore, the bit rate is not a critical condition in this case. In mMTC, simplicity is a very relevant requirement because power consumption is of utmost importance and most devices have limited HW and SW. Sensors are a typical example for this type of scenario. Regarding the downlink in mMTC, OFDM is a proper candidate due to its simplicity, robustness to the ARoF system and capability to have smooth MIMO integration. For the uplink, multi-CAP and SC-FDM present better resilience to the ARoF impairments than the single carrier waveform options. Nevertheless, multi-CAP demands complex channel equalizer structure and it increases complexity for an ARoF scheme. Furthermore, its less efficient MIMO integration constitutes a problem in a system where there is a huge quantity of users employing the resources. Hence, SC-FDM still being the best option for the mMTC uplink, like in LTE.

Focusing on the main requirement of URLLC, pure single-carrier waveforms are the best solution to reach extremely low latency because of their low block processing delays. On the other hand, the reliability can be achieved by adapting the modulation order according to the channel conditions. We can reduce the modulation order because the bit rate is not critical in this scenario. SC amplitude and phase waveforms allow more flexibility to change the modulation order compared to SC amplitude only waveforms. Therefore, SC amplitude and phase waveforms are good candidate waveforms in URLLC both for downlink and uplink.

An alternative solution could consist in adaptive waveform formats according to the type of service. Namely, to select the waveform that best adapts to the requirements of a particular service. This can be achieved through intelligent software-defined radio (SDR) [49] and software-defined networking (SDN) [56].

6. Conclusions

In this paper, we have briefly described the prospective waveform candidates for 5G and beyond. In this regard, we have presented the main key requirements determining the performance of the waveforms in an ARoF system. Next, we have presented the current SoA of waveforms used in ARoF experiments, indicating the trend in the last ten years. In this SoA, and to the best of our knowledge, a deep comparison involving all waveform candidates for 5G with regard to ARoF was missing. In this work, we present such an SoA in terms of the requirements for ARoF based systems. Even so,

it remains difficult to select a potential best candidate for all situations. For that reason, IMT-2020 defined three types of scenarios [55].

Furthermore, in this paper, we have concluded the best waveform candidates for eMBB, mMTC, and URLLC for both downlink and uplink, respectively. The waveforms have to enable asynchronous multiple access in the uplink. Concerning eMBB, we conclude UFMC is one of the best solutions to achieve the highest bit rate in the downlink. On the other side, multi-CAP could be a very considerable successor of SC-FDM in the eMBB uplink. Regarding mMTC, we have remarked that simplicity is a considerable factor due to the SW and HW limitations of the devices in this type of scenario. Therefore, we have determined that OFDM and SC-FDM are the best waveforms because of their low complexity in downlink and uplink, respectively. Finally, for URLLC, pure SC waveforms could be the best candidates both for uplink and downlink to minimize latency. In particular, SC amplitude and phase modulation is one of the best options because it provides very low latency and flexibility to adapt the modulation order depending on the channel conditions.

At this point, it is important to highlight that the waveforms of the comparison presented are under different conditions. Therefore, an experimental comparison between all these modulation formats in an ARoF set-up with wireless transmission would be required to perform a fully comprehensive performance analysis. This experiment should be divided into three steps referring to each scenario. Each waveform should be adapted to achieve the best result in terms of the requirements of each scenario. In other words, the parameters of each waveform are modified to achieve the maximum bit rate for eMBB, the massive device support for mMTC and the lowest latency for URLLC. Therefore, the best candidate could be identified under realistic conditions and with an equal playing field to select the most promising waveforms for the mobile communication standards beyond 5G.

Author Contributions: J.P.S., S.R., and U.J. defined the scope of the review manuscript. J.P.S. compiled the necessary information to elaborate this review manuscript. J.P.S., S.R. and A.J.-N. wrote the article. J.P.S., S.R., A.J.-N., U.J. and I.T.M. reviewed and edited the manuscript. All authors have read and agreed to the published version of the manuscript.

Funding: This research was funded by the European Commission through H2020 ITN 5G STEP FWD (grant agreement 722429) and H2020 blueSPACE (grant agreement 762055) projects.

Conflicts of Interest: The authors declare no conflict of interest.

References

- Chin, W.H.; Fan, Z.; Haines, R. Emerging technologies and research challenges for 5G wireless networks. *IEEE Wirel. Commun.* **2014**, *21*, 106–112. [\[CrossRef\]](#)
- ITU. *FG IMT-2020: Report on Standards Gap Analysis*; ITU: Geneva, Switzerland, 2016.
- Konstantinou, D.; Morales, A.; Rommel, S.; Raddo, T.; Johannsen, U.; Monroy, I.T. Analog radio over fiber fronthaul for high bandwidth 5G millimeter-wave carrier aggregated OFDM. In Proceedings of the 21st International Conference on Transparent Optical Networks (ICTON), Angers, France, 9–13 July 2019; pp. 1–4, doi:10.1109/ICTON.2019.8840525. [\[CrossRef\]](#)
- Rommel, S.; Perez-Galacho, D.; Fabrega, J.M.; Muñoz, R.; Sales, S.; Tafur Monroy, I. High-Capacity 5G Fronthaul Networks Based on Optical Space Division Multiplexing. *IEEE Trans. Broadcast.* **2019**, *65*, 434–443. [\[CrossRef\]](#)
- Akdeniz, M.R.; Liu, Y.; Samimi, M.K.; Sun, S.; Rangan, S.; Rappaport, T.S.; Erkip, E. Millimeter Wave Channel Modeling and Cellular Capacity Evaluation. *IEEE J. Sel. Areas Commun.* **2014**, *32*, 1164–1179. [\[CrossRef\]](#)
- Brenes, J.; Lagkas, T.D.; Klonidis, D.; Muñoz, R.; Rommel, S.; Landi, G.; Tafur Monroy, I.; Grivas, E.; Pikasis, E.; Bernini, G.; et al. Network slicing architecture for SDM and analog-radio-over-fiber-based 5G fronthaul networks. *J. Opt. Commun. Netw.* **2020**, *12*, B33–B43. [\[CrossRef\]](#)
- Rohde, H.; Gottwald, E.; Rosner, S.; Weis, E.; Wagner, P.; Babenko, Y.; Fritzsche, D.; Chaouch, H. Trials of a Coherent UDWDM PON Over Field-Deployed Fiber: Real-Time LTE Backhauling, Legacy and 100G Coexistence. *J. Light. Technol.* **2015**, *33*, 1644–1649. [\[CrossRef\]](#)
- European Project: 5G System Technological Enhancements Provided by Fiber Wireless Deployments (5G STEP FWD). Available online: <https://www.5gstepfwd.eu/> (accessed on 3 June 2020).

9. Chuenchom, R.; Babel, S.; Steeg, M.; Stöhr, A. Impact of WDM channel spacing on millimeter-wave wireless access using wireless coherent radio-over-fiber (CRoF) channels. In Proceedings of the 2015 Optical Fiber Communications Conference and Exhibition (OFC), Los Angeles, CA, USA, 22–26 March 2015; pp. 1–3. [\[CrossRef\]](#)
10. Ghosh, A.; Zhang, J.; Andrews, J.G.; Muhamed, R. *Fundamentals of LTE*, 1st ed.; Prentice Hall Press: Upper Saddle River, NJ, USA, 2010.
11. Banelli, P.; Buzzi, S.; Colavolpe, G.; Modenini, A.; Rusek, F.; Ugolini, A. Modulation Formats and Waveforms for 5G Networks: Who Will Be the Heir of OFDM?: An overview of alternative modulation schemes for improved spectral efficiency. *IEEE Signal Process. Mag.* **2014**, *31*, 80–93. [\[CrossRef\]](#)
12. Maziar, N.; Yue, W.; Milos, T.; Shangbin, W.; Yinan, Q.; Mohammed, A.I. Overview of 5G modulation and waveforms candidates. *J. Commun. Inf. Netw.* **2016**, *1*, 44–60. [\[CrossRef\]](#)
13. ITU. Report ITU-R M.2410-0: ‘Minimum Requirements Related to Technical Performance for IMT-2020 Radio Interface(s)’; ITU: Geneva, Switzerland, 2017.
14. Aitchison, C.S.; Mbabele, M.; Moazzam, M.R.; Budimir, D.; Ali, F. Improvement of third-order intermodulation product of RF and microwave amplifiers by injection. *IEEE Trans. Microw. Theory Tech.* **2001**, *49*, 1148–1154. [\[CrossRef\]](#)
15. 3GPP. Technical Specification Group Services and System Aspects; Release 15 Description; Summary of Rel-15 Work Items; 3GPP: Valbonne, France, 2019.
16. ITU. Report ITU-R M.2320: ‘Future Technology Trends of Terrestrial IMT Systems’; ITU: Geneva, Switzerland, 2014.
17. Liu, Y.; Chen, X.; Zhong, Z.; Ai, B.; Miao, D.; Zhao, Z.; Sun, J.; Teng, Y.; Guan, H. Waveform Design for 5G Networks: Analysis and Comparison. *IEEE Access* **2017**, *5*, 19282–19292. [\[CrossRef\]](#)
18. Hemadeh, I.A.; Satyanarayana, K.; El-Hajjar, M.; Hanzo, L. Millimeter-Wave Communications: Physical Channel Models, Design Considerations, Antenna Constructions, and Link-Budget. *IEEE Commun. Surv. Tutor.* **2018**, *20*, 870–913. [\[CrossRef\]](#)
19. Ahmed, I.; Khammari, H.; Shahid, A.; Musa, A.; Kim, K.S.; De Poorter, E.; Moerman, I. A Survey on Hybrid Beamforming Techniques in 5G: Architecture and System Model Perspectives. *IEEE Commun. Surv. Tutor.* **2018**, *20*, 3060–3097. [\[CrossRef\]](#)
20. Chowdhury, T.A.; Ghuri, M.M.A.; Kibria, R. Millimeter wave generation based on optical frequency multiplication in radio over fiber systems. In Proceedings of the 2016 9th International Conference on Electrical and Computer Engineering (ICECE), Dhaka, Bangladesh, 20–22 December 2016; pp. 94–97. [\[CrossRef\]](#)
21. Agrawal, G. *Fiber-Optic Communication Systems*, 4th ed.; WILEY: New York, NY, USA, 2012; doi:10.1002/9780470918524. [\[CrossRef\]](#)
22. Christianson, A.J.; Henrie, J.J.; Chappell, W.J. Higher Order Intermodulation Product Measurement of Passive Components. *IEEE Trans. Microw. Theory Techn.* **2008**, *56*, 1729–1736. [\[CrossRef\]](#)
23. Luo, X.; Tu, X.; Song, J.; Ding, L.; Fang, Q.; Liow, T.Y.; Yu, M.; Lo, G.Q. Slope efficiency and spurious-free dynamic range of silicon Mach-Zehnder modulator upon carrier depletion and injection effects. *Opt. Express* **2013**, *21*, 16570–16577. [\[CrossRef\]](#) [\[PubMed\]](#)
24. Zaidi, A.A.; Baldemair, R.; Tullberg, H.; Bjorkegren, H.; Sundstrom, L.; Medbo, J.; Kilinc, C.; Silva, I.D. Waveform and Numerology to Support 5G Services and Requirements. *IEEE Commun. Mag.* **2016**, *54*, 90–98. [\[CrossRef\]](#)
25. Taheri, R.; Nilsson, R.; van de Beek, J. Asymmetric Transmit Windowing for Low-Latency and Robust OFDM. In Proceedings of the 2016 IEEE Globecom Workshops (GC Wkshps), Washington, DC, USA, 4–8 December 2016; pp. 1–5. [\[CrossRef\]](#)
26. Lim, B.; Ko, Y. SIR Analysis of OFDM and GFDM Waveforms With Timing Offset, CFO, and Phase Noise. *IEEE Trans. Wirel. Commun.* **2017**, *16*, 6979–6990. [\[CrossRef\]](#)
27. Gerzaguet, R.; Bartzoudis, N.; Baltar, L.; Berg, V.; Doré, J.B.; Ktenas, D.; Font-Bach, O.; Mestre, X.; Payaro, M.; Färber, M.; et al. The 5G candidate waveform race: A comparison of complexity and performance. *EURASIP J. Wirel. Commun. Netw.* **2017**, 2017. [\[CrossRef\]](#)
28. Datta, R.; Michailow, N.; Lentmaier, M.; Fettweis, G. GFDM Interference Cancellation for Flexible Cognitive Radio PHY Design. In Proceedings of the 2012 IEEE Vehicular Technology Conference (VTC Fall), Quebec City, QC, Canada, 3–6 September 2012; pp. 1–5. [\[CrossRef\]](#)

29. Gaspar, I.; Matthé, M.; Michailow, N.; Leonel Mendes, L.; Zhang, D.; Fettweis, G. Frequency-Shift Offset-QAM for GFDM. *IEEE Commun. Lett.* **2015**, *19*, 1454–1457. [\[CrossRef\]](#)
30. Olmedo, M.I.; Zuo, T.; Jensen, J.B.; Zhong, Q.; Xu, X.; Popov, S.; Monroy, I.T. Multiband Carrierless Amplitude Phase Modulation for High Capacity Optical Data Links. *J. Lightw. Technol.* **2014**, *32*, 798–804. [\[CrossRef\]](#)
31. Rommel, S.; Puerta, R.; Olmos, J.J.V.; Monroy, I.T. Capacity enhancement for hybrid fiber-wireless channels with 46.8Gbit/s wireless multi-CAP transmission over 50m at W-band. In Proceedings of the 2017 Optical Fiber Communications Conference and Exhibition (OFC), Los Angeles, CA, USA, 19–23 March 2017; pp. 1–3. [\[CrossRef\]](#)
32. Garrido-Balsells, J.M.; Garcia-Zambrana, A.; Puerta-Notario, A. Variable weight MPPM technique for rate-adaptive optical wireless communications. *Electron. Lett.* **2006**, *42*, 43–57. [\[CrossRef\]](#)
33. Liu, C.; Zhang, L.; Zhu, M.; Wang, J.; Cheng, L.; Chang, G. A Novel Multi-Service Small-Cell Cloud Radio Access Network for Mobile Backhaul and Computing Based on Radio-Over-Fiber Technologies. *J. Lightw. Technol.* **2013**, *31*, 2869–2875. [\[CrossRef\]](#)
34. Zhu, M.; Zhang, L.; Wang, J.; Cheng, L.; Liu, C.; Chang, G. Radio-Over-Fiber Access Architecture for Integrated Broadband Wireless Services. *J. Lightw. Technol.* **2013**, *31*, 3614–3620. [\[CrossRef\]](#)
35. Rodriguez, S.; Morales, A.; Rommel, S.; Olmos, J.J.V.; Monroy, I.T. Real-time measurements of an optical reconfigurable radio access unit for 5G wireless access networks. In Proceedings of the 2017 Optical Fiber Communications Conference and Exhibition (OFC), Los Angeles, CA, USA, 19–23 March 2017; pp. 1–3. [\[CrossRef\]](#)
36. Chung, Y.; Choi, K.; Sim, J.; Yu, H.; Kim, J. A 60-GHz-Band Analog Optical System-on-Package Transmitter for Fiber-Radio Communications. *J. Lightw. Technol.* **2007**, *25*, 3407–3412. [\[CrossRef\]](#)
37. Kong, M.; Zhou, W. Delivery of 12QAM Single Carrier Signal in a MIMO Radio-Over-Fiber System at 60 GHz. *IEEE Photon. J.* **2017**, *9*, 1–7. [\[CrossRef\]](#)
38. Argyris, N.; Giannoulis, G.; Kanta, K.; Iliadis, N.; Vagionas, C.; Papaioannou, S.; Kalfas, G.; Apostolopoulos, D.; Caillaud, C.; Debrégeas, H.; et al. A 5G mmWave Fiber-Wireless IFoF Analog Mobile Fronthaul Link With up to 24-Gb/s Multiband Wireless Capacity. *J. Lightw. Technol.* **2019**, *37*, 2883–2891. [\[CrossRef\]](#)
39. Chen, M.; Xiao, X.; Yu, J.; Li, F.; Huang, Z.R.; Zhou, H. Demonstration of Software-Reconfigurable Real-Time FEC-Enabled 4/16/64-QAM-OFDM Signal Transmission in an X-Band RoF System. *IEEE Photon. J.* **2016**, *8*, 1–8. [\[CrossRef\]](#)
40. Hugues-Salas, E.; Zhang, Q.; Giddings, R.P.; Wang, M.; Tang, J. Adaptability-enabled record-high and robust capacity-versus-reach performance of real-time dual-band optical OFDM signals over various OM1/OM2 MMF systems [invited]. *IEEE J. Opt. Commun. Netw.* **2013**, *5*, A1–A11. [\[CrossRef\]](#)
41. Dat, P.T.; Kanno, A.; Kawanishi, T. Performance of high throughput WLAN signal on a seamless radio-over-fiber and 90-GHz wireless convergence system. In Proceedings of the 2014 OptoElectronics and Communication Conference and Australian Conference on Optical Fibre Technology, Melbourne, Australia, 6–10 July 2014; pp. 1030–1032.
42. Chen, M.; Yu, J.; Xiao, X. Real-Time Q-Band OFDM-RoF Systems With Optical Heterodyning and Envelope Detection for Downlink Transmission. *IEEE Photon. J.* **2017**, *9*, 1–7. [\[CrossRef\]](#)
43. Sung, M.; Cho, S.; Kim, J.; Lee, J.K.; Lee, J.H.; Chung, H.S. Demonstration of IFoF-Based Mobile Fronthaul in 5G Prototype With 28-GHz Millimeter wave. *J. Lightw. Technol.* **2018**, *36*, 601–609. [\[CrossRef\]](#)
44. Xu, M.; Zhang, J.; Lu, F.; Wang, J.; Cheng, L.; Cho, H.J.; Khalil, M.I.; Guidotti, D.; Chang, G. FBMC in Next-Generation Mobile Fronthaul Networks With Centralized Pre-Equalization. *IEEE Photon. Technol. Lett.* **2016**, *28*, 1912–1915. [\[CrossRef\]](#)
45. Dat, P.T.; Kamio, A.; Yamamoto, N.; Kawanishi, T. Performance of 5G waveform and multiple radio access technique over a fiber-wireless fronthaul. In Proceedings of the 2017 International Topical Meeting on Microwave Photonics (MWP), Beijing, China, 23–26 October 2017; pp. 1–3. [\[CrossRef\]](#)
46. Borges, R.M.; Marins, T.R.R.; Cunha, M.S.B.; Filgueiras, H.R.D.; da Costa, I.F.; da Silva, R.N.; Spadoti, D.H.; Mendes, L.L.; Sodré, A.C. Integration of a GFDM-Based 5G Transceiver in a GPON Using Radio Over Fiber Technology. *J. Lightw. Technol.* **2018**, *36*, 4468–4477. [\[CrossRef\]](#)

47. Browning, C.; Farhang, A.; Saljoghei, A.; Marchetti, N.; Vujicic, V.; Doyle, L.E.; Barry, L.P. 5G wireless and wired convergence in a passive optical network using UF-OFDM and GFDM. In Proceedings of the 2017 IEEE International Conference on Communications Workshops (ICC Workshops), Paris, France, 21–25 May 2017; pp. 386–392. [\[CrossRef\]](#)
48. Delmade, A.; Browning, C.; Farhang, A.; Marchetti, N.; Doyle, L.E.; Koilpillai, D.; Barry, L.P.; Venkitesh, D. Performance analysis of optical front-hauling for 5G Waveforms. In Proceedings of the 2017 Conference on Lasers and Electro-Optics Europe European Quantum Electronics Conference (CLEO/Europe-EQEC), Munich, Germany, 25–29 June 2017; p. 1. [\[CrossRef\]](#)
49. Rico-Martinez, M.; Vasquez, C.C.C.; Rodriguez, S.I.; Duran, G.M.V.; Monroy, I.T. Comparison of performance between OFDM and GFDM in a 3.5GHz band 5G hybrid Fiber-Wireless link using SDR. In Proceedings of the 2018 International Topical Meeting on Microwave Photonics (MWP), Toulouse, France, 22–25 October 2018; pp. 1–4. [\[CrossRef\]](#)
50. Altabas, J.A.; Rommel, S.; Puerta, R.; Izquierdo, D.; Garces, J.I.; Lazaro, J.A.; Olmos, J.J.V.; Monroy, I.T. Nonorthogonal Multiple Access and Carrierless Amplitude Phase Modulation for Flexible Multiuser Provisioning in 5G Mobile Networks. *J. Lightw. Technol.* **2017**, *35*, 5456–5463. [\[CrossRef\]](#)
51. Puerta, R.; Rommel, S.; Olmos, J.J.V.; Monroy, I.T. Optically generated single side-band radio-over-fiber transmission of 60Gbit/s over 50m at W-band. In Proceedings of the 2017 Optical Fiber Communications Conference and Exhibition (OFC), Los Angeles, CA, USA, 19–23 March 2017; pp. 1–3. [\[CrossRef\]](#)
52. Puerta, R.; Yu, J.; Li, X.; Xu, Y.; Olmos, J.V.; Monroy, I.T. Demonstration of 352 Gbit/s Photonic-enabled D-Band Wireless Delivery in one 2×2 MIMO System. In Proceedings of the Optical Fiber Communication Conference, Optical Society of America, Los Angeles, CA, USA, 19–23 March 2017; p. Tu3B.3. [\[CrossRef\]](#)
53. Rahmatallah, Y.; Mohan, S. Peak-To-Average Power Ratio Reduction in OFDM Systems: A Survey And Taxonomy. *IEEE Commun. Surv. Tutor.* **2013**, *15*, 1567–1592. [\[CrossRef\]](#)
54. Cui, W.; Qu, D.; Jiang, T.; Farhang-Boroujeny, B. Coded Auxiliary Pilots for Channel Estimation in FBMC-OQAM Systems. *IEEE Trans. Veh. Technol.* **2016**, *65*, 2936–2946. [\[CrossRef\]](#)
55. Popovski, P.; Trillingsgaard, K.F.; Simeone, O.; Durisi, G. 5G Wireless Network Slicing for eMBB, URLLC, and mMTC: A Communication-Theoretic View. *IEEE Access* **2018**, *6*, 55765–55779. [\[CrossRef\]](#)
56. Rastegarfar, H.; Djordjevic, I.B. Physical-layer adaptive resource allocation in software-defined data center networks. *IEEE J. Opt. Commun. Netw.* **2018**, *10*, 1015–1026. [\[CrossRef\]](#)



© 2020 by the authors. Licensee MDPI, Basel, Switzerland. This article is an open access article distributed under the terms and conditions of the Creative Commons Attribution (CC BY) license (<http://creativecommons.org/licenses/by/4.0/>).

P2: Experimental Assessment of Modulation Formats for Beyond 5G mm-Wave ARoF Systems

J. P. Santacruz, A. Morales, S. Rommel, U. Johannsen, A. Jurado-Navas, and I. Tafur Monroy, “Experimental Assessment of Modulation Formats for Beyond 5G mm-Wave ARoF Systems,” in *2020 European Conference on Networks and Communications (EuCNC)*, Dubrovnik, Croatia: IEEE, Jun. 2020, pp. 300–304.
DOI: 10.1109/EuCNC48522.2020.9200955

Experimental Assessment of Modulation Formats for Beyond 5G mm-Wave ARoF Systems

Javier Pérez Santacruz*, Alvaro Morales*, Simon Rommel*, Ulf Johannsen†, Antonio Jurado Navas‡, and Idelfonso Tafur Monroy*

*Institute for Photonic Integration, Eindhoven University of Technology, 5600MB Eindhoven, The Netherlands

†Centre for Wireless Technology, Eindhoven University of Technology, 5600MB Eindhoven, The Netherlands

‡Department of Communications Engineering, University of Málaga, 29071 Málaga, Spain

Email: {j.perez.santacruz, a.morales.vicente, s.rommel, u.johannsen, i.tafur.monroy}@tue.nl, navas@ic.uma.es

Abstract—Fifth-generation (5G) mobile networks consist of a range of novel technologies to fulfill different and exigent requirements and serve a wide range of services. To reach this, analog radio over fiber (ARoF) fronthaul with millimeter-wave (mm-wave) cells is a firm candidate to be part of the 5G architecture. Nonetheless, combined mm-wave and ARoF systems present new challenges such as high free-space path loss (FSPL), phase noise, chromatic dispersion, and other impairments. Therefore, the selection of the modulation format is crucial to reduce these effects and their impact. This work compares and analyzes different modulation formats in this type of system in order to choose the best waveform candidate for mm-wave 5G and beyond with ARoF fronthaul. An experimental comparison of OFDM, SC-FDM, UFMC, GFDM, and multi-CAP, shows that the standard OFDM may not be the best choice for mm-wave 5G.

Keywords—5G, ARoF, fronthaul, mm-wave, waveforms, modulation formats.

I. INTRODUCTION

The fifth generation (5G) of wireless systems will bring an important improvement in terms of data rate, reliability, latency, cost, and number of connected devices. A way to reach the 5G capacity demands is to move from the current congested band toward higher frequency bands, in the millimeter-wave (mm-wave) domain. Analog radio over fiber (ARoF) systems are considered a suitable technique to transport mm-wave signals through the radio access network [1]. Moreover, centralized radio access network (C-RAN) is a preferred option in terms of flexibility, latency, and energy consumption [2]. Therefore, ARoF is a strong candidate to implement C-RAN in a scalable fashion for high-bandwidth 5G architectures [3]. An example of this architecture is shown in Fig. 1. In this figure, each cell contains one remote unit (RU). These RU's are connected to a central office (CO) through an optical fronthaul link that can use different technologies such as wavelength division multiplexing (WDM) or space division multiplexing (SDM) [1]. The CO manages and regulates the communication link by means of software-defined networking (SDN) and network function virtualization (NF) control plane [4]. A number of scenarios are illustrated in Fig. 1: a mobile cell where the terminals are phones; a factory cell whose machines can be controlled remotely through a wireless link; a vehicular transmission supported by a serial of base stations connected to an RU and distributed along the highway. ARoF supports these scenarios either as fronthaul solution for high-capacity

mm-wave cells or to extend the fiber-based fronthaul with an mm-wave segment, establishing a hybrid ARoF and mm-wave fronthaul link.

The use of ARoF directly combines the optical and wireless channels and thus combines their respective impairments so that they must be treated jointly. The major ones are the following: the free-space path loss (FSPL) due to the high mm-wave frequencies and the attenuation due to the atmospheric absorption [5]; the increased phase noise when generating the mm-wave carrier; the chromatic dispersion introduced by the optical fiber; the non-linearity of some devices such as Mach-Zehnder modulators (MZMs) and radio frequency (RF) amplifiers. A possible way to reduce the impact of these impairments lies in implementing advanced waveform formats.

Orthogonal frequency division multiplexing (OFDM) is the chosen modulation format in the first 5G standards by the 3rd generation partnership project (3GPP) [6]. However, it is not proven that OFDM is the optimum modulation format for ARoF systems with mm-wave links [7], [8]. OFDM has several limitations for ARoF systems due to its high peak-to-average power ratio (PAPR) and weakness to phase noise [9]. Consequently, other modulation formats have risen to be strong candidates for the beyond 5G [10], [11]. Therefore, a thorough analysis is required towards future mobile access networks beyond 5G. In this work, we experimentally evaluate a 5G scenario through an ARoF setup at 25 GHz (K-Band), i.e., within the n258 band assigned for mm-wave 5G in Europe [6]. This allows for direct evaluation and comparison of the performance of OFDM and the other main modulation format candidates for ARoF systems.

This paper is organized as follows: Section II describes and compares qualitatively the evaluated modulation formats; Section III shows the characteristics and configuration of the digital signal processing (DSP) and devices used in the setup; Section IV presents and analyzes the obtained results; Section V summarizes the paper and provides concluding remarks.

II. EVALUATED MODULATION FORMATS

In this paper, we compare the most relevant waveform format candidates for beyond 5G in terms of bit error rate (BER) according to [10] and [11]. These waveform formats can be divided into two categories: multi-carrier (MC) and single-carrier (SC) waveforms, both groups have different

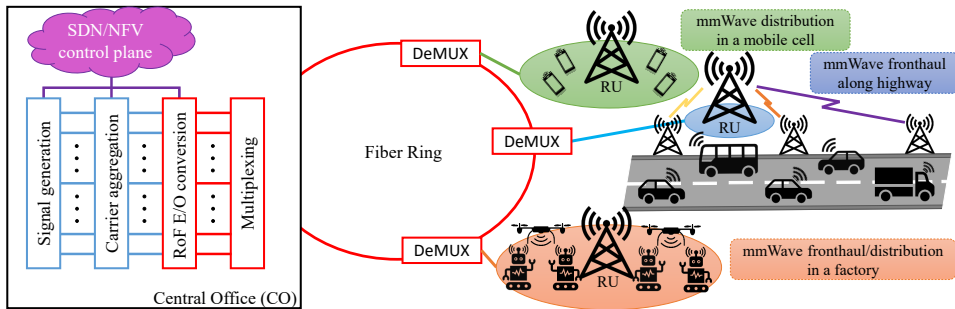


Fig. 1. C-RAN architecture employing ARoF fronthaul between the central office (CO) and remote radio nodes for three different scenarios.

attractive features. The employed MC waveforms are: OFDM, universal-filtered multi-carrier (UFMC) and generalized frequency division multiplexing (GFDM). On the other hand, the utilized SC waveforms are: single-carrier frequency division multiplexing (SC-FDM) and multiband carrierless amplitude phase modulation (multi-CAP). It is necessary to mention that SC-FDM and multi-CAP are not pure SC waveforms like, e.g., quadrature amplitude modulation.

First, the evaluated waveforms are compared in terms of a number of key requirements for ARoF systems:

Peak-to-average power ratio: PAPR of the used waveform in ARoF systems requires to be low. A high PAPR leads to considerable degradation introduced by MZM, RF amplifier, digital-to-analog converter (DAC) and analog-to-digital converter (ADC) due to the large peaks of the transmitted signal [12]. Moreover, high PAPR is related to elevated power consumption of the system. Regarding the examined modulations, SC waveforms show lower PAPR than MC waveforms.

Robustness to phase noise: phase noise is one of the major limiting factors to overall performance in ARoF systems, especially if optical heterodyning of free-running lasers is employed for mm-wave generation, in which case phase noise is the result of the combined linewidths of the optical tones [13]. The robustness to phase noise is directly related with the duration of the waveform symbol [14]. Therefore, SC waveforms present better yield in terms of phase noise than MC waveforms due to their short symbol durations.

Spectral efficiency: this requirement defines the maximum bit rate for a given bandwidth. GFDM and UFMC are the most spectrally efficient because UFMC do not use a cyclic prefix (CP) and GFDM can use shorter CP length than OFDM and SC-FDM [10], [15].

Robustness to multipath channels: due to the high frequency of the mm-wave signals, the attenuation of the multipath components is high and therefore, their number is reduced [5]. Hence, the multipath effect is less intense in mm-wave scenarios. MC waveforms offer more robustness to multipath channels than SC waveforms. This fact is because multipath propagation affects few of the subcarriers in the MC waveforms and the full band band in the SC waveforms.

Complexity: this indicator determines the final latency of the system because it is related with the block processing

TABLE I. COMPARISON BETWEEN EXAMINED WAVEFORM FORMATS FOR MM-WAVE ARoF.

	OFDM	SC-FDM	UFMC	GFDM	M-CAP
PAPR	H	L	H	H	L
Robust. to phase noise	M	M/H	M	M/H	M/H
Spectral efficiency	H	H	Very H	Very H	M/H
Robust. to multi. chan.	H	M/H	H	H	M/H
Complexity	M	M/H	M/H	H	M/L

*H → high. M → medium. L → low.

delays. Furthermore, the complexity of the waveform is linked with the requirements of the DSP equipment. In the evaluated waveforms, GFDM is the most complex modulation [10].

Table I gives a more detailed comparison between the presented waveform formats regarding the indicators explained above. Some modulation formats exhibit high performances in determined requirements and low in others. For instance, GFDM allows very high spectral efficiency and high robustness to multipath channels, however, the PAPR and complexity of this modulation format are high. On the other hand, SC-FDM shows PAPR and complexity lower than GFDM, but it is less robust to multipath channels and less spectrally efficient. Hence, it is difficult to decide the best modulation format for ARoF systems only with a qualitative comparison. Therefore, it is necessary to compare the examined waveform formats experimentally to more accurately determine the best modulation format for this type of system.

III. EXPERIMENTAL SETUP

Figure 2 (a) shows the experimental setup used to compare the performance of different waveform formats in an ARoF system. First, an external cavity laser (ECL) generates an optical carrier at 1550 nm. Next, the first MZM, biased at the null point, modulates the optical carrier with a sinusoid of 12.5 GHz produced by a vector signal generator (VSG). Therefore, two optical tones, corresponding to the first harmonics, are produced with a frequency separation of 25 GHz (see Fig. 2 (b)). Then, the signal is boosted by an erbium-doped fiber amplifier (EDFA) and modulated by the second MZM using an arbitrary waveform generator (AWG) of 12 GSa/s.

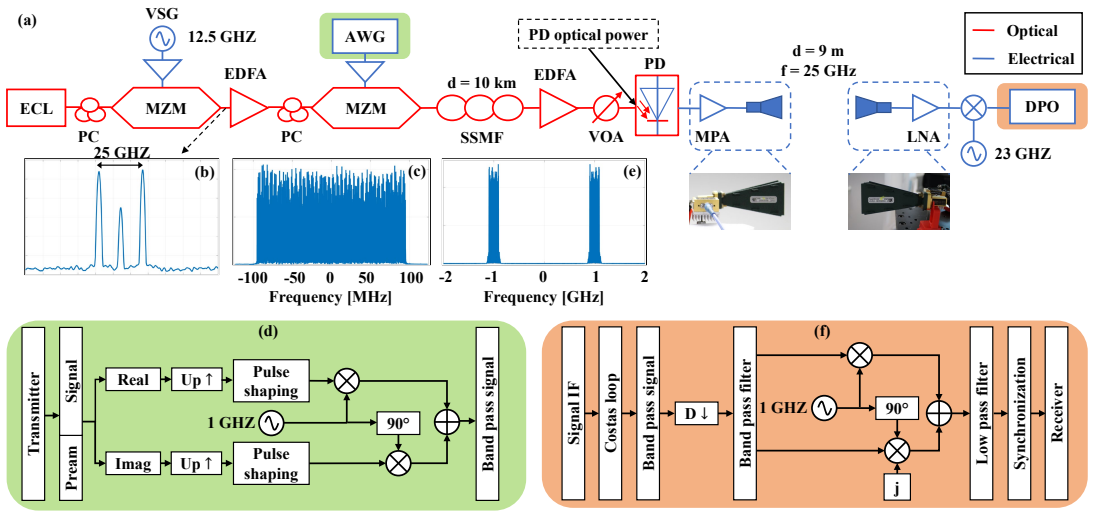


Fig. 2. Setup for the experimental comparison of waveform schemes proposed for beyond 5G: (a) experimental setup, (b) optical signal spectrum after the first MZM, (c) spectrum of the transmitted OFDM baseband signal, (d) block diagram of the transmitter DSP, (e) spectrum of the transmitted bandpass signal, (f) block diagram of the receiver DSP. PC stands for polarization controller.

The signal of each modulation described above is generated in the AWG. The spectrum of the baseband signal is represented in Fig. 2 (c). The DSP to generate the waveform signals in the ARoF system is described in Fig. 2 (d). First, a preamble is introduced to synchronize the signal in the receiver. Next, the signal is separated in its real and imaginary parts. Then, the upsampling and pulse shaping processes are realized in each branch. The real and imaginary parts are multiplied by a cosine and sine at 1 GHz, respectively. Finally, the signals of both branches are added and sent to the second MZM. The spectrum of the resulting signal is shown in Fig. 2 (e).

After the second MZM, the modulated signals are transmitted through 10 km of standard single-mode fiber (SSMF) to a second EDFA. This fiber emulates the connection between the CO and the RU in the ARoF architecture of Fig. 1. The input power of the photodiode (PD) is controlled by a variable optical attenuator (VOA). In the PD, the two optical lines are beaten and converted to an RF signal at 25 GHz carrying the modulation previously introduced. After the PD, the electrical signal is boosted by a 30 dB medium power amplifier (MPA). The PD with the MPA constitutes an RU. The mm-wave signal is transported by a wireless link through two 18.5 dBi horn antennas with a separation of 9 m.

At the output of the received antenna, the signal is amplified by a 40 dB low noise amplifier (LNA) and mixed with a local oscillator (LO) at 23 GHz. The signal with an intermediate frequency (IF) of 2 GHz is sampled by a digital phosphor oscilloscope (DPO) with a sampling rate of 12.5 GSa/s. The receiver DSP diagram is shown in Fig. 2 (f). The IF signal is down-converted to the bandpass signal through a Costas loop process. Subsequently, the processed signal is downsampled and bandpass filtered. Next, the phase and quadrature components are separated and recovered. Then,

the baseband signal is filtered again and synchronized using the preamble. Finally, the receiver of each waveform format acquires the signal.

According to the configuration of the evaluated modulation formats, the parameters of the used OFDM signal in the experimental setup are: subcarrier spacing of 60 kHz, CP of 1.2 μ s, 4096 total subcarriers, 3168 active subcarriers, 928 null subcarriers (464 in each edge of the band) to reduce the out-of-band (OOB) emissions, and one pilot tone inserted on every 12th active subcarrier. These parameters follow the first 5G standard of 3GPP [6]. Using the mentioned parameters, the employed bandwidth is 245.76 MHz and the final throughput is $\log_2(M) \cdot 162.5$ Mbps, where M is the modulation order. For example, utilizing quadrature phase-shift keying (QPSK) and 16-quadrature amplitude modulation (16-QAM), the throughput would be 325 Mbps and 650 Mbps, respectively. Regarding the parameters of the remaining waveforms, the used UFMC configuration employs 128 subbands; GFDM utilizes 3 sub-symbols; and multi-CAP uses 9 subbands. The rest of the parameters are adapted to the OFDM configuration described before. It is important to highlight that all the modulation formats use the same bandwidth and throughput to have a fair comparison in respect of the spectral efficiency.

The experimental setup is mainly dominated by: non-linearity from the RF amplifiers, MZMs, DAC of the AWG, and ADC of the DPO; phase noise introduced in the mm-wave tone generation and down-conversion to IF of the received signal; and amplitude noise produced by the ECL, EDFAs, PD, MPA, LNA, and wireless link. The chromatic dispersion can be considered negligible due to the short length of the utilized optical fiber.

Moreover, the multipath effect is slight because the wireless channel is line of sight (LOS) and the antennas are not moving.

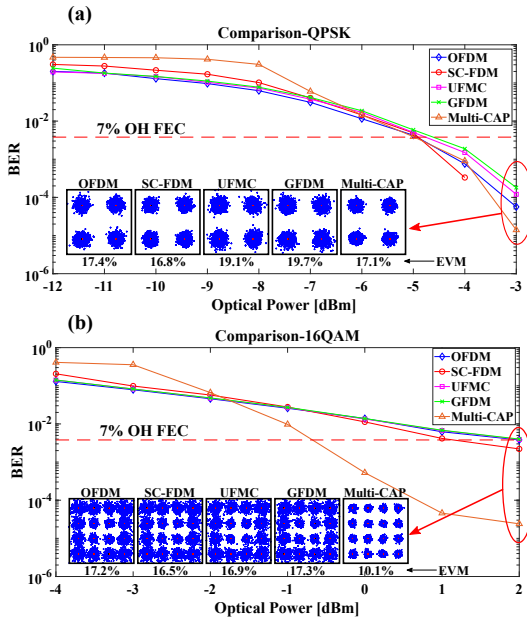


Fig. 3. BER as a function of the input power at the PD for diverse waveform formats using two different modulation orders (QPSK on the top and 16-QAM on the bottom); the constellation diagrams are depicted for the last optical power point of each graph. EVM stands for error vector magnitude.

Hence, the fundamental path is the most dominant and the Doppler effect is practically null. Furthermore, for being a mm-wave channel, multipath and Doppler effect are less intense than in lower frequencies. Then, the equalization of our system has to be the maximum robust against phase and amplitude noise and enough good to compensate the impulse response of the mm-wave wireless channel. In addition, it does not have to introduce long delay to approach the 5G latency requirements.

IV. RESULTS AND INTERPRETATION

Figure 3 shows the results of the described waveform comparison experiment. This figure exhibits two graphs where the evaluated waveform formats are compared with different modulation orders (QPSK and 16-QAM in Fig. 3 (a) and (b), respectively). Moreover, the 7% overhead (OH) hard-decision forward error correction (FEC) limit ($BER < 3.8 \cdot 10^{-3}$) is also showed. Furthermore, the error vector magnitude (EVM) in percent and the constellation of each modulation format for the maximum optical power are presented in both graphs. Comparing the graphs, the optical power required to reach the 7% OH FEC is approximately 7 dBm less in QPSK than in the 16-QAM case.

The BER behavior of OFDM, SC-FDM, UPMC, and GFDM is quite similar in both graphs. However, multi-CAP has a steeper slope and starts with a worse BER. Multi-CAP requires roughly 2 dB less in the FEC limit than the others for 16-QAM. This difference implies larger coverage radius of the

mm-wave cell when multi-CAP signals are used. One reason for this difference lies in the use of different equalization techniques. In the multi-CAP case, a decision feedback equalizer (DFE) with the least mean square (LMS) algorithm is utilized, while for the rest of the waveform formats, a least-squares (LS) equalizer is used. Multi-CAP is the only waveform that employs DFE because the equalization process is performed on each subband independently as an SC waveform, and the LS equalizer is not suitable for compensating the channel on an SC waveform.

In addition, it can be seen that SC-FDM presents better performance than OFDM, UPMC and, GFDM in spite of using the same equalizer technique. This is because the PAPR of SC-FDM is the lowest and, hence, the nonlinear distortions introduced by the MZM and the RF amplifiers are minor. Nonetheless, SC-FDM is slightly more complex than OFDM because it adds a discrete Fourier transform (DFT) block and an inverse DFT (IDFT) process. It can be concluded that the selected equalization strategy and waveform format for ARoF systems and their implementation in beyond 5G architectures are crucial to achieve high-speed bit rates. Moreover, according to these results, waveform formats like multi-CAP and SC-FDM are better solutions than OFDM for ARoF systems delivering high capacity with high spectral efficiency.

V. CONCLUDING REMARKS

In this paper, it has been highlighted that the ARoF architecture with mm-wave signals plays a fundamental role for the future 5G. Next, a qualitative comparison of different modulation formats according to the main requirements for ARoF systems has been realized. The right choice of the modulation format is key, as it is directly related to 5G requirements such as throughput, power consumption, and latency. Then, the evaluated modulation formats have been compared experimentally in an ARoF setup. The results obtained in this experiment have been analyzed and discussed. These results show that modulation formats such as SC-FDM and multi-CAP, outperform the standard OFDM in terms of BER and should, therefore, be considered for beyond 5G systems.

ACKNOWLEDGMENT

This work was partially funded by the 5G STEP FWD (GA no. 722429) and blueSPACE projects (GA no. 762055) which have received funding from the European Union's Horizon2020 research and innovation programme.

REFERENCES

- [1] S. Rommel *et al.*, "High-Capacity 5G Fronthaul Networks Based on Optical Space Division Multiplexing," *IEEE Trans. Broadcast.*, vol. 65, no. 2, pp. 434-443, Jun. 2019.
- [2] M. Fiorani *et al.*, "Modeling energy performance of C-RAN with optical transport in 5G network scenarios," *J. Opt. Commun. Netw.*, vol. 8, no. 11, pp. B21-B34, Nov. 2016.
- [3] D. Konstantinou *et al.*, "5G RAN architecture based on analog radio-over-fiber fronthaul over UDWDM-PON and phased array fed reflector antennas," *Opt. Commun.*, vol. 454, paper 124464, Jan. 2020.
- [4] J. Brenes *et al.*, "A network slicing architecture for SDM and ARoF-based 5G fronthaul networks," *J. Opt. Commun. Netw.*, vol. 12 no. 4, 2020.

- [5] I. A. Hemadeh *et al.*, "Millimeter-Wave Communications: Physical Channel Models, Design Considerations, Antenna Constructions, and Link-Budget," *IEEE Commun. Surveys Tuts.*, vol. 20, no. 2, pp. 870-913, Second quarter 2018.
- [6] 3GPP, *3rd Generation Partnership Project; Technical Specification Group Services and System Aspects; Rel. 15 Description; Summary of Rel-15 Work Items (Rel. 15)*, Feb. 2019.
- [7] C. Browning *et al.*, "5G wireless and wired convergence in a passive optical network using UF-OFDM and GFDM," *IEEE Int. Conf. Commun. Workshops*, Paris, France, May 2017, pp. 386-392.
- [8] M. Wu *et al.*, "On OFDM and SC-FDE transmissions in millimeter wave channels with beamforming," *IEEE Veh. Technol. Conf. Spring*, Nanjing, China, May 2016, pp. 1-5.
- [9] A. A. Zaidi *et al.*, "Waveform and Numerology to Support 5G Services and Requirements," *IEEE Commun. Mag.*, vol. 54, no. 11, pp. 90-98, Nov. 2016.
- [10] R. Gerzaguet *et al.*, "The 5G candidate waveform race: a comparison of complexity and performance," *EURASIP J. Wireless Commun. Netw.*, vol. 2017, pp. 1687-1499, Dec. 2017.
- [11] Y. Liu *et al.*, "Waveform Design for 5G Networks: Analysis and Comparison," *IEEE Access*, vol. 5, pp. 19282-19292, 2017.
- [12] O. Omomukuyo *et al.*, "Experimental demonstration of the impact of MZM non-linearity on direct-detection optical OFDM," 2012 *IEEE Wireless Commun. Netw. Conf.*, Shanghai, China, 2012, pp. 3753-3757.
- [13] C. Browning *et al.*, "Gain-Switched Optical Frequency Combs for Future Mobile Radio-Over-Fiber Millimeter-Wave Systems," *J. Light. Technol.*, vol. 36, no. 19, pp. 4602-4610, 2018.
- [14] A. Delmude *et al.*, "OFDM Baud Rate Limitations in an Optical Heterodyne Analog Fronthaul Link using Unlocked Fibre Lasers," *Int. Topical Meeting Microw. Photon.*, Ottawa, Canada, 2019, pp. 1-4.
- [15] I. Parvez *et al.*, "A Survey on Low Latency Towards 5G: RAN, Core Network and Caching Solutions," *IEEE Commun. Surv. Tuts.*, vol. 20, no. 4, pp. 3098-3130, 4th Quart., 2018.

P3: Probabilistic Amplitude Shaping to Enhance ARoF Fronthaul Capacity for Mm-Wave 5G/6G Systems

J. P. Santacruz, S. Rommel, A. Jurado-Navas, and I. Tafur Monroy, “Probabilistic Amplitude Shaping to Enhance ARoF Fronthaul for Mm-Wave 5G/6G Systems,” in *2022 European Conference on Networks and Communications (EuCNC)*, Grenoble, France: IEEE, Jun. 2022, pp. 1–6. DOI: 10.1109/EuCNC/6GSummit54941.2022.9815694

Probabilistic Amplitude Shaping to Enhance ARoF Fronthaul Capacity for Mm-Wave 5G/6G Systems

Javier Pérez Santacruz*, Simon Rommel*, Antonio Jurado Navas†, and Idelfonso Tafur Monroy*

*Institute for Photonic Integration, Eindhoven University of Technology, 5600MB Eindhoven, The Netherlands

†Institute of Telecommunication Research (TELMA), University of Málaga, CEI Andalucía Tech., Málaga E-29010, Spain

Email: {j.perez.santacruz, s.rommel, i.tafur.monroy}@tue.nl, navas@ic.uma.es

Abstract—Analog radio-over-fiber (ARoF) technology has proven to be a promising solution to be part of the future millimeter-wave (mm-wave) 5G/6G architecture due to its attractive benefits such as simplified remote antenna units (RAUs), low-power consumption, and low cost. However, ARoF channels present hefty drawbacks that need to be addressed. The probabilistic amplitude shaping (PAS) technique is able to reduce the impact of such drawbacks, allowing a fine optimization of channel capacity. In particular, enumerative sphere shaping (ESS) implementation stands out as an excellent PAS approach because of its energy-efficiency and low complexity for short blocklengths. In this work, for the first time to the best of our knowledge, an ESS scheme is evaluated in an experimental bidirectional mm-wave ARoF setup oriented towards 5G communications. Furthermore, a novel soft ESS demapping algorithm is proposed and explained. The experimental results confirm the ESS technique, together with the proposed algorithm, as a convenient solution to enhance the channel capacity of mm-wave ARoF systems for 5G/6G fronthaul.

Keywords—5G, 6G, ARoF, fronthaul, mm-wave, ESS, probabilistic shaping, OFDM, PAS, soft demapping.

I. INTRODUCTION

The emergence of new types of services such as virtual reality, 4K/8K video streaming, or Internet of things (IoT) demands a substantial enhancement in mobile networks. Improvements in terms of data rate, latency, number of connected devices, energy consumption, and reliability are crucial key performance indicators (KPIs) to guarantee a good user experience [1]. The fifth generation of mobile networks (5G) aims to upgrade the mentioned KPIs. The ongoing deployment of the 5G network is mainly focused on the usage of sub-6 GHz bands. Nonetheless, sub-6 GHz bands are congested and, thus, bandwidth limitation is a major impediment to increase the mobile network data rate. Since millimeter-wave (mm-wave) bands are the next operational frequencies to be exploited, one of the next steps for future mobile networks as 5G-advanced and 6G consists of the utilization of mm-wave signals. However, the employment of higher frequencies brings with it an increase in free-space path loss (FSPL), which consequently reduces the coverage radius of mobile cells. Thereby, the number of mobile cells will enormously increase compared to current mobile networks to cover the same area [2], making simplicity of the remote antenna unit (RAU) as an essential requirement to accomplish a scalable mm-wave 5G/6G network [3].

Analog radio-over-fiber (ARoF) raises as a suitable solution

to simplify the complexity of the RAU, since radio frequency (RF) upconversion, digital-to-analog converters (DAC), and analog-to-digital converters (ADC) are not required in the RAU. Moreover, ARoF brings other attractive benefits such as large bandwidth, low latency, and high spectral efficiency [3], [4]. However, phase noise is considered a high limiting factor in 5G/6G scenarios due to the relatively low subcarrier spacing of the orthogonal frequency-division multiplexing (OFDM) signals established in the 3rd Generation Partnership Project (3GPP) standardization [5], [6]. In addition, additive white Gaussian noise (AWGN) and nonlinearity effects are also two of the other main impairments in OFDM ARoF systems [4]. In conclusion, ARoF channels are complex to the level that simple bit-loading schemes cannot fully exploit the maximum capacity. Therefore, rate adaptability methods are highly recommended to optimize the final performance in ARoF systems [7], [8]. Conventional modulation and coding schemes (MCSs) use uniform quadrature amplitude modulation (QAM) with variable forward error correction (FEC) rates. Nevertheless, according to [9] and [10], probabilistic amplitude shaping (PAS) QAM with a fixed FEC rate outperforms the mentioned MCSs in terms of rate adaptability and performance in optical fiber communications. Furthermore, the works carried out in [7] and [8] experimentally demonstrate that PAS-OFDM is a method of great rate adaptability to achieve the maximum capacity in ARoF fronthaul.

Constant composition distribution matching (CCDM) is the most evaluated and investigated architecture to reach PAS in the communication systems literature due to its low complexity [11]. However, CCDM is inefficient in terms of rate loss and energy-efficiency for short blocklengths [12], [13]. Long PAS blocks imply a severe inconvenience in wireless communications since PAS frames are encapsulated in OFDM symbols. Thus, if the PAS blocks are excessively long, they are contained in more than one OFDM symbol, increasing the overall delay. Hence, CCDM is not a preferred solution for 5G/6G wireless applications where latency is a critical factor. The enumerative sphere shaping (ESS) realization proposed in [12] is an excellent solution for performing PAS-QAM in fiber wireless communications due to its high energy-efficiency, low rate loss, and low computational complexity for short blocklengths [13], [14].

By taking advance of the shaping redundancy employed in the PAS signals, soft PAS demapping can be performed and, thus, the bit error rate (BER) can be reduced [14]. In this work, for the first time (to the best of the authors'

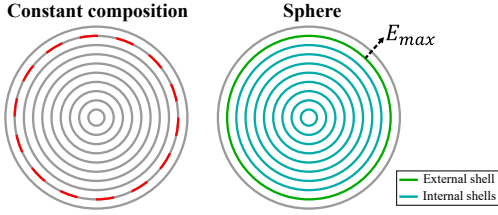


Fig. 1. Comparison between the sequences utilized by CCDDM (left) and SS (right) architectures. Each circle corresponds to an N-dimensional shell where the radius is proportional to the PAS block energy. The colored segments refer to the sequence used in the respective PAS approach.

knowledge), an algorithm for softly demapping ESS blocks is presented and explained. The concept of this algorithm can be extrapolated to other PAS solutions. Moreover, for the first time, an ESS scheme is experimentally evaluated on a mm-wave bidirectional ARoF fronthaul adhering to the 5G numerology [6]. Additionally, hard and soft ESS demapping methods are compared in the experimental setup, showing a slightly improvement in performance when soft demapping is applied. Finally, the experimental ESS results show a substantial enhancement over the bit-loading technique, highlighting PAS implementation, and ESS in particular, as a promising candidate for optimizing channel capacity in mm-wave 5G/6G ARoF fronthauls.

II. PROBABILISTIC AMPLITUDE SHAPING FOR THE ARoF 5G/6G FRONTHAUL

As mentioned above, ARoF is an excellent solution to deploy the future mm-wave 5G/6G fronthaul. However, the utilization of ARoF technology brings several drawbacks and these are the following:

Phase noise: according to the phase noise model of Leeson, the phase noise level is proportional to the carrier frequency [15]. Thus, mm-wave RF sources offer higher phase noise than other lower frequency bands. In ARoF systems, two optical tones must be generated with a separation of the desired frequency carrier. To accomplish this, there are different techniques to generate these two optical tones. Nevertheless, the two-tone generation techniques present a good trade-off between phase noise and optical output power [16], achieving phase noise levels comparable to pure RF solutions. Moreover, in mm-wave heterodyne systems, the contribution of the RF sources involved in up and downconversion affects the final phase noise level [17]. Furthermore, 5G New Radio (NR) signals are not robust in phase noise channels, as the OFDM subcarrier spacing values (15 to 240 kHz) are relatively low [5], [6]. Therefore, mm-wave OFDM ARoF systems are highly limited by phase noise.

AWGN: since high FSPL is inherently related to mm-wave wireless communications, a low-power signal is received when the user is relatively far from the RAU. Moreover, in an ARoF system, the AWGN noise floor is augmented by the devices involved in the system, such as lasers, RF amplifiers, or photodiodes (PD). Thereby, mm-wave ARoF channels are limited in terms of signal-to-noise ratio (SNR).

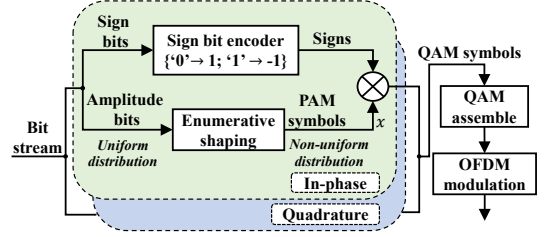


Fig. 2. Block diagram for generating PAS-OFDM signals using ESS.

Nonlinearity effects: signals transmitted through ARoF channels suffer from distortion. This distortion effect originates from components such as DACs, ADCs, RF amplifiers, Mach-Zehnder modulators (MZMs), and optical fibers due to their nonlinear transfer functions or finite resolutions. The distortion effect of these components increases for higher input signal powers, delimiting a distortion region and consequently reducing the dynamic range of the system [18].

The impacts of the three drawbacks explained above are gradually reduced by employing different PAS configurations on the data subcarriers of the transmitted OFDM signal [8], [19]. Therefore, applying PAS in mm-wave OFDM ARoF scenarios is a well-suited solution to maximize channel capacity utilization [7], [8]. As mentioned in Section I, ESS algorithms provide an excellent trade-off between energy-efficiency, rate loss, computational complexity, and blocklength compared to other solutions such as CCDDM [12], [14]. In the following subsections, the concept of ESS and the proposed soft ESS demapping method will be presented and explained.

A. Enumerative sphere shaping for PAS approach

The PAS approach aims to optimize the communication channel capacity by altering the probabilistic distribution of the M-QAM symbols. To achieve this, PAS algorithms increase the probability of low-power M-QAM symbols in respect to high-power symbols, moving from a uniform distribution to a Maxwell-Boltzmann distribution [12]. The way to perform this distribution conversion consists of including PAS redundancy and, hence, the throughput is reduced. In order to have higher probabilities on the lower power M-QAM symbols or, in other words, to reach a more confined Maxwell-Boltzmann distribution, it is necessary to add more PAS redundancy. Thus, the M-QAM signal can gradually adapt to the channel conditions by correctly choosing the most fitted PAS configuration. The most studied and investigated PAS architecture is CCDDM due to its low computational complexity [11]. However, sphere shaping (SS) is a more preferred solution than CCDDM. This preference is because SS is able to use all the sequences inside of the sphere while CCDDM utilizes some of the sequences located on the surface of the sphere (see Fig. 1) [12]. Therefore, SS solutions offer more energy-efficient PAS blocks than by using CCDDM and, thus, the rate loss is lower [12].

The ESS algorithms proposed in [12] employ the SS architecture and lexicographical ordering. These algorithms are computationally less complex than other SS solutions such as shell mapping (SM) [14]. Thereby, the benefits of

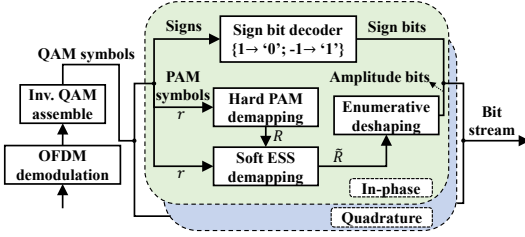


Fig. 3. Block diagram for demodulating PAS-OFDM signals using ESS.

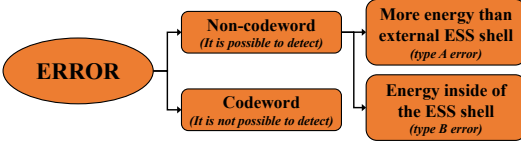


Fig. 4. Type of errors in the received ESS blocks.

using SS architectures to perform PAS with low complexity can be realized by using the ESS algorithms of [12]. Specifically, these ESS algorithms are two: the enumerative shaping algorithm whose goal consists of transforming the uniform distribution of the input pulse amplitude modulation (PAM) symbols into a Maxwell-Boltzmann distribution; the enumerative deshaping algorithm realizes an inverse process to obtain the initial PAM symbols. To realize PAS-QAM, the enumerative shaping algorithm is applied independently for in-phase and quadrature PAM symbols and the signs of the M-QAM symbols are included as shown in Fig. 2. For a PAS-OFDM implementation, the enumerative shaping algorithm is employed on the data M-QAM subcarriers before OFDM modulation on the transmitter side, as illustrated in Fig. 2. On the receiver side, Fig. 3 shows the inverse procedure for decoding the received PAS-OFDM blocks. Observing Fig. 3, a hard PAM demapping block is needed before the enumerative deshaping algorithm. Furthermore, in this work, a novel soft ESS demapping algorithm is proposed to improve final yields by taking advance of PAS redundancy. The soft ESS demapping process is included in the block diagram of Fig. 3 and will be explained in the next subsection.

B. Soft ESS demapping

PAS redundancy included during the ESS shaping can be used to determine if the received ESS block belongs to the ESS codebook. A simple way to identify an ESS non-codeword is to check if the energy of the received ESS block is located inside of the ESS sphere (see Fig. 1). The flowchart of Fig. 4 classifies the different types of ESS blocks received with errors. An errored ESS block means that the transmitted and received ESS blocks differ by one or more PAM symbols. The worst case occurs when the received ESS block belongs to the ESS codebook. In this case, the error detection is not feasible to realize using only PAS redundancy. On the contrary, when the errored ESS block is a non-codeword, this can be classified in terms of energy: non-codewords with more energy than the ESS external shell -type A error- and non-codewords with energy inside of the ESS shell -type B error-. The ESS

Algorithm 1 Soft ESS demapping algorithm

Given r_1, r_2, \dots, r_N and R_1, R_2, \dots, R_N :

- 1) Calculate hard demapped ESS block energy as

$$E_r = \sum_{k=1}^N |R_k|^2 \quad (1)$$

- 2) Exit the algorithm if E_r is inside of the ESS shell
if ($E_r \leq E_{max}$) **then**
 Exit algorithm
end if
- 3) Calculate the Euclidean distance for each PAM symbol of the received ESS block as

$$d_k = R_k - r_k \quad (2)$$

- 4) Modify R in order to obtain a demapped ESS block energy inside of the ESS shell

```

 $k = 1$                                 ▷ Initialization
 $\tilde{R} = R$ 
 $E_{diff} = E_r - E_{max}$ 
 $d' = d$ 
while [( $E_{diff} > 0$ ) and ( $k \leq N$ )] do
     $n = \underset{k}{\operatorname{argmax}}(d'_k)$ 
     $m = \underset{k}{\operatorname{argmax}}(\mathcal{A}_k = R_n)$ 
    if  $m > 1$  then
         $\tilde{R}_n = \mathcal{A}_{m-1}$ 
         $E_{diff} = E_{diff} - |\mathcal{A}_m^2 - \mathcal{A}_{m-1}^2|$ 
    end if
     $d'_n = -\infty$ 
     $k = k + 1$ 
end while

```

blocks with type A error are very simple to detect and most non-codewords fall into this category. Concerning the type B error, since the lexicographical ordering is utilized, some non-codewords are inside of the ESS shell and, thus, the ESS deshaping algorithm must be employed to identify them. Fortunately, the number of ESS blocks with type A error is significantly larger than those with type B error because most errors come from wrong demappings where the demapped PAM symbols have higher power than the transmitted ones. This fact is because the probability of transmitting low-power PAM symbols is larger than that of transmitting high-power PAM symbols. Therefore, for an appropriate trade-off between performance and complexity, the proposed soft ESS demapping algorithm focuses on the detection and correction of received ESS blocks with type A error.

Algorithm 1 describes the proposed soft ESS demapping method where R , \tilde{R} , N , and E_{max} are the hard and soft demapped symbols, the ESS blocklength, and the maximum energy of the ESS codebook, respectively. This algorithm is applied for each received ESS block r (see Fig. 3). Furthermore, in algorithm 1, \mathcal{A} refers to the PAM alphabet $\{1, 3, 5, 7, \dots\}$ [12]. The proposed algorithm is composed of four steps: the first two steps aim to identify if the received ESS block is a non-codeword with type A error; the third step calculates the Euclidean distance which is used as a figure of merit to determine the less reliable PAM symbols to modify;

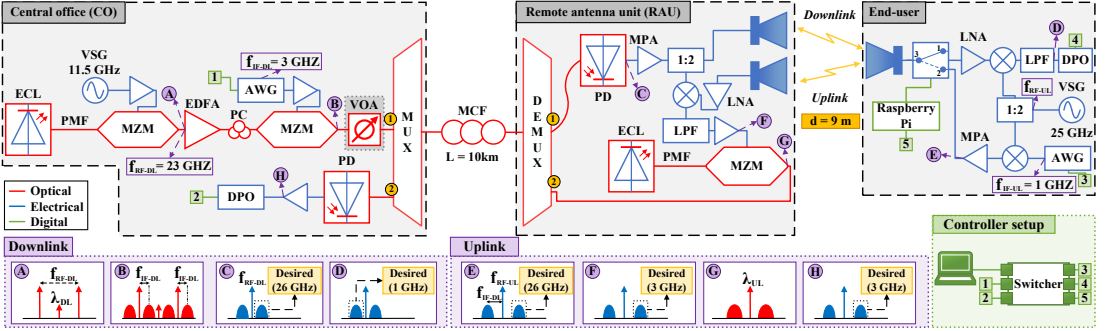


Fig. 5. Experimental setup to realize a bidirectional mm-wave 5G fronthaul.

TABLE I. ESS CONFIGURATION PARAMETERS.

Config.	A	B	C	D	E	F	G	H	I	J	K	L
M-QAM	16	16	16	16	16	16	64	64	64	64	64	64
Uniform	No	No	No	No	No	Yes	No	No	No	No	No	Yes
N	10	10	10	10	10	-	18	18	18	18	18	-
L	8	7	6	5	4	-	19	16	14	12	10	-
OH PAS [%]	33.3	23.5	16.3	12.4	8.7	-	29.9	25	20.5	14.9	11.1	-
Effective bits/symbol	3	3.24	3.44	3.56	3.68	4	4.62	4.8	4.98	5.22	5.4	6

the fourth step modifies the less reliable PAM symbols of the hard demapped ESS block. The intention of this fourth step is to correct the wrong PAM symbols of the hard demapped ESS block. To achieve this, the fourth step attempts to modify the less reliable symbols of the hard demapped ESS block to obtain an ESS block energy within the ESS sphere. This modification consists of replacing the selected symbol by the previous PAM symbol of the alphabet \mathcal{A} (e.g., $3 \rightarrow 1$ or $5 \rightarrow 3$) and, then, E_{diff} is diminished. In addition, the reliability of the PAM symbols is indicated by the Euclidean distance. In algorithm 1, the maximum value of d' is set to $-\infty$ to ensure that the selected PAS symbol is not considered in subsequent iterations. Lastly, it is important to highlight that the correction success of algorithm 1 is inversely proportional to the number of erroneous PAM symbols within the hard demapped ESS block.

III. EXPERIMENTAL SETUP

Fig. 5 shows the bidirectional experimental setup to perform a 5G mm-wave fronthaul based on ARoF [4]. This experimental setup is the same as presented in [4] with the difference that an RF switch and variable optical attenuator (VOA) are used after the end-user antenna and before the multicore fiber (MCF) of the downlink path, respectively. The gray boxes in Fig. 5 delimit the different segments involved in the 5G fronthaul: central office (CO), RAU, and end-user. The configuration of the setup is according to the mm-wave 5G standard [6]: OFDM as modulation format; 240 kHz of subcarrier spacing; time-division duplexing (TDD) as multiplexing scheme; 26 GHz is the carrier frequency (center of n258 band); and 245.76 MHz of bandwidth. One of the objectives of this bidirectional setup consists of sharing the vector signal generators (VSGs) between both directions, reducing

complexity, cost, and power consumption [4]. More details about the experimental setup can be found in [4]. Additionally, the spectrum shapes for various points of the experimental setup are illustrated at the bottom of Fig. 5.

In the CO of the downlink part, first, an external cavity laser (ECL) emits an optical carrier at C-band. Then, the generated optical carrier is modulated with an RF carrier of 11.5 GHz using a null-biased MZM. In this way, two optical tones are produced with a separation of 23 GHz (Fig. 5 (A)). Next, the two optical tones are boosted and modulated with the OFDM signal by employing an erbium-doped fiber amplifier (EDFA) and a second MZM, respectively (Fig. 5 (B)). Subsequently, the modulated optical signal passes through a 10 km MCF. In the downlink RAU side, the optical signal beats on a PD, generating a modulated RF signal at 26 GHz (Fig. 5 (C)). Then, the RF signal is boosted by a medium power amplifier (MPA) and sent over a 9 m wireless link with a horn antenna. The end-user antenna catches the downlink transmitted signal. Consequently, RF amplification, downconversion, and filtering processes are performed (Fig. 5 (D)). Lastly, the resulting signal is sampled with a digital phosphor oscilloscope (DPO).

In the uplink path of the end-user, the OFDM signal is generated with an arbitrary waveform generator (AWG). Next, the signal is upconverted and boosted. After that, the mm-wave signals pass through the wireless link. The second horn antenna of the RAU side receives the uplink transmitted signal at 26 GHz. Then, the RF signal is amplified with a low noise amplifier (LNA), downconverted, and filtered with a low-pass filter (LPF) (Figs. 5 (E) and (F)). The resulting RF signal is used to modulate an optical carrier generated by a second ECL. Hence, the uplink modulated optical signal passes through the MCF. At the CO, a second PD is used to convert the optical signal into the electrical domain. Finally, the resulting

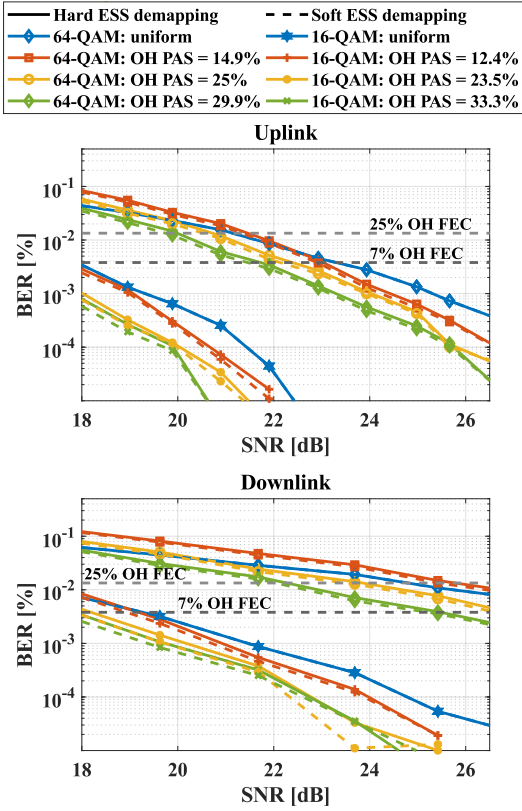


Fig. 6. BER results of the experimental setup as a function of the SNR for the different ESS configurations: uplink results (top graph); downlink results (bottom graph).

electrical signal is captured and sampled by a second DPO.

Since the end-user only disposes of one horn antenna and both directions use the same frequency band, an RF switch is required. The commutation of this RF switch is determined by the slot time of each direction according to the TDD schedule. A Raspberry Pi is employed to control the RF switch. For a proper TDD implementation, the AWGs and DPOs of each direction, and the Raspberry Pi must be synchronized. For simplicity, this synchronization is carried out in the controller setup where a central computer sends the commands to each instrument (see green box in Fig. 5). Furthermore, in order to evaluate the ESS solution in a mm-wave 5G fronthaul, different ESS configurations are transmitted in the presented setup. Table I shows the main parameters of these ESS configurations, where M is the modulation order, N is the number of PAM symbols per ESS block, and L is the number of energy levels at the last stage of the ESS trellis [12]. It can be observed that the ESS scheme under evaluation permits a gradual entropy (effective bits/symbol) adaptation. Moreover, to evaluate the performance of the ESS signals transmitted in the experimental setup under different SNR conditions, a

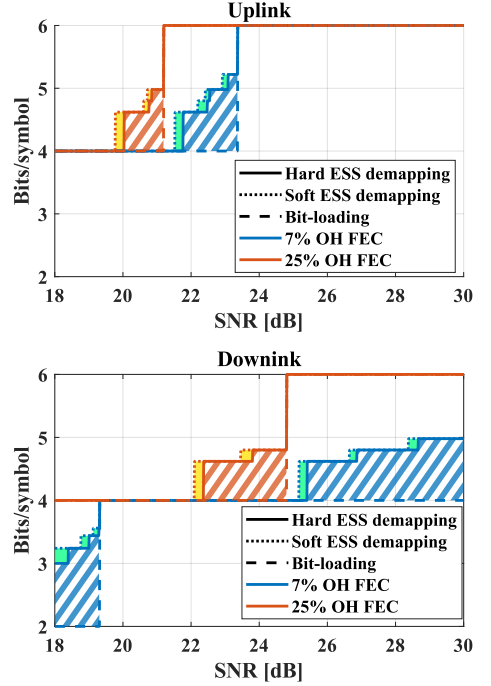


Fig. 7. Entropy results of the experimental setup as a function of the SNR by using ESS and bit-loading schemes: uplink results (top graph); downlink results (bottom graph).

power sweep is realized on the downlink and uplink paths by tuning the VOA voltage and the power of the end-user VSG, respectively.

IV. EXPERIMENTAL RESULTS

Fig. 6 depicts the BER results as a function of the SNR by employing some configurations of Table I in the experimental setup explained in Section III. The top graph refers to the uplink direction, while the bottom one concerns the downlink. Furthermore, the 25% and 7% overhead (OH) FEC thresholds are also illustrated in Fig. 6 as dotted gray lines. The dotted and continuous BER results refer to when the soft ESS demapping algorithm 1 is applied or not, respectively. In this way, the yields of the proposed soft ESS demapping method can be appraised. Examining Fig. 6, it can be noticed that the uplink BER results perform better under the same SNR conditions. This difference in performance between both directions is due to the fact that the signal transmitted through the downlink path suffers from more nonlinearities. Moreover, by inspecting Fig. 6, a gap between 16-QAM and 64-QAM BER results can be detected for both directions. This gap is because PAS 64-QAM configurations contain many more QAM symbols to demap and, hence, the BER increases substantially. Nevertheless, it can be noticed a gradual decrease in BER in the 16-QAM and 64-QAM regions when using the different ESS configurations.

The configuration with maximum entropy (effective bits/symbol) of Table I is estimated when its BER value is below the 7% or 25% OH FEC thresholds. This process is done by an SNR step size of 0.01 dB. To achieve this SNR granularity, a linear interpolation of the SNR results of Fig. 6 is realized. With this procedure, the entropy results of Fig. 7 are obtained. The bit-loading solution is also displayed along with the soft and hard ESS implementations. The striped colored areas of Fig. 7 refer to the entropy improvement when using hard ESS implementation relative to the bit-loading method. Observing both graphs in Fig. 7, there is a significant enhancement when using the ESS implementation since the bit-loading technique offers large entropy steps ($\log_2(M)$ bits/symbol) while ESS allows for a more gradual entropy range. Therefore, the ESS scheme under evaluation concedes intermediate entropy values between bit-loading steps, approaching the channel capacity utilization to the Shannon limit. In addition, respecting the bit-loading technique, the ESS enhancement of Fig. 7 is greater in the downlink results because there are more nonlinearities in this direction and PAS-OFDM can be greater harnessed. Thereby, the presented ESS scheme is highly recommended in mm-wave ARoF fronthaul systems that suffer from severe nonlinearities.

The flat colored areas in Fig. 7 correspond to the increase in entropy of applying the soft ESS demapping with respect to the hard method. In this case, the entropy improvement is small, but appreciable. Nevertheless, the proposed algorithm 1 has low computational complexity and hence even small gains may justify its application. In addition, for future works, the reliability of the soft ESS demapped block can be quantified with a figure of merit. This figure of merit determines the reliability of the received ESS block respecting the ESS codebook. Thus, in combination with channel coding, such a figure of merit can be employed in an iterative decoding scheme as turbo codes do [20]. In such a manner, the final BER can be substantially reduced.

V. CONCLUSION

In this work, firstly, the advantages of using PAS for mm-wave ARoF fronthaul are presented. In particular, ESS algorithms are highlighted as a suitable solution to implement PAS due to their low rate loss and high energy-efficiency. Next, a novel soft ESS demapping algorithm is explained and presented. Then, a specific ESS scheme is experimentally evaluated in a bidirectional mm-wave ARoF setup attached to the 5G standard with 9 m of wireless link. Respecting the bit-loading technique, the experimental results show a significant improvement in terms of channel capacity utilization when using the under-test ESS scheme. Moreover, the proposed soft ESS demapping algorithm outperforms the hard solution, marking it as an adequate complement for ESS implementations. Furthermore, by comparing the results of the different directions, it is experimentally proven that ESS is especially useful in channels with nonlinearities as it can help overcome their effects. Finally, as a remarkable conclusion, the experimental results validate the PAS solution and, in particular ESS, as an excellent method to optimize the channel capacity in mm-wave OFDM ARoF systems for 5G/6G communications.

Acknowledgements The presented work was partially financed by the 5G STEP FWD and blueSPACE projects (GA nos. 722429

and 762055). Also, J. Pérez Santacruz would like to thank Yunus Can at Eindhoven University of Technology for his suggestions.

REFERENCES

- [1] W. Jiang, B. Han, M. A. Habibi, and H. D. Schotten, "The Road Towards 6G: A Comprehensive Survey," *IEEE Open J. Commun. Soc.*, vol. 2, pp. 334–366, Feb. 2021.
- [2] I. A. Hemadeh *et al.*, "Millimeter-Wave Communications: Physical Channel Models, Design Considerations, Antenna Constructions, and Link-Budget," *IEEE Commun. Surv. Tutor.*, vol. 20, no. 2, pp. 870–913, Apr.–Jun. 2018.
- [3] S. Rommel *et al.*, "Towards a Scaleable 5G Fronthaul: Analog Radio-over-Fiber and Space Division Multiplexing," *J. Light. Technol.*, vol. 38, no. 19, pp. 5412–5422, Oct. 2020.
- [4] J. P. Santacruz *et al.*, "Bidirectional mm-Wave ARoF Fronthaul over Multicore Fiber for 5G and Beyond," in *2021 International Topical Meeting on Microwave Photonics (MWP)*, Pisa, Italy, 2021, pp. 1–4.
- [5] J. P. Santacruz, S. Rommel, U. Johannsen, A. Jurado-Navas, and I. T. Monroy, "Analysis and Compensation of Phase Noise in Mm-Wave OFDM ARoF Systems for Beyond 5G," *J. Lightwave Technol.*, vol. 39, no. 6, pp. 1602–1610, Mar. 2021.
- [6] 3GPP, *FG IMT-2020: User Equipment (UE) radio transmission and reception. 3GPP TR 38.101-2, version 16.5.0*, Jul. 2020.
- [7] R. a. o. Zhang, "Joint Optimization of Processing Complexity and Rate Allocation through Entropy Tunability for 64-/256-QAM Based Radio Fronthauling with LDPC and PAS-OFDM," in *2020 Optical Fiber Communications Conference and Exhibition (OFC)*, San Diego, CA, USA, May 2020, pp. 1–3.
- [8] K. Wu *et al.*, "Probabilistic Amplitude Shaping for a 64-QAM OFDM W-Band RoF System," *IEEE Photon. Technol. Lett.*, vol. 31, no. 13, pp. 1076–1079, Jul. 2019.
- [9] J. Cho and P. J. Winzer, "Probabilistic Constellation Shaping for Optical Fiber Communications," *J. Light. Technol.*, vol. 37, no. 6, pp. 1590–1607, Mar. 2019.
- [10] J. Shi *et al.*, "Improved Performance of high-order QAM OFDM Based on Probabilistically Shaping in the Datacom," in *2018 Optical Fiber Communications Conference and Exposition (OFC)*, San Diego, CA, USA, Jun. 2018, pp. 1–3.
- [11] P. Schulte and G. Böcherer, "Constant Composition Distribution Matching," *IEEE Trans. Inf. Theory*, vol. 62, no. 1, pp. 430–434, 2016.
- [12] Y. Gültekin *et al.*, "Enumerative Sphere Shaping for Wireless Communications With Short Packets," *IEEE Trans. Wirel. Commun.*, vol. 19, no. 2, pp. 1098–1112, 2020.
- [13] S. Goossens *et al.*, "First Experimental Demonstration of Probabilistic Enumerative Sphere Shaping in Optical Fiber Communications," in *2019 24th OptoElectronics and Communications Conference (OECC)*, Fukuoka, Japan, Aug. 2019, pp. 1–3.
- [14] Y. C. Gültekin *et al.*, "Probabilistic Shaping for Finite Blocklengths: Distribution Matching and Sphere Shaping," *Entropy*, vol. 22, no. 5, May 2020.
- [15] X. Huang, F. Tan, W. Wei, and W. Fu, "A Revisit To Phase Noise Model Of Leeson," in *2007 IEEE International Frequency Control Symposium Joint*, Geneva, Switzerland, October 2007, pp. 238–241.
- [16] J. P. Santacruz *et al.*, "Experimental ARoF System Based on OPLL Mm-Wave Generation for Beyond 5G," in *26th OptoElectronics and Communications Conference (OECC)*, Hong Kong, China, Jul. 2021, p. W2B.2.
- [17] T. Shao *et al.*, "Investigation on the Phase Noise and EVM of Digitally Modulated Millimeter Wave Signal in WDM Optical Heterodyning System," *J. Light. Technol.*, vol. 30, no. 6, pp. 876–885, Jan. 2012.
- [18] D. Novak and R. Waterhouse, "Advanced radio over fiber network technologies," *Opt. Express*, vol. 21, no. 19, pp. 23001–23006, Sep. 2013.
- [19] J. P. Santacruz *et al.*, "Probabilistically Shaped OFDM for Gradual Capacity Adaptation in 5G ARoF Systems," in *26th OptoElectronics and Communications Conference (OECC)*, Hong Kong, China, Jul. 2021, p. W1B.4.
- [20] T. S. V. Gautham, A. Thangaraj, and D. Jaliha, "Common architecture for decoding turbo and LDPC codes," in *2010 National Conference On Communications (NCC)*, Chennai, India, Mar. 2010, pp. 1–5.

Phase noise in OFDM mm-wave ARoF systems

This chapter aims to comprehensively respond to the research question **RQ-4**. One of the main reasons for answering to this research question lies in the fact that the phase noise level of an RF oscillator is directly proportional to its carrier frequency [87]. Besides, the phase noise level is more likely to be higher in mm-wave ARoF scenarios than in RF approaches. Therefore, since 5G NR signals are transmitted in FR2 bands with higher frequency carriers than in its predecessor (LTE), phase noise may be a limiting factor for some scenarios, especially in mm-wave ARoF cases. Furthermore, the OFDM signal degradation due to phase noise is inversely proportional to the subcarrier spacing (Δf) [121]. For this reason, the 3GPP 5G standard defines a set of new subcarrier spacing values [19]. This set of Δf values is also known as 5G numerology in which the numerology number μ is related to the subcarrier spacing value as follows: [19]:

$$\Delta f[kHz] = 2^\mu \cdot 15. \quad (4.1)$$

Specifically, the 3GPP 5G standard defines five possible subcarrier spacing values. These values are depicted in Table 4.1. Moreover, Table 4.1 specifies which numerologies μ are allowed to be used in each FR band (FR1, FR2). Examining Table 4.1, it can be noted that FR1 uses low 5G numerology values while FR2 utilizes high numerology. One of the main reasons for this fact is that relatively low bandwidths are employed in FR1 bands, with respect to the bandwidths used in FR2. However, as commented above, in some mm-wave ARoF scenarios, phase noise can be one of the major limiting factors due to the relative low subcarrier spacing values defined in the 5G standard [129]. Therefore, thorough investigations related to the analysis, study, and compensation of phase noise in OFDM ARoF systems oriented towards mm-wave 5G/6G communications are highly required.

Table 4.1: 5G numerology for FR1 and FR2 bands as defined by the 5G standard [19].

μ	Δf [kHz]	FR1	FR2
0	15	✓	✗
1	30	✓	✗
2	60	✓	✓
3	120	✗	✓
4	240	✗	✓
5*	480*	✗	✓

(*) \rightarrow not yet standardized

Thereby, the organization of this chapter is structured as follows: Section 4.1 focuses on the phase noise channel model; Section 4.2 indicates and describes the types of degradation that occur in the OFDM signal due to phase noise; next, Section 4.3 profoundly explains several DSP algorithms to compensate for phase noise in OFDM signals (most of these presented DSP algorithms have been proposed in the contribution papers of this dissertation); Section 4.4 describes and explains the mm-wave ARoF testbeds that have been employed to apply the DSP algorithms presented in Section 4.3; finally, Section 4.5 frames in the SOTA the contribution papers of this dissertation that are related to phase noise compensation in OFDM mm-wave ARoF systems.

4.1 Transmission channel model with phase noise

This section aims to explain the phase noise channel model both in the time and frequency domains. In the time domain case, the received signal of a channel, which is corrupted by phase noise, can be expressed as follows [130]:

$$r(t) = x(t) \cdot e^{j\varphi(t)}, \quad (4.2)$$

where $x(t)$ and $\varphi(t)$ are the transmitted waveform signal and phase noise, respectively. As it can be observed in Eq. (4.2), the received signal is multiplied by a complex exponential whose argument (φ) varies in time. This temporal variation of the phase noise φ can be approximated as a Wiener process for simplicity of theoretical analysis and simulation. For the discrete time-model representation, the phase noise samples, that follow a Wiener process, can be calculated as follows [130]:

$$\varphi[n] = \varphi[n-1] + W[n], \quad (4.3)$$

where W is a real Gaussian process with mean 0 and variance σ_{PN}^2 which is equal to $2\pi T_s \beta_{PN}$. T_s is the sampling period and β_{PN} is denominated as the full-width at half-maximum (FWHM). Figure 4.1(a) illustrates an example of how $\varphi[n]$ evolves over time by using Eq. (4.3). Figure 4.1(a) is the typical representation of a Wiener

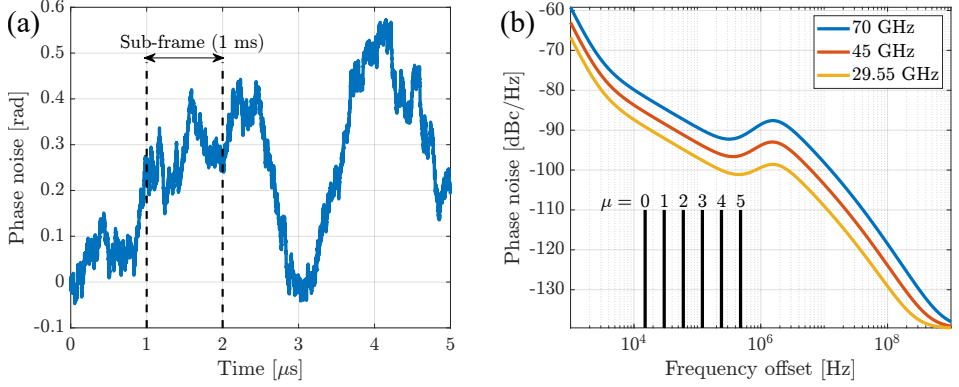


Figure 4.1: Phase noise channel model: (a) Wiener process in the time domain [130]; (b) 3GPP phase noise channel model in the frequency domain [131].

process. The Wiener process in Fig. 4.1(a) can be interpreted as a random walk, since the current value depends on the previous one plus a random number.

For the frequency domain characterization of the phase noise, it is necessary to analyze the spectral form of the expression $e^{j\varphi(t)}$. The power spectral density (PSD) of $e^{j\varphi(t)}$ can be simplified as a Lorentzian function with single-sided PSD [132]:

$$L(f) = \frac{2}{\pi} \cdot \frac{(\beta_{PN}/2)}{f^2 + (\beta_{PN}/2)^2} \quad (4.4)$$

The Lorentzian spectrum shape of Eq. (4.4) is characterized by its 20 dB/decade decay that occurs after the FWHM point (β_{PN}). Figure 4.1(b) depicts the phase noise PSD for different RF frequency carriers. These PSD forms have been obtained according to the phase noise model established in the 3GPP 5G standard [131]. The phase noise model of [131] is expressed by the following formula:

$$S(f) = PSD0 \cdot \frac{\prod_{z'=1}^Z 1 + \left(\frac{f}{f_{z,z'}}\right)^{\alpha_{z,z'}}}{\prod_{p'=1}^P 1 + \left(\frac{f}{f_{p,p'}}\right)^{\alpha_{p,p'}}}, \quad (4.5)$$

where $PSD0$ is the value of $S(f)$ at frequency 0. The parameters f_z and f_p of Eq. (4.5) refer to the different zero and pole frequencies, respectively. α_z and α_p mark the decay slope for its corresponding frequency. The phase noise model of Eq. (4.5) can be seen as the product of multiple Lorentzian functions with different frequency and slope characteristics. This overlapping spectrum phenomenon can be noticed in the curves of Fig. 4.1(b) where three decay patterns are disclosed. From approximately 1.5 MHz, the three curves in Fig. 4.1(b) show a slope decay of

20 dB/decade, as Lorentzian function does. Therefore, PSD curves in Fig. 4.1(b) follow the Lorentzian function of Eq. (4.4) from approximately 1.5 MHz of frequency offset. In addition, as Fig. 4.1(b) illustrates, the phase noise PSD is larger for higher frequency values. Moreover, Fig. 4.1(b) displays the 5G numerologies of Table 4.1. This numerology representation permits observing the impact of phase noise in the OFDM signals as a function of the subcarrier spacing value. To be more precise, the phase noise PSD values related to a specific 5G numerology in Fig. 4.1(b) are lower for higher Δf configurations. Hence, larger subcarrier spacing configurations are less sensitive to the degradation induced by phase noise. The relation between signal degradation due to phase noise and subcarrier spacing is explained in more detail in Section 4.2.

4.2 Phase noise impact on OFDM signals

The goal of this section focuses on the degradations that occur on the OFDM signal when it passes through a channel corrupted by phase noise. For that, the OFDM signal in the discrete time domain needs to be formulated [133]:

$$x_m[n] = \frac{1}{\sqrt{N_{SC}}} \sum_{k=0}^{N_{SC}-1} X_m[k] e^{j \frac{2\pi n k}{N_{SC}}}, \quad (4.6)$$

where N_{SC} is the number of subcarriers and $X_m[k]$ is the k -th subcarrier complex value in the m -th OFDM symbol. When the OFDM signal passes through an AWGN wireless channel with phase noise, the received signal can be calculated with the following equation [133]:

$$r_m[n] = [x_m[n] \otimes \mathcal{F}^{-1}(H_m[k])] \cdot e^{j\varphi[n]} + z[n], \quad (4.7)$$

where \otimes and \mathcal{F}^{-1} refer to the circular convolution and IDFT operations, respectively. In Eq. (4.7), H is the frequency channel response and can be modelled as the 3GPP standard of [86] determines (see Fig. 2.7). The parameter z of Eq. (4.7) indicates the AWGN noise. As discussed in the previous section, the phase noise φ of Eq. (4.7) can be modelled as a simple Wiener process or it can follow the phase noise model of [131]. After the discrete Fourier transform (DFT) process in the OFDM demodulator, the k -th received subcarrier is expressed with the following equation [133]:

$$R_m[k] = X_m[k] H_m[k] I_m[0] + \underbrace{\sum_{l=0, l \neq k}^{N_{SC}-1} X_m[l] H_m[l] I_m[l-k]}_{ICI_m[k]} + Z_m[k], \quad (4.8)$$

where $I[k]$ and $Z[k]$ are the DFT responses of $e^{j\varphi[n]}$ and $z[n]$, respectively. From Eq. (4.8), it can be deduced that OFDM subcarriers suffer from two impairments

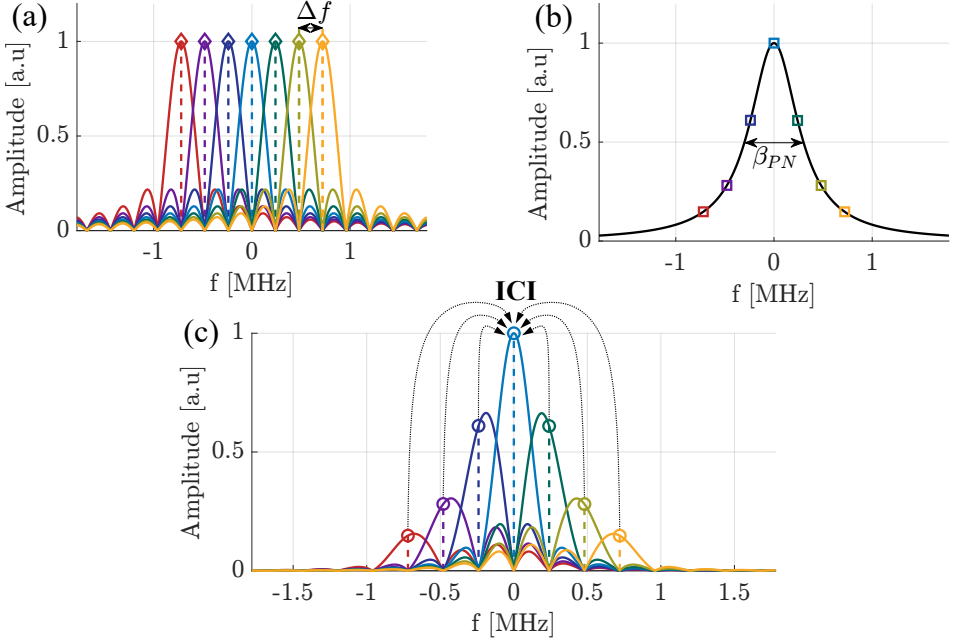


Figure 4.2: Spectral representation of the ICI induced by phase noise in OFDM subcarriers: (a) spectrum of seven OFDM subcarriers; (b) Lorentzian function that is related to the spectrum of $e^{j\varphi(t)}$; (c) result of the convolution between the subcarrier shapes of (a) and the Lorentzian function of (b). Notice that the displayed markers correspond to the discrete sampling points for each subcarrier. It is important to mention that this figure aims to visualize the ICI effect on OFDM subcarriers due to phase noise. Nonetheless, this visualization is not strictly mathematically accurate since only amplitude values are considered.

due to phase noise: a common phase error (CPE) that equally affects all the subcarriers of a specific m -th OFDM symbol; and inter-carrier interference (ICI). CPE value is determined by $I_m[0]$ of Eq. (4.8). CPE compensation is relatively simple as it involves a constant rotation of the received constellation points in each OFDM symbol [134]. Thus, the CPE value of each OFDM symbol can be extracted from the pilot subcarriers included in these OFDM symbols [134]. Nonetheless, since the phase noise level is relatively high in mm-wave bands, the CPE values of consecutive OFDM symbols differ substantially. Hence, for a proper CPE compensation in mm-wave communications, a certain quantity of pilots must be included in all the OFDM symbols. These pilots to compensate for the CPE are denoted as phase-tracking reference signal (PT-RS) in the 3GPP 5G standard [135], [136].

As discussed above, phase noise causes ICI in each subcarrier of the transmitted OFDM symbols. As it can be seen in Eq. (4.8), the ICI factor depends on the number of subcarriers (N_{SC}), complex values of the adjacent subcarriers

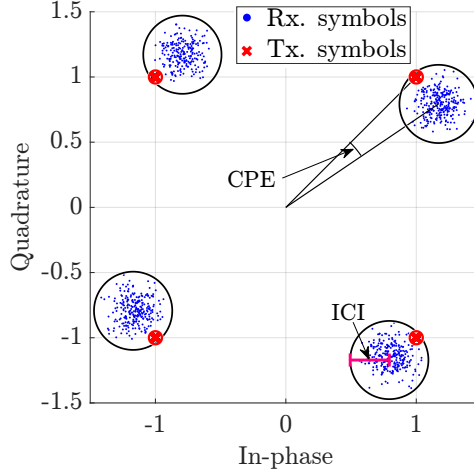


Figure 4.3: Constellation diagram of the transmitted and received QPSK subcarriers of an OFDM symbol in a channel where the phase noise is the only impairment. The received QPSK points suffer from CPE and ICI.

(X), DFT response of $e^{j\varphi[n]}$ (I), and frequency channel response (H). Assuming a channel with flat frequency response and zero-phase, the ICI factor of a given subcarrier can be seen as the convolution between the $X_m[k]$ subcarriers and the spectrum of $e^{j\varphi[n]}$. In addition, as indicated in Section 4.1, the DFT response of $e^{j\varphi[n]}$ can be simply modelled as a Lorentzian function whose decay, from FWHM points, is 20 dB/decade. Therefore, the ICI factor of Eq. (4.8) ($ICI_m[k]$) is mainly contributed by the nearest adjacent subcarriers. Figure 4.2 shows the spectral representation of the originated ICI due to phase noise on a specific OFDM subcarrier. Specifically, Fig. 4.2(a) depicts the spectrum shape of seven subcarriers with 240 kHz of subcarrier spacing. In particular, the ICI induced by phase noise of the central subcarrier is the ICI represented in Fig. 4.2. The diamond markers of Fig. 4.2(a) refer to the sampling points of each subcarrier. Figure 4.2(b) displays a Lorentzian function, which is centred at the central frequency point of the subcarrier under evaluation and has a given β_{PN} value (see Eq. (4.4)).

The curves in Fig. 4.2(c) are obtained by multiplying the subcarrier shapes in Fig. 4.2(a) with the Lorentzian spectrum in Fig. 4.2(b). Hence, and following Eq. (4.8), the final ICI factor of the central subcarrier in Fig. 4.2(a) is the sum of the values of the circle markers in Fig. 4.2(c), except the value of the central marker. Observing Fig. 4.2, it can be concluded that the ICI level due to phase noise is directly proportional to the number of adjacent subcarriers (related to N_{SC}) and inversely proportional to the subcarrier spacing Δf . For being more precise, the ICI induced by phase noise is affected by the phase and amplitude of the adjacent subcarriers. Therefore, for larger M-QAM modulation orders, the ICI level is likely to be higher.

Figure 4.3 represents a constellation diagram of the received subcarriers of one OFDM symbol for a channel only corrupted by phase noise. In Fig. 4.3, the two aforementioned impairments that phase noise produces in OFDM subcarriers are illustrated: CPE and ICI. The received constellation points in Fig. 4.3 for each QPSK symbol are outlined in different black circles. The angle between these black circles and their corresponding transmitted symbol point (red cross) is equal to the CPE induced by phase noise. The radii of the black circles in Fig. 4.3 indicate the ICI factor. Since one subcarrier is affected by the remaining subcarriers and assuming that data on adjacent subcarriers are independent, the ICI impact on the OFDM subcarriers can be viewed as an AWGN process. Therefore, the compensation of the ICI induced by phase noise is more complicated and complex than the CPE compensation [137]. The next section focuses on different algorithms and methods to mitigate the impact of phase noise on OFDM signals.

4.3 Algorithms to mitigate phase noise in OFDM signals

The objective of this section consists of providing several algorithms to compensate for the degradation caused by phase noise in OFDM signals. The phase noise algorithms applied in the published papers of this dissertation are the following:

- a) **RF pilot-assisted:** this method can be used for any type of waveform, including OFDM, since it is executed before the waveform demodulation process, in the IF domain. RF pilot-assisted method stands out as the best algorithm on this list in terms of compensating for the signal degradation due to phase noise. Nonetheless, this method requires a reference carrier that suffers from the same phase noise as the data signal. In this way, the phase noise can be extracted from the reference carrier and used to compensate for phase noise in the data signal. This usage of a reference RF carrier implies the transmission of such carrier in the wireless domain. Transmission of an RF carrier in the wireless spectrum signifies a reduction in spectral efficiency, what is not suitable for wireless scenarios where the spectrum is limited.

In addition, RF pilot-assisted method requires a reference carrier with sufficient SNR for adequate extraction of phase noise. Furthermore, the transportation of the reference carrier throughout the ARoF system implies a power budget reduction in devices such as RF amplifiers and RF mixers, since this RF carrier substantially increases the overall power of the transmitted signal. Therefore, there is a trade-off between accurate phase noise extraction, which is related to the SNR of the reference carrier, and the power budget reduction because of the RF carrier transport. **P6** and **P7** utilize the RF pilot-assisted method to compensate for the phase noise of an ARoF setup based on OPLL mm-wave two-tone generation. **P6** presents

the schematic of the RF pilot-assisted method. Since this method is carried out in the IF domain, it can be performed in the digital or analog domain. For the analog domain realization, an RF filter must isolate the RF reference carrier to, subsequently, mix it with the received data signal.

- b) **Advanced linear interpolation based ICI estimation (LI-CPE)**: this algorithm is an advanced version of the LI-CPE method proposed in [134]. In the LI-CPE method of [134], the CPE of each OFDM symbol is calculated by using the pilot subcarriers. Next, a rough estimate of the phase noise is made by linearly interpolating the obtained CPE values. Then, the degradation induced by phase noise in the OFDM subcarriers is mitigated by using this estimate. Since the phase noise estimate is carried out by using a few points (consecutive CPE values of the OFDM symbols), the computational complexity of the LI-CPE method is low. Nevertheless, LI-CPE offers poor performance in terms of phase noise compensation.

Additionally, another of the drawbacks of LI-CPE is that in order to perform the linear phase noise interpolation, the CPE estimate of the next OFDM symbol is necessary. This fact implies an OFDM symbol period increase in the global delay of the system. One of the techniques to avoid this OFDM symbol delay consists of using the cyclic prefix (CP) redundancy to estimate the slope of the phase noise in the current OFDM symbol. In this way, having two reference points (CPE and slope) allows to realize a linear interpolation of the phase noise, avoiding the delay of one OFDM symbol. **P5** and [138] propose this utilization of CP to improve the LI-CPE method. **P5** explains in more detail the advanced LI-CPE method. Also, **P5** experimental compares the performance of LI-CPE with its advanced version. In the experimental results of **P5**, the advanced LI-CPE method exhibits better performance than its predecessor, especially for larger subcarrier spacing configurations. This better performance at higher Δf values is due to the fact that the linear interpolation granularity is finer at high subcarrier spacing values and, thus, the phase noise can be better estimated. Finally, since the advanced LI-CPE method employs OFDM subcarrier references, this method is realized in the baseband (BB) domain.

- c) **Iterative decision feedback (IDF) with adaptive LPF**: an extended way of estimating the phase noise in OFDM signals lies in the use of the demodulated M-QAM symbols. With these demodulated symbols, the transmitted OFDM signal in the time domain can be estimated. In such a manner, a phase noise estimate can be obtained applying Eq. (4.2). A lower number of errors after the demodulation process gives a better performance of this phase noise estimate. The obtained phase noise estimate is then utilized to compensate for phase noise in the received OFDM signal. After this phase noise compensation process, the M-QAM symbols can be demodulated again and, if the phase noise estimate was adequate, the estimate of the transmit-

ted time domain OFDM signal is more precise than in the previous iteration. Hence, to reduce the number of erroneous M-QAM demodulated symbols, the mentioned process can be carried out iteratively. Algorithms that use this strategy are commonly denominated as iterative decision feedback (IDF) methods. For phase noise compensation, [139] proposes an IDF algorithm in which an LPF is included after the phase noise estimate. This LPF allows reducing the abrupt peaks that occur in the phase noise estimate.

As an advanced version of [139], **P4** presents and proposes a phase noise compensation algorithm based on IDF strategy where the shape of the LPF spectrum changes with the number of iterations. In this way, a finer phase noise estimate can be achieved after the LPF block and thus, reducing the final BER. In other words, the adaptive LPF becomes less restrictive for subsequent iterations, allowing the residual phase noise, that was not removed in previous iterations, to be estimated more accurately. **P4** describes in detail the novel IDF with adaptive LPF method. Moreover, for better yields, **P4** demonstrates that the LPF response within the loop should be designed by taking into account the phase noise spectral shape. IDF with adaptive LPF offers better performance in terms of BER than the advanced LI-CPE method. However, since the OFDM receiver blocks must be realized for each iteration, plus additional blocks to estimate and compensate for phase noise, the computational complexity of IDF with adaptive LPF is higher than the advanced LI-CPE method. Another drawback of IDF methods lies in the fact that the phase noise estimate is based on the accuracy of the time domain OFDM signal estimate. Thereby, if the demodulated M-QAM symbols contain many errors, the time domain OFDM estimate becomes very imprecise and, consequently, the phase noise estimate is not adequate. This error propagation effect can lead to convergence problems of the iterative algorithm, making its application infeasible for some scenarios where many erroneous M-QAM symbols occur in the first iteration.

- d) **Hybrid scattered pilots with decision feedback (SPDF)**: another strategy to estimate and compensate for phase noise in OFDM signals consists of the use of the scattered pilots [137]. Since the transmitted values of the reference pilots are known at the receiver, the phase noise estimate based on the usage of these pilots is not affected by errors. However, as the number of scattered pilot subcarriers is, in most scenarios, relatively much lower than the number of data subcarriers, the number of reference points for phase noise estimate is lower than in the IDF case. Therefore, when the demodulated M-QAM symbols contain no errors, IDF algorithms perform better than pilot scattered algorithms. Nonetheless, as mentioned above, the convergence stability of IDF algorithms is lower since it depends on the degradation of the received OFDM signal.

Taking into account the advantages and disadvantages of IDF and scattered pilot methods to compensate for phase noise, **P7** proposes and presents,

Table 4.2: Qualitative comparison between OFDM phase noise compensation algorithms.

Algorithm	Computational complexity	RF tone required	Operation region	Performance	Convergence problem
RF pilot-assisted	High (depends on IF)	Yes	IF domain	High	No
Advanced LI-CPE	Low	No	BB domain	Low	No
IDF with adaptive LPF	Medium/high*	No	BB domain	Medium*	Yes (medium)
Hybrid SPDF	High*	No	BB domain	Medium/high*	Yes (low)

BB: baseband. (*) \rightarrow it depends on the number of iterations of the IDF loop.

for the first time to the author's knowledge, a hybrid phase noise compensation algorithm that combines these two strategies. In this manner, the robustness of scattered pilot algorithms is combined with the accuracy of IDF algorithms, reducing the convergence problem. In particular, **P7** uses the unconstrained least-squares (ULS) approach to implement the scattered pilot strategy [140] and, consequently, the IDF algorithm proposed in **P4** is applied. In such a manner, the ULS algorithm realizes a coarse phase noise compensation to ensure error reduction in the demodulation block. Then, the IDF algorithm of **P4** suffers fewer convergence problems since the first iteration of the loop contains fewer errors due to the previous application of the ULS algorithm. This hybrid SPDF algorithm is well detailed in **P7**. Respecting the proposed phase noise compensation algorithm in **P4**, the hybrid SPDF method of **P7** provides more convergence consistency and better performance, allowing to reduce the number of loop iterations for the same channel conditions. However, the proposed hybrid SPDF algorithm is computationally more complex for the same number of loop iterations than applying the IDF technique alone since it merges two different algorithms. This increase in complexity lies in the inclusion of the scattered pilot method selected to perform the initial phase compensation, with ULS being the chosen option in **P7** [140].

Table 4.2 presents a qualitative comparison between the phase noise compensation algorithms explained above. Observing Table 4.2, it can be determined that the selection to apply one of these algorithms shows a trade-off between computational complexity and final performance. Therefore, for a specific communication system, the adequate choice of one of these algorithms is conditioned by the phase noise level of said system. Hence, the computational complexity of the selected algorithm in Table 4.2 is linked to the signal degradation intensity caused by phase noise. Furthermore, it is important to mention that applying the PAS technique explained in Section 3.2 allows for gradually reducing the impact of phase noise in OFDM signals. **P8** studies and evaluates the implementation of PAS to gradually decrement the OFDM signal degradation due to phase noise in an experimental mm-wave ARoF setup. The results of **P8** prove that the PAS technique is a suitable modulation scheme to enhance the channel capacity usage in OFDM

mm-wave ARoF systems where phase noise is one of the major impairments.

All the algorithms explained in this section are capable of reducing the impact of CPE, ICI induced by phase noise, and carrier frequency offset (CFO). However, and except for the RF-pilot assisted method, the ICI and CPE compensation yields of these algorithms are reduced when CFO is not pre-compensated. Thus, for proper utilization of these algorithms, it is strongly recommended to apply either a coarse or fine CFO compensation before [141]. Also, for an adequate use of the IDF and hybrid SPDF algorithms, CPE mitigation process should be included after the CFO compensation block. In this manner, the IDF and hybrid SPDF algorithms perform a better compensation of the ICI induced by phase noise. The usage of IDF and hybrid SPDF algorithms only to compensate for ICI is due to the fact that ICI is more complex and difficult to mitigate than CPE and CFO in OFDM signals (see Fig. 4.3). Moreover, all the algorithms in Table 4.2 show better performance for high SNR values. In other words, the yields of these phase noise compensation algorithms are strongly related to the SNR level of the received signal. Also, it is worth mentioning that all the algorithms presented in this section, except for the RF pilot-assisted method, are designed for the reduction of the phase noise impact in OFDM systems. Nevertheless, the concepts, techniques, and strategies used in such algorithms can be extrapolated to compensate for phase noise in other types of waveforms.

4.4 Experimental analysis of phase noise on OFDM mm-wave ARoF systems

The purpose of this section consists of explaining the mm-wave ARoF setups that are employed to experimentally evaluate the phase noise compensation algorithms of the previous section. For these testbeds, the phase noise level is one of the main impairments of the communication system. Specifically, two different mm-wave ARoF setups are used for this experimental evaluation:

- a) **mm-wave ARoF setup to gradually increase the phase noise level:** the aim of this setup dwells on gradually controlling the final phase noise of the system. This control of the phase noise system enables to evaluate the transmitted OFDM signal under different channel conditions. In this way, the phase noise compensation algorithms can be evaluated under various phase noise conditions. In particular, the advanced LI-CPE and IDF with adaptive LPF methods are experimentally evaluated in this setup (**P4**, **P5**). Also, **P8** uses this setup for assessing the PAS-OFDM solution in an experimental mm-wave ARoF system under different phase noise levels. The scheme of this experimental setup is the same as the one displayed in Fig. 2.3(d). More specifically, this setup utilizes the external modulation technique to perform the optical two-tone generation (see Fig. 2.2(a)). As discussed in Section 2.1, the external modulation technique offers low phase

noise PSD (see Table 2.1). Thereby, to gradually increase the phase noise of the system, several patch cords with different lengths are included in the unmodulated lower branch of Fig. 2.3(d), modifying $\Delta\phi$. By inserting these patch cords, the coherence between the tones is reduced and, consequently, the final phase noise is increased. Then, the phase noise level of the system can be gradually increased by adding longer patch cords. In such a manner, the phase noise levels of the two-tone generation techniques of Table 2.1 can be investigated in a single experimental setup. Besides, the performance of phase noise compensation algorithms can be appraised in this setup to assess their applicability for different two-tone generation techniques. **P4** explains in more detail this gradual phase noise ARoF testbed where the OFDM signal is modulated at 26 GHz (n258).

- b) **mm-wave ARoF setup based on OPLL two-tone generation:** the scheme of this setup is based on the architecture of Fig. 2.3(c). In this case, OPLL is the two-tone generation technique as shown in Fig. 2.2(d). In this experimental setup, the generated mm-wave OFDM signal is centred at 25.75 GHz (n258). The phase noise level resulting from this second experimental setup is larger than the worst phase noise scenario evaluated in the setup explained above. For this reason, the RF pilot-assisted and hybrid SPDF algorithms are evaluated in this setup, since the IDF method shows convergence inconsistencies due to the large number of errors in the first iteration of the loop. **P6** uses the RF pilot-assisted method in the DSP to reduce the impact of the phase noise caused by the OPLL technique. **P7** employs the RF pilot-assisted and hybrid SPDF methods to mitigate the phase noise in the received OFDM signals. More details on the employed mm-wave ARoF setup based on OPLL can be found in **P7**.

Both experimental setups explained above dispense with long-distance optical fiber and mm-wave wireless link since the research objective focuses on the compensation of phase noise produced in the mm-wave ARoF generation. Therefore, for proper isolation of other impairments that can disturb the analysis and compensation of the produced phase noise, the already explained experimental setups in this section are simplified. Besides, the phase noise, introduced by the optical fiber and wireless link, is negligible compared to the phase noise levels addressed in the two employed experimental setups. Also, the phase noise introduced at the receiver of the aforementioned experimental setups is the same as it would be for a system with wireless transmission.

4.5 State-of-the-art of phase noise compensation in mm-wave ARoF systems

This section aims to frame the contribution papers presented in Chapter 4 with respect to SOTA, highlighting the research gaps that these papers fill. Table 4.3

Table 4.3: Overview of the phase noise study, analysis, and compensation in mm-wave AROF systems for 5G/6G communications.

Date	Opt. two-tone gen. technique	Operation frequency	System description	Modulation format	PN comp. technique	Ref
04/'11	External modulation	60 GHz	Exp. ARoF wireless setup	OFDM	Decision-aided phase noise suppression (DA-PNS)	[142]
09/'12	-	Sim. PN	Vehicular chan. simulation	OFDM (LTE)	Iterative decision feedback (IDF)	[139]
10/'14	OFCG with DFB laser and WSS	60 GHz	Exp. ARoF wired setup	OFDM	Time delay precomp.	[143]
10/'14	External modulation	100 GHz	Exp. ARoF wireless setup	OFDM	DA-PNS + digital and analog PA-PNS	[144]
04/'15	OFCG with DFB laser and WSS	60 GHz	Exp. ARoF wired setup	OFDM	External injected gain switched (EIGS)	[145]
12/'17	OFCG with DFB laser and WSS	60 GHz	Exp. ARoF wired setup	UF-OFDM	Time delay precomp.	[146]
10/'18	OFCG with DFB laser and WSS	54.8 GHz	Exp. ARoF wired setup	UF-OFDM	Time delay precomp. and EIGS	[147]
09/'21	External modulation	26 GHz	Exp. ARoF wired setup	OFDM (5G)	Advanced LI-CPE	P5
01/'21	Two free run. lasers and MLLs	61 GHz	Exp. ARoF wireless setup	OFDM	DD-LMS alg. and mm-wave analog Rx	[148]
03/'21	MLLs	25 GHz	Exp. ARoF wireless setup	SC-QAM	-	[149]
03/'21	External modulation	26 GHz	Exp. ARoF wired setup	OFDM (5G)	IDF with adaptive LPF	P4
07/'21	OPLL	25.75 GHz	Exp. ARoF wired setup	OFDM (5G)	Digital RF-pilot assisted method	P6
07/'21	External modulation	26 GHz	Exp. ARoF wired setup	OFDM (5G)	PAS-OFDM for gradual channel adaptation	P8
03/'22	Direct mm-wave data upconversion	28.2 & 35.3 GHz	Exp. ARoF wired setup	OFDM (5G)	OIL	[150]
TBD	OPLL	25.75 GHz	Exp. ARoF wired setup	OFDM (5G)	Hybrid SPDF and digital RF-pilot assisted method	P7

PN: phase noise; DFB: distributed feedback; PA-PNS: pilot-aided phase noise suppression; UF-OFDM: universally filtered OFDM; DD-LMS: decision directed least mean square; TBD: to be defined.

shows the current summary of scientific papers related to the study, analysis, and mitigation of phase noise in mm-wave ARoF systems for 5G/6G communications. This summary is displayed in a chronological order. Moreover, Table 4.3 includes the contribution papers of this dissertation that have been explained throughout this chapter. As it can be observed in Table 4.3, the scientific papers, which do not belong to this dissertation, do not use the OFDM 5G numerology as established by the 3GPP standard [19]. Hence, **P4**, **P5**, **P6**, **P7**, and **P8** stand out for their comprehensive evaluation and study of 5G numerology in mm-wave ARoF setups with relatively high phase noise, providing empirical assessments for the realization of future standards related to 5G/6G mm-wave communications.

Furthermore, **P4**, **P5** and **P8** highlight in the SOTA of Table 4.3 for their comprehensive study, analysis, and evaluation of the received OFDM signals in an experimental mm-wave ARoF setup under an ample range of phase noise conditions. In such a manner, **P4**, **P5**, and **P8** test and investigate the performance of phase noise algorithms in many types of phase noise scenarios, serving as experimental support to determine the feasibility of such algorithms.

Examining Table 4.3 and the remaining papers related to the research topic under study, **P6** and **P7** stand out as the first experimental demonstrations of OFDM 5G signal transmission over a mm-wave ARoF setup based on OPLL, to the best of the author's knowledge. Then, the viability of transporting 5G NR signals over a mm-wave ARoF system based on OPLL two-tone generation is validated with the experimental results of **P6** and **P7**. Hence, the advantages of using OPLL can be harnessed, over other optical two-tone generation techniques such as external modulation (see Table 2.1). In summary, the contribution papers presented in this chapter cover a research gap concerning phase noise compensation by using different DSP algorithms in different OFDM mm-wave ARoF scenarios, following 5G standards.

P4: Analysis and Compensation of Phase Noise in Mm-Wave OFDM ARoF Systems for Beyond 5G

J. P. Santacruz, S. Rommel, U. Johannsen, A. Jurado-Navas, and I. Tafur Monroy, “Analysis and Compensation of Phase Noise in Mm-Wave OFDM ARoF Systems for Beyond 5G,” *Journal of Lightwave Technology*, vol. 39, pp. 1602–1610, 6 Mar. 2021. DOI: 10.1109/JLT.2020.3041041

Analysis and Compensation of Phase Noise in Mm-Wave OFDM ARoF Systems for Beyond 5G

Javier Pérez Santacruz¹, Simon Rommel², *Member, IEEE, Member, OSA*, Ulf Johannsen³, *Member, IEEE*, Antonio Jurado-Navas⁴, *Member, OSA*, and Idelfonso Tafur Monroy⁵, *Senior Member, IEEE*

Abstract—Fifth-generation mobile networks (5G) are the solution for the demanding mobile traffic requirements, providing technologies that fulfill the requisites of different type of services. The utilization of the millimeter-wave (mm-wave) band is the straightforward technique to achieve high bit rates. Moreover, analog radio-over-fiber (ARoF) brings outstanding benefits such as low cost, low power consumption, and high spectral efficiency, among others. Thereby, mm-wave ARoF is a strong candidate to pave the way for common public radio interface (CPRI) in the fronthaul for the future 5G architecture. As orthogonal frequency-division multiplexing (OFDM) is the adopted waveform in the 5G standard, it should be also utilized in mm-wave ARoF systems for 5G. However, phase noise is one of the most degrading factors in mm-wave OFDM ARoF systems. Therefore, in this work, an analysis of the phase noise is carried out through an experimental setup up. The configuration of this setup enables to gradually modify the final phase noise level of the system. Furthermore, an original and novel algorithm to compensate the phase noise in OFDM receivers is proposed. The performance of this algorithm is experimentally evaluated through the setup for different phase noise levels and different subcarrier spacings. The obtained results show the effectiveness of the proposed algorithm under those conditions, highlighting the viability of mm-wave OFDM ARoF for 5G and beyond.

Index Terms—5G, ARoF, mm-wave, OFDM, phase noise.

I. INTRODUCTION

MOBILE network data has exponentially grown in the last years. The fifth-generation (5G) of mobile networks is the adopted solution for this increasing traffic trend. 5G will support a huge enhancement in terms of capacity, bit rate, latency, reliability, energy efficiency, and number of connected devices [1]. Many technologies have appeared to fulfill these

demanding requirements [2]. Thus, to achieve high bit rates, the need for achieving higher data rates leads is forcing operators to move toward high-frequency bands, being the millimeter-wave (mm-wave) domain a very promising one due to its inherent bandwidth. Transmitting signals at mm-wave frequencies implies high free-space path loss (FSPL) and, for that reason, the area of mm-wave cells does not exceed 200 m [3]. Therefore, a larger number of mm-wave cells, compared to the current mobile network, are required to cover the same surface.

Since centralized radio access network (C-RAN) implies higher flexibility, lower latency, and lower power consumption than distributed radio access network (D-RAN), this centralized architecture is a more preferable solution for 5G [4]. Digital radio-over-fiber (DRoF) is the adopted technology in common public radio interface (CPRI) to develop C-RAN in the mobile network. However, CPRI requires constant bitrate signals and implies sampling rates of hundred of Gbit/s. Thereby, DRoF is clearly not a scalable solution for the future mm-wave 5G architecture [5]. On the other hand, analog radio-over-fiber (ARoF) reduces the complexity, cost, and latency in the remote unit (RU), avoiding the high demanding analog-to-digital converters (ADCs) and digital-to-analog converters (DACs) used in DRoF [4]. Therefore, C-RAN architecture employing ARoF is a suitable solution for the mm-wave 5G fronthaul since it brings attractive benefits such as low latency, low cost, high scalability, high spectral efficiency, and low power consumption [6]–[8].

Orthogonal frequency-division multiplexing (OFDM) is the 5G waveform standardized by 3rd Generation Partnership Project (3GPP) [9]. In the new radio (NR), 5G defines different numerologies for OFDM [9] associated to subcarrier spacing values from 15 kHz to 240 kHz. OFDM offers solid wireless communications due to its robustness to frequency selective channels, high spectral efficiency, low out-of-band (OOB) emissions, and efficient multiple-input and multiple output (MIMO) integration [10], [11]. Accordingly, mm-wave cells over ARoF with OFDM is a strong candidate to be part of the beyond 5G architecture. However, the phase noise has been demonstrated to be one of the major performance limiting factor in OFDM mm-wave ARoF systems because of the relatively low subcarrier spacing used in 5G [5], [12].

Strategies to compensate the signal degradations due to the phase noise have already been analyzed and evaluated in OFDM mm-wave ARoF systems: thus, the phase noise is mitigated by hardware in [13], [14]; and dispersion-induced phase noise (DPN) included by the chromatic dispersion of the fiber is

Manuscript received September 14, 2020; revised November 18, 2020; accepted November 23, 2020. Date of publication November 27, 2020; date of current version March 16, 2021. This work was supported by the ITN 5G STEP-FWD and blueSPACE Projects which has received funding from the European Union's Horizon 2020 Research and Innovation Program under Grant 722429 and Grant 762055. (Corresponding author: Javier Pérez Santacruz.)

Javier Pérez Santacruz, Simon Rommel, and Idelfonso Tafur Monroy are with the Institute for Photonic Integration, Eindhoven University of Technology, 5600 Eindhoven, The Netherlands (e-mail: j.perez.santacruz@tue.nl; simon.rommel@ieee.org; i.tafur.monroy@tue.nl).

Ulf Johannsen is with the Centre for Wireless Technology, Eindhoven University of Technology, 5600 Eindhoven, The Netherlands (e-mail: u.johannsen@tue.nl).

Antonio Jurado-Navas is with the Communication Engineering Department, University of Málaga, 29071 Málaga, Spain (e-mail: navas@ic.uma.es).

Color versions of one or more of the figures in this article are available at <https://doi.org/10.1109/JLT.2020.3041041>.

Digital Object Identifier 10.1109/JLT.2020.3041041

compensated for long fiber distance in [15], [16]. Moreover, the impact of phase noise has been studied and analyzed in [12] for OFDM signals with different numerologies. Other modulation formats, such as universal filtered-OFDM (UF-OFDM), have also been evaluated in terms of phase noise in this type of systems [17], [18]. Nevertheless, the performance of a technique to mitigate the phase noise for different phase noise levels and different numerologies in OFDM mm-wave AROf scenarios has not yet been realized. For this reason, in this work, a novel OFDM algorithm to compensate phase noise is proposed and explained. Next, the mm-wave AROf phase noise is studied and analyzed in an experimental setup at 25 GHz (K-band). This setup allows to gradually increase the phase noise level. Then, the OFDM performance is experimentally evaluated under different phase noise conditions and for all 5G numerologies. The proposed algorithm is used to enhance the performance of the received OFDM signals. The experimental results prove that the proposed OFDM receiver allows to achieve 5G requirements for different phase noise levels and different subcarrier spacings.

This manuscript is organized as follows: Section II describes the fundamentals of the proposed OFDM algorithm to mitigate the phase noise. Section III explains the employed AROf setup to progressively increment the phase noise. Section IV studies the phase noise in the proposed AROf scheme. Section V discusses the obtained results. Finally, Section VI presents some concluding remarks.

II. PROPOSED ALGORITHM TO COMPENSATE THE PHASE NOISE IN OFDM SYSTEMS

Phase noise is one of the major issues in OFDM systems. This impairment introduces a twofold degradation in the transmitted OFDM signal [15]: first, a common phase error (CPE), which affects to all the subcarriers similarly, can be compensated with the channel equalizer; and, second, an inter-carrier interference (ICI), deteriorating the subcarriers asymmetrically. Therefore, an additional method has to be performed in the OFDM receiver to compensate the ICI introduced by the phase noise. Furthermore, since phase noise degrades the orthogonality of the subcarriers in each OFDM symbol, the ICI level added by the phase noise is proportional to the OFDM symbol duration. The subcarrier spacing is inversely proportional to the symbol duration in OFDM systems. Thus, the subcarrier spacing is a relevant OFDM parameter that determines the ICI intensity introduced by the phase noise.

In this work, a novel algorithm to compensate the ICI induced by the phase noise in OFDM systems is presented and explained. This section is structured as follows: first, the fundamentals of the proposed algorithm are shown. Then, the keys to achieve high performance in this algorithm are detailed. Finally, some complexity and latency considerations about the algorithm are expounded.

A. Fundamentals of the Algorithm

The classical block diagram for an OFDM transmitter is represented in Fig. 1(a), where the process sequence is as follows: the flow of bits is mapped into the constellation symbols through

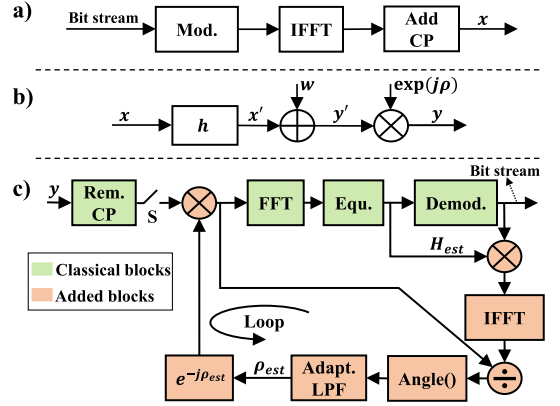


Fig. 1. (a) Classical OFDM transmitter. (b) Phase noise channel model. (c) Block diagram of the proposed algorithm to compensate the phase noise in OFDM receivers (the switch S turns off after the first iteration).

the modulator; then, the inverse fast Fourier transform (IFFT) is performed; and, finally, the cyclic prefix (CP) is added to each OFDM symbol. In addition, the typical system model of a phase noise channel is shown in Fig. 1(b) [19]. There, the transmitted signal x is convolved with the channel response h , obtaining x' . Then, the additive white Gaussian noise (AWGN) w is included, to obtain y' . The output signal y of the system model is generated by multiplying y' with the complex exponential of the phase noise ($\exp(-j\rho)$). Lastly, the block diagram of the proposed algorithm is shown in Fig. 1(c). This algorithm is based on re-constructing the transmitted OFDM signal x in the time-domain. Then, this re-constructed signal is used as reference to estimate the phase noise. The only assumption required by the algorithm is that the phase noise spectrum behaves as a low-pass signal. Since phase noise follows a Wiener process in most communication scenarios [20], the low-pass nature assumption for phase noise is adequate for the majority of the mm-wave AROf systems. An algorithm based on this assumption and strategy to estimate and compensate the phase noise is also used in [19], [21], [22]. This type of algorithms performs better when the channel is mainly dominated by the phase noise.

The block diagram of Fig. 1(c) is structured in two parts: one part is compounded by the classical blocks in an OFDM receiver; the second part constitutes the additional blocks to estimate and compensate the phase noise. Regarding the first part, the classical OFDM receiver sequence is formed by the next constitutive elements: an initial one for removing the CP of each OFDM symbol; then, the fast Fourier transform (FFT) can be performed to move into the frequency-domain; next, the channel frequency response is estimated using the distributed pilot subcarriers and compensating the remaining subcarriers with this estimation; and, finally, the demodulation of the equalized symbols is accomplished according to the constellation used in the transmitter.

After the demodulation block, the additional elements to estimate and compensate the phase noise start. First, the demodulated symbols are multiplied by the estimated channel

frequency response that is obtained in the equalizer block. Then, the resulting signal passes to the time-domain by performing an IFFT. In this way, an estimation of the transmitted time-domain OFDM signal filtered by the channel response (x') is achieved. If both the demodulation procedure is error-free and the channel estimation error is negligible, such that the estimated time-domain signal becomes x' .

After the IFFT process, the estimated time-domain transmitted signal is divided by the received signal. Next, the angle of this division is calculated. Hence, a first estimation of the phase noise is accomplished. If the received signal only suffers the adverse effects of phase noise and of multipath channel degradations; and if there is no errors in the estimation of x' , then no differences are appreciated between the initial estimation and the real phase noise. However, degradations in the received signal cause errors in the demodulation process and, thus, in both the phase noise and x' estimations. A way to enhance the phase noise estimate consists of filtering it according to the spectral shape of the phase noise. Then, in order to reduce the error in the estimation, the initial phase noise estimate is filtered. Next, the received signal is multiplied by the complex exponential of the inverse of the estimated phase noise ($\exp(-j\hat{\rho}_{est})$). In this respect, the estimated phase noise is compensated in the received signal. Finally, the FFT, the channel equalizer, and the demodulator processes are performed again.

The proposed algorithm can be used iteratively to enhance the estimate of the phase noise and its compensation in each iteration. The first iteration contains more errors in the demodulation process than subsequent iterations because the phase noise was not compensated previously. In the second iteration, the phase noise is compensated by using the phase noise estimate from the first iteration before the demodulation and, thus, fewer errors appear in the demodulation process than in the previous iteration. Consequently, since the re-built time-domain signal is closer to x' , the phase noise estimate enhances in the second iteration. Subsequent iterations calculate and compensate the residual phase noise that was not estimated in the previous iterations. Therefore, the number of errors due to the phase noise decrease with the number of iterations of this algorithm because the phase noise compensation is improved in each iteration.

This iterative process is applied on all subcarriers. Since the null subcarriers in the edge of the OFDM band are known in the receiver, the equalization and demodulation processes do not need to process these subcarriers in the algorithm, considering them null values. Therefore, the multiplication between the estimation of the channel (H_{est}) with the demodulated symbols includes only the active subcarriers. For the remaining added blocks of the algorithm, all subcarriers are involved in the process.

An additional block can be added after the demodulator block to decide when to leave the algorithm loop. This decision is based on an estimate of the signal-to-interference-plus-noise ratio (SINR) in the current iteration. Two parameters are evaluated for the aforementioned decision: an SINR threshold and an SINR step, that expresses the SINR improvement between the current iteration and the previous one. The algorithm loop can be finished when the SINR estimate is above the threshold or

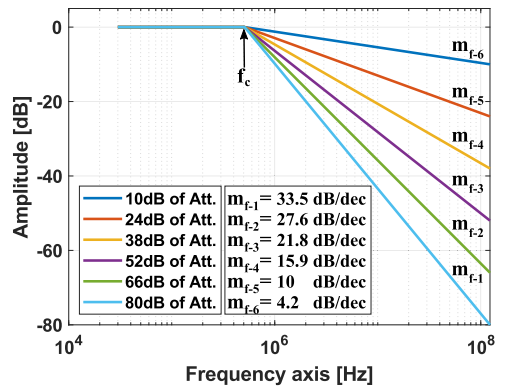


Fig. 2. Example of an adaptive low-pass filter design for the proposed algorithm.

when the SINR step falls below a predefined limit value. In this way, infinite loops and unnecessary iterations can be avoided.

B. Filter Design Strategies

The low-pass filter (LPF) block plays a crucial role in the algorithm of Fig. 1(c) by reducing the fast fluctuations of the pre-filtered phase noise estimate in each iteration. Such fast fluctuations, caused by high frequency components, do not adhere to the low-pass nature of the phase noise. Therefore, the low-pass filter allows a better estimate of the phase noise.

As mentioned in the previous subsection, the low-pass filter adjust to the spectral shape of the phase noise. This spectral shape can be characterized by two parameters: the cutoff frequency (f_c) and the decay slope (m_f). These two parameters can be obtained from the preamble of the transmitted signal. Hence, the low-pass filter can be designed with a flat amplitude until f_c and a linear logarithmic decay from f_c with a slope value defined by m_f .

The pre-filtered phase noise estimate yields less accurate results at the first iterations due to the higher number of errors in the demodulation process and, thus, this estimate contains more fluctuations at high frequencies. Hence, the strictness of the filter has to decrease progressively for these high frequencies in each iteration. This strictness can be translated to the m_f value of the filter. Thus, m_f decreases with the number of iterations, implementing an adaptive low-pass filter in the presented algorithm. In this way, its performance can be enhanced and optimized.

Fig. 2 shows an adaptive low-pass filter example. This is composed of six filters with decreasing m_f values. Therefore, the more attenuation in the filter, the earlier iteration we are considering. The f_c value of this example is 0.5 MHz. From this frequency point until half the sampling frequency of the signal (0.12 GHz, in this case), the attenuation in the edge of the adaptive filter decreases proportionally from 80 to 10 dB. The related values of m_f (in dB/decade) to these attenuation values are shown in the inset of Fig. 2. Comparing with the algorithms proposed in [19], [21], [22], the novelty of this algorithm lies in the adaptability of the inserted low-pass filter for each iteration

to improve performance. Furthermore, since the characteristics of the used low-pass filter implies a big impact in the phase noise estimate [21], the guidelines to design the low-pass filter have been shown in this section.

C. Complexity and Latency Analysis

The complexity associated to the digital signal processing (DSP) is a decisive factor in mobile communications. The additional complexity factor (C_F) of the proposed algorithm with respect to the standard OFDM receiver can be calculated approximately as:

$$C_F = \frac{I \cdot N \cdot (7.75 + 2.5 \cdot \log_2(N))}{N \cdot (2.5 + \log_2(N))} \quad (1)$$

with N being the number of subcarriers to process in the FFT and IFFT blocks, where I denotes the total number of iterations in the algorithm. The numerator of the Eq. (1) refers to the total number of complex multiplications of the algorithm, whereas the denominator corresponds to the number of complex multiplications of the standard OFDM receiver (see green blocks in Fig. 1(c)). Thereby, the additional complexity factor of the algorithm is roughly 2.5 per iteration. This rate is valid for most of N values since Eq. (1) is linear in terms of N . This shows that there is a trade-off between complexity and performance, since yield increases as shown in Section V. Since the power consumption is highly related to the complexity of the algorithm in terms of number of multiplications, the additional power consumption, added by the algorithm, is also approximately 2.5 times more than the conventional OFDM receiver.

Assuming a pipeline process where all the blocks of the algorithm can be performed in parallel, the additional latency factor in terms of multiplication latency is:

$$L_F = \frac{I \cdot (18 + 4 \cdot \log_2(N))}{4 + \log_2(N)} \quad (2)$$

Eq. (2) has been calculated considering that most of the multiplications of the algorithm can be performed in parallel. However, the FFT and IFFT processes require a certain number of stages that cannot be realized in parallel. The $\log_2(N)$ terms of Eq. (2) correspond to the delay of these stages. In addition, the numerator of this equation refers to the multiplication latencies of the algorithm, whereas the denominator corresponds to the number of multiplication latencies of the classical OFDM receiver. The additional latency factor (L_F) of the proposed algorithm can be approximated to 4 per iteration. The main reason of this high latency factor value is the use of a high-selectivity frequency filter. Since the proposed algorithm increases the final latency of the link in terms of tens of microseconds per iteration and the final latency of the link is in terms of hundreds of microseconds, the increased latency factor of the algorithm is not critical respecting the final latency [23].

Finally it should be noted that in terms of system or standardization complexity, this algorithm is not expected to cause any interoperability issues. As it is entirely local to the receiver and does not require adaptation of the modulation format or signaling, it can be introduced by any equipment/phone manufacturer

in their receiver to improve performance in the presence of phase noise, e.g., as a special variant or differentiating feature.

III. EXPERIMENTAL SETUP

The experimental setup used to study and analyze the phase noise in OFDM mm-wave AROF systems is shown in Fig. 3(a). First, an external cavity laser (ECL) generates the optical carrier at 1550 nm. Next, this optical carrier is modulated by a 25 GHz Mach-Zehnder modulator (MZM), biased in the null point, and driving with a sinusoid of 12.5 GHz generated by a vector signal generator (VSG). Therefore, two optical tones are produced with a frequency separation of 25 GHz. The spectrum of these two tones can be observed in Fig. 3(a.1). The optical two-tone signal is boosted by an erbium-doped fiber amplifier (EDFA). Next, the two tones are separated by a wavelength selective switch (WSS). The left tone is processed in the lower branch (see Fig. 3(a.2)), and the right tone in the upper branch (see Fig. 3(a.3)).

One tone is modulated by a second 10 GHz MZM, biased in the quadrature point, with the OFDM signal. This OFDM signal is produced by an arbitrary waveform generator (AWG) with a sampling rate of 12 GSa/s. In the lower branch, the second tone is delayed with respect to the upper tone. This delay is performed by patch cords with different lengths. Thus, the phase noise of the system can be increased gradually by adding longer patch cords. Then, the modulated and delayed tones are recombined in an optical coupler. The optical spectrum of the combined signal is shown in Fig. 3(a.4). A polarization controller (PC) is added to the lower branch in order to match the polarization of two branches.

The recombined optical tones beat on a 40 GHz photodiode (PD) producing a modulated RF signal at 26 GHz. The spectrum of this modulated RF signal is represented in Fig. 3(a.5). In this figure, both the OFDM double sideband with an intermediate frequency (IF) of 1 GHz and the 25 GHz carrier can be observed. Thereby, one OFDM sideband is generated at 24 GHz, whereas the other is at 26 GHz. Considering the wireless link to be implemented in this system, an RF filter, whose task consists of removing the RF carrier at 25 GHz and one of the OFDM sidebands, should be necessary to add before the antenna. Then, the electrical signal is boosted by a 30 dB medium power amplifier (MPA) with 18 to 40 GHz of bandwidth. Next, the boosted signal is mixed with a sinusoid of 23 GHz generated by a second VSG. Consequently, the electrical signal is down-converted to a second IF of 2 GHz. Therefore, the total IF is 3 GHz. Last, the IF signal is sampled and stored by a digital phosphor oscilloscope (DPO) with 12.5 GSa/s of sampling rate.

In the tables of Fig. 3(b), the values of the measured optical and electrical power values for certain points of the experimental setup are shown. The optical power value with index seven is marked with an asterisk because it depends on the length of the used patch cord. Moreover, the transmitter block diagram of the OFDM DSP is detailed in Fig. 3(c). First, a pseudorandom bit stream is generated. Then, these bits are modulated according to a quadrature amplitude modulation (QAM), producing complex QAM symbols. These symbols correspond to the data subcarriers of the OFDM signal. After this process, pilot symbols

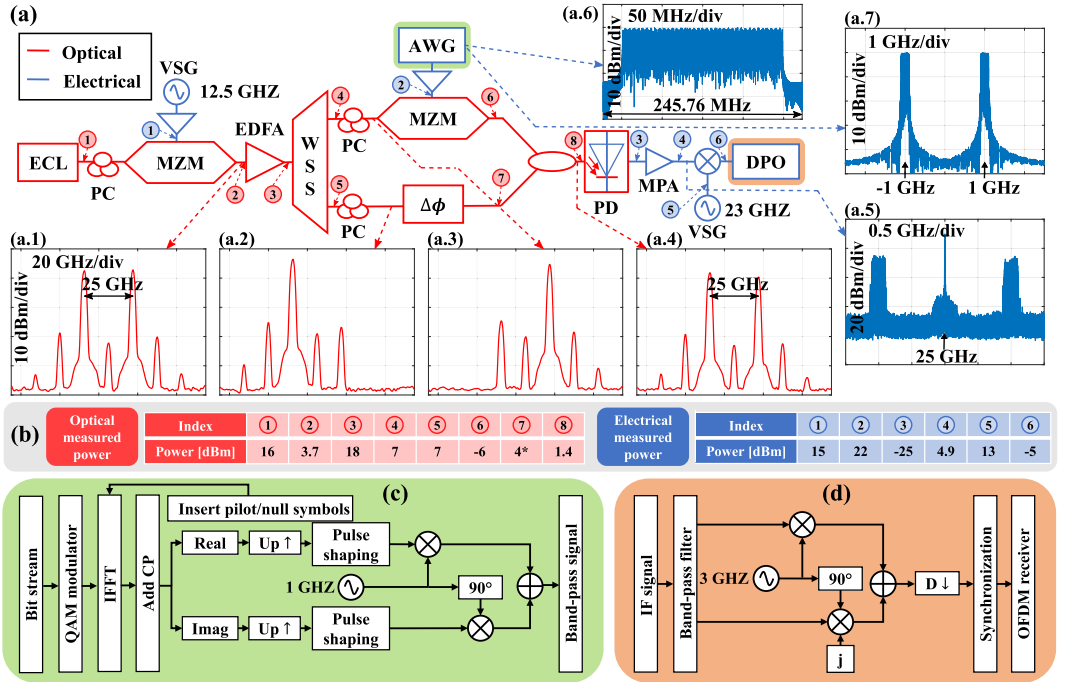


Fig. 3. Experimental testbed: (a) scheme of the setup, (b) tables with the measured power values in several points of the experimental setup, (c) block diagram of the DSP in the transmitter, (d) and block diagram of the DSP in the receiver.

are equally distributed between the generated data subcarriers. Moreover, null subcarriers are added in the edges of the OFDM band, achieving lower out-of-band (OOB) emissions. Next, an IFFT is performed and CP is added to the time-domain OFDM signal. The spectrum of the OFDM signal after this process is shown in Fig. 3(a.6). Then, the real and imaginary parts are divided and upsampled. A pulse shaping process is carried out in the real and imaginary branches independently. Next, the real and imaginary signals are multiplied by a cosine and sine of 1 GHz, respectively. Last, the signals from both branches are combined, producing an OFDM band-pass signal with an IF of 1 GHz (see Fig. 3(a.7)).

The receiver DSP process is shown in Fig. 3(d). The IF signal sampled in the DPO is filtered by a band-pass filter. Then, the filtered signal is down-converted to baseband by multiplying with a cosine and sine of 3 GHz (total IF) for the real and imaginary parts, respectively. Next, the complex baseband signal is downsampled and synchronized. Finally, the OFDM receiver of Fig. 1(c) is used. It is important to mention that all DSP processes are offline. Different OFDM numerologies are transmitted and compared using this setup. All these OFDM configurations have the same bandwidth (245.76 MHz) and bit rate (677.18 Mbps), getting an equal spectral efficiency value (2.76 bit/s/Hz) and, thus, a fair comparison is achieved. The common parameters for all the used OFDM configurations are the next: 16-QAM as modulation; the 80.5% of the total subcarriers are active; and one pilot inserted on every 12th subcarrier. The rest of the parameters

TABLE I
OFDM CONFIGURATION PARAMETERS

Config.	1	2	3	4	5
Δf [KHz]	15	30	60	120	240
N	2^{14}	2^{13}	2^{12}	2^{11}	2^{10}
T_{cp} [μ s]	4.8	2.4	1.2	0.6	0.3

are presented in Table I: subcarrier spacing (Δf), total number of subcarriers (N), and CP period (T_{cp}).

IV. PHASE NOISE ANALYSIS IN AROF SYSTEMS

This section is focused on analyzing, estimating and simulating the phase noise level for different time delay values in the setup of Fig. 3(a). The power spectral density (PSD) of the phase noise is measured before the DPO by an electrical spectrum analyzer (ESA) for different lengths of the patch cord. These PSD measures are shown in Fig. 4(a). The PSD of the phase noise is measured for path length differences between 0 m and 190 m. The delay corresponding to these path lengths can be calculated as:

$$\Delta\tau = \frac{n \cdot \Delta L}{c}, \quad (3)$$

where n is the refractive index of the fiber, ΔL denotes the length of the patch cord, with c being the speed of light in vacuum. In Fig. 4(a), it can be noticed that the PSD level of the phase noise

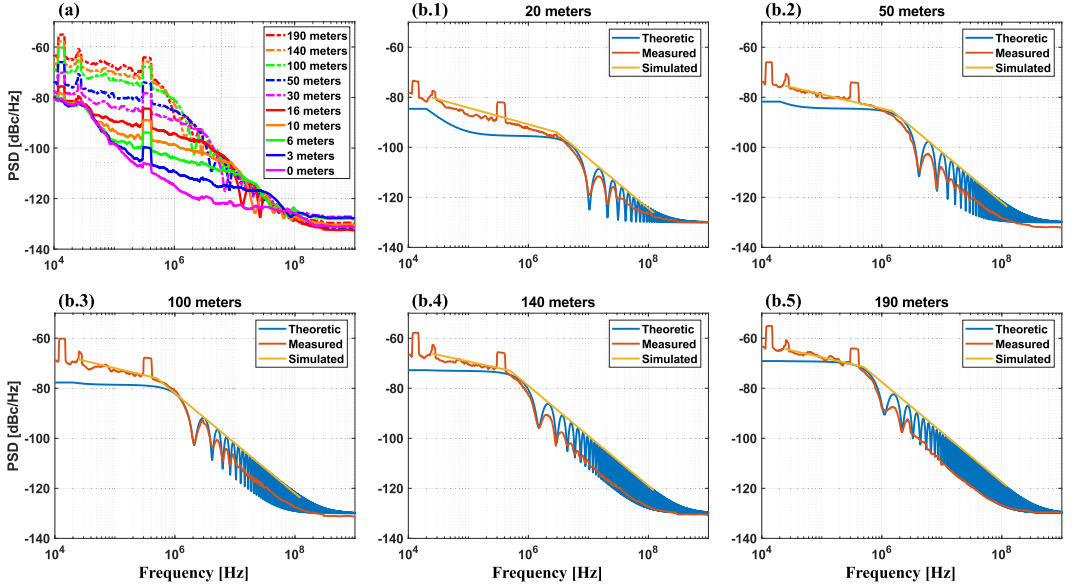


Fig. 4. (a) PSD of the phase noise measured before the DPO for different path delays. (b) Theoretic, measured, and simulated PSD of the phase noise for different path lengths: (b.1) 20 m, (b.2) 50 m, (b.3) 100 m, (b.4) 140 m, and (b.5) 190 m.

increases with the path length, 0 m being the condition with minimum phase noise and 190 m the maximum one. This phase noise increment is due to the decorrelation between two tones as distance increases. Furthermore, the phase noise of the 0 m case is not zero because the AWG and VSGs form phase noise to the system [24]. The phase noise added by the AWG and the VSGs are present in all the cases of Fig. 4(a). Moreover, from a 10 m-path length, the phase noise PSD shows a fading pattern because the two branches of the setup form an interferometric structure. As a common remarkable feature in all the phase noise measures, the PSD level starts to decrease with higher decay slope from 0.5 MHz of frequency. This cutoff frequency is crucial for the design of the adaptive low-pass filter of the proposed algorithm presented in Section II. The PSDs of the phase noise for these path delays can be estimated as [24]:

$$S(f) = \left\{ \left(\exp(B_{OP}|\tau_d|) - B_{OP} \frac{\sin(2\pi f|\tau_d|)}{2\pi f} - \cos(2\pi f|\tau_d|) \right) \times \frac{2B_{OP} \exp(-B_{OP}|\tau_d|)}{(\sqrt{2}B_{OP})^2 + (2\pi f)^2} \right\} \times \frac{2B_{LO}}{(2B_{LO})^2 + (2\pi f)^2} \quad (4)$$

where B_{OP} is the angular full linewidth at half maximum (FWHM) of the optical laser, τ_d is the delay difference between the two branches, and B_{LO} is the FWHM of the first VSG. Both the theoretical calculation and actual measurements of the phase noise PSD are shown in Fig. 4(b) for the different path lengths indicated above. It can be observed that the theoretical fading pattern matches the measured PSD one. However, the amplitudes of these PSDs do not coincide completely. This fact is due to the

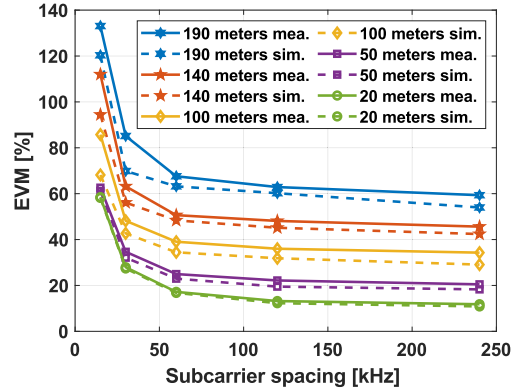


Fig. 5. Simulated (solid lines) and experimental (dashed lines) EVM as function of the subcarrier spacing for different path delays.

resolution of the ESA used to obtain the PSD measures not being high enough. Furthermore, the PSD of the phase noise used in the simulations is also depicted in Fig. 4(b). The simulated phase noise approximates the theoretical one through three points.

V. RESULTS AND DISCUSSION

In this section, the simulation and experimental results are discussed and analyzed. The OFDM configurations of Table I are evaluated under different path delays: 20 m, 50 m, 100 m, 140 m, and 190 m. The error vector magnitude (EVM) values in percent for the different OFDM configurations and different phase noise

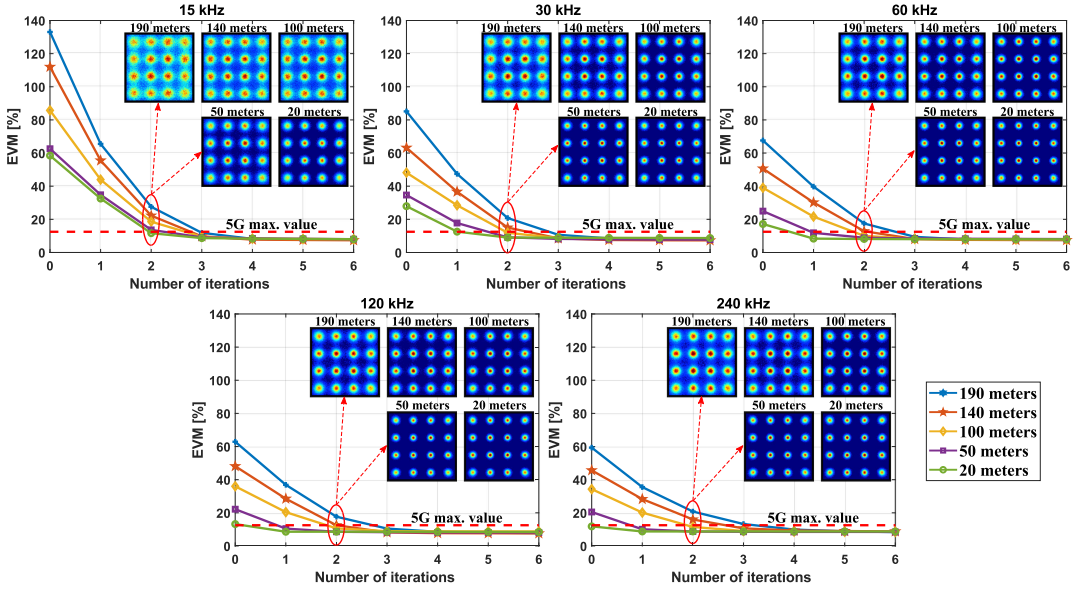


Fig. 6. EVM as a function of the number of iteration in the proposed OFDM receiver for different subcarrier spacings and under different phase noise levels.

conditions are shown in Fig. 5. The standard OFDM receiver (green blocks in Fig. 1(c)) is utilized to obtain the EVM values of this graph. The simulation results are also illustrated in Fig. 5. The simulated channel only includes phase noise (according to the simulated PSD of the phase noise in Fig. 4(b)) and AWGN, reproducing the same signal-to-noise ratio (SNR) level as in the experimental setup (26 dB). It can be observed in Fig. 5 that the simulation and experimental results match well.

Examining Fig. 5, the EVM follows a decreasing exponential curve as OFDM subcarrier spacing increases. This decay of the EVM is due to the fact that the ICI induced by the phase noise is proportional to the OFDM subcarrier spacing as explained in Section II. Moreover, as the phase noise level increases with the path length, the EVM values of the standard OFDM receiver do too. For most cases, the EVM values shown in Fig. 5 are considerably high for a 16-QAM constellation. Therefore, a method to mitigate the phase noise is truly required to establish a proper communication quality.

Fig. 6 shows the EVM values for the OFDM configurations in Table I and for different path lengths by employing the algorithm introduced in Section II. These EVM values are presented as a function of the concrete number of iterations of the proposed algorithm. In addition, the constellations of the processed signal using two iterations are also displayed for the different path delays. The EVM threshold of 12.5% for 16-QAM, determined by the 3GPP [9], is also indicated.

As the PSD level seen in Fig. 4(b) starts to decrease from, approximately 0.5 MHz in a more remarkable manner, the used adaptive low-pass filter shapes for six iterations are the same that shown in Fig. 2. For the remaining iterations, the attenuation of the edge of the filters is as linear steps between 80 and 10 dB. For instance, for three iterations, the attenuation values for the used filter are 80, 45, and 10 dB, respectively. Furthermore, this

TABLE II
NUMBER OF ITERATIONS TO REACH 5G EVM REQUIREMENTS FOR 16-QAM

Δf [KHz]	15	30	60	120	240
20 m	2	2	1	1	0
50 m	3	2	1	1	1
100 m	3	2	2	2	2
140 m	3	3	3	3	3
190 m	3	3	3	3	4

filtering process is performed in the frequency-domain to configure and approximate in a more accurate way the desired frequency shape. Therefore, this filtering block implies an additional FFT and IFFT stages. It is also worth mentioning that the equalizer block considers to be flat the amplitude of the estimated channel. In this respect, since the channel of the experimental setup does not present significant fading in the frequency domain, the performance of the results enhances.

Observing Fig. 6, it can be noticed that the EVM threshold of 12.5% for 16-QAM in 5G is achieved for all OFDM configurations and all the different phase noise levels. The required number of iterations to achieve the 5G threshold for all the different cases is shown in Table II. This shows that the required number of iterations of the algorithm increases as phase noise increases. At this point, we must highlight that the number of iterations increases the complexity of the system. Hence, more complexity in the receiver is demanded when higher phase noise levels are mitigated. Furthermore, since the ICI induced by the phase noise decreases with the subcarrier spacing, the required number of iterations of the algorithm, to satisfy EVM values lower than 12.5%, is lower for higher subcarrier spacings. However, for 140 m of path length, the needed iterations maintain constant and, for the 190 m case, 240 kHz of subcarrier spacing presents

the highest value of iterations. This fact is because higher subcarrier spacing configurations use less number of pilot tones and, thus, the equalization process contains more noise in higher path lengths than in lower subcarrier spacing values. Therefore, due to the degradation in the equalizer, high subcarrier spacing values, as 240 kHz, perform worse in channels with high phase noise level.

Furthermore, the OFDM receiver signal suffers frequency offset (FO) due to the frequency mismatch between the transmitter and receiver oscillators. In the experimental setup of Fig. 3(a), the measured FO value is 20 kHz. Therefore, the proposed algorithm can handle the degradation of the signal induced by FO. However, since the EVM increases as the FO increases, more iterations are needed for higher FO values to achieve the 5G requirements. Then, when large FOs are present, it is common to have a dedicated coarse FO estimation and compensation before the OFDM processing [25] and the same should be applied here. Thereby, the number of iterations of the algorithm do not need to increase when FO increases.

VI. CONCLUSION

This article discussed the relevance of studying and compensating phase noise in mm-wave AROF systems for 5G. A novel and efficient algorithm to mitigate phase noise in the OFDM receiver was presented, its complexity analyzed and performance simulated. Moreover, a mm-wave AROF setup at 25 GHz was implemented to experimentally analyze the impact of phase noise on 5G NR OFDM signals. The configuration of this setup allowed to gradually scale the phase noise level in the received signal.

OFDM signals with different subcarrier spacings, according to the 5G NR numerology, were evaluated in the experimental setup under different phase noise conditions. First, the standard OFDM receiver was utilized to process the received OFDM signals. The results of this process in terms of EVM were shown and matched with simulations. Then, the proposed algorithm was used to compensate the degradation due to phase noise and to decode the received signal, showing substantial improvements in performance and reduction of EVM, especially at high levels of phase noise. As a result, the proposed AROF system can reach the EVM requirements posed by 5G standards even in the presence of substantially higher phase noise levels than acceptable with a standard OFDM receiver.

The experimental results validate the proposed algorithm under different phase noise conditions and with different OFDM subcarrier spacings. By providing an efficient algorithm for compensation of phase noise in mm-wave AROF systems employing OFDM signals, this work proves the viability of mm-wave AROF links for 5G and beyond.

REFERENCES

- [1] D. Konstantinou *et al.*, "5G RAN architecture based on analog radio-over-fiber fronthaul over UDWDM-PON and phased array fed reflector antennas," *Opt. Commun.*, vol. 454, Jan. 2020, Art. no. 124464.
- [2] W. H. Chin, Z. Fan, and R. Haines, "Emerging technologies and research challenges for 5G wireless networks," *IEEE Wireless Commun.*, vol. 21, no. 2, pp. 106–112, Apr. 2014.
- [3] M. R. Akdeniz *et al.*, "Millimeter wave channel modeling and cellular capacity evaluation," *IEEE J. Sel. Areas Commun.*, vol. 32, no. 6, pp. 1164–1179, Jun. 2014.
- [4] J. Brenes *et al.*, "Network slicing architecture for SDM and analog-radio-over-fiber-based 5G fronthaul networks," *J. Opt. Commun. Netw.*, vol. 12, no. 4, pp. B33–B43, Apr. 2020.
- [5] S. Rommel *et al.*, "Towards a scaleable 5G fronthaul: Analog radio-over-fiber and space division multiplexing," *J. Lightw. Technol.*, vol. 38, no. 19, pp. 5412–5422, 2020.
- [6] S. Rommel, D. Perez-Galacho, J. M. Fabrega, R. Muoz, S. Sales, and I. Tafur Monroy, "High-capacity 5G fronthaul networks based on optical space division multiplexing," *IEEE Trans. Broadcast.*, vol. 65, no. 2, pp. 434–443, Jun. 2019.
- [7] L. C. P. Cavalcante, S. Rommel, R. Dinis, L. G. Q. S. Junior, L. F. Q. Silveira, and I. T. Monroy, "Performance evaluation of wavelet-coded OFDM on a 4.9 Gb/s w-band radio-over-fiber link," *J. Lightw. Technol.*, vol. 35, no. 14, pp. 2803–2809, Jul. 2017.
- [8] J. A. Altbas *et al.*, "Nonorthogonal multiple access and carrierless amplitude phase modulation for flexible multiuser provisioning in 5G mobile networks," *J. Lightw. Technol.*, vol. 35, no. 24, pp. 5456–5463, Dec. 2017.
- [9] 3GPP, "FG IMT-2020: User Equipment (UE) radio transmission and reception; Part 2: Range 2 Standalone. 3GPP TS 38.101-2," Version 16.5.0, 2020.
- [10] J. P. Santacruz, S. Rommel, U. Johannsen, A. Jurado-Navas, and I. T. Monroy, "Candidate waveforms for AROF in beyond 5G," *Appl. Sci.*, vol. 10, no. 11, Jun. 2020, Art. no. 3891.
- [11] J. P. Santacruz, A. Morales, S. Rommel, U. Johannsen, A. Jurado-Navas, and I. T. Monroy, "Experimental assessment of modulation formats for beyond 5G mm-Wave AROF systems," in *Proc. Eur. Conf. Netw. Commun.*, Dubrovnik, Croatia, 2020, pp. 300–304.
- [12] A. Delmède *et al.*, "OFDM baud rate limitations in an optical heterodyne analog fronthaul link using unlocked fiber lasers," in *Proc. Int. Topical Meeting Microw. Photon.*, Nov. 2019, pp. 1–4.
- [13] E. P. Martin *et al.*, "25-Gb/s OFDM 60-GHz radio over fiber system based on a gain switched laser," *J. Lightw. Technol.*, vol. 33, no. 8, pp. 1635–1643, Jan. 2015.
- [14] T. Shao *et al.*, "Chromatic dispersion-induced optical phase decorrelation in a 60 GHz OFDM-RoF system," *IEEE Photon. Technol. Lett.*, vol. 26, no. 20, pp. 2016–2019, Aug. 2014.
- [15] C. Wei, C. Lin, H. Huang, W. Liang, and S. Chi, "Estimation and suppression of dispersion-induced phase noise in w-band direct-detection OFDM radio-over-fiber systems," *J. Lightw. Technol.*, vol. 32, no. 20, pp. 3874–3884, May 2014.
- [16] H.-T. Huang, W.-L. Liang, C.-C. Wei, C.-T. Lin, and S. Chi, "150-km 103-GHz direct-detection OFDM-RoF system employing pilot-aided phase noise suppression," in *Proc. Opt. Fiber Commun. Conf.*, Mar. 2014, pp. 1–3.
- [17] C. Browning, E. P. Martin, A. Farhang, and L. P. Barry, "60 GHz 5G radio-over-fiber using UF-OFDM with optical heterodyning," *IEEE Photon. Technol. Lett.*, vol. 29, no. 23, pp. 2059–2062, Oct. 2017.
- [18] C. Browning *et al.*, "Gain-Switched optical frequency combs for future mobile radio-over-fiber millimeter-wave systems," *J. Lightw. Technol.*, vol. 36, no. 19, pp. 4602–4610, May 2018.
- [19] V. Syrjälä and M. Valkama, "Flexible adjacent channel interference and phase noise suppression in energy-efficient OFDMA receivers," in *Proc. IEEE 17th CAMAD*, Oct. 2012, pp. 221–225.
- [20] A. Demir, A. Mehrotra, and J. Roychowdhury, "Phase noise in oscillators: A unifying theory and numerical methods for characterization," *IEEE Trans. Circuits Syst. I: Fundam. Theory Appl.*, vol. 47, no. 5, pp. 655–674, May 2000.
- [21] V. Syrjälä and M. Valkama, "Receiver DSP for OFDM systems impaired by transmitter and receiver phase noise," in *Proc. IEEE Int. Conf. Commun.*, Jul. 2011, pp. 1–6.
- [22] C.-T. Lin, C.-C. Wei, and M.-I. Chao, "Phase noise suppression of optical OFDM signals in 60-GHz RoF transmission system," *Opt. Express*, vol. 19, no. 11, pp. 10423–10428, May 2011.
- [23] I. Parvez, A. Rahmati, I. Guvenc, A. I. Sarwat, and H. Dai, "A survey on low latency towards 5G: RAN, core network and caching solutions," *IEEE Commun. Surv. Tutor.*, vol. 20, no. 4, pp. 3098–3130, May 2018.
- [24] T. Shao, F. Paresys, G. Maury, Y. L. Guennec, and B. Cabon, "Investigation on the phase noise and EVM of digitally modulated millimeter wave signal in WDM optical heterodyning system," *J. Lightw. Technol.*, vol. 30, no. 6, pp. 876–885, Jan. 2012.
- [25] T. M. Schmidl and D. C. Cox, "Robust frequency and timing synchronization for OFDM," *IEEE Trans. Commun.*, vol. 45, no. 12, pp. 1613–1621, Dec. 1997.

Javier Pérez Santacruz received the B.Sc. degree in telecommunication engineering, and the double M.Sc. degrees in telecommunications engineering and telematic, and telecommunication networks from the University of Málaga, Málaga, Spain, in 2016 and 2018, respectively. He completed his thesis entitled “Simulator of a Bandwidth Modem for Underwater Acoustic Channels.” He is currently working toward the Ph.D. degree with the Eindhoven University of Technology, Eindhoven, Netherlands. He is a member of the ITN project 5G STEP FORWARD. His research is focused on modulation formats and digital signal processing in millimeter wave analog-radio-over-fiber systems for 5G and beyond.

Simon Rommel (Member, IEEE) received the B.Sc. degree from the University of Stuttgart, Stuttgart, Germany, in 2011, the M.Sc. degree in photonic networks engineering from Aston University, Birmingham, U.K. and Scuola Superiore Sant’Anna, Pisa, Italy, in 2014, and the Ph.D. degree from the Technical University of Denmark, Kongens Lyngby, Denmark, in 2017, with research focused on photonic-wireless convergence and millimeter-wave radio-over-fiber links. In 2017, he visited the National Institute of Information and Communications Technology, Tokyo, Japan, for a research stay. Since 2017, he has been with the Eindhoven University of Technology, Eindhoven, The Netherlands, as a Postdoctoral Researcher, continuing his work on photonic and radio frequency technologies with a strong focus on implementations for 5G. He has contributed to multiple national and European research projects, including H2020 blueSPACE as a Technical Manager. His research interests include the fields of fiber-optic and wireless communications and the associated digital signal processing. Dr. Rommel is a member of the Institution of Engineering and Technology and the Verband der Elektrotechnik Elektronik Informationstechnik e.V (VDE).

Ulf Johannsen (Member, IEEE) received the Dipl.-Ing. degree from the Hamburg University of Technology, Hamburg, Germany, in 2009, and the Ph.D. degree from the Eindhoven University of Technology (TU/e), Eindhoven, The Netherlands, in 2013. In 2013, he was a Senior Systems Engineer with ATLAS ELEKTRONIK GmbH, Bremen, Germany, where he worked as a System Designer and Engineering Manager on autonomous underwater vehicle systems with sonar payloads. His responsibilities included the specification and architecting of the entire systems as well as the lead of multidisciplinary development teams in order to meet those specifications within time and budget. Since 2016, he has been an Assistant Professor with the Electromagnetics Group, TU/e. Moreover, he leads the Ultra-High-Data-Rate programme within TU/e’s Centre for Wireless Technology. His research focus lies on (sub-)millimeter-wave antenna systems for various applications. He is the Chairperson of the IEEE Benelux Joint AP/MTT chapter.

Antonio Jurado-Navas received the Ph.D. degree in telecommunication engineering from the University of Málaga, Málaga, Spain, in 2009. From 2002 to 2004, he was a Consultant at Vodafone-Spain. He was the recipient of a Spanish Ministry of Education and Science scholarship from 2004 to 2008. From 2009 to 2011, he was at the Department of Communications Engineering (Ingeniería de Comunicaciones), University of Málaga, as a Postdoctoral Researcher. In 2011, he became an Assistant Professor at the same department. From 2012 to 2015, he was at Ericsson, Spain, where he was working on geolocation tools for mobile networks. From 2015 to 2017, he was a Marie-Curie Fellow at the Technical University of Denmark, Kongens Lyngby, Denmark. In 2017, he joined the Technical University of Eindhoven to work for the Electro-Optical Communications Group as an Invited Researcher. Since 2018, he has been an Associate Professor with the Communication Engineering Department, Universidad de Málaga, Málaga, Spain. His research interests span a diverse set of topics in the wide areas of communication theory and wireless communications: free-space optical communications, stochastic processes, wireless channel modeling, OCDMA, physical-layer security, adaptive optics, and efficient transmission techniques.

Idelfonso Tafur Monroy (Senior Member, IEEE) received the M.Sc. degree from the Bonch-Bruевич Institute of Communications, St. Petersburg, Russia, a Technology Licentiate degree in telecommunications theory from the Royal Institute of Technology, Stockholm, Sweden, and the Ph.D. degree from the Eindhoven University of Technology, Eindhoven, The Netherlands. Since 2017, he has been a Professor of photonic terahertz systems with the Department of Electrical Engineering, Eindhoven University of Technology, and in 2018, became the Director of the Photonic Integration Technology Center. He started his academic career with the Kharkov Polytechnic Institute in Ukraine. He coordinates the 5G PPP BLUESPACE project on technologies for 5G wireless systems and the ITN CELTA project with 15 Ph.D. students working on convergence of electronics and photonics technologies for applications, such as terahertz communications, sensing, and imaging. He is the Co-Founder of a start-up Bifrost Communications on optical fiber access solutions. He is a Professor of photonics communication technologies with the Technical University of Denmark, Kongens Lyngby, Denmark, a Guest Professor with the Beijing University of Post and Telecommunications, Beijing, China, a Visiting Scientist with the University of California at Berkeley, Berkeley, CA, USA, and a Fellowship Professor with the ITMO University, St Petersburg, Russia. He is the coauthor of more than 500 journal and conference papers and has graduated 22 Ph.D. students. His research interests are in the area of photonics technologies for terahertz systems, converged electronic-photonics integrated circuits for applications in secure communications, sensing, and computing.

P5: Experimental Study of the Phase Noise in K-band ARoF systems for Low Complexity 5G receivers

J. P. Santacruz, S. Rommel, A. Jurado-Navas, U. Johannsen, and I. Tafur Monroy, “Experimental Study of the Phase Noise in K-band ARoF systems for Low Complexity 5G receivers,” in *2020 National Symposium of the International Scientific Radio Union (URSI)*, Málaga, Spain: arXiv, Sep. 2020, pp. 1–4. arXiv: 2109.07392 [eess.SP]

EXPERIMENTAL STUDY OF THE PHASE NOISE IN K-BAND AROF SYSTEMS FOR LOW COMPLEXITY 5G RECEIVERS

A PREPRINT

✉ **Javier Pérez Santacruz**

Institute for Photonic Integration
Eindhoven University of Technology
5600 MB Eindhoven, the Netherlands
j.perez.santacruz@tue.nl

✉ **Simon Rommel**

Institute for Photonic Integration
Eindhoven University of Technology
5600 MB Eindhoven, the Netherlands
s.rommel@tue.nl

✉ **Ulf Johannsen**

Centre for Wireless Technology
Eindhoven University of Technology
5600 MB Eindhoven, the Netherlands
u.johannsen@tue.nl

✉ **Antonio Jurado-Navas**

Communication Engineering Department
University of Málaga
29071 Málaga, Spain
u.johannsen@tue.nl

✉ **Idelfonso Tafur Monroy**

Institute for Photonic Integration
Eindhoven University of Technology
5600 MB Eindhoven, the Netherlands
i.tafur.monroy@tue.nl

September 16, 2021

ABSTRACT

In this paper, an experimental analysis of the phase noise in an OFDM AROF setup at 25 GHz for beyond 5G is presented. The configuration of the setup allows to gradually scale the final phase noise level of the system. Moreover, an OFDM phase noise mitigation method with low complexity and delay is proposed and explained. The proposed method is an advanced version of the LI-CPE algorithm. The advanced LI-CPE version avoids the one OFDM symbol delay of its antecedent. In addition, the yields of using both methods are shown under different phase noise levels and with different subcarrier spacings. Finally, it is experimentally proven that the proposed method performs better than its previous version.

Keywords AROF · OFDM · phase noise · 5G

1 Introduction

The exponential growth of the mobile network data has motivated to research about new technologies that can support future traffic requests. The fifth-generation (5G) of wireless networks is the established solution to these demanding requirements. Moreover, new types of services with multiple requirements are emerging, and the mobile network has to adapt to them. Therefore, 5G proposes three types of scenarios to fulfill such services [2019]: enhanced mobile broadband (eMBB) to high bit rate services; massive machine-type communications (mMTC) to support a huge quantity of low power connected devices; and ultra-reliable and low latency communications (URLLC) where latency and reliability are the priorities.

One of the most prominent ways to increase the bit rate is moving from the current saturated band to higher frequencies, in the millimeter-wave (mm-wave) domain. Furthermore, analog radio-over-fiber (ARoF) is a suited technology due to

its long reach distances, low cost, wide bandwidth, high spectral efficiency, and low power consumption [2019]. In addition, the centralized-radio access network (C-RAN) is a trending architecture because it offers attractive benefits such as flexibility, low latency, and reduced energy consumption. Hence, mm-wave ARoF over a C-RAN scheme is a strong candidate to be part of the future 5G structure. However, mm-wave ARoF presents several drawbacks such as phase noise, chromatic dispersion, nonlinearities, or high free-space path loss (FSPL).

Orthogonal frequency division multiplexing (OFDM) is the modulation format chosen by the 3GPP 5G standard [2019]. OFDM communications bring advantages like robustness to frequency selective channels, high spectral efficiency, or efficient multiple-input multiple-output (MIMO) integration. Nonetheless, one of the major OFDM degrading impairments is the phase noise. Thence, a phase noise compensation algorithm has to be performed in an mm-wave OFDM ARoF system. There are three types of OFDM phase noise mitigation techniques [2017]: decision-feedback-based schemes, blind estimation schemes, and pilot-based schemes. Decision-feedback and blind estimation schemes are complex iterative methods. Moreover, these iterative algorithms show difficulties to converge in some cases. Then, these types of techniques are not suitable for mMTC and URLLC scenarios. Pilot-based schemes are appropriate phase noise compensation methods for these 5G scenarios due to its simplicity and low latency process.

In this work, the phase noise degradations are studied and analyzed in an experimental OFDM ARoF setup at 25 GHz (K-band). The setup scheme can increment gradually the final phase noise of the received signal in the system. Furthermore, an OFDM phase noise mitigation algorithm with low complexity and latency is proposed. This algorithm is compared with another method and probed experimentally. The proposed method is analyzed under different OFDM configurations and with different phase noise levels.

2 Phase noise effect on OFDM systems and proposed algorithm to compensate it

Phase noise causes two degradations in OFDM signals. The first one is a common phase error (CPE) that affects all the subcarriers in the same way and can be compensated by performing the zero-forcing (ZF) equalizer. The second degradation consists of inter-carrier interference (ICI). ICI can not be mitigated by a normal equalizer. Hence, an additional method has to be included to compensate for the ICI caused by the phase noise. The OFDM symbol duration plays an important role in a phase noise channel. This fact is because the ICI originated by the phase noise is proportional to the OFDM symbol period. The subcarrier spacing is inversely proportional to the OFDM symbol duration. Then, the phase noise degradation decreases with the subcarrier spacing in OFDM systems.

Furthermore, most of the phase noise comes from the oscillators in a communication system and follows a Wiener process [2000]. A very simple method to estimate the phase noise in this type of scenario consists of the interpolation of the CPEs that belong to consecutive OFDM symbols [2011]. This method is based on the CPE represents the middle phase noise point of the OFDM symbol in the time domain. A way to estimate the CPE by using pilot subcarriers is [2011]:

$$\text{CPE}^m = \text{angle}(\mathbf{Y}_k^m \times \text{conj}(\mathbf{H}_k^m \cdot \mathbf{X}_k^m)), \quad k \in \text{PSC} \quad (1)$$

where \mathbf{Y} is the received symbols after the fast Fourier transform (FFT) process; \mathbf{H} represents the estimated channel in the frequency domain; \mathbf{X} is the vector of the transmitted subcarriers; k is the subindex of the pilot subcarriers (PSC) in the vectors \mathbf{Y} , \mathbf{H} , and \mathbf{X} ; the operators \times and \cdot determine a vector multiplication and a multiplication element by element, respectively; the hyperindex m concerns with the OFDM symbol index. After this CPE estimation, the phase noise can be linear interpolated and compensated. This method is called linear interpolation based ICI estimation technique (LI-CPE) [2011]. The main advantages of LI-CPE are its low complexity and its robustness because a noniterative process is implemented. However, applying LI-CPE supposes a delay of one OFDM symbol since it is necessary to calculate the CPE of the next OFDM symbol for the phase noise estimation of the current OFDM symbol.

The proposed OFDM mitigation algorithm is an advanced technique of the LI-CPE method. This advance is based on using the redundancy of the OFDM structure where the prefix cyclic (CP) is a copy of the last part of the OFDM symbol. It is possible to estimate the phase noise slope in each OFDM symbol by processing the CP and the last part of the symbol. This slope can be roughly calculated by employing the next formula:

$$\Delta\phi^m = \left(\sum_{i=1}^{N_{cp}} \text{angle} \left(\frac{\mathbf{r}_{i+N}^m}{\mathbf{r}_i^m} \right) \right) / (N_{cp} \cdot N) \quad (2)$$

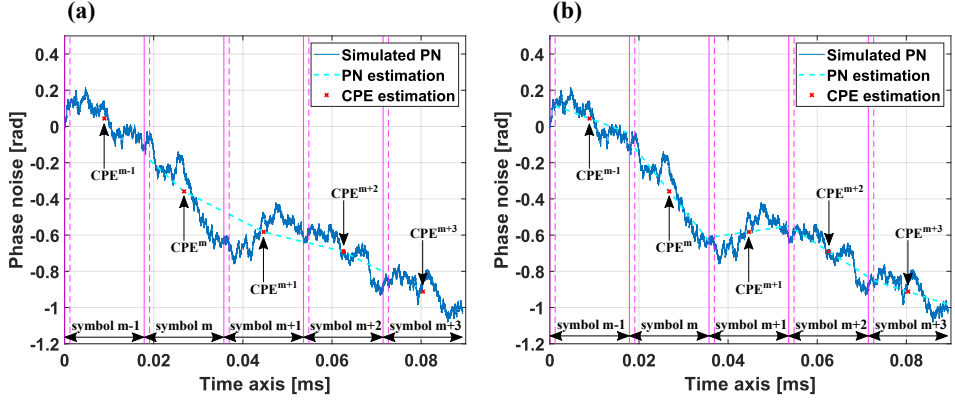


Figure 1: Phase noise interpolation based on CPE: LI-CPE in [2011] (a) and proposed LI-CPE (b).

where N is the total number of subcarriers; N_{cp} is the number of CP samples; \mathbf{r} is the received signal in the time domain (including the CP). Therefore, a linear interpolation of the phase noise can be performed by using the CPE and this slope. So, the phase noise estimation is reached although the next linear equation:

$$\hat{\rho}_k^m = \Delta\phi^m \cdot \left(k - \frac{N_T}{2}\right) + \text{CPE}^m, \quad k \in [0, N_T - 1] \quad (3)$$

where N_T is the sum of N and N_{cp} . In this way, the delay of one OFDM symbol is avoided because the phase noise can be independently estimated in each symbol. Moreover, the phase noise estimation is more accurate than in the normal LI-CPE because the interpolation process has more reference points. This idea to estimate the phase noise was initially used in [2013].

Fig. 1 shows two graphs to visually see and compare the LI-CPE method proposed in [2011] (Fig. 1 (a)) and the advanced version of LI-CPE explained in this section (Fig. 1 (b)). These graphs have been obtained through simulations. The simulated phase noise is created according to a Wiener process [2000] with a two-sided 3-dB bandwidth (β) of 150 Hz. Additive white Gaussian noise (AWGN) and fading channel are not included to see more clearly the phase noise estimation performance of each algorithm. The relevant OFDM parameters used in these simulations are the following: 60 kHz of subcarrier spacing, 1.2 μ s of CP period, the total duration of an OFDM symbol is 17.87 μ s, 4096 active subcarriers, and one pilot tone inserted on every 12th active subcarrier.

The ICI level introduced by the phase noise is directly related to the ratio between the OFDM symbol duration and the two-sided 3-dB bandwidth of the phase noise. Moreover, it should be noted that the CPE estimation improves with the number of pilots (see equation 1). In addition, the phase noise affects more to the lower frequency subcarriers due to its low-pass spectrum nature.

In both graphs, the blue line represents the simulated phase noise to estimate; the dotted cyan plot corresponds to the estimated phase noise; the red crosses are the estimated CPEs; and the vertical solid purple lines show the borders between each OFDM symbol. The period between the vertical purple solid and dotted lines represents the CP duration. The LI-CPE method lacks the first and last phase noise estimation because it is necessary to know the previous and next CPE values to determine the phase noise in each OFDM symbol. Observing the two graphs in Fig. 1, it can be seen that the phase noise interpolation of the proposed LI-CPE method is better suited. For this example, the mean square error (MSE) values of the phase noise estimation are 0.0106 and 0.0037 for the normal LI-CPE and the advanced LI-CPE, respectively.

3 Experimental setup

The experimental testbed scheme is shown in Fig. 2 (a). The main purpose of this setup is to adjust the phase noise level in an mm-wave ARoF system. Then, an analysis of the phase noise and its degradations in OFDM signals can be realized. First, an electrical cavity laser (ECL) generates an optical carrier at 1550 nm of wavelength. Next, a

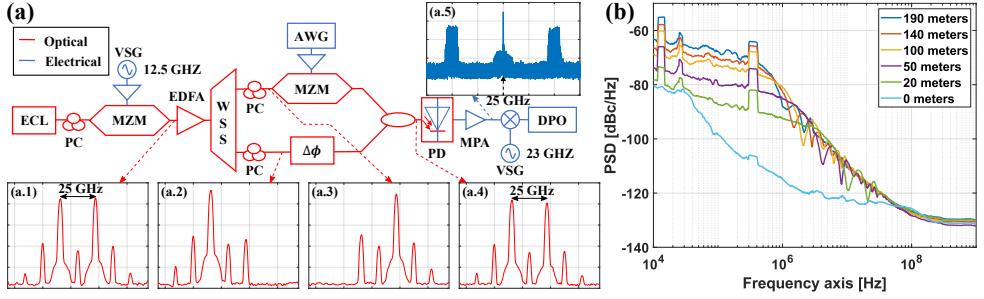


Figure 2: Experimental mm-wave ARoF setup (a) and PSD of the measured phase noise with different path lengths.

Table 1: OFDM configuration parameters.

Config.	1	2	3	4	5
Δf [KHz]	30	60	120	240	480
N	2^{13}	2^{12}	2^{11}	2^{10}	2^9
T_{cp} [μ s]	2.4	1.2	0.6	0.3	0.15

Mach-Zehnder modulator (MZM), biased in the null point, modulates the optical carrier with an RF carrier of 25 GHz. This RF carrier is produced by a vector signal generator (VSG). Therefore, two optical tones, corresponding to the second harmonics of the MZM, are generated with a frequency separation of 25 GHz. The spectrum of these two tones are exhibited in Fig. 2 (a.1). After the laser, a polarization controller (PC) is utilized because MZMs are sensitive to optical polarization. Then, the optical signal is boosted by an erbium-doped fiber amplifier (EDFA).

The next step consists of splitting the two tones through a wavelength switch selector (WSS). The graphs (a.2) and (a.3) of Fig. 2 show the optical spectrum of the split tones after the filter process. The tone from the upper branch is modulated with the OFDM signal through a second MZM. The OFDM signal is produced by an arbitrary waveform generator (AWG) of 12 GSa/s. The other tone is delayed regarding the modulated tone by a patch core in the lower branch. This delay is the key to the scheme to increment gradually the phase noise. The final phase noise level of the system is proportional to the delay between the two branches [2012]. The modulated and delayed tones are recombined in a coupler. The optical spectrum of this combination is shown in Fig. 2 (a.4). It is relevant to mention that, to get the maximum power in the coupler, the polarization of both tones has to be the same. For this reason, one polarization controller is employed in each branch.

In the photodiode (PD), the recombined tones are beaten and converted to an RF signal of 25 GHz. Next, the electrical signal is boosted by a 30 dB medium power amplifier (MPA). Fig. 2 (a.5) exhibits the electrical spectrum at the MPA output. The OFDM bands and the 25 GHz carrier can be observed in this spectrum. Then, the electrical signal is mixed with a 23 GHz sinusoid produced by a second VSG. Consequently, the signal is downconverted to an intermediate frequency (IF) at 2 GHz. Finally, the IF signal is sampled by a digital phosphor oscilloscope (DPO) of 12.5 GSa/s.

The power spectral density (PSD) of the phase noise is measured before the DPO for several delay values: 0 ns, 96 ns, 240 ns, 480 ns, 672 ns and 912 ns. These measures are shown in Fig. 2 (b). The 0 meters case corresponds to the lowest phase noise level. As the path length increases, the PSD phase noise also increments. For path lengths higher than 20 meters, the phase noise depicts a fading pattern in the PSD. This fact is because the two branches of the scheme start to perform as an interferometer from 20 meters of delay. The PSD phase noise can be calculated through the equations presented in [2012].

Different OFDM configurations are transmitted in the experimental setup. The common parameters of all the configurations used are: quadrature phase-shift keying (QPSK) modulation, one pilot tone inserted on every 12th active subcarrier, and 80% of all subcarriers are active. The rest of the parameters are shown in Table 1 following this order: subcarrier spacing (Δf), total number of carriers (N), and CP period (T_{cp}). The configuration two is according to the 3GPP 5G standard [2019]. The parameters of the remaining configurations are proportional to this configuration for a fair comparison (same bandwidth and bit rate).

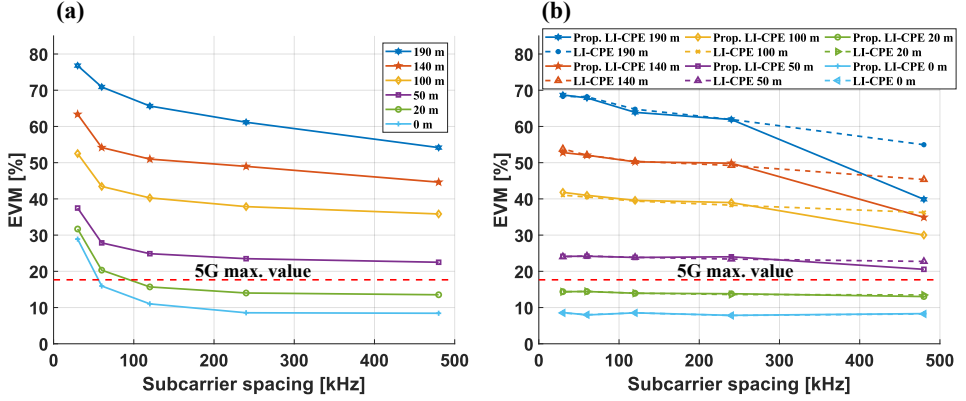


Figure 3: EVM as a function of the subcarrier spacing for several path length values: using the standard OFDM receiver (a); adding the LI-CPE method of [2011] and the proposed LI-CPE to the standard OFDM receiver (b).

4 Results

Fig. 3 exhibits the experimental results of the previous section. These results are represented in terms of error vector magnitude (EVM) in percent. The horizontal axis of both graphs depicts the different OFDM configurations in Table 1. Fig. 3 (a) corresponds to the EVM by employing the standard OFDM receiver. The standard OFDM receiver consists of the following blocks in this order: remove the CP, FFT, ZF equalizer, and QPSK demodulator. The graph of Fig. 3 (b) adds the LI-CPE methods explained in section 2 before the ZF equalizer: proposed LI-CPE technique (solid line) and LI-CPE algorithm of [2011] (dotted line). The maximum 5G EVM value of 17.5 % for QPSK modulations is also represented as a dotted red line in both graphs [2019]. Observing Fig. 3 (a), the EVM is higher for longer path delays (see Fig. 2 (b)). In addition, for shorter subcarrier spacing, the EVM is also higher because the OFDM symbol period is larger and the phase noise degrades more the signal.

On the other hand, the EVM also increments with the path length in Fig. 3 (b). Nonetheless, the EVM curves for the different delays are flatter than in Fig. 3 (a). These flat curves mean that the OFDM symbol period is less related to the ICI introduced by the phase noise if one of the LI-CPE methods is performed. Therefore, the EVM improvement of applying these methods is higher for shorter subcarrier spacing values. Moreover, the EVM values of the proposed LI-CPE are lower for higher subcarrier spacing configurations because the phase noise is better estimated as it was mentioned in section 2. Thence, these results prove that the proposed LI-CPE has two big advantages regarding the LI-CPE method presented in [2011]: one OFDM symbol delay less and better EVM values. The only minor disadvantage is the added process to calculate the phase noise slope through equation 2. Nevertheless, this calculation requires a few extra operations. Furthermore, for delay lengths above 20 meters, the EVM values exceed the 17.5 % requirement limit of 5G standard. Hence, a more complex phase noise mitigation algorithm has to be used in these conditions.

5 Conclusions

An analysis of the phase noise has been shown in an experimental ARoF setup for K-band (25 GHz). The importance of employing low complex and latency phase noise mitigation techniques in this type of system for mMTC and URLLC scenarios has been explained too. Moreover, an OFDM phase noise mitigation method with low complexity and latency has been proposed. This method is an advanced version of the LI-CPE technique. Both methods have been studied and compared for different phase noise conditions and subcarrier spacing in the experimental ARoF setup. The results prove that the proposed method outperforms LI-CPE in terms of EVM and, in addition, supposes one OFDM symbol delay less.

Acknowledgements

This work has been partially supported by 5G STEP FWD (GA no. 722429) and blueSPACE (GA no. 762055) projects which have received funding from the European Union's Horizon 2020 research and innovation programme.

References

- 3rd Generation Partnership Project; Technical Specification Group Services and System Aspects; Rel. 15 Description; Summary of Rel-15 Work Items (Rel. 15), Feb. 2019.
- S. Rommel *et al.*, "High-Capacity 5G Fronthaul Networks Based on Optical Space Division Multiplexing," *IEEE Trans. Broadcast.*, vol. 65, no. 2, pp. 434-443, Jun. 2019.
- P. Mathecken *et al.*, "Constrained Phase Noise Estimation in OFDM Using Scattered Pilots Without Decision Feedback," in *IEEE Trans. Signal Process.*, vol. 65, no. 9, pp. 2348-2362, May. 2017.
- A. Demir *et al.*, "Phase noise in oscillators: a unifying theory and numerical methods for characterization," in *IEEE Trans. Circuits Syst. I, Fundam. Theory Appl.*, vol. 47, no. 5, pp. 655-674, May. 2000.
- M. E. Mousa-Pasandi and D. V. Plant, "Noniterative Interpolation-Based Partial Phase Noise ICI Mitigation for CO-OFDM Transport Systems," in *IEEE Photon. Technol. Lett.*, vol. 23, no. 21, pp. 1594-1596, Nov. 2011.
- Y. Ha and W. Chung, "A Feedforward Partial Phase Noise Mitigation in the Time-Domain using Cyclic Prefix for CO-OFDM Systems," in *J. Opt. Soc. Korea* 17, pp. 467-470, 2013.
- T. Shao *et al.*, "Investigation on the Phase Noise and EVM of Digitally Modulated Millimeter Wave Signal in WDM Optical Heterodyning System," in *J. Light. Technol.*, vol. 30, no. 6, pp. 876-885, Mar. 2012.
- N. Mohamed *et al.*, "Review on system architectures for the millimeter-wave generation techniques for RoF communication link," in *Proc. IEEE Int. RF Microw. Conf. (RFM)*, pp. 326-330, Dec. 2008.

P6: Experimental ARoF System Based on OPLL Mm-Wave Generation for Beyond 5G

J. P. Santacruz, D. Dodane, J. Bourderionnet, *et al.*, “Experimental ARoF System Based on OPLL Mm-Wave Generation for Beyond 5G,” in *26th Optoelectronics and Communications Conference (OECC)*, Hong Kong, China: Optica Publishing Group, Jul. 2021, W2B.2. DOI: 10.1364/OECC.2021.W2B.2

Experimental ARoF System Based on OPLL Mm-Wave Generation for Beyond 5G

Javier Pérez Santacruz¹, Delphin Dodane², Jerome Bourderionnet², Simon Rommel¹, Antonio Jurado-Navas³, Ulf Johannsen¹, and Idelfonso Tafur Monroy¹

¹Institute for Photonic Integration (IPI), Eindhoven University of Technology, 5600 MB Eindhoven, the Netherlands

²Thales Research & Technology, 91767 Palaiseau Cedex, France

³Department of Communications Engineering, University of Málaga, Campus de Teatinos, 29071 Málaga, Spain
j.perez.santacruz@tue.nl

Abstract: We experimentally analyze the ARoF based on OPLL mm-Wave generation performance for 5G fronthaul. Remarkable performance improvements are achieved for all 5G NR numerologies and different OPLL configurations despite their inherently high phase noise level.

OCIS codes: (060.5625) Radio frequency photonics; (060.4510) Optical communications.

1. Introduction

The fifth-generation (5G) of mobile networks aims to satisfy the upcoming applications demands. 5G new radio (NR) will bring a large enhancement in terms of data rate and latency among others. Exploiting the millimeter-Wave (mm-Wave) domain is required to achieve the 5G data rate goals. However, since mm-Wave signals present high free-space path loss (FSPL), the number of mm-Wave remote units (RUs) will be much larger than in the current mobile network. Then, analog radio-over-fiber (ARoF) technology arises as an adequate solution for the beyond 5G fronthaul since it offers interesting benefits such as low latency, low complex RUs, and efficient spectrum usage [1, 2]. Hence, ARoF enables a scalable deployment of the mm-Wave RUs for the future 5G architecture.

The optical mm-Wave generation is key to achieve a stable ARoF communication (see Fig. 1 (a)), with external modulation and optical phase locked loop (OPLL) being two of the most popular techniques (see their schematics in Fig. 1 (b)). Since external modulation technique uses the high order harmonics produced by applying the RF source to the modulator, the generation of the two-tone suffers high attenuation [3]. On the other hand, OPLL technique presents better performance in terms of power efficiency. Nevertheless, OPLL implies higher phase noise level (see Fig. 1 (c)).

Orthogonal frequency division multiplexing (OFDM) is the standardized 5G waveform by 3rd Generation Partnership Project (3GPP) [4]. However, phase noise is one of the major limiting factors in OFDM mm-Wave ARoF systems because of the low subcarrier spacing utilized in 5G [5]. Therefore, 5G ARoF systems based on OPLL mm-Wave generation have to implement phase noise compensation in the receiver and, thus, the benefits of employing OPLL technique, as the power efficiency, can be taken. In this paper, we present an experimental ARoF setup up based on OPLL mm-Wave generation. Different OPLL configurations and all 5G NR numerologies are tested in this setup. The experimental results achieve the 5G requirements for both 16-quadrature amplitude modulation (16-QAM) and 64-QAM. Hence, the viability of employing power efficient ARoF systems based on OPLL for the beyond 5G infrastructure is demonstrated.

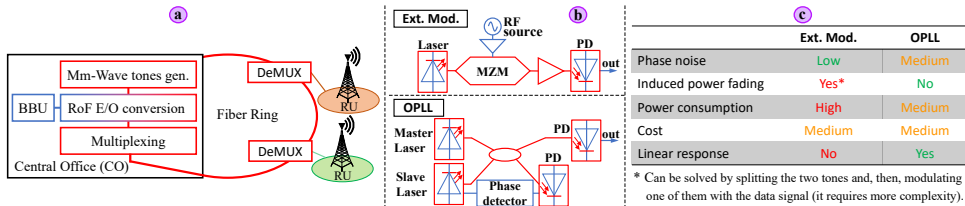


Fig. 1. (a) ARoF fronthaul for beyond 5G. (b) External modulation and OPLL schemes. (c) Comparative table between external modulation and OPLL techniques. BBU: base band unit, DeMUX: demultiplexer.

2. Experimental testbed

Figure 2 (a) shows the experimental setup employed in this work. First, two distributed feedback lasers (DFB), operating at C-band, generate two optical carriers with a separation of 24.75 GHz (K-band). DFB 1 and DFB 2 constitute the master and slave lasers, respectively. Next, the generated tones are combined by a 50/50 optical coupler. One of the outputs of the coupler is employed to track the phase difference between the two tones. For that, the mm-Wave carrier output is generated from the beat signal formed between the two tones, which is detected by a photodiode (PD). Then, the resulting signal is boosted and its phase is compared to the reference signal from a local oscillator (LO) using an RF mixer. The phase error signal is introduced in the RF loop filter (LF) and is used to adjust the frequency of the slave laser, forcing it to track the master laser [3]. Hence, the phase difference between the two lasers is adjusted, producing optical tones more correlated, thus reducing the final phase noise of the system.

The other output of the coupler is used to modulate the two optical tones with the OFDM signal by a Mach-Zehnder modulator (MZM), biased in the quadrature point. An isolator protects the OPLL from reflections. The OFDM signal is generated by an intermediate frequency (IF) of 1 GHz with an arbitrary waveform generator (AWG) of 12.5 GSa/s. Then, the modulated optical signal beats in a second PD, producing RF sidebands at 23.75 and 25.75 GHz. Next, this RF signal is downconverted by mixing with a second LO of 23 GHz, producing a second IF of 1.75 GHz. Thereby, the RF sidebands move to 0.75 and 2.75 GHz, respectively. Last, the downconverted signal is boosted by a 22 dB RF amplifier and sampled by a digital phosphor oscilloscope (DPO) at 12.5 GSa/s.

The graph of Fig. 2 (b) illustrates the power spectral density (PSD) of the phase noise in the RF signal after the second PD for different bandwidth values of the OPLL LF. Observing Fig. 2 (b), it can be noticed that the phase noise PSD amplitude decreases as the OPLL LF bandwidth increments. However, the 700 kHz and 1000 kHz bandwidth cases depict high PSD peaks at its cut off frequencies. Thereby, it is not clear what it is the best OPLL configuration for an OFDM communication system and, then, these configurations should be compared. Furthermore, different OFDM configurations are transmitted through the setup. These OFDM configurations embrace all 5G NR numerologies (15–240 kHz) and their main parameters are presented in table of Fig. 2 (c) [4]: subcarrier spacing (Δf), total number of subcarriers (N), and cyclic prefix (CP) period (T_{cp}). Moreover, a photo of the main components of the OPLL block is shown in Fig. 2 (d).

Finally, Figs. 2 (e) and (f) show the digital signal processing (DSP) block diagrams at the transmitter and receiver sides, respectively. At the transmitter side, a classical OFDM transmitter is used and, then, an IF upconversion process is performed. At the receiver side, first, the sampled signal by the DPO is separated in two branches. The upper branch realizes a band-pass filter (BPF), maintaining the RF carrier and OFDM sidebands. In the lower branch, the RF carrier is obtained by a low-pass filter (LPF). Then, the outputs of the two branches are multiplied, moving the OFDM signal to the initial IF of 1 GHz. This technique is called RF-pilot-assisted and allows to mitigate the phase noise by using the RF tone for the downconversion process. Last, the IF downconversion, the synchronization, the carrier frequency offset (CFO) compensation, and the OFDM receiver blocks are performed.

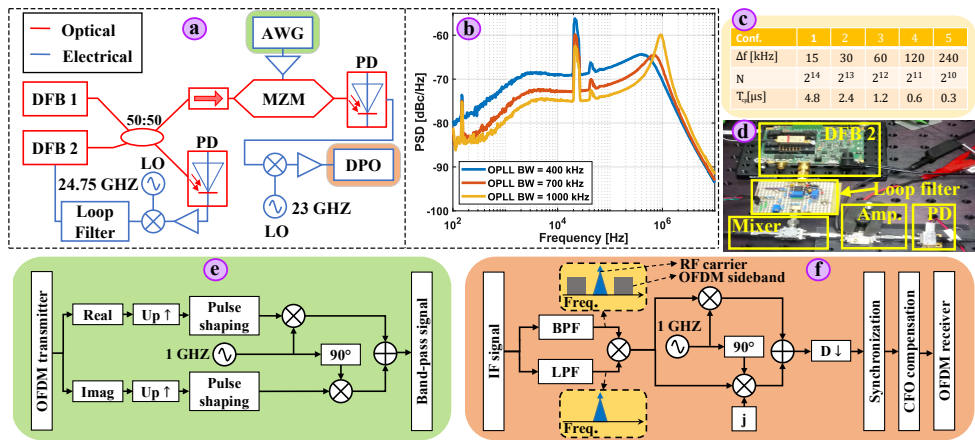


Fig. 2. Experimental testbed: (a) schematic of the setup, (b) PSD of the phase noise for different OPLL LF bandwidths, (c) table with the parameters of the used OFDM configurations, (d) transmitter DSP block diagram in the AWG, (e) and receiver DSP block diagram in the DPO.

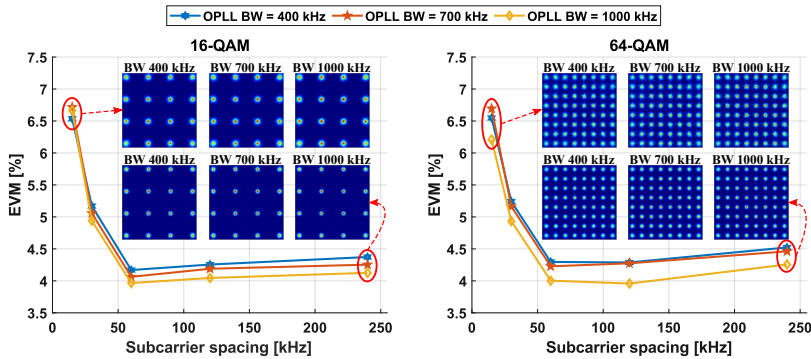


Fig. 3. EVM as a function of the subcarrier spacing for the under test OPLL configurations.

3. Experimental results and discussions

Figure 3 shows the results of the experimental setup. These results are expressed in terms of error vector magnitude (EVM) for different subcarrier spacing values and several OPLL configurations. Two modulation orders have been evaluated: 16-QAM (left graph) and 64-QAM (right graph). In both graphs, it can be noticed that EVM decreases as the subcarrier spacing value increases. This fact is because the inter-carrier interference (ICI) level induced by the phase noise is higher for lower subcarrier spacing values [2]. Furthermore, a slight increase of the EVM values is observed for larger subcarrier spacing values because the density of pilots is lower for these configurations and thus the equalization process performs worse.

Moreover, both graphs show that the OPLL configuration of 1000 kHz is the best case in terms of EVM because the used RF-pilot-assisted technique compensates the phase noise better due to the PSD shape of this OPLL configuration (see graph of Fig. 2 (b)). The EVM results are below the 5G EVM threshold: 12.5 % and 8 % for 16-QAM and 64-QAM, respectively. Thus, all the evaluated numerologies fulfill the 5G requirements. However, the subcarrier spacing configurations between 60–240 kHz exhibit better performance than the 15 and 30 kHz cases. 3GPP 5G standard recommends to employ subcarrier spacing values of 60, 120, and 240 kHz for bearer frequencies above 6 GHz [4]. Therefore, the experimental results of this work consolidate the aforementioned 5G recommendation.

4. Conclusions

An ARoF system based on OPLL K-band mm-Wave generation has been experimentally validated. Different OPLL configurations and all 5G NR numerologies have been evaluated through this setup. Moreover, the RF-pilot-assisted technique has been employed to mitigate the relatively high phase noise level originating from the OPLL technique. Our experimental results satisfy the 5G requirements for both 16-QAM and 64-QAM constellations. Thereby, the viability of using the OPLL technique for mm-Wave generation is proven in ARoF systems oriented towards 5G. Hence, this work supports ARoF as a suitable solution for the fronthaul in the 5G architecture and beyond.

Acknowledgments This work has been supported by blueSPACE (GA no. 762055) and the 5G STEP FWD (GA no. 72242) projects funded by the European Union's Horizon2020 research and innovation program.

References

1. S. Rommel *et al.*, "Towards a Scaleable 5G Fronthaul: Analog Radio-over-Fiber and Space Division Multiplexing," *J. Lightw. Technol.*, vol. 38, no. 19, pp. 5412–5422, 2020.
2. J. Perez Santacruz *et al.*, "Analysis and Compensation of Phase Noise in mm-Wave OFDM ARoF Systems for Beyond 5G," *J. Lightw. Technol.*, 2020, in press.
3. I. Degli-Eredi *et al.*, "Millimeter-wave Generation Using Hybrid Silicon Photonics," *Journal of Optics*, 2020, in press.
4. 3GPP, 3rd Generation Partnership Project; Technical Specification Group Radio Access Network; Study on New Radio (NR) access technology. 3GPP TR 38.912, version 16.0.0, 2020.
5. A. Delmade *et al.*, "OFDM Baud Rate Limitations in an Optical Heterodyne Analog Fronthaul Link using Unlocked Fibre Lasers," 2019 International Topical Meeting on Microwave Photonics (MWP), Ottawa, ON, Canada, 2019.

P7: Optical Phase-Locked Loop Phase Noise in 5G Mm-Wave OFDM ARoF Systems

D. Dodane, **J. P. Santacruz**, J. Bourderionnet, *et al.*, “Optical Phase-Locked Loop Phase Noise in 5G mm-Wave OFDM ARoF Systems,” *Optics Communications*, vol. 526, p. 128 872, Aug. 2022, [under review, format in preliminary version for review]. DOI: 10.1016/j.optcom.2022.128872



Optical phase-locked loop phase noise in 5G mm-wave OFDM ARoF systems

Delphin Dodane^a, Javier Pérez Santacruz^{b,*}, Jerome Bourderionnet^a, Simon Rommel^b, Gilles Feugnet^a, Antonio Jurado-Navas^c, Laurent Vivien^d, Idelfonso Tafur Monroy^b

^a Thales Research & Technology, 1 avenue Augustin Fresnel, 91767 Palaiseau Cedex, France

^b Institute for Photonic Integration, Eindhoven University of Technology, 5600MB Eindhoven, The Netherlands

^c Wireless Optical Communications Lab., University Institute of Telecommunication Research (TELMA), University of Málaga, CEI Andalucía Tech., Málaga E-29071, Spain

^d Université Paris-Saclay, CNRS, Centre de Nanosciences et de Nanotechnologies, 10 boulevard Thomas Gobert, 91120 Palaiseau, France

ARTICLE INFO

Keywords:

5G
Phase noise
OPLL
ARoF
OFDM
Mm-wave

ABSTRACT

The use of millimeter-wave (mm-wave) frequencies is required in order to support the increasing number of connected devices expected from the fifth generation (5G) of mobile communications. Subsequently, the generation of radio-frequency (RF) carriers ranging from 10 GHz to 300 GHz and their transport through optical distribution network (ODN) is a key element of the future 5G fronthaul. Optically assisted RF carrier generation is one of the most promising solutions to tackle this issue, allowing a wide use of analog radio-over-fiber (ARoF) architectures. However the main limitation of these optical methods is related to the finite coherence of lasers sources, which can dramatically degrade data transmission in analog formats. To mitigate its impact, the use of orthogonal frequency-division multiplexing (OFDM) as the 5G standard allows employing efficient phase noise compensation algorithms. Therefore, in this study, we present an experimental demonstration of a mm-wave generation technique based on an optical phase-locked loop (OPLL) that fulfills the frequency specifications for 5G. Then, an algorithm is introduced that improves data recovery at reception and reduces the impact of a possible high phase noise carrier. Finally, a back-to-back data transmission experiment is performed, demonstrating the efficiency of the algorithm to reach the 5G requirements. These results emphasize the use of OPLLs as a viable solution to generate mm-wave carriers for 5G and beyond.

1. Introduction

The fifth generation (5G) of mobile communications has been thought to support one of the widest increase in data rate in telecom history [1], namely the incoming internet of things (IoT) and its underlying galaxy of connected devices. These non-human users, or let say machines, are expected to constitute the major part of the data exchanges within the 2020 decade [2], and the current network architecture is not capable to satisfy such a high demand. One of the reasons is that usual frequency bands are already fully occupied in many countries and the natural solution to solve this is to look toward the next available bands: mm-wave frequencies (<300 GHz) [3,4]. The benefits are obvious since there is tens of times more available spectrum than in the traditional sub-6 GHz frequency range. However, the shorter range of mm-wave, despite allowing massive paralleling and optimized spatial efficiency [5,6], sets always more stringent constraints in terms of consumption, compactness and costs [7]. This statement emphasizes the limits of the current widespread digital radio-over-fiber (DRoF) architecture and especially its lack of scalability toward the increasing number of cells [8]. Therefore the hardware implementation of the

fronthaul network has to be re-thought, leading to a progressive shift from digital to analog radio-over-fiber (ARoF) [9–11].

The utilization of ARoF supports the need for highly scalable low-complexity mm-wave cells, which number will rise substantially due to their short range (<200 m), resulting in network densification. While allowing few technologies to be more efficient, as for instance spatial division multiplexing (SDM) and phase array antennas (PAA), ARoF is able to handle with both the need for simple and compact remote units (RU) and a more complex analog processing [12]. It relies on the centralization of all the processing in the central office (CO), including digital-to-analog (DAC) conversion, in order to feed mm-waves cells with a “ready-to-emit” signal. The cornerstone of this architecture is actually to replace a mm-wave RF source at the RU by a remote-fed optical local oscillator (LO) that can be sent through the optical distribution network (ODN) together with the processed data.

Yet, mm-wave optical LO generation is challenging because the RF emitted signal results from the beating of two optical tones, which usually results in a rather low purity RF carrier compared to electronic sources. A diversity of methods already exist to deal with optically

* Corresponding author.

E-mail address: j.perez.santacruz@tue.nl (J.P. Santacruz).

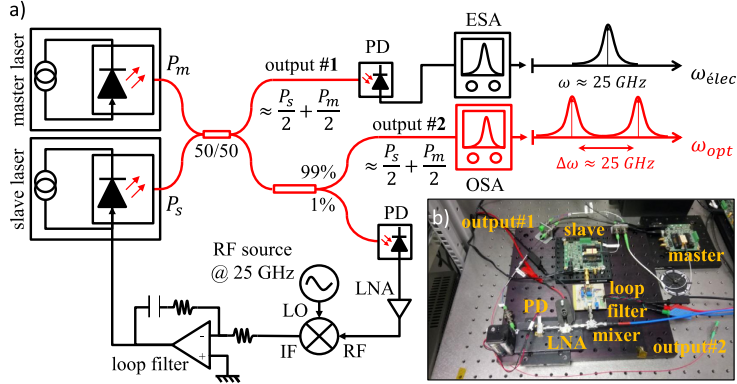


Fig. 1. (a) Description of the OPLL setup and b) picture of the experiment. Optical parts of the setup are depicted in red and electrical ones in black. PD: photodiode, LNA: low-noise amplifier, OSA/ESA: optical/electrical spectrum analyzer.

assisted mm-wave generation, among which self-heterodyne solutions are very common, as for instance suppressed-carrier Mach-Zehnder modulators (SC-MZMs) [13,14], mode-lock lasers (MLLs) or various other frequency combs [15]. As these methods generate intrinsically multiple optical carriers they require also amplifiers as well as filters to get rid of unwanted harmonics. On the other hand, purely heterodyne methods utilize optical tones from different lasers, generally implying to tackle with phase noise issues [16,17]. However, recent progress in the field of integrated semiconductor lasers (SCLs) shows very promising results, allowing fabricating compact high-power low-linewidth sources [18,19]. Another well-known heterodyne approach is to make two sources artificially coherent through the use of an optical phase lock loop (OPLL) [20–25]. This method is derived from SCL frequency stabilization mechanisms and benefits from a high available optical power, even though it is very dependent from feedback electronics and exhibits generally higher phase noise than self-heterodyne techniques.

Moreover, the 5G adopted standard being OFDM, phase noise of the mm-wave carrier becomes an even more stringent requirement to maintain orthogonality between subcarriers [26,27]. To solve this, two approaches are to be considered: the development of lower phase noise sources and the improvement of transmission robustness by the mean of compensation methods. In the latter, OFDM properties are combined with numerical algorithms to recover data even with high carrier phase noise. By mitigating the impact of optical coherence these algorithms are a path to relax the constraints on sources purity [28], allowing a widespread use of cheap and common laser sources in OFDM mm-wave transmissions. In particular this can be used to make OPLLs a better candidate for the generation of remote-fed optical LOs and it represents a very promising and viable method for the new 5G AroF fronthaul.

In this manuscript we first present in Section 2 an OPLL implementation that allows generating two high-power locked optical tones for mm-wave carriers with offset frequencies up to 25 GHz (K-band) based on commercially available solutions. We also discuss the interest of using an OPLL compared to other methods, based on their respective phase noise performances. Section 3 will be dedicated to the description of a new phase noise compensation algorithm aimed to reduce the impact of phase noise over OFDM and complex data formats. Moreover, the proposed algorithm will be compared with a more traditional method for compensating the phase noise. Then, in Section 4, we apply algorithms depicted in Section 3 to the OPLL of Section 2 in order to evaluate how much of the intrinsic OPLL phase noise can be mitigated in the scope of a mm-wave transmission in the K-band. Finally, Section 5 will provide some remarks as well as perspectives toward future work.

2. Optical phase lock loop

The OPLL implemented in this work has been previously used in another transmission experiment [8], including multi-core fiber and free space transmission with real-time processing. However, results have shown that it was not suitable in that case, the OPLL phase noise being still too high for real-time processing. The main goal of this work is then to demonstrate that a dedicated digital signal processing (DSP) can circumvent this issue and make the OPLL suitable for 5G fronthaul. In this section, we will first describe the experimental implementation of our OPLL based on commercially available bulk components and working in the K-band carrier frequencies. Then, an evaluation of the phase noise performance of the loop is carried out to quantify accurately the amount of noise that has to be overcome by the mitigation algorithms. It is also compared with phase noise in several mm-wave optically assisted generation methods and a discussion on the interest of using an OPLL for OFDM transmission in AroF is carried out.

2.1. OPLL setup

In its electrical version, the phase lock loop (PLL) [29] has become a widespread technique to deal with clock signals synchronization, frequency up-conversion and demodulation. The OPLL is no more than its optical equivalent and is aimed to compensate the phase noise difference between two laser sources. The resulting beating of both sources is then apparently “free” from phase noise since the sources are made artificially coherent within the operating bandwidth (BW) of the loop.

The overall setup is described in Fig. 1 and is aimed to up-convert an OFDM signal from baseband (BB) to mm-wave n258 band, centered at 25 GHz. It is built using two commercial 1.55 μm distributed feedback (DFB) lasers manufactured by Gooch & Housego (100 kHz linewidth, up to 100 mW optical power). These DFB lasers are butterfly-packaged and driven using low-noise current sources commercially available from Koheron. The main assets of the current drivers are their relatively small footprint ($7.5 \times 8.5 \text{ cm}^2$), which limits the loop propagation delay, and their modulation entry allowing a dynamic frequency tuning up to 10 MHz. DFB lasers are thermally tuned so that their frequency offset matches the desired mm-wave carrier frequency and then optical signals are mixed using fiber couplers. In order to minimize propagation delay within the feedback loop, these couplers have been shortened down to $\approx 20 \text{ cm}$ each (including coupler itself, fibers and pigtails). A 2×2 coupler operates the mixing and ensures both tones are in quadrature while a 99/1 coupler is used to extract a small portion of the optical power to operate the feedback. This setup provides two

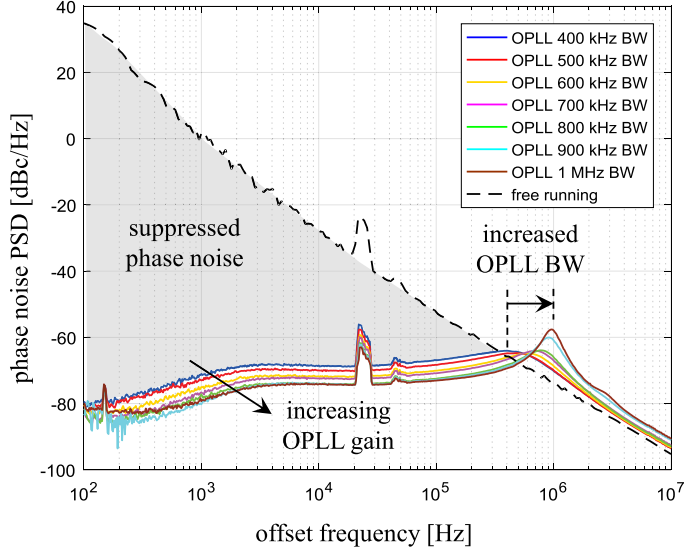


Fig. 2. Experimental measurements of the single sideband (SSB) OPLL phase noise for different open loop gains/BW. Beating is centered on 25 GHz. Gray area represents the suppressed phase noise compared to free running operation.

equivalent outputs that can be used independently. In Section 4 for instance one will feed the transmission experiment while the other will monitor the locking. The 1% output serves as error signal and is sent on a high-speed photodiode (PD), followed by a low-noise amplifier (LNA) and a wide-band mixer which role is to down-convert the error signal to baseband. Finally, the error signal is fed trough a single-amp proportional integral (PI) corrector and applied to the modulation entry of the laser driver. At maximum power working point OPLL outputs deliver 100 mW each, which means a total of 23 dBm available optical power. Such an implementation consists in delivering a locked two-tones high-power optical signal which can be utilized in many ways: it can be sent to remote unit to serve as an RF LO [8,11], it can also be directly modulated with data or for instance be filtered in order to process one of the tone while keeping the coherence with the second tone for a final beating. Finally, it can be combined with complex photonic integrated circuits (PICs), as for instance an optical beamforming network [30], in the context of future 5G and beyond fronthaul. The main asset is to have a powerful coherent input that can be split into several paths without using fibered amplifiers nor on-chip semiconductor amplifiers.

2.2. OPLL performance

As the OPLL described in the previous section is based on DFB lasers then it is necessary to operate the feedback on the laser gain section. Yet, it is well-known that this intrinsically limits the OPLL BW [31]. Indeed, a competition between thermal and carrier tuning of the laser frequency takes place in the DFB laser and the switch between them occurs in the MHz range, reversing the sign of the feedback [32,33]. This cannot be easily nor efficiently overcome and that is why it represents an intrinsic limit of the loop. However, the loop performance can be dramatically lowered by another factor, namely the loop delay, which can be even more limiting than the laser frequency tuning. Here, as mentioned earlier, great care has been taken to shorten the optical path within the feedback loop. This results in a loop delay of the order of 25 ns, that is low enough to make the laser becoming the limiting factor. Then, in the following, the maximum OPLL BW achieved with this implementation is no more than 1 MHz, which is lower than

what can be done for instance with sampled-grating distributed Bragg reflector (SG-DBR) lasers [34,35].

The operating range of the OPLL is dependent from each component BW and in particular PD, LNA and mixer. In the current implementation the locking has been demonstrated from 17 GHz to 26 GHz, which are the lower BW of the LNA and the upper BW of the PD, respectively.

Finally, the OPLL implemented here is perfectly stable over long times which makes it proper to transmission experiments and phase noise measurements, especially in the region close to carrier frequency (here down to 100 Hz). Such a measurement is done using an electrical signal source analyzer (Keysight E5052B, equipped with its 26 GHz down-converter) fed with one of the OPLL outputs through a high-speed PD. We present in Fig. 2 measurements of the locked OPLL phase noise for various loop gains, leading to a set of OPLL BW ranging from 400 kHz to 1 MHz. The optical phase noise of the free running beating tone of the lasers is also shown (dot curve) and thus one can observe that the OPLL suppresses a high amount a phase noise (gray area) compared to the free-running operation. The peak in the phase noise located around 20 kHz offset frequency is an electronic noise coming from the driving circuitry. The equation giving the locked phase noise of the beating shown in Fig. 2 is the following [36]:

$$S_{\phi}^{OPLL}(\nu) = (S_{\phi_m}(\nu) + S_{\phi_s}(\nu)) \cdot |1 - H(2i\pi\nu)|^2 + S_{\phi_{RF}}(\nu) \cdot |H(2i\pi\nu)|^2 \quad (1)$$

with indexes m and s referring to master and slave respectively, H being the closed loop transfer function and $S_{\phi_{RF}}$ the phase noise of the RF source. The effect of an increasing open loop gain (equivalent to $H \rightarrow 1$) on the phase noise of the beating is clearly shown in Eq. (1) and Fig. 2: the higher the gain the lower the optical phase noise of the beating, especially at low offset frequencies. The counterpart is that the OPLL is pushed toward its stability limit, resulting in the appearance of a peak in the phase noise. This defines the actual BW of the loop, i.e. the offset frequency at which the open loop transfer function becomes lower than unity. Above this particular frequency the beating tone phase noise progressively tends toward the free-running phase noise. That peak appears to be problematic because its contribution to the total phase error variance of the beating is high. Indeed, the single

Table 1

Phase error variance values for various OPLL BW. Integration is made from 100 Hz to 10 MHz.

OPLL BW [kHz]	400	600	700	900	1000
σ_φ^2 [rad ²]	0.3266	0.2949	0.3395	0.5885	0.8025

sideband (SSB) phase error variance is related to the phase noise power spectral density (PSD) by the following relation [37]:

$$\sigma_\varphi^2 = \int_0^\infty S_\varphi(\nu) d\nu \quad (2)$$

Since optical phase noise tends toward zero at high frequencies from the carrier, then Eq. (2) implies that phase error variance tends asymptotically toward a finite value, which is mostly imposed by the peak located around the loop BW in our case (see Fig. 2 brown curve around 1 MHz). Some phase error variance values for different OPLL BW are given in Table 1 (integrated from 100 Hz to 10 MHz), from which we can see that σ_φ^2 is more than doubled when in stability limit compared to great stability/low BW. Yet it has to be compared to the free running phase error variance which is 1.77×10^5 rad² (from the dot curve of Fig. 2), proving that the OPLL method can considerably reduce the phase noise of an heterodyne beating even for high phase noise lasers.

2.3. Performance comparison with other optical two-tone generation techniques

To give an interpretation of our OPLL performances described in the previous subsection we have to remind that our aim is to mitigate an heterodyne optical beating tone phase noise using specific algorithms. This approach can also be applied to a completely free running lasers beating. In our case, and presumably using any semiconductor lasers with higher linewidths, this will lead to a beating phase noise much too high to be mitigated by our algorithms.

One of the reasons is linked to the low offset frequency part of the phase noise (< 1 kHz), which actually describes the slow frequency drift of the beating tone and has to be kept low to satisfy the 5G standard [38]. For the sake of comparison, we measured the free beating tone of very pure fiber lasers (NKT photonics E15, < 10 Hz linewidth) over the same offset frequency range (100 Hz to 10 MHz) and found 14 rad², namely one to two orders of magnitude higher than levels showed in Table 1. The main contribution to this value is located at few hundreds Hz offset frequency and below. The advantage of the OPLL regarding this point is that it cancels the lower part of the free running phase noise, getting rid of the slow frequency drifts. Ultimately, the OPLL phase noise is limited by the purity of the RF source used to down-convert the error signal within the loop (Eq. (1)). This basically means that slow variations of the locked optical beating reproduce those of the RF source, which is extremely stable over time. A comparison of performances, advantages and drawbacks of some mm-wave generation methods are listed in Table 2.

The other main reason is more obvious and is linked to phase noise for offset frequencies above 1 kHz: these variations are fast enough to make the phase fluctuate within the duration of one OFDM symbol, which can severely impact the transmission. That is why the phase error variance, and consequently the phase noise of the laser sources, is critical for data transmission with analog modulation formats like QAM because the information is partially encoded into the phase of the transmitted signal. As a consequence a high carrier phase noise can lead to wrong interpretation of a transmitted bit, with high order modulation being even more sensitive. In addition to this, the OFDM method relies on the orthogonality between subcarriers which condition is also dependent on phase noise in order to be kept valid. Usually it is considered that a 10° standard deviation (0.03 rad²) over a frequency range from 1 kHz to 1 GHz is a reasonable target [24], which is one

Table 2

Comparison between various approaches for generating optical two-tone signals.

Criteria	Free-running lasers	OPLL	Ext. modulation
Phase error variance ^a in rad ²	> 14 ^b	≈ 0.5	typ. 10 ⁻⁴ to 10 ^{-5c}
Power efficiency	Very high	High	Low
Frequency range	< 100's THz	10's GHz	10's GHz
Architecture complexity	Low	Medium	High

^aFrom 100 Hz to 10 MHz.

^bWith commercially available sources.

^cFor a commercial RF source in the mm-wave.

order of magnitude below the best performance of our implementation. To face this, self-heterodyne methods like external modulation by using MZMs are interesting because they will reproduce not only slow phase variations but the whole phase noise spectrum of the RF source. This will lead to an overall much better phase noise performance though it is still limited in terms of architecture complexity. For instance it is heavily dependent on optical filtering and amplifiers, as well as equalizing optical paths to keep optical coherence. These aspects are also included in Table 2.

Taking into account all points listed in the Table 2 we considered that using a self-heterodyne method, even though it gives better phase noise, requires too many elements and is a less flexible approach for 5G fronthaul. On the contrary, free beating is the simplest solution but still suffers from phase noise issues at frequencies close to the carrier, even for low linewidth lasers. Our approach, using an OPLL, is to benefit from both methods to get a highly stable beating combined with great flexibility and high available power. The choice of DFB laser diodes is driven by the will to use commercial low cost and small footprint components at the expense of the phase noise, which has then to be mitigated to lower its impact on the OFDM transmitted signal. This will be done using compensation algorithms, which are described in the next section.

3. Phase noise compensation methods

Phase noise compensation has already been performed in optical coherent systems [39,40]. Nonetheless, in the research literature of optical communications, single-carrier (SC) modulation formats are mainly utilized. The signal degradation induced by the phase noise in SC modulation formats is less than in multi-carrier (MC) signals such as OFDM. This is because the symbol duration of SC modulation formats is typically shorter than in the OFDM scenario. Moreover, OFDM signals suffer from severe impairments due to phase noise. As high phase noise levels are associated with optically assisted mm-wave generation, it is then one of the major performance limiting factors for using this method within OFDM systems. Thus compensation techniques are more complex in mm-wave OFDM scenarios. The works of [41–43] are examples of OFDM transmission over a mm-wave ARoF setup. However, in these works, the employed subcarrier spacing of the transmitted OFDM signal is larger than in the 5G numerology, lowering phase noise impact. The investigation carried out in [44] aims to bring experimental assessments on the transmission of OFDM signals with 5G numerology over a mm-wave ARoF setup under different phase noise levels. To go further, the work we present here is, to the best of the authors' knowledge, the first experimental demonstration of OFDM signal transmission with 5G numerologies over a mm-wave ARoF setup based on OPLL two-tone generation. Since phase noise is the main impairment due to the use of 5G numerologies and OPLL configuration, the utilization of DSP algorithms to compensate for the phase noise is essential for proper communication performance.

This section explains the fundamentals of the used methods to compensate the phase noise produced by the aforementioned OPLL implementation. In particular, two digital signal processing methods are utilized: RF-pilot assisted method and a novel algorithm named hybrid scattered pilots with decision feedback (SPDF). In this section,

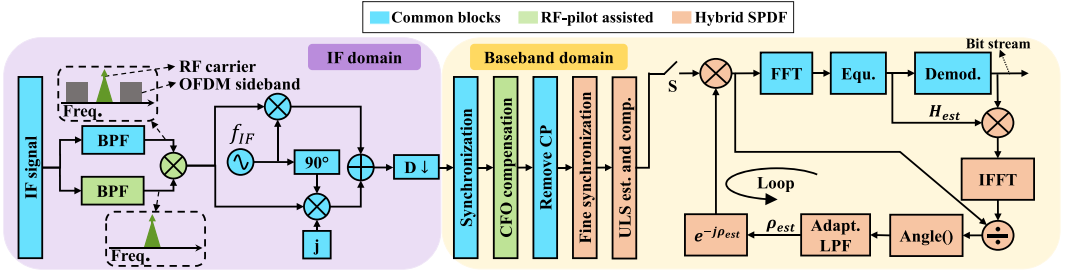


Fig. 3. DSP block diagram in the receiver side for both employed algorithms to compensate the phase noise: RF-pilot assisted (green) and hybrid SPDF methods (orange). Blocks depicted in green and orange are exclusive to the related employed method while blue blocks are common for both.

we describe these two methods, while in next section we will compare their performances using the OPLL transmission setup.

The RF-pilot assisted method relies on using the carrier associated with the modulated signal to compensate for the phase noise at the receiver side. It can be applied to any modulation format and is also used for instance in [45]. However, the RF-pilot assisted method introduces an additional process in the intermediate frequency (IF) domain, increasing the complexity of the system because a higher number of samples are processed in this domain, with respect to BB domain. Furthermore, the RF-pilot assisted method requires to transmit the RF tone through the transmission channel, reducing the available bandwidth, which is already highly limited in wireless scenarios. Moreover, transmitting the RF tone reference throughout the communication system increases the overall power of the transmitted signal, which reduces the power level of the data signal at the output of devices such as RF amplifiers and RF mixers. For proper extraction of the phase noise by using the RF-pilot assisted method, the signal-to-noise ratio (SNR) level of the received RF reference carrier must be sufficiently high. Therefore, there is a trade-off between SNR of the received data signal and phase noise compensation efficiency of the RF-pilot assisted method.

For a mm-wave mobile scenario, the RF reference carrier is needed to be sent through wireless channel if applying the RF-pilot assisted method. This fact implies a reduction of the spectrum efficiency, which is quite important in wireless communications. Another drawback of the RF-pilot assisted method is that it operates in the IF domain, increasing the sampling rate requirements in the case of a DSP implementations. Besides, low received power is one of the major limitations in mm-wave wireless. Thereby, all the mentioned drawbacks related to the RF-pilot assisted method make baseband DSP algorithms for phase noise compensation a more suitable option for mm-wave wireless systems, as it does not require any RF tone reference.

As a parallel solution, we present a hybrid SPDF algorithm that operates only at baseband and do not require an RF reference carrier, being more well-suited for mm-wave wireless communications than the aforementioned RF-pilot assisted method. Furthermore, DSP in the IF domain is not needed and analog-to-digital converters (ADC) with lower sampling frequency can be used. However, this hybrid SPDF can only be applied to OFDM signals, combining two strategies to estimate the phase noise [46]: a coarse initial phase noise estimation is performed using the scattered pilots of the OFDM signal and, then, a fine phase noise estimation is achieved by applying decision feedback in the received OFDM signal. By targeting a determined error vector magnitude (EVM) output value, this decision feedback method is more flexible in terms of complexity to mitigate the phase noise than the scattered pilots method because it can be iteratively performed in a loop [44,46]. Therefore, once the EVM target value is reached, the loop procedure can be finalized. The employed strategy of the decision feedback methods is based on recovering the time-domain transmitted signal to estimate the phase noise. Nevertheless, iterative decision

feedback methods often suffer from convergence issues because its performance is intrinsically related to the initial bit error rate (BER) of the received signal. In the other hand, scattered pilots algorithms are more robust since they do not depend on the received BER. Therefore, a scattered pilots method can be performed before a decision feedback method to combine the benefits of both strategies: robustness, accuracy, and flexibility in the phase noise estimation. These are the reasons why hybrid SPDF is proposed as a suitable solution to compensate the inherent high phase noise of mm-wave OPLL systems for an OFDM communication.

In our implementation, the unconstrained least-squares (ULS) approach is the chosen scattered pilot method to obtain an initial phase noise estimation by using the discrete cosine transform (DCT) [47]. Yet, there exists other scattered pilot algorithms that could have also been implemented in our hybrid SPDF [46]. Concerning the decision feedback method, some previous work on the topic [44] will be adapted and can prove to be very effective here because it synergizes well with the OPLL dynamic behavior by the mean of an adaptive low-pass filter (LPF).

Fig. 3 shows the DSP receiver block diagram employed to perform the aforementioned algorithms. This receiver process assumes an OFDM signal with an IF at the reception. In Fig. 3, the cyan blocks correspond to the common blocks for both algorithms. The green and orange blocks refer to the particular processing for the RF-pilot assisted and the hybrid SPDF methods, respectively. First, in the IF domain, the IF signal is filtered by a band-pass filter (BPF), keeping the RF carrier and one of the OFDM sidebands. If RF-pilot is applied then the IF signal is split into a secondary branch, where the sole RF-tone is obtained by filtering the rest of the frequency components with a second BPF [45]. Then, the isolated RF-tone can be multiplied by the IF signal of the other branch, compensating the phase noise contained in this RF-tone. Next, an IF demodulation and down-sampling processes are performed to convert the IF signal into the baseband domain. The IF domain exposed in Fig. 3 can be done by hardware, reducing the requirements for the DACs. However, a specific narrowband BPF must be designed in the RF-pilot assisted case.

Now in the baseband domain of Fig. 3, a synchronization process is performed by employing the preamble of the transmitted signal. Then, a coarse frequency offset (CFO) compensation is used when applying the RF-pilot assisted method because this method only reduces the signal deterioration due to the phase noise [45]. On the other hand, the hybrid SPDF method can avoid the CFO compensation because this method compensates both phase noise and frequency offset (FO). Next, the cyclic prefix (CP) of the OFDM signal is removed. Finally, for the RF-pilot assisted method, the classical OFDM receiver is performed, namely fast Fourier transform (FFT), frequency-domain channel equalization, and final demodulation. The zero-forcing technique is the selected channel estimation method due to its simplicity. For the hybrid SPDF, an initial phase noise estimation is achieved using the ULS algorithm. However, a fine synchronization must be performed before

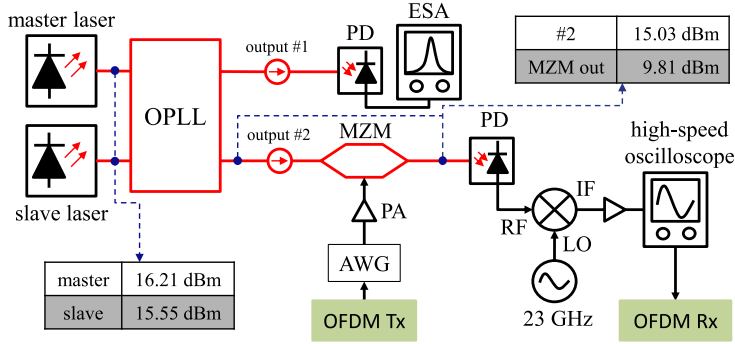


Fig. 4. Description of the OFDM setup. The OPLL output is intensity modulated using an arbitrary waveform generator fed with the OFDM Tx signal. An oscilloscope is used to make the acquisition of the Rx down-converted signal.

this initial estimate because the ULS algorithm is highly sensitive to synchronization errors. This fine synchronization process is realized by calculating the time position of the first ray in the estimated impulse channel response. After the ULS process, the decision feedback loop is realized for the hybrid SPDF method. The procedure of this loop aims to estimate and compensate the residual phase noise that was not compensated in the ULS block. The strategy to compensate for the phase noise in the decision feedback loop consists of estimating the transmitted OFDM signal. With the estimate of the OFDM transmitted signal, the phase noise can be estimated later by performing an inverse process than that of the communication channel [44]. Hence, the phase noise estimate is improved by using an LPF whose spectrum shape is linked to the phase noise PSD [44]. The filtered phase noise estimate is then used to compensate the received OFDM signal. As a consequence, when performing another iteration in this loop, the number of errors after the demodulation block is lower than in the initial iteration and a better phase noise estimate can be obtained. Thereby, this decision feedback loop can be iterated to improve the final yields. Furthermore, better performance can be achieved if spectrum shape of the inner LPF of the loop is modified according to the number of iterations.

4. Experimental study of OPLL phase noise impact on OFDM mm-wave transmitted signal

In this section, we will first describe how the OPLL from Section 2 is implemented into an OFDM back-to-back experiment. Then, the obtained results are analyzed through the use of the phase noise compensation method described in Section 3 to study the intrinsic tolerance of OFDM to the OPLL phase noise.

4.1. Experimental setup

The experimental setup is described in Fig. 4 and is constituted as follows: one of the OPLL outputs is used to monitor the locking through the use of a PD, and the other output is fed through a Mach-Zehnder modulator to encode the OFDM data. The data are generated by the mean of an arbitrary waveform generator (AWG) (Tektronix 25 GSa/s) and its spectral band is centered on 1 GHz IF frequency. A power amplifier (PA) is used to drive the modulator, which is biased at its quadrature point. Then, the modulated signal is directly detected with a high-speed PD and down-converted with a mixer to ≈ 2 GHz in order to avoid spectral aliasing. The obtained temporal trace is then post-processed with the phase noise compensation algorithm described in Section 3.

The signal analyzed here is the one which would be transmitted to a RU for free space emission in a real fronthaul scheme. Potential phase fluctuations due to fiber dispersion and free space propagation

Table 3
OFDM configuration parameters.

Config.	1	2	3	4	5
Δf [kHz]	15	30	60	120	240
N	2^{14}	2^{13}	2^{12}	2^{11}	2^{10}
T_{cp} [μ s]	4.8	2.4	1.2	0.6	0.3

are not accounted here as our goal is to study the OPLL contribution to phase noise of the RF carrier. Yet, the aforementioned contributions are typically small compared to OPLL phase noise in our case. In order not to saturate the PD used to convert the K-band Tx signal, the OPLL setting point is fixed approximately at half the maximum power of the lasers. While the phase noise of the lasers is slightly lower in this case, most of the difference is due to thermal effects happening at high currents. These effects are located at frequencies close to the carrier and are perfectly corrected by the loop so that the OPLL phase noise is the same whether it is used at half or maximum optical power. Optical powers measured at the different stages of the setup are shown in Fig. 4.

The different phase noise configurations that will be investigated here corresponds to BW of 400 kHz, 700 kHz and 1 MHz, with a maximum factor of 2.5 in their phase error variances. Modulation formats used in the experiment are 16-QAM and 64-QAM, for all 5G subcarrier spacings (15, 30, 60, 120 and 240 kHz) [38]. The main parameters of the different employed OFDM numerologies are shown in Table 3: subcarrier spacing (Δf), total number of subcarrier (N), and CP period (T_{cp}). For all the OFDM configurations, the total BW is 245.76 MHz, the percentage of active subcarriers is 80.5 %, and one pilot subcarrier is inserted on every 12th active subcarrier.

4.2. Experimental results

For each of the tested configurations described above we performed a set of different measurements in order to have significant statistical evaluation. Figs. 5 and 6 show the experimental results for both receiver algorithms applied to the OPLL transmitted OFDM signal: Fig. 5 corresponds to the RF-pilot assisted method while Fig. 6 refers to our hybrid SPDF method.

The experimental results using the RF-pilot assisted method are presented in terms of EVM in percentage as a function of subcarrier spacing, for different bandwidths of the OPLL loop filter (see Fig. 5). Moreover, 16-quadrature amplitude modulation (QAM) and 64-QAM constellations are also presented in Fig. 5(a) and (b), respectively. From Fig. 5, it can be noticed that the EVM decreases as the subcarrier spacing value increases. This is explained by the fact that lower subcarrier spacing is more prone to interference [44]. It can also be noticed that there is a slight increment of the EVM for 240 kHz of subcarrier spacing. The reason of this EVM behavior is due to the large frequency

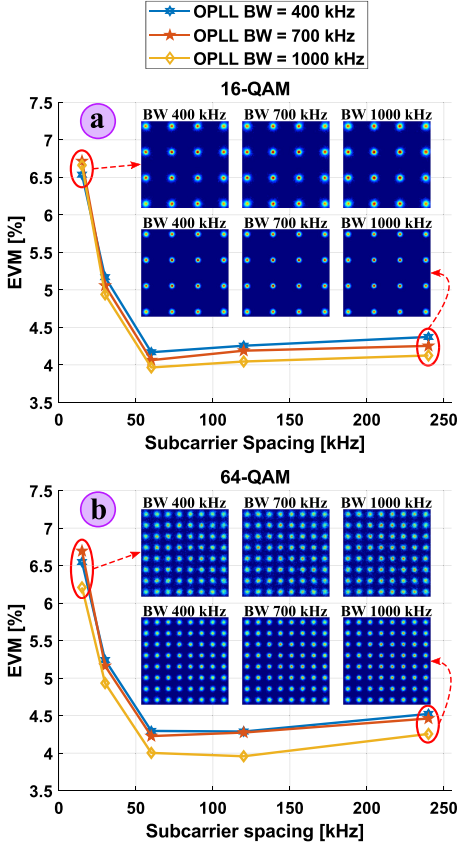


Fig. 5. Experimental results employing the RF-pilot assisted method of Section 3. The results are presented in terms of EVM as a function of the subcarrier spacing for different modulation orders (16-QAM and 64-QAM). These results are also compared concerning the bandwidth of the loop filter in the OPLL block.

spacing between pilots and the lower total number of pilots for higher subcarrier spacing values, leading to a poorer channel estimation. Furthermore, in Fig. 5, the distribution of the constellation points are depicted for the different OPLL configurations and for subcarrier spacing values of 15 kHz and 240 kHz. The experimental EVM results by applying the RF-pilot assisted method are under the EVM 5G threshold for both used modulation orders (12.5% for 16-QAM, and 8% for 64-QAM [38]). In addition, one can notice that EVM is slightly better for 1 MHz OPLL BW, although its phase error variance is higher. This behavior could be due to the lower carrier phase noise within the BPF BW used to isolate the RF tone.

The graphs of Fig. 6 are the experimental results obtained by employing the proposed hybrid SPDF method with 16-QAM modulation format. These results are presented in terms of EVM as a function of the number of iterations in the decision feedback loop for different BWs of the OPLL and for the different 5G numerologies. In Fig. 6, the iteration zero refers to the EVM in the output of the channel equalizer without any iteration in the decision feedback loop of Fig. 3. Examining Fig. 6, it can be noticed that the EVM decreases with the number of iterations of the decision feedback loop. Therefore, for 16-QAM the decision feedback adequately converges for all the different 5G numerologies

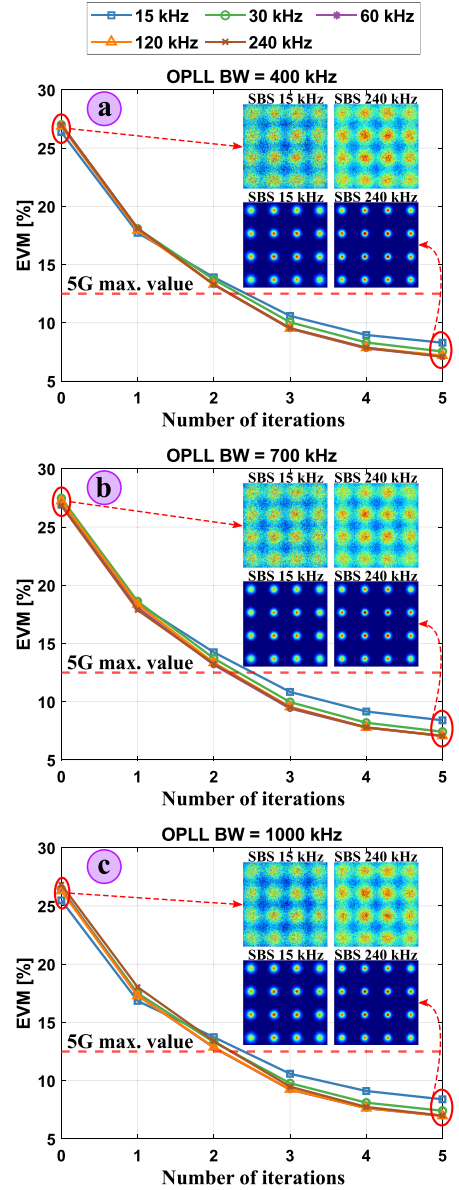


Fig. 6. Experimental results utilizing the hybrid SPDF method of Section 3. The EVM curves are exhibited as a function of the number of iterations of the decision feedback loop for 16-QAM modulation.

and OPLL configurations. On the other hand, the 64-QAM has not been successfully treated with our hybrid SPDF algorithm. This is essentially due to the fact that 64-QAM is more sensitive to phase fluctuations than 16-QAM and the initial constellation, before the first iteration, is too noisy to allow the algorithm to converge. At this stage, the algorithm is still very dependent from the initial EVM to work properly and our OPLL phase noise is not low enough to consistently deal with 64-QAM.

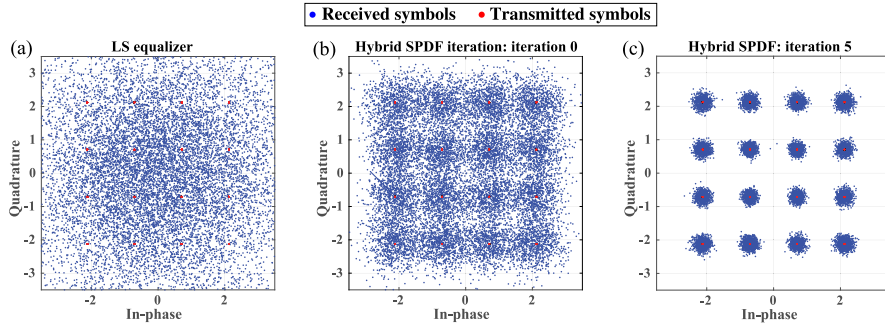


Fig. 7. IQ constellation points for different DSP receivers where the subcarrier spacing is 120 kHz and OPLL loop BW is 400 MHz: (a) standard OFDM receiver with least-squares (LS) equalizer corresponding to the blue blocks of Fig. 3; (b) hybrid SPDF method at iteration zero (after ULS estimation and compensation block of Fig. 3); (c) hybrid SPDF method after five iterations of the feedback loop.

Fig. 7 allows visualizing the BER reduction made by the proposed hybrid SPDF method. The received constellation points of Fig. 7(a) are obtained by using the standard OFDM receiver with least-squares (LS) equalizer (blue blocks in Fig. 3 of the manuscript). In Figs. 7(b) and (c), the hybrid SPDF method is applied with zero and five iterations, respectively. The hybrid SPDF algorithm starts with IQ constellation points similar to those in Fig. 7(a). Then, with the ULS estimation and compensation block, the IQ constellations are as depicted in Fig. 7(b). Consequently, after five iterations in the decision feedback loop, the degradation induced by phase noise is almost completely compensated, as Fig. 7(c) shows. With this IQ constellation evolution through the hybrid SPDF method, the EVM and BER reductions of the proposed phase noise compensation method are clearly illustrated.

It is necessary to highlight that the channel equalizer in the decision feedback loop assumes a flat channel amplitude in order to achieve better performance. This assumption is because the channel of the experimental setup does not include fades in the amplitude. Moreover, the cut-off frequency of the adaptive LPF in the decision feedback loop is set to be 2.5 MHz because the shape of this filter is adequately fitted respecting the OPLL phase noise of Fig. 2. Therefore, the attenuation of this adaptive filter decreases proportionally to the iteration number within the feedback loop from 30 to 5 dB. In this way, reduced restrictiveness of the adaptive filter is obtained and, thus, phase noise is estimated with more accuracy. Furthermore, the number of training pilots used in the ULS block is 35% of the total number of subcarrier pilots in the OFDM symbol [47]. Resulting from all these aspects, for each OPLL and OFDM configurations the number of required iterations of the decision feedback loop is three to accomplish the 5G requirements of 12.5% in 16-QAM, and better performance can be achieved using more iterations. Moreover, distributions of the constellations points are depicted in Fig. 6, for subcarrier spacing values of 15 kHz and 240 kHz and for different number of iterations of the decision feedback loop. This illustrates clearly the effective gain allowed by the hybrid SPDF method after 5 iterations. However, the achieved EVM tends toward a lower limit of the order of 5%–6%, which can be seen as the intrinsic limitation of the OPLL in terms of phase noise. These few percents represent the data that is, in average, not recovered because the added phase error is too high. This can be improved either by a more efficient algorithm or by a lower OPLL phase noise.

Finally, by comparing the graphs of Figs. 5 and 6, it can be determined that for 16-QAM the EVM converge point of the hybrid SPDF method is roughly equal to the achieved EVM using the RF-pilot assisted method (between 4 and 7.5% in every case). Then for this modulation format both methods satisfy the specifications according to 5G numerologies. Yet, concerning 64-QAM, the RF-pilot assisted method is still better due to the intrinsic phase noise of our OPLL being too high. An improved OPLL could be more suited to further

evaluate the SPDF algorithm performance. That being said, the lower complexity at the IF stage of the proposed SPDF method makes it more advantageous in terms of resources from a system point of view. Therefore, this novel hybrid SPDF method is a promising path to be applied in OFDM AroF systems with relatively high intrinsic phase noise, as for instance OPLLs, and using 5G numerologies.

5. Conclusions

In conclusion, we demonstrate in this study that the implemented OPLL is suitable for 16-QAM OFDM 5G data transmission in the n258 range if it is associated with a proper phase noise compensation method. This is a significant improvement compared to our previous experiment [8] where the phase noise was the limiting factor. The proposed OPLL setup allies high available optical power, high stability, standard commercial components and wide operating range as a counterpart of its medium phase noise. To exploit these advantages it is necessary to use a phase noise compensation method at the receiver side in order to mitigate its impact. Both methods used in this study, RF-pilot assisted and SPDF methods, are shown to be efficient enough to compensate the phase noise of the OPLL to meet the 5G requirements in the target frequency band. This has been shown experimentally for 16-QAM for both methods and for 64-QAM modulation format with RF-pilot assisted method. From a hardware point of view, a way to improve the OPLL would be either to use lower phase noise lasers, or to increase the BW of the loop, which is not easy given the fact we use DFB lasers. With a lower loop phase error variance then 64-QAM may eventually converge with the current hybrid SPDF algorithm but this has still to be investigated. As well the algorithm itself can still be improved, especially to make it compatible with real-time processing in order to ensure that enough iterations can be reached within a reasonable time compared to the rest of the processing. While AroF has become one of the major solutions for the new mm-wave 5G fronthaul, the possibility to use relatively high phase noise but flexible implementation such as OPLLs is a very promising path toward future exploitation of mm-wave carriers for mobile communications.

Declaration of competing interest

The authors declare the following financial interests/personal relationships which may be considered as potential competing interests: This work was partially financed by the 5G STEP FWD and blueSPACE projects (GA nos. 722429 and 762055).

Data availability

Data will be made available on request.

Acknowledgments

This work was partially supported by the ITN 5G STEP-FWD and blueSPACE projects which have received funding from the European Union's Horizon2020 research and innovation programme under grant agreements No. 722429 and 762055.

References

- [1] J.G. Andrews, et al., What will 5G be? *IEEE J. Sel. Areas Commun.* 32 (6) (2014) 1065–1082, <http://dx.doi.org/10.1109/JSAC.2014.2328098>.
- [2] Cisco, Visual networking index, 2020, white paper URL <https://www.cisco.com>.
- [3] T.S. Rappaport, et al., Millimeter wave mobile communications for 5G cellular: It will work!, *IEEE Access* 1 (2013) 335–349, <http://dx.doi.org/10.1109/ACCESS.2013.2260813>.
- [4] M. Xiao, et al., Millimeter wave communications for future mobile networks, *IEEE J. Sel. Areas Commun.* 35 (9) (2017) 1909–1935, <http://dx.doi.org/10.1109/JSAC.2017.2719924>.
- [5] A. Macho, M. Morant, R. Llorente, Next-generation optical fronthaul systems using multicore fiber media, *J. Lightwave Technol.* 34 (20) (2016) 4819–4827, <http://dx.doi.org/10.1109/JLT.2016.2573038>.
- [6] C. Roeloffzen, et al., Enhanced coverage through optical beamforming in fiber wireless networks, in: 2017 19th International Conference on Transparent Optical Networks, ICTON, IEEE, Girona, Spain, 2017, pp. 1–4, <http://dx.doi.org/10.1109/ICTON.2017.8025129>.
- [7] J. Liu, M. Sheng, L. Liu, J. Li, Network densification in 5G: From the short-range communications perspective, *IEEE Commun. Mag.* 55 (12) (2017) 96–102, <http://dx.doi.org/10.1109/MCOM.2017.1700487>.
- [8] S. Rommel, et al., Towards a scalable 5G fronthaul: Analog radio-over-fiber and space division multiplexing, *J. Lightwave Technol.* 38 (19) (2020) 5412–5422, <http://dx.doi.org/10.1109/JLT.2020.3004416>.
- [9] D. Che, Analog vs digital radio-over-fiber: A spectral efficiency debate from the SNR perspective, *J. Lightwave Technol.* 39 (16) (2021) 5325–5335, <http://dx.doi.org/10.1109/JLT.2021.3102220>.
- [10] A. Delmède, et al., Optical heterodyne analog radio-over-fiber link for millimeter-wave wireless systems, *J. Lightwave Technol.* 39 (2) (2021) 465–474, <http://dx.doi.org/10.1109/JLT.2020.3032923>.
- [11] J. Brenes, et al., Network slicing architecture for SDM and analog-radio-over-fiber-based 5G fronthaul networks, *J. Opt. Commun. Netw.* 12 (4) (2020) B33–B43, <http://dx.doi.org/10.1364/JOCN.381912>.
- [12] D. Konstantinou, et al., 5G RAN architecture based on analog radio-over-fiber fronthaul over UDWDM-PON and phased array fed reflector antennas, *Opt. Commun.* 454 (2020) 0030–4018, <http://dx.doi.org/10.1016/j.optcom.2019.124464>.
- [13] J. Yu, Z. Jia, L. Yi, Y. Su, G.-K. Chang, T. Wang, Optical millimeter-wave generation or up-conversion using external modulators, *IEEE Photonics Technol. Lett.* 18 (1) (2006) 265–267, <http://dx.doi.org/10.1109/LPT.2005.862006>.
- [14] J. Yao, Microwave photonics, *J. Lightwave Technol.* 27 (3) (2009) 314–335, <http://dx.doi.org/10.1109/JLT.2008.2009551>.
- [15] P.J. Delfyett, et al., Optical frequency combs from semiconductor lasers and applications in ultrawideband signal processing and communications, *J. Lightwave Technol.* 24 (7) (2006) 2701–2719, <http://dx.doi.org/10.1109/JLT.2006.875948>.
- [16] A. Delmède, et al., OFDM baud rate limitations in an optical heterodyne analog fronthaul link using unlocked fibre lasers, in: 2019 International Topical Meeting on Microwave Photonics, MWP, Ottawa, ON, Canada, 2019, pp. 1–4, <http://dx.doi.org/10.1109/MWP.2019.8892190>.
- [17] E.P. Martin, et al., 25-Gb/s OFDM 60-GHz radio over fiber system based on a gain switched laser, *J. Lightwave Technol.* 33 (8) (2015) 1635–1643, <http://dx.doi.org/10.1109/JLT.2015.2391994>.
- [18] K.-J. Boller, et al., Hybrid integrated semiconductor lasers with silicon nitride feedback circuits, *Photonics* 7 (1, 4) (2020) <http://dx.doi.org/10.3390/photonics7010004>.
- [19] M.A. Tran, D. Huang, J.E. Bowers, Tutorial on narrow linewidth tunable semiconductor lasers using Si/III-V heterogeneous integration, *APL Photonics* 4 (11) (2019) 111101, <http://dx.doi.org/10.1063/1.5124254>.
- [20] J.B. Armior, S.R. Robinson, Phase-lock control considerations for coherently combined lasers, *Appl. Opt.* 18 (18) (1979) 3165–3175, <http://dx.doi.org/10.1364/AO.18.003165>.
- [21] U. Gliese, et al., A wideband heterodyne optical phase-locked loop for generation of 3–18 GHz microwave carriers, *IEEE Photonics Technol. Lett.* 4 (8) (1992) 936–938, <http://dx.doi.org/10.1109/68.149915>.
- [22] L. Langley, et al., Packaged semiconductor laser optical phase-locked loop (OPLL) for photonic generation, processing and transmission of microwave signals, *IEEE Trans. Microw. Theory Tech.* 47 (7) (1999) 1257–1264, <http://dx.doi.org/10.1109/22.775465>.
- [23] S. Ristic, et al., An optical phase-locked loop photonic integrated circuit, *J. Lightwave Technol.* 28 (4) (2009) 526–538, <http://dx.doi.org/10.1109/JLT.2009.2030341>.
- [24] K. Balakier, L. Ponnampalam, M.J. Fice, C.C. Renaud, A.J. Seeds, Integrated semiconductor laser optical phase lock loops, *IEEE J. Sel. Top. Quantum Electron.* 24 (1) (2017) 1–12, <http://dx.doi.org/10.1109/JSTQE.2017.2711581>.
- [25] S. Arafin, A. Simsek, M. Lu, M.J. Rodwell, L.A. Coldren, Heterodyne locking of a fully integrated optical phase-locked loop with on-chip modulators, *Opt. Lett.* 42 (19) (2017) 3745–3748, <http://dx.doi.org/10.1364/OL.42.003745>.
- [26] A.A. Zaidi, et al., Waveform and numerology to support 5G services and requirements, *IEEE Commun. Mag.* 54 (11) (2016) 90–98, <http://dx.doi.org/10.1109/MCOM.2016.1600336CM>.
- [27] J.P. Santacruz, S. Rommel, U. Johannsen, A. Jurado-Navas, I.T. Monroy, Candidate waveforms for AroF in beyond 5G, *Appl. Sci.* 10, 3891 (11) (2020) <http://dx.doi.org/10.3390/app10113891>.
- [28] D. Dass, S. O'Duill, A. Delmède, C. Browning, Analysis of phase noise in a hybrid photonic/millimetre-wave system for single and multi-carrier radio applications, *Appl. Sci.* 10, 5800 (17) (2020) <http://dx.doi.org/10.3390/app10175800>.
- [29] F.M. Gardner, *Phaselock Techniques*, John Wiley & Sons, 2005.
- [30] R. Muñoz, et al., Experimental demonstration of dynamic optical beamforming for beyond 5G spatially multiplexed fronthaul networks, *IEEE J. Sel. Top. Quantum Electron.* 27 (6) (2021) 1–16, <http://dx.doi.org/10.1109/JSTQE.2021.3079726>.
- [31] F. Ashtiani, P. Sanjari, M.H. Idjadi, F. Aflatouni, High-resolution optical frequency synthesis using an integrated electro-optical phase-locked loop, *IEEE Trans. Microw. Theory Tech.* 66 (12) (2018) 5922–5932, <http://dx.doi.org/10.1109/TMTT.2018.2878567>.
- [32] W. Liang, A. Yariv, A. Kewitsch, G. Rakuljic, Coherent combining of the output of two semiconductor lasers using optical phase-lock loops, *Opt. Lett.* 32 (4) (2007) 370–372, <http://dx.doi.org/10.1364/OL.32.000370>.
- [33] L.A. Coldren, S.W. Corzine, M.L. Mashanovitch, *Diode Lasers and Photonic Integrated Circuits*, Vol. 218, John Wiley & Sons, 2012.
- [34] L. Ponnampalam, et al., Monolithically integrated photonic heterodyne system, *J. Lightwave Technol.* 29 (15) (2011) 2229–2234, <http://dx.doi.org/10.1109/JLT.2011.2158186>.
- [35] M. Lu, et al., An integrated 40 Gbit/s optical costas receiver, *J. Lightwave Technol.* 31 (13) (2013) 2244–2253, <http://dx.doi.org/10.1109/JLT.2013.2265075>.
- [36] A. Bordonalli, C. Walton, A.J. Seeds, High-performance phase locking of wide linewidth semiconductor lasers by combined use of optical injection locking and optical phase-lock loop, *J. Lightwave Technol.* 17 (2) (1999) 328, <http://dx.doi.org/10.1109/50.744252>.
- [37] L.S. Cutler, C.L. Searle, Some aspects of the theory and measurement of frequency fluctuations in frequency standards, *Proc. IEEE* 54 (2) (1966) 136–154, <http://dx.doi.org/10.1109/PROC.1966.4627>.
- [38] 3GPP, FG IMT-2020: User equipment (UE) radio transmission and reception; part 2: Range 2 standalone. 3GPP TS 38.101-2, version 17.4.0, release 17, 2021.
- [39] K. Zeb, Z. Lu, J. Liu, Y. Mao, G. Liu, P.J. Poole, C. Song, M. Rahim, G. Pakulski, P. Barrios, X. Zhang, A quantum dash mode-locked laser-based photonic aided broadband multi-Gb/s wireless signal delivery system at 5G NR, in: *Broadband Access Communication Technologies XV*, Vol. 11711, 2021, pp. 65–70, <http://dx.doi.org/10.1117/12.2583066>.
- [40] G. Jacobsen, T. Xu, S. Popov, J. Li, A.T. Friberg, Y. Zhang, Receiver implemented RF pilot tone phase noise mitigation in coherent optical nPSK and nQAM systems, *Opt. Express* 19 (15) (2011) 14487–14494, <http://dx.doi.org/10.1364/OE.19.014487>.
- [41] T. Shao, E. Martin, P.M. Anandarajah, C. Browning, V. Vujicic, R. Llorente, L.P. Barry, Chromatic dispersion-induced optical phase decorrelation in a 60 GHz OFDM-RoF system, *IEEE Photonics Technol. Lett.* 26 (20) (2014) 2016–2019, <http://dx.doi.org/10.1109/LPT.2014.2344314>.
- [42] C.-C. Wei, C.-T. Lin, H.-T. Huang, W.-L. Liang, S. Chi, Estimation and suppression of dispersion-induced phase noise in W-band direct-detection OFDM radio-over-fiber systems, *J. Lightwave Technol.* 32 (20) (2014) 3874–3884, <http://dx.doi.org/10.1109/JLT.2014.2322601>.
- [43] A. Delmède, C. Browning, T. Veroleto, J. Poette, A. Farhang, H.H. Elwan, R.D. Koelpillai, G. Aubin, F. Lelarge, A. Ramdane, D. Venkitesh, L.P. Barry, Optical heterodyne analog radio-over-fiber link for millimeter-wave wireless systems, *J. Lightwave Technol.* 39 (2) (2021) 465–474, <http://dx.doi.org/10.1109/JLT.2020.3032923>.
- [44] J. Perez Santacruz, S. Rommel, U. Johannsen, A. Jurado-Navas, I. Tafur Monroy, Analysis and compensation of phase noise in mm-wave OFDM AroF systems for beyond 5G, *J. Lightwave Technol.* 39 (6) (2021) 1602–1610, <http://dx.doi.org/10.1109/JLT.2020.3041041>.
- [45] W.-R. Peng, T. Tsuritani, I. Morita, Simple carrier recovery approach for RF-pilot-assisted PDM-CO-OFDM systems, *J. Lightwave Technol.* 31 (15) (2013) 2555–2564, <http://dx.doi.org/10.1109/JLT.2013.2270551>.
- [46] P. Matheeken, T. Riihonen, S. Werner, R. Wichman, Constrained phase noise estimation in OFDM using scattered pilots without decision feedback, *IEEE Trans. Signal Process.* 65 (9) (2017) 2348–2362, <http://dx.doi.org/10.1109/TSP.2017.2655481>.
- [47] R.A. Casas, S.L. Biracree, A.E. Youtz, Time domain phase noise correction for OFDM signals, *IEEE Trans. Broadcast.* 48 (3) (2002) 230–236, <http://dx.doi.org/10.1109/TBC.2002.803711>.

P8: Probabilistically Shaped OFDM for Gradual Capacity Adaptation in 5G ARoF Systems

J. P. Santacruz, S. Rommel, A. Jurado-Navas, U. Johannsen, and I. Tafur Monroy, “Probabilistically Shaped OFDM for Gradual Capacity Adaptation in 5G ARoF Systems,” in *26th Optoelectronics and Communications Conference (OECC)*, Hong Kong, China: Optica Publishing Group, Jul. 2021, W1B.4. DOI: 10.1364/OECC.2021.W1B.4

Probabilistically Shaped OFDM for Gradual Capacity Adaptation in 5G ARoF Systems

Javier Pérez Santacruz¹, Simon Rommel¹, Antonio Jurado-Navas², Ulf Johannsen¹
and Idelfonso Tafur Monroy¹

¹Institute for Photonic Integration (IPI), Eindhoven University of Technology, 5600 MB Eindhoven, the Netherlands

²Department of Communications Engineering, University of Málaga, Campus de Teatinos, 29071 Málaga, Spain
j.perez.santacruz@tue.nl

Abstract: This work studies and experimentally evaluates the performance enhancement by using PS-OFDM in a 5G mm-Wave ARoF system at 25 GHz for all 5G numerologies and with different phase noise levels.

OCIS codes: (060.5625) Radio frequency photonics; (060.4510) Optical communications.

1. Introduction

Fifth-generation mobile networks (5G) aim to fulfill the demanding mobile traffic requirements. Moving to millimeter-wave (mm-Wave) domain is a straightforward way to increase the bit-rate due to its large available bandwidths. However, working at mm-Wave frequencies implies high free-space path loss (FSPL) and, thus, the mm-Wave cell coverage is approximately in the rage of 10–200 m, resulting in an increase of the number of cells. Centralized-radio access network (C-RAN) combined with analog radio-over-fiber (ARoF) is a very suitable solution to deploy the large number of mm-Wave cells in the beyond 5G architecture since it reduces the complexity at the remote unit (RU) or cell [1]. Fig. 1 (a) shows a schematic of a C-RAN ARoF architecture for 5G fronthaul, where the main intelligence and signal processing are established in the central office (CO). Moreover, C-RAN mm-Wave ARoF brings other attractive benefits such as low latency, low power consumption, high scalability, and high spectral efficiency [1].

Orthogonal frequency division multiplexing (OFDM) has been adopted as waveform in the 5G standard by 3GPP [2]. However, the phase noise has been proven to be one of the biggest performance limiting factors in OFDM mm-Wave ARoF systems due to the relatively low subcarrier spacing employed in 5G (15–240 kHz) [2, 3]. On the one hand, the widely adopted bit-loading technique cannot continuously change the bit-rate of the OFDM signal in channels affected by additive white Gaussian noise (AWGN) and/or phase noise. Hence, bit-loading does not fully exploit the channel capacity [4]. Probabilistic shaping (PS), on the other hand, provides a fine granularity bit-rate source, approaching to the maximum channel capacity (see Fig. 1 (b)) [4]. PS-OFDM has been demonstrated to improve the performance in mm-Wave ARoF systems by focusing on the AWGN impairment [4]. In this paper, for the first time to our knowledge, we experimentally demonstrate the feasibility of using PS-OFDM to maximize the channel capacity in terms of phase noise for 5G ARoF systems at 25 GHz (K-band). For that, in our proposed experimental setup, 5G numerology is utilized, and the phase noise level is gradually modified [5]. Our experimental results show that the bit-rate improves efficiently by using PS-OFDM.

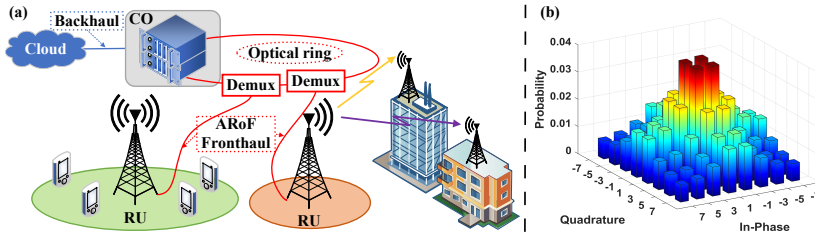


Fig. 1. (a) C-RAN architecture employing ARoF fronthaul for beyond 5G, (b) PS-64-QAM constellation. Demux: demultiplexer.

2. Principle of operation and experimental setup

Phase noise produces inter-carrier interference (ICI) and common phase error (CPE) in the OFDM signal. CPE can be compensated by the channel equalizer. However, an additional process has to be included to compensate or reduce ICI induced by phase noise. Implementing PS on the OFDM data subcarriers allows decreasing the probability of subcarriers with the higher power constellation points. Therefore, since the ICI contribution is strongly dominated by the highest power subcarriers, the impact of phase noise can be reduced by using PS-OFDM configurations with different overhead values. Furthermore, phase noise degrades more OFDM signals with smaller subcarrier spacing configurations [5], as the OFDM symbol period is inversely proportional to the subcarrier spacing. Those OFDM signals with longer symbol periods are affected by phase noise over longer intervals, deteriorating their subcarrier orthogonality and, thus, the signal quality.

Figure 2 (a) represents our experimental schematic to analyze and study the phase noise in PS-OFM ARoF systems [5]. First, an external-cavity laser (ECL) emits the optical carrier at 1550 nm. It is modulated by a Mach-Zehnder modulator (MZM), biased in the null point, and driven with a sinusoid at 12.5 GHz produced by a vector signal generator (VSG). In this way, two optical tones with a separation of 25 GHz are generated [5]. The two-tone signal is boosted by an erbium-doped fiber amplifier (EDFA). Then, the two tones are separated by a wavelength selective switch (WSS). The tone of the upper branch is modulated by a second MZM, biased in the quadrature point, and driven with the OFDM signal at 1 GHz of intermediate frequency (IF). The OFDM signal is generated by an arbitrary waveform generator (AWG) with a sampling frequency of 12 GSa/s. Different OFDM configurations, according to 5G standard, are transmitted in this setup. The table of Fig. 2 (b) shows the main parameters of these configurations: subcarrier spacing (Δf), number of subcarriers (N), and period of the cyclic prefix (T_{cp}). Moreover, different PS configurations are employed on the data subcarrier for 16-QAM and 64-QAM with scalable overhead, allowing a bit-rate - and thus link capacity - adjustment with high granularity.

The tone of the lower branch is delayed in regards to the upper one by using different lengths of patch cord (0–190 m). In this way, since this delay modifies the decorrelation between the two tones, the phase noise in the OFDM transmitted signal can be progressively increased [5], allowing to study its effect. Then, the signals from both branches are recombined in an optical coupler and the two tones beat on a photodiode (PD), producing RF sidebands at 24 and 26 GHz [5]. Then, the electrical signal is boosted by a 30 dB medium power amplifier (MPA) and mixed with a 23 GHz sinusoid. Consequently, the RF signal is downconverted to a second IF of 2 GHz, moving the sidebands to 1 and 3 GHz, respectively. Finally, the IF signal is sampled by a digital phosphor oscilloscope (DPO) at 12.5 GSa/s. Furthermore, the transmitter and receiver digital signal processing (DSP) are depicted in the block diagrams of Fig. 2 (c) and (d), respectively. The DSP receiver processes the sideband signal at 3 GHz.

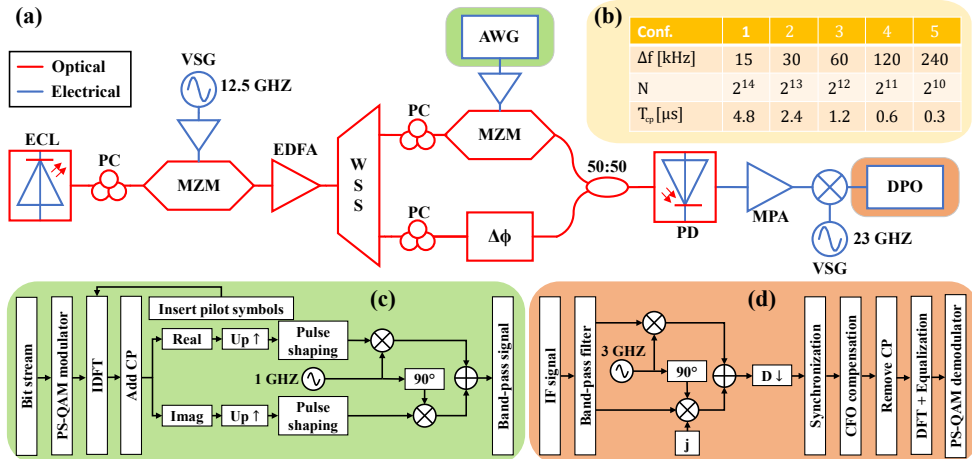


Fig. 2. Experimental testbed: (a) schematic of the experimental setup, (b) parameters of the used OFDM configurations, (c) DSP block diagram in the transmitter side, (d) and DSP block diagram in the receiver side. PC: polarization controller, CFO: carrier frequency offset, DFT: discrete Fourier transform.

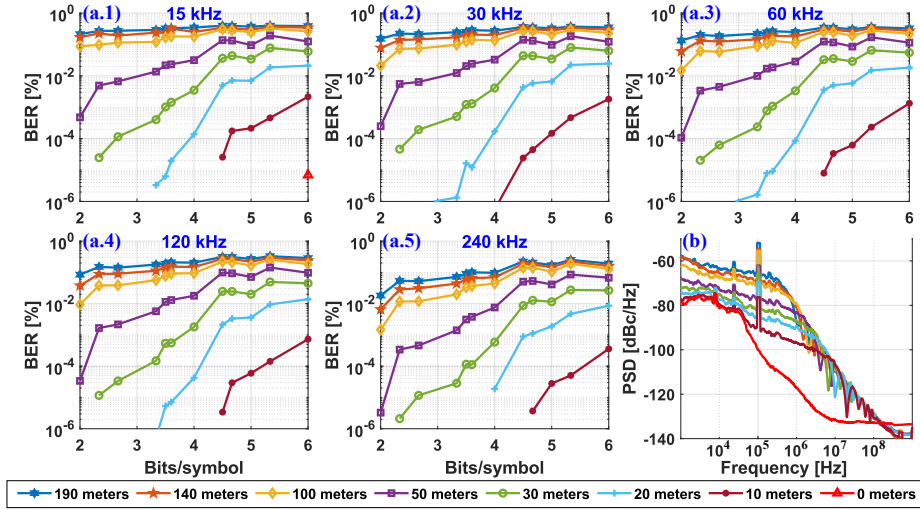


Fig. 3. (a) BER as a function of the entropy (bits/symbol) for diverse subcarrier spacing configurations and patch cord lengths. (b) Measured PSD of the phase noise before the DPO for several patch cord lengths.

3. Results and interpretation

Fig. 3 (a) depicts the experimental results for the different PS-OFDM configurations and several patch cord lengths. These graphs represent the bit error rate (BER) as a function of the entropy (bits per symbol) of the data subcarriers. Moreover, the power spectral density (PSD) of the phase noise for different patch cord lengths is shown in Fig. 3 (b). These PSD shapes are measured before the DPO without the data modulation. It can be realized that the final phase noise of the system can be progressively increased by incrementing the patch cord length of the lower branch in the experimental setup [5]. Our experimental results show that the achievable BER gets worse as the patch cord length increases because of the artificial phase noise added to the system. Furthermore, the BER decreases as the subcarrier spacing increases since the degradation induced by the phase noise is lower for high subcarrier spacing configurations, as was previously explained. Regarding the bit-loading technique, the achievable entropy values are integers. By using PS, the entropy values can be non-integers, allowing a fine bit-rate tunability. Analyzing Fig. 3 (a), it can be seen that the fine adaptability of PS-OFDM allows a grained capacity adjustment for the different OFDM configurations and different phase noise levels. Hence, the experimental results prove that applying PS-OFDM enables to gradually adapt the data subcarrier to channels dominated by phase noise and, thus, finely optimizing the link capacity in a mm-Wave ARoF scenario.

4. Concluding remarks

An analysis and study of PS-OFDM for phase noise dominated mm-Wave ARoF systems has been performed using an experimental setup where phase noise can be increased gradually. The experimental results validate that PS-OFDM enables more gradual adjustment of the capacity for different subcarrier spacing values and different phase noise levels than bit loading. Therefore, PS-OFDM offers advantages over bit-loading allowing 5G and beyond mm-Wave ARoF systems to dynamically adapt to varying channel conditions and/or the presence of phase noise.

Acknowledgments This work was partially supported by the 5G STEP FWD (GA no. 72242) and blueSPACE (GA no. 762055) projects financed from the European Union's Horizon2020 research and innovation programme.

References

1. S. Rommel *et al.*, "Towards a Scaleable 5G Fronthaul: Analog Radio-over-Fiber and Space Division Multiplexing," *J. Lightw. Technol.*, vol. 38, no. 19, pp. 5412–5422, 2020.
2. 3GPP TR 38.912, "Study on New Radio (NR) access technology," version 16.0.0, 2020.
3. A. Delmède *et al.*, "OFDM Baud Rate Limitations in an Optical Heterodyne Analog Fronthaul Link using Unlocked Fibre Lasers," in *Microwave Photonics (MWP)* 2019.
4. R. Zhang *et al.*, "Joint Optimization of Processing Complexity and Rate Allocation through Entropy Tunability for 64-/256-QAM Based Radio Fronthauling with LDPC and PAS-OFDM," in *Optical Fibre Communications (OFC)*, 2020.
5. J. Perez Santacruz *et al.*, "Analysis and Compensation of Phase Noise in mm-Wave OFDM ARoF Systems for Beyond 5G," *J. Lightw. Technol.*, 2020, in press.

Optimized mm-wave 5G/6G deployment based on ARoF

The purpose of this chapter consists of providing the key elements, in terms of DSP and system level considerations, to realize and implement a scalable, optimized, and robust mm-wave fronthaul for future 5G/6G networks. In this way, a comprehensive answer to the research question **RQ-5** can be accomplished. As discussed in Chapter 1, the expected number of mm-wave RAUs will be huge compared to the current sub-7 GHz mobile network. Therefore, to harness the inherent benefits tied to C-RAN architectures, a scalable mm-wave fronthaul deployment is essential where the complexity and number of RAU operations are minimized. In such a manner, the operating expenditure (OPEX) and capital expenditure (CAPEX) of the future mm-wave mobile network can be affordable for operators [151], [152]. More specifically, C-RAN architectures facilitate the control and maintenance of the mobile network operation due to its centralized structure, reducing OPEX. On the other hand, the use of fronthaul technologies, such as ARoF, allows reducing the RAU complexity, minimizing OPEX and CAPEX. However, the utilization of the ARoF solution for the mm-wave fronthaul implies severe non-linear effects and phase noise impairments, among others drawbacks (see Chapter 2).

Taking into account the considerations discussed in the previous paragraph, this chapter is organized as follows: Section 5.1 presents, explains, and compares different technologies to implement future mm-wave fronthaul systems; Section 5.2 shows an experimental bidirectional mm-wave ARoF setup that follows 5G standards and provides empirical assessments for the mm-wave fronthaul deployment based on ARoF; Section 5.3 experimentally evaluates the PAS technique to optimize the channel capacity usage in ARoF systems for mm-wave fronthaul.

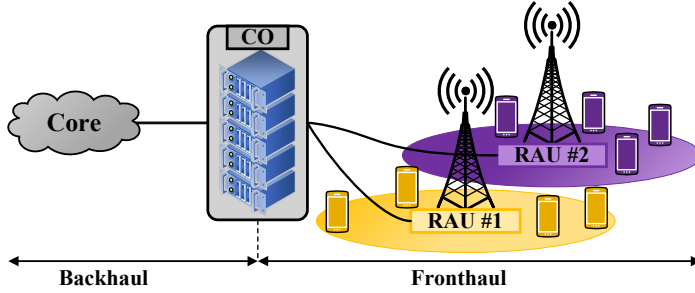


Figure 5.1: General scheme of a mobile network based on C-RAN.

5.1 Fronthaul architectures for mm-wave 5G/6G networks

As introduced in Chapter 1, C-RAN is the preferred mobile network architecture due to its attractive benefits such as low maintenance, and reduced energy consumption [22], [24]. Nonetheless, the implementation of C-RAN signifies a new entity in the mobile network: the CO. Such a CO operates as an intermediary node between the RAUs and the core of the network. Each CO contains a set of baseband units (BBUs) to process the baseband 5G NR signals. In this respect, the fronthaul allows the connection between BBUs to their assigned RAUs. Figure 5.1 depicts a general scheme of the C-RAN, where the backhaul and fronthaul links are also represented. Since the fronthaul segment in a mobile network benefits from extremely low attenuation to maintain the quality of the signal along, in occasions, long distances, then a deployment with optical fibers used to be the most extended solution, whose advantages were discussed in Chapter 2. Thus, by using RoF technologies, data signals are transported through the optical fronthaul link and, subsequently, sent to the wireless domain in the RAU.

In LTE, CPRI was the first DRoF solution [153], allowing the implementation of the C-RAN architecture [153]. However, CPRI has certain limitations: bandwidth expansion of the transmitted optical signal; potential bottleneck in the fronthaul for broadband signal transport; exigent DAC and ADC requirements for large bandwidth transmissions; increase in the overall latency because of the overload processing in the RAUs; and high complexity in the RAUs. A DRoF scheme for the mobile fronthaul is shown in Fig. 5.2(a). In this scheme, the OFDM signals are generated at the CO. Subsequently, for a DRoF realization, those generated OFDM signals are transported through the optical fiber in a digital format. This digitization transportation is performed by the serializer (SER). The SER quantizes the OFDM samples into bits for digital transportation, using an on-off keying (OOK) modulation format for this case. Therefore, SERs are made up of DACs, whose sampling rate requirements are directly linked to both the number of bits to

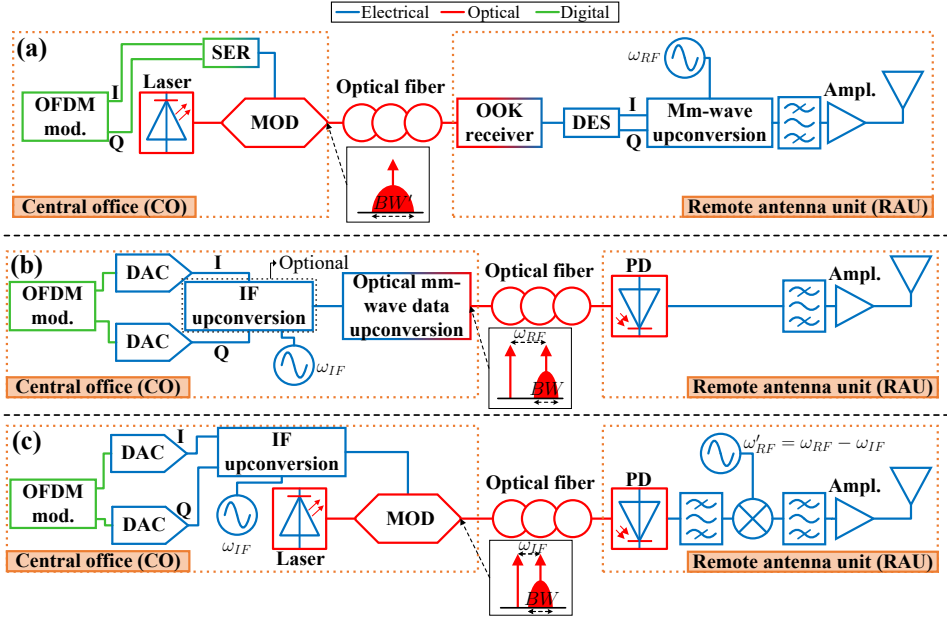


Figure 5.2: Signal transport technologies through optical fiber for mm-wave mobiles networks based on C-RAN: (a) DRoF fronthaul; (b) mm-wave ARoF fronthaul; (c) IFoF fronthaul. SER: serializer; DES: deserializer.

be quantified per analog sample, and to the bandwidth of the analog signal [153]. For a numerical example where 15 bits are used for the digitization of each analog sample, a sampling rate of 0.9216 Gbps is required for each IQ dimension in the case of the largest bandwidth case of LTE (20 MHz) [153]. However, for FR2 frequencies, 1 GHz is the maximum channel bandwidth considered in the 3GPP 5G standard [154]. This bandwidth increment implies a factor of increase in the sampling rate of approximately 50, in the case of applying the maximum bandwidth established by the 5G standard. Thereby, these exigent DAC and ADC requirements make DRoF infeasible for the future mm-wave fronthaul.

In Fig. 5.2(a), after the serialization process, the RF signal is sent through the optical fiber with digital format. Then, at the RAU site, an OOK receiver is used to decode the respective IQ signals. Later, an inverse process to that performed in the serialization is carried out with a deserializer (DES), to retrieve the transmitted OFDM signal. The DES block contains a pair of DACs to perform the deserialization process. Finally, the retrieved OFDM signal is upconverted to the mm-wave domain for wireless transmission. Since the DES block encloses a pair of DACs, the RAU cost becomes dramatically high for large bandwidth signals such as in mm-wave communications. Besides, a mm-wave upconversion procedure is required on the RAU side, which intensifies the cost, power consumption, and

RAU complexity. Furthermore, a bandwidth expansion originates in the optical domain (B'), which is directly proportional to the number of quantification bits per analog sample. Nevertheless, the signal degradation due to the quantification process is inversely proportional to the number of quantification bits. Thereby, there is a trade-off between signal degradation due to the quantification process and optical spectral efficiency [28]. Moreover, the serialization and deserialization procedures in Fig. 5.2(a) increase the total delay of the communication system. In addition, for massive multiple-input multiple-output (MIMO), where multiple signals from the same RAU are transmitted in the optical fiber, a bottleneck can be originated in the fronthaul due to the bandwidth expansion phenomenon in DRoF systems, highlighting the importance to evaluate and standardize alternative technologies [27].

As a great alternative to DRoF, ARoF technology emerges as an excellent solution since its implementation dispenses with the OOK receiver, the serialization, and deserialization processes. Besides, ARoF does not imply an expansion of the RF signal when it is converted into the optical domain. Thus, with respect to DRoF, ARoF offers low complexity RAUs and reduces the bottleneck in the mm-wave fronthaul. Furthermore, since the buffering of the serialization and deserialization processes is avoided in ARoF systems, the overall delay is lower, compared to DRoF solutions.

In this dissertation, two types of ARoF fronthaul are considered: mm-wave ARoF and intermediate frequency-over-fiber (IFoF). Figure 5.2(b) illustrates a mm-wave ARoF scheme for the mobile fronthaul. As it can be observed in Fig. 5.2(b), the RAU is only composed of a PD, an RF filter, an RF amplifier, and an antenna or AA. This simplicity of the RAU brought by mm-wave ARoF is ideal for deploying, in a scalable and efficient manner, the enormous quantity of mm-wave cells expected for future 5G/6G networks. It is important to mention that in the ARoF architecture of Fig. 5.2(b) the mm-wave signal is transported in the optical fiber as two-tone signal, allowing mm-wave upconversion in the PD by optical heterodyne. In this way, by moving the RF oscillator to the CO, the mm-wave upconversion is avoided at the RAU site. Thus, in this mm-wave ARoF architecture, the majority of the system components are allocated in the CO, facilitating its monitoring and maintenance in the overall C-RAN. At the CO site of Fig. 5.2(b), the optical mm-wave data upconversion block can be implemented with one of the techniques illustrated in Fig. 2.3. For the optical spectrum shown in Fig. 5.2(b), an SSB mm-wave data upconversion technique is employed. As a final comment on the ARoF architecture of Fig. 5.2(b), an IF upconversion can be used previous to the optical mm-wave data upconversion block. The IF upconversion can be performed in the electrical domain as it is illustrated in Fig. 5.2(b), or by DSP in the digital domain.

However, due to the fact that the analog signal is directly modulated to the optical domain in ARoF systems, the retrieved OFDM signal at the output of the optical fiber suffers from more degradation than in the DRoF case. Another reason for this increased degradation in mm-wave ARoF systems is the relative high phase

Table 5.1: Qualitative comparison between fronthaul transportation technologies for the mm-wave fronthaul.

Fronthaul technology	CO complexity	RAU complexity	Phase noise level	Impact of non-linear. in opt. fiber
mm-wave ARoF	High	Low	Medium/High*	Medium
IFoF	Medium	Medium	Low*	Medium
DRoF	Medium	High	Low*	Low

(*) → it depends on the used RF oscillators and the employed mm-wave upconversion technology in the optical domain.

noise level commonly inherent to the two optical tones generation techniques, compared to traditional electrical oscillators [27]. Besides, OFDM signals suffer from severe degradation due to phase noise effects, as explained in Chapter 4. Hence, one intermediate solution between mm-wave ARoF and DRoF consists of moving the mm-wave upconversion procedure to the RAU by using an RF oscillator. In this way, the final phase noise level is similar to the one in the DRoF case, having the same RF oscillators. Moreover, the bandwidth requirements of optical modulators and PDs are reduced since the mm-wave transport is avoided in the optical fiber. The aforementioned intermediate frequency RoF implementation is called IFoF. An IFoF system for the mm-wave fronthaul is displayed in Fig. 5.2(c). For this IFoF implementation, an IF upconversion process in the CO is required and can be implemented in the electrical or digital domain. If the IF upconversion is performed in the digital domain, a higher DAC sampling rate is needed with the benefit of dispensing with the IF oscillator. Finally, at the end-user side, any of the techniques in Fig. 2.8 can be employed to recover the OFDM signal received from the mm-wave wireless link.

Table 5.1 shows a qualitative comparison between the mentioned RoF technologies for the mm-wave fronthaul in terms of the following performance indicators: CO system complexity, RAU system complexity, total phase noise level of the system, and impact of the non-linearities on the signal due the optical fiber transmission. As discussed above, mm-wave ARoF is highlighted for its low complexity RAUs, moving most of the complexity to the CO. On the contrary, DRoF implies complex mm-wave RAUs for broadband communications. However, the degradation suffered by the transmitted signal in ARoF systems is higher than in DRoF scenarios. The reduction of the impact due to ARoF impairments was addressed in previous chapters: Chapter 3 proposes PAS over OFDM data subcarriers to alleviate the non-linearities that the transmitted signal suffers throughout the ARoF link; Chapter 4 studies and analyzes phase noise mitigation techniques for OFDM signals in mm-wave ARoF setups. Furthermore, as it can be seen in Table 5.1, the IFoF solution offers intermediate features between mm-wave ARoF and DRoF, which results in a preferred choice in specific scenarios. Additionally, it is worth mentioning that there are other RoF solutions such as DRoF based on delta-sigma modulation or ARoF based on phase modulation [155], [156]. However, these solutions are outside the scope of this dissertation.

5.2 Bidirectional ARoF experimental demonstration for mm-wave 5G scenarios

In the previous section, the advantages of implementing mm-wave ARoF and IFoF, with respect to the DRoF solution, were highlighted. However, there is a research gap in bidirectional ARoF experimental setups adhering to the 5G standard. **P9** and **P10** present and explain a novel bidirectional mm-wave ARoF wireless scheme for the mobile fronthaul. These papers investigate the communication performance of using ARoF solution for mm-wave 5G communications and provide empirical assessments. **P10** further explains the mm-wave ARoF setup under test.

One of the main advantages of the mm-wave ARoF wireless scheme proposed in **P9** and **P10** is the use of MCFs to multiplex the downlink and uplink in the optical domain, which signifies a reduction in cross-talk between both directions compared to WDM technology [157], [158]. In addition, the utilization of MCF enables the usage of a single laser that can be employed for all the cores, reducing the complexity of the system compared to the WDM solution. Furthermore, since the delay mismatch between the different cores of the MCF is small, an RF carrier from the CO can be transported through one of the cores. Then, the transported RF carrier can be used for the downlink conversion on the RAU side, reducing the overall complexity because both uplink and downlink processes are carried out with the same RF carrier. This RF carrier transport implementation is realized in [27]. An additional advantage of using MCF for the ARoF fronthaul is its highly efficient integration with optical beamforming, since the relative delays between the different cores of the MCF are negligible for mm-wave applications [159]. Optical beamforming is thoroughly presented in Chapter 6.

Nowadays, the MCF amplification is a less mature technology than conventional SSF amplification. Nevertheless, as the distance between the CO and RAU ranges from 10 km to 20 km [26], optical amplification is not necessary in most applications. Moreover, as another drawback, the MCF technology is not yet widely deployed, which implies that in most cases a new fiber deployment would be required for its utilization.

Another novelty of the ARoF scheme presented in **P9** and **P10** resides in the RF carrier reuse for the uplink and downlink, which implies dispensing with an RF oscillator at the RAU side. Hence, the total power consumption and cost of the system are reduced. This RF carrier reuse is feasible since a TDD multiplexing technology is performed in the wireless link for both directions. In the 5G standard, a TDD multiplexing procedure is established for FR2 bands [19].

As an additional comment on the bidirectional scheme proposed in **P9** and **P10**, a mm-wave ARoF transport is carried out for the downlink in the MCF. Hence, the downlink structure of the proposed fronthaul scheme is similar to the scheme in Fig. 5.2(b), with the difference that the IF upconversion is performed in the digital domain. On the other hand, in the proposed bidirectional scheme of

Table 5.2: Overview of experimental ARoF setups for bidirectional mm-wave 5G/6G communications.

Date	Operation frequency	System description	Opt. multiplexing technology	Wireless configuration	Modulation format	Bandwidth and bit rate	Ref
08/'12	35.75 GHz (DL & UL)	Config. 1	WDM with opt. circulators	BTB wireless transmission	ASK	5 GHz DL: 2.5 Gbps 5 GHz UL: 2.5 Gbps	[160]
11/'12	53 GHz (DL) & 60 GHz (UL)	Config. 1	WDM with opt. circulators	FDD & SISO (0.91 m)	QPSK or NRZ	5.36 GHz DL: 2.68 Gbps 4 GHz UL: 2 Gbps	[97]
01/'16	92.5 GHz (DL) & 96 GHz (UL)	Config. 1	WDM with opt. circulators	FDD & 2x2 MIMO (3 m)	OFDM (DL) & SC-FDM (UL)	80 MHz DL: 480 Mbps 40 MHz UL: 240 Mbps	[161]
10/'16	2.2 GHz (DL & UL)	Config. 2	MCF	2 sets of 2x2 MIMO (0.4 m)	OFDM/OQAM	2x0.6 GHz DL: 4.4 Gbps 2x0.6 GHz UL: 4.4 Gbps	[162]
07/'18	92 GHz (DL & UL)	Config. 3	WDM with opt. circulators	2 sets of 2x2 MIMO (2.5 m)	OFDM & LTE-A (PDM)	2 GHz DL: 7.7 Gbps 2 GHz UL: 7.7 Gbps	[163]
03/'19	99.1 GHz (DL) & 95 GHz (UL)	Config. 1	WDM with opt. circulators	FDD & 2x2 MIMO (1 m)	Nyquist-SCM	10 GHz DL: 45 Gbps 5 GHz UL: 20 Gbps	[164]
11/'21	26 GHz (DL & UL)	Config. 1	MCF	TDD & 2x2 MIMO (9 m)	OFDM (5G)	1 GHz DL: 4 Gbps 1 GHz UL: 4 Gbps	P9 P10

BTB: back-to-back; ASK: amplitude-shift keying; FDD: frequency division duplex; SISO: Single-input single-output; QPSK: quadrature phase-shift keying; NRZ: non-return-to-zero; OQAM: offset-QAM; PDM: polarization-division multiplexing; SCM: subcarrier modulation.
 Config. 1 \rightarrow mm-wave ARoF for DL and IFoF for UL.
 Config. 2 \rightarrow IFoF for DL and UL.
 Config. 3 \rightarrow IFoF for DL and UL with optical remote mm-wave generation.

P9 and **P10**, the uplink transport through the MCF is realized by employing the IFoF technique (similar to Fig. 5.2(c)).

For the evaluation of 5G numerologies in an experimental ARoF fronthaul, all the subcarrier spacing configurations, established in the 5G standard [19], are appraised in the testbed of **P10**. The experimental results show that subcarrier spacing values of 120 kHz and 240 kHz are the best Δf configurations for both directions and all the bandwidth settings under test. Subsequently, in **P10**, the BER results are shown for the downlink and uplink directions, setting the subcarrier spacing value to 240 kHz. These BER results are also for different bandwidth configurations: 245.76 MHz, 491.52 MHz, and 983.04 MHz. For an adequate comparison of the experimental BER results between both directions, the x-axis of the obtained graphs is in terms of the same parameter (RF sideband power). By comparing the BER graphs of the downlink and uplink, it can be observed that the uplink performs better in terms of BER. After Monte Carlo simulations, it is concluded that the downlink direction shows more non-linearities than in the uplink. This difference in non-linearities is mainly caused by non-linear devices such as MZM and RF amplifiers, since their transfer functions compress the transmitted signal.

As discussed above, the presented bidirectional ARoF experiment of **P9** and **P10**, following the 5G standards, provides quantified assessments regarding the performance of the ARoF technology for the future mm-wave 5G/6G fronthaul. To the best of the author's knowledge, the work presented in **P9** and **P10** is the first experimental bidirectional ARoF fronthaul for mm-wave 5G communications. Nonetheless, there are other scientific articles evaluating a bidirectional ARoF

setup for the mm-wave mobile fronthaul. However, these papers are not strictly in accordance with 5G standards, as can be seen in Table 5.2. Moreover, it can be noted that there is a gap in bidirectional mobile fronthaul experimentation using MCF, apart from [162] where sub-7 GHz bands are evaluated. Therefore, the contribution of the work in **P9** and **P10** fills a research gap concerning the experimental evaluation of the mm-wave ARoF fronthaul based on MCF for future 5G/6G networks.

5.3 Performance optimization in mm-wave ARoF systems

As discussed in Section 3, PAS allows to gradually reduce the impact of the main impairments of mm-wave ARoF systems: phase noise, AWGN, and non-linearities. This section aims to provide the benefits of PAS to enhance the channel capacity usage in the mm-wave fronthaul based on ARoF solutions. For that, first, as mentioned in Section 4, **P8** proposes PAS-OFDM as a modulation scheme to gradually mitigate the impact of phase noise on OFDM subcarriers. To quantify the benefits of PAS-OFDM in phase noise channels, all 5G numerologies are tested in an experimental setup where the phase noise level is artificially increased. Then, the enhancement of using PAS-OFDM with respect to the impact of phase noise is quantified, isolating the phase noise impairment from the rest of the drawbacks of mm-wave ARoF systems. The experimental results of **P8** demonstrate that PAS-OFDM allows a fine and optimized channel capacity usage in links mainly corrupted by phase noise.

Furthermore, as commented in Section 3, **P3** uses an ESS modulation scheme over a bidirectional mm-wave fronthaul based on ARoF. The setup employed in **P3** is similar to that used for **P9** and **P10**, with the difference that in **P3** an RF switch is utilized in the end-user for the TDD communication, enabling a single antenna in the end-user site. The results of **P3** highlight ESS to optimize the channel capacity usage in mm-wave ARoF systems where phase noise, AWGN, and non-linearities are the main drawbacks. Specifically, as discussed in the previous section, the downlink presents more non-linearities than the uplink. In the results of **P3**, the ESS improvement, compared to the bit-loading technique, is greater in the downlink than in the uplink. Therefore, a conclusion induced by interpreting these experimental results is that PAS and, in particular ESS, provide larger benefits in channels with high non-linearities. A summary of the contribution in **P8** and **P3** is that PAS is an excellent technique to combine with OFDM in order to optimize the channel capacity usage in mm-wave fronthauls based on ARoF for future 5G/6G networks.

P9: Bidirectional mm-Wave ARoF Fronthaul over Multicore Fiber for 5G and Beyond

J. P. Santacruz, G. Nazarikov, S. Rommel, A. Jurado-Navas, and I. Tafur Monroy, “Bidirectional mm-Wave ARoF Fronthaul over Multicore Fiber for 5G and Beyond,” in *2021 International Topical Meeting on Microwave Photonics (MWP)*, Pisa, Italy: IEEE, Nov. 2021, pp. 1–4. DOI: 10.1109/MWP53341.2021.9639425

Bidirectional mm-Wave ARoF Fronthaul over Multicore Fiber for 5G and Beyond

Javier Pérez Santacruz
Institute for Photonic Integration
Eindhoven University of Technology
Eindhoven, The Netherlands
j.perez.santacruz@tue.nl

Gleb Nazarikov
Institute for Photonic Integration
Eindhoven University of Technology
Eindhoven, The Netherlands
g.i.nazarikov@tue.nl

Simon Rommel
Institute for Photonic Integration
Eindhoven University of Technology
Eindhoven, The Netherlands
s.rommel@tue.nl

Antonio Jurado-Navas
Department of Communications Engineering
University of Málaga
Málaga, Spain
navas@ic.uma.es

Idelfonso Tafur Monroy
Institute for Photonic Integration
Eindhoven University of Technology
Eindhoven, The Netherlands
i.tafur.monroy@tue.nl

Abstract—In this work we present, analyze, and demonstrate an efficient bidirectional ARoF system for K-band 5G fronthaul based on multicore fiber. As the 5G standard establishes, the experimental testbed is configured regarding the time division duplex scheduling and tested by transmitting OFDM signals. Furthermore, the configuration of the setup enables the reusability of several components for both directions, allowing the reduction of the power consumption, complexity, and cost of the system. The bidirectional testbed is experimentally evaluated under different bandwidth configurations and power levels, achieving a maximum throughput of 4 Gbit/s over 9 m of wireless link. The experimental results prove and validate the proposed bidirectional ARoF scheme as a promising solution for the future mm-Wave 5G fronthaul.

Index Terms—5G; Analog radio-over-fiber; Fronthaul; OFDM; Bidirectional; mm-Wave; Multicore fiber.

I. INTRODUCTION

The fifth generation (5G) of mobile networks aims to fulfill the highly demanding data requirements in terms of bit rate, latency, and energy efficiency, among others [1], [2]. The millimeter-wave (mm-Wave) spectrum provides large available bandwidths compared to the saturated frequency bands (under 6 GHz) employed in the current mobile networks and can thus support substantially larger data rates. However, since the free-space path losses (FSPL) increases as the frequency does, the number of mm-Wave cells will be much larger than the current number of sub-6 GHz cells to cover the same area. Moreover, centralized radio access network (C-RAN) is a preferred option in terms of flexibility, latency, and energy consumption.

To avoid the bottleneck that the already implemented 5G technologies (common public radio interface (CPRI) or enhanced CPRI (eCPRI)) cause in the fronthaul, analog radio-over-fiber (ARoF) is an excellent solution for the transport of high-bandwidth mm-Wave signals due to their attractive benefits such as high spectral efficiency, large bandwidth, and low complexity [3]. ARoF fronthaul over optical multiplexing

solutions, such as dense wavelength-division multiplexing (DWDM) and space-division multiplexing (SDM), offers a highly scalable architecture that can support the enormous number of future 5G mm-Wave cells. Furthermore, the scalability of this solution enables centralized optical beamforming that reduces the complexity in the remote antenna unit (RAU) [3]. Moreover, employing optical SDM enhances the communication performance for bidirectional links rather than utilizing single optical fibers [4].

The works realized in [5] and [6] experimental demonstrated a bidirectional ARoF system under the Long Term Evolution (LTE) standardization. However, there is still an investigation gap in bidirectional ARoF systems over SDM oriented to 5G fronthaul. For that reason, this paper presents and demonstrates a novel mm-Wave ARoF scheme that allows an efficient bidirectional communication for 5G signals. In addition, the configuration of the experimental setup permits a K-band wireless link at 26 GHz (n258 band) by using time division duplexing (TDD), as defined for mm-Wave in the 5G standards [7]. Orthogonal frequency-division multiplexing (OFDM) signals are sent through the setup with different bandwidths (250 MHz to 1000 MHz) and a subcarrier spacing value of 240 kHz. Furthermore, several key aspects of the experimental configuration are discussed to optimize the final performance. The experimental results show bit error rate (BER) under the forward error correction (FEC) thresholds proving that the proposed scheme is a suitable solution for the future mm-Wave 5G fronthaul.

II. SCALABLE ARCHITECTURE OF ARoF FOR MM-WAVE 5G FRONTHAUL

Fig. 1 shows the general architecture of the ARoF fronthaul to support mm-Wave signal transport from the central office (CO) to the 5G RAUs or cells. The CO performs all the signal processing, management, and monitoring, reducing the complexity in the RAUs. First, the corresponding OFDM

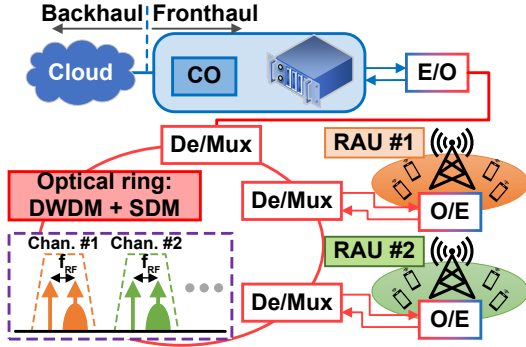


Fig. 1. Overview of the ARoF fronthaul architecture for 5G mm-Wave cells. CO: central office; Mux: multiplexer.

modulated signals for each RAU are generated in the CO. Next, these modulated signals are up-converted to the mm-Wave domain and transported through the optical fibre. The spectrum of the transported optical signals are represented in Fig. 1. The optical mm-Wave up-conversion can be realized in different manners, with launch power and phase noise being two of the key parameters that determine the communication stability of this process [8], [9].

After the optical fiber ring, the transported optical signals corresponding to each RAU can be multiplexed into independent DWDM channels (see graph of the spectrum inserted in Fig. 1). Later, a DWDM demultiplexer process is carried out to select the desired optical signal. By converting the selected optical signal into the electrical domain, a mm-Wave signal is obtained and can be directly used in the RAU without employing electrical up-conversion. Hence, the hardware requirement on each RAU is highly reduced, allowing the viability of deploying the enormous expected number of mm-Wave cells in the future 5G fronthaul. In the demultiplexing blocks, SDM can be realized to achieve bidirectional communication and optical beamforming monitored from the CO [3]. The uplink procedure follows a similar strategy in the opposite direction. In this way, the bidirectional communication of a large number of mm-Wave cells can be provided in a very scalable manner.

III. EXPERIMENTAL SETUP

The experimental schematic of the proposed bidirectional ARoF system for the mm-Wave ARoF fronthaul is shown in Fig. 2. First, in the downlink direction, an optical carrier is generated at 1550 nm in an external cavity laser (ECL). Next, two optical tones with a separation of 23 GHz are produced by using a Mach-Zehnder modulator (MZM), biased in the null point. These two optical tones are boosted with an erbium-doped fiber amplifier (EDFA). Then, the boosted optical tones are modulated with the data signal by employing an arbitrary waveform generator (AWG) and a second MZM, biased in the quadrature point. The data signal of the downlink corresponds to an OFDM modulation with a subcarrier spacing of 240 kHz

and an intermediate frequency (IF) of 3 GHz. This signal procedure for the downlink is realized in the CO.

Then, the modulated optical tones travel through a multi-core fiber (MCF) of 10 km that represents the distance between the CO and the RAU. In the downlink part of the RAU, the optical signals beat on a photodiode (PD), generating the electrical RF carrier at 23 GHz and two OFDM sidebands at 20 GHz and 26 GHz. The OFDM sideband of 26 GHz is the desired data signal for both directions of the communication in the wireless domain. Later, the obtained electrical signal is boosted and launched to a wireless link of 9 m by utilizing a medium power amplifier (MPA) and a horn antenna, respectively. Next, the receiver antenna of the end-user receives the transmitted signal. This received signal is amplified by a low noise amplifier (LNA) and mixed with a sinusoid of 25 GHz, moving the desired OFDM sideband to an IF of 1 GHz. Finally, the resulting electrical signal is captured with a digital phosphor oscilloscope (DPO) and processed offline.

For the uplink direction, the end-user generates an OFDM signal at 1 GHz of IF in a second AWG with the same configuration as the downlink data signal. Next, this OFDM signal is mixed with the local oscillator (LO) of 25 GHz, reusing the frequency synthesizer also employed in the down-conversion of the downlink. Therefore, two OFDM sidebands are produced at 24 GHz and 26 GHz, the 26 GHz sideband signal being the desired. Then, the electrical signal is boosted and sent to the wireless by a second MPA and another horn antenna. In the RAU, the captured signal in the receiver antenna is amplified by a second LNA and mixed with the 23 GHz carrier of the downlink. It is feasible to reuse the downlink 23 GHz carrier because a TDD communication is performed and, thus, the downlink carrier is unmodulated when it is needed for down-conversion of the uplink. Therefore, the desired OFDM sideband is moved to an IF of 3 GHz. The non-desired high frequency components of the down-converted signal are suppressed with a low-pass filter (LPF).

Later, the filtered signal is amplified and converted into the optical domain by using a third MZM and a second ECL that generates an optical carrier at 1548 nm. This optical uplink signal is thrown to a different core of the MCF than for the downlink. Then, in the CO, the uplink optical signal is detected by a second PD, converting the signal into the electrical domain. Finally, the resulting electrical signal is amplified, sampled by a DPO, and processed offline. It is important to highlight that the reuse of RF carriers for the down and up-conversion in both direction of the communication highly reduces the hardware complexity of the system and the power consumption [10]. Moreover, the signal spectrum in some points of the schematic are shown in the bottom of Fig. 2 and some photographs of the experimental testbed are illustrated in Fig. 3.

Respecting the different configurations evaluated in the setup, the tested bandwidths are 250 MHz, 500 MHz, and 1000 MHz. The reason for these selected bandwidth values is because the 5G standard establishes wireless communication above 6 GHz with a channel bandwidth between 100 MHz

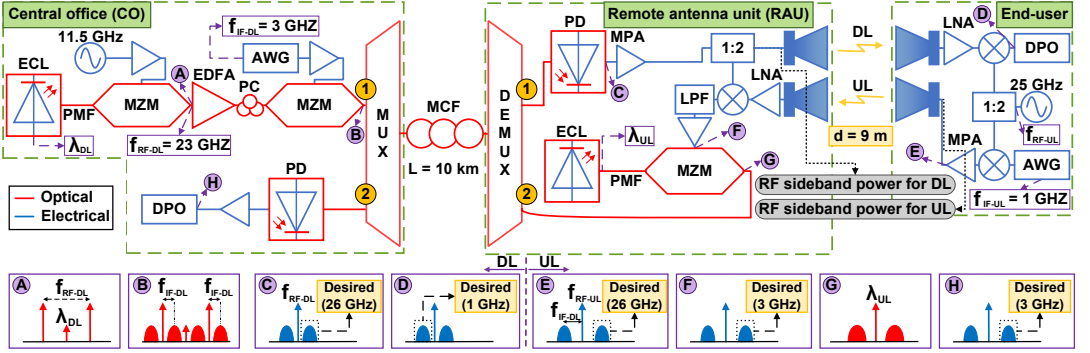


Fig. 2. Experimental testbed of the bidirectional ARoF fronthaul for 5G communications.

and 1 GHz [7]. In addition, the common OFDM parameters of these selected bandwidth configurations are the following: 80% of active subcarriers, 7% cyclic prefix (CP) overhead, subcarrier spacing of 240 kHz, demodulation reference signals (DM-RS) on every every 14th OFDM symbol or slot, and a phase tracking reference signal (PT-RS) on every 8th resource block. Furthermore, 16-QAM and 64-QAM modulations are utilized for all the different bandwidth configurations. By employing 64-QAM modulation in the data subcarriers, the achieved throughputs are 1 Gbit/s, 2 Gbit/s and 4 Gbit/s for 250 MHz, 500 MHz, and 1000 MHz bandwidth configurations, respectively. The resulting throughput by using 16-QAM modulation can be easily calculated by dividing the 64-QAM throughput values by a factor of 1.5.

In order to mitigate the deterioration of the signal due to the impairments of the experimental system, several digital signal processing (DSP) blocks are carried out. These DSP processes are realized for both directions and are the next: a synchronization process by using the added preamble in the beginning of the

transmitted signal; a coarse carrier frequency offset (CFO) procedure by using the synchronization preamble; a channel equalizer by using the DM-RS signals allocated in very slot; and a linear interpolation based intercarrier interference (ICI) estimation technique (also called LI-CPE) that uses the PT-RS signals and CP of every OFDM symbol to compensate the common phase error (CPE) produced by the phase noise [11].

IV. BIDIRECTIONAL TRANSMISSION RESULTS

The experimental results are shown in Fig. 4 in terms of BER. The RF sideband power of the desired data signal at 26 GHz is measured before the transmitter antenna for each direction (see gray labels of Fig. 2) and is utilized in the x-axis of Fig. 4 in order to represent the BER of both direction at the same plot: uplink (continuous) and downlink (dashed). Furthermore, the aforementioned bandwidth configurations are evaluated and compared for both directions and modulation orders of 16-QAM and 64-QAM. Moreover, the 7% and 25% overhead (OH) FEC thresholds are also represented in this figure. Observing Fig. 4, it can be noticed that BER is higher for larger bandwidth values since the signal-to-noise ratio (SNR) decreases as the bandwidth increases while the signal power stays the same.

Examining the results of Fig. 4, the downlink BER performs worse than the uplink results under the same power condition. The main reason of this fact is because the SNR of the uplink is larger than in the downlink. One of the main noise sources in the communication system of Fig. 2 is the EDFA that is only employed in the downlink part. Furthermore, the noise contribution of the EDFA becomes higher since no filtering process of the desired optical signal is performed before the PD. Therefore, the utilization of an optical filtering process, the usage of the EDFA, and its location in the system are keys to increase the SNR of both directions. A way to avoid the need of using the EDFA in the downlink is by performing another technique for the two-tone generation with high-power output rather than the employed external modulation method [9]. However, most of the high-power

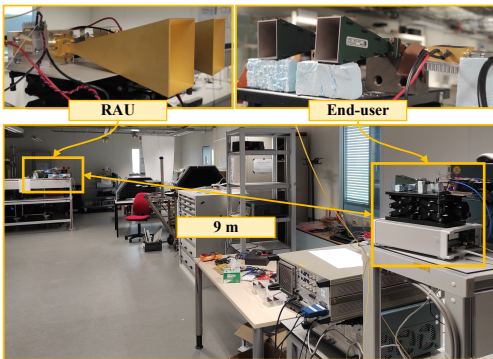


Fig. 3. Photographs of the laboratory wireless link.

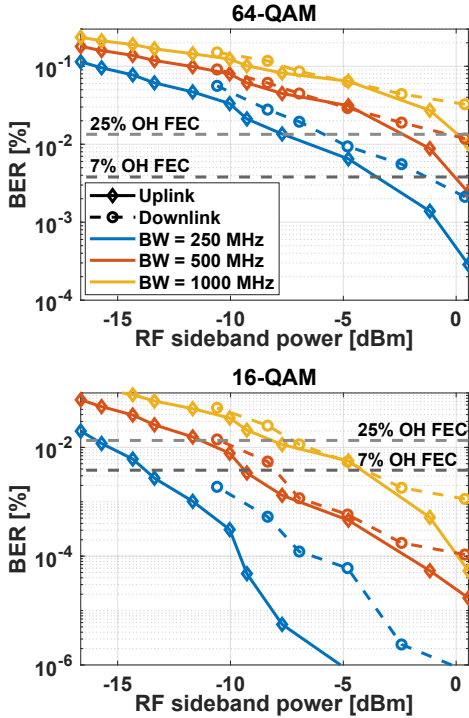


Fig. 4. BER as a function of the RF sideband power for both directions, several bandwidth configurations, and different modulation orders: 64-QAM (top) and 16-QAM (bottom).

two-tone generation techniques contains higher phase noise levels which extremely deteriorates the performance when 5G numerologies are employed [8], [12]. Lastly, regarding Fig. 4, it is relevant to mention that the 16-QAM BER results of all the experiment configurations at the maximum power are below the 7% OH FEC threshold. The same occurs for the 64-QAM results considering the 25% OH FEC limit with the exception of the 1000 MHz downlink result case.

V. CONCLUSIONS

A novel bidirectional ARoF scheme for mm-Wave 5G fronthaul has been proposed and experimentally demonstrated. The usage of ARoF over MCF allows a highly scalable bidirectional architecture for the numerous expected mm-Wave cells. The experimental testbed has been configured conforming to the 5G standard for different bandwidth values and the results show BER values under the FEC limits. Therefore, this work serves to highlight the viability of ARoF links for mm-Wave 5G and beyond by proposing and proving an efficient bidirectional ARoF fronthaul based on MCF.

ACKNOWLEDGMENT

This work was partially financed by the 5G STEP FWD (GA no. 722429) and blueSPACE (GA no. 762055) projects.

REFERENCES

- [1] D. Konstantinou *et al.*, “5G RAN architecture based on analog radio-over-fiber fronthaul over UDWDM-PON and phased array fed reflector antennas,” *Optics Communications*, vol. 454, p. 124464, Jan. 2020.
- [2] J. P. Santacruz, S. Rommel, U. Johannsen, A. J. Navas, and I. Tafur Monroy, “Candidate Waveforms for ARoF in Beyond 5G,” *Appl. Sci.*, vol. 10, no. 11, Jun. 2020.
- [3] S. Rommel *et al.*, “Towards a Scaleable 5G Fronthaul: Analog Radio-over-Fiber and Space Division Multiplexing,” *J. Lightwave Technol.*, vol. 38, no. 19, pp. 5412–5422, Oct. 2020.
- [4] A. Kaszubowska-Anandarajah, A. Delmade, E. Martin, P. Anandarajah, L. Barry, and C. Browning, “Bidirectional fiber transmission of mmW signals using remote downconversion and wavelength reuse,” in *Conference on Lasers and Electro-Optics, Munich, Germany*. Optical Society of America, May 2019, p. SM4G.2.
- [5] P. T. Dat, A. Kanno, N. Yamamoto, and T. Kawanishi, “Full-Duplex Transmission of LTE-A Carrier Aggregation Signal Over a Bidirectional Seamless Fiber-Millimeter-Wave System,” *J. Lightwave Technol.*, vol. 34, no. 2, pp. 691–700, Jan. 2016.
- [6] P. T. Dat *et al.*, “Performance Evaluation of Full-Duplex MIMO Seamless Fiber-Wireless System in W -Band,” *IEEE Photon. Technol. Lett.*, vol. 30, no. 13, pp. 1175–1178, Jul. 2018.
- [7] 3GPP, *FG IMT-2020: Study on New Radio (NR) access technology*. 3GPP TR 38.912, version 16.0.0, Jul. 2020.
- [8] I. Degli-Eredi *et al.*, “Millimeter-wave generation using hybrid silicon photonics,” *Journal of Optics*, vol. 23, no. 4, p. 043001, Mar. 2021.
- [9] J. P. Santacruz *et al.*, “Experimental ARoF System Based on OPLL Mm-Wave Generation for Beyond 5G,” in *2021 Opto-Electronics and Communications Conference (OECC)*, Jul. 2021, pp. 1–3, in press.
- [10] A. Morales *et al.*, “Bidirectional K-Band Photonic/Wireless Link for 5G Communications,” in *2019 44th International Conference on Infrared, Millimeter, and Terahertz Waves (IRMMW-THz)*, Paris, France, Sep. 2019, pp. 1–2.
- [11] Y. Ha and W. Chung, “A Feedforward Partial Phase Noise Mitigation in the Time-Domain using Cyclic Prefix for CO-OFDM Systems,” *Journal of the Optical Society of Korea*, vol. 17, no. 6, pp. 467–470, Nov. 2013.
- [12] J. P. Santacruz, S. Rommel, U. Johannsen, A. Jurado-Navas, and I. T. Monroy, “Analysis and Compensation of Phase Noise in Mm-Wave OFDM ARoF Systems for Beyond 5G,” *J. Lightwave Technol.*, vol. 39, no. 6, pp. 1602–1610, Mar. 2021.

P10: Bidirectional ARoF Fronthaul over Multicore Fiber for Beyond 5G Mm-Wave Communications

J. P. Santacruz, G. Nazarikov, S. Rommel, A. Jurado-Navas, and I. Tafur Monroy, “Bidirectional ARoF Fronthaul over Multicore Fiber for Beyond 5G Mm-Wave Communications,” *Optics Communications*, vol. 521, p. 128 591, Jun. 2022. DOI: 10.1016/j.optcom.2022.128591



Bidirectional ARoF fronthaul over multicore fiber for beyond 5G mm-wave communications

Javier Pérez Santacruz^{a,*}, Gleb Nazarikov^a, Simon Rommel^a, Antonio Jurado-Navas^b, Idelfonso Tafur Monroy^a

^a Institute for Photonic Integration, Eindhoven University of Technology, 5600MB Eindhoven, The Netherlands

^b Department of Communications Engineering, University of Málaga, 29071 Málaga, Spain

ARTICLE INFO

Keywords:

5G
ARoF
Bidirectional
Multicore fiber
OFDM
mm-wave

ABSTRACT

Fifth-generation mobile networks (5G) is the established solution to satisfy the highly demanding key performance indicators such as traffic volumes, bit-rate, latency, and power consumption, among others of the future telecommunication infrastructure. The already saturated sub-6 GHz spectral band does not accommodate such requirements and forces the move towards higher frequencies, with the millimeter-wave (mm-wave) domain being an adequate band to operate. However, the exploitation of mm-wave signals in the mobile cells implies the deployment of an enormous quantity of small cells with associated equipment, footprint, and control. Thus, analog radio-over-fiber (ARoF) emerges as a suitable technology because of their attractive benefits such as low latency, low hardware complexity, and reduced power consumption. However, through investigation of experimental ARoF systems adhering to the 5G standard is scarce. Therefore, in this work, a novel and efficient bidirectional ARoF scheme based on multicore fiber (MCF) and oriented to 5G mm-wave communications is proposed and experimentally validated. The setup configurations are according to the 5G standard, enabling a wireless link at 26 GHz (n258, K-band) and time division duplex (TDD) communication. The proposed scheme is thoroughly evaluated under all the 5G numerologies and with different bandwidth settings. Moreover, key design considerations of the experimental testbed are explained and discussed to optimize the final yields of the system. The experimental results of both transmission directions are compared and analyzed, and prove the viability of the proposed bidirectional ARoF system as an excellent solution to be part of the future 5G mm-wave network.

1. Introduction

The surging of new applications and services, such as 4K video streaming, internet of things (IoT), augmented reality, and autonomous driving, demands a substantial enhancement in mobile networks [1]. In order to adapt to the upcoming data traffic demands, the current mobile networks must be upgraded and improved in terms of capacity, latency, number of connected devices, and data rate. For this reason, the fifth generation (5G) of mobile networks arises as solution to satisfy the exigent performance indicators. The ongoing deployment of 5G technology aims to fulfill most requisites of the arising services and applications by exploiting the sub-6 GHz band [2]. However, looking at a further perspective, the already congested sub-6 GHz band cannot provide sufficient bandwidth to satisfy the exponential growth of mobile data traffic [3,4].

Therefore, moving towards higher frequency bands is the straightforward manner to achieve a great improvement in terms of data rate, with the millimeter-wave (mm-wave) domain being the next band on

the market to become operational. Nonetheless, the use of mm-wave signals implies a significant decrease of the cell coverage area due to the increase of the free-space path loss (FSPL) [5]. Thus, respecting the current mobile network, the number of mm-wave cells required to cover the same surface will be much larger. This enormous number of expected mm-wave cells implies a huge increment of the complexity in the radio access network (RAN). However, the arrival of mm-wave cells or remote access units (RAUs) will increase drastically the data traffic in the fronthaul. To solve this severe issue, analog radio-over-fiber (ARoF) emerges as an excellent solution by highly reducing the complexity in the RAUs, allowing a scalable deployment of the mm-wave cells for beyond 5G [6]. Moreover, other benefits such as high spectral efficiency, low latency, and large bandwidth are inherently related to ARoF [7].

Previous works reported in [8–11] present and validate bidirectional mm-wave ARoF systems by using simple modulation formats such as amplitude-shift keying (ASK) and quadrature phase-shift keying

* Corresponding author.

E-mail address: j.perez.santacruz@tue.nl (J.P. Santacruz).

(QPSK). In [12,13], more realistic mm-wave mobile network scenarios based on bidirectional ARoF setups are demonstrated by transmitting long-term evolution (LTE) signals. However, concerning bidirectional ARoF fronthaul systems adhered to the 5G standard, there is a gap of experimental investigation in the state of the art. Therefore, the contribution of this work aims to pave the road towards a highly scalable bidirectional mm-wave 5G fronthaul based on ARoF. For this, a novel and efficient bidirectional ARoF scheme over multicore fiber (MCF) is proposed and experimentally demonstrated.

Spatial division multiplexing (SDM) is the chosen multiplexing technology to split the downlink and uplink. Compared to other multiplexing solutions, such as wavelength division multiplexing (WDM) or the usage of optical circulators, using SDM to divide the uplink and downlink allows crosstalk between both directions to be reduced [14–16]. In this manner, the final yields of the system improves. Furthermore, analysis of the phase noise and the signal-to-noise ratio (SNR) behavior of both directions are carried out. Design considerations of the experimental setup and the utilized digital signal processing (DSP) process are also explained. Moreover, the presented bidirectional scheme is highlighted for its efficiency in power consumption because it allows the reuse of carriers between both directions.

The experimental setup is configured according to the 5G standard, operating at 26 GHz (n258, K-band) with orthogonal frequency-division multiplexing (OFDM) as modulation format and time-division multiplexing (TDD) as multiplexing process. Different modulation orders (16-QAM and 64-QAM), subcarrier spacing values (15 kHz to 480 kHz), and bandwidths (250 MHz to 1000 MHz) are evaluated in the system for both directions as the 5G standard establishes [17]. The experimental results show bit error rates (BER) under forward error correction (FEC) limits, proving the efficiency and validity of the proposed scheme and consolidating ARoF as a high potential solution to be part of the beyond 5G fronthaul.

The organization of this manuscript is as follows: Section 2 focuses on design implementations to achieve a scalable 5G mm-wave fronthaul. Section 3 thoroughly explains the experimental setup in the digital signal processing and hardware aspects. Section 4 profoundly analyzes and interprets the obtained measurements and results, remarking crucial considerations to enhance the final performance. Finally, Section 5 presents the most relevant conclusions of this work.

2. High scalable mm-wave 5G fronthaul

The goal of this section consists of describing the high scalability capacity that ARoF can offer to mm-wave 5G communications. The mobile network architecture has been moved from distributed to centralized operation. Distributed-RAN (D-RAN) directly connects the antenna site, where the baseband processing is performed, with the core of the network. In the other hand, centralized-RAN (C-RAN) includes the central office (CO) as an additional node in the mobile network. In the C-RAN, several processes and operations are moved from the RAUs to the CO, reducing the complexity of the RAUs and diminishing the operating expenses (OPEX). Furthermore, respecting D-RAN, C-RAN offers other benefits such as higher flexibility, lower latency, lower maintenance, and reduced energy consumption [18]. For these reasons, C-RAN is the operating architecture for LTE-Advanced (LTE-A) and 5G networks. Nonetheless, the implementation of C-RAN implies a new segment between the CO and RAU, called fronthaul [6].

Common public radio interface (CPRI) is the used C-RAN technology in LTE-A. For 5G networks, enhanced-CPRI (eCPRI) is the adopted C-RAN solution, with next generation fronthaul interfaces (NGFI) an added alternative. However, the arrival of mm-wave RAUs will drastically increase the data transmission in the mobile fronthaul [6]. In addition to this, the implementation of multiple-input and multiple-output (MIMO) and beamforming solutions become essential to overcome the high FSPL in the mm-wave domain, further increasing the data rate requirements of the future 5G fronthaul [6].

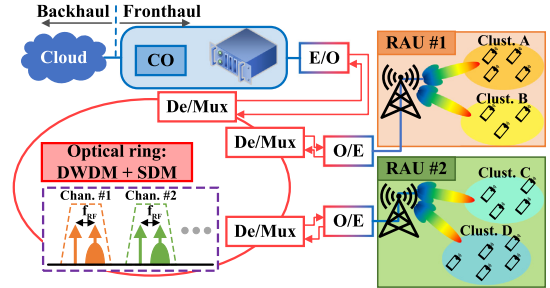


Fig. 1. General schematic of a scalable bidirectional mm-wave 5G fronthaul based on ARoF and supported by centralized beamforming and multiplexing solutions such as DWDM and SDM.

Thus, bottlenecks can appear in the fronthaul due to these demanding transport requirements [6]. Therefore, as mentioned in Section 1, ARoF surges as an excellent solution for the 5G mm-wave network since it implies low complexity RAUs, enabling a scalable deployment, and it relaxes the data requirements in the fronthaul, avoiding possible bottlenecks. Moreover, the combination of ARoF with multiplexing technologies, such as dense wavelength-division multiplexing (DWDM) and SDM, increases the scalability of ARoF systems and optimizes the cointegration with beamforming technologies [6,14].

Optical beamforming (OBF) has emerged as an efficient alternative of the conventional electrical beamforming because of its high dynamic beam steering properties, footprint capacity for scalable and low power solutions, and multi-beam transmission based on beamforming matrices [19]. MCF technology has a great potential to support optical MIMO or beamforming implementations since it enables an efficient manner to manage and control the spatial resources and the beamformed signals [20]. In addition, centralized OBF is an attractive implementation because the beamforming resources can be optimally assigned and the RAU dispenses with the optical beamformer, simplifying the complexity of the RAU. However, locating the optical beamformer in the CO results highly challenging in order to maintain the phase synchronicity of the beamformed signals [19]. A solution of this phase synchronicity problem consists of locating the optical beamformer in the RAU and thus lose the centralized beamforming feature. In conclusion, OBF is a promising and in-process technology that needs to be taken into account for the future 5G network.

Bidirectional communication must be considered for the validation of commercially viable solutions. The scheme of Fig. 1 shows a C-RAN architecture of an ARoF system combined with SDM and WDM to achieve a highly scalable 5G fronthaul. This architecture supports bidirectional communication with centralized beamforming to provide mm-wave wireless connectivity to end-users grouped into clusters. In the downlink direction, the CO realizes all the signal processing, management, and monitoring, simplifying the complexity of the mm-wave RAUs. The CO generates signals that are multiplexed with respect to the end-users and the RAU where the corresponding end-user is located. Then, these signals are transported through the optical fiber ring. DWDM channels are assigned to each RAU as illustrated in the spectrum signals of Fig. 1. By performing a demultiplexing process, the desired signal for each RAU is extracted and directly unconverted through optical heterodyning. Next, the resulting electrical signal is sent to the end-user through a mm-wave wireless link. For the uplink direction, an equivalent process is carried out. Respecting Fig. 1, it is important to mention that the two optical links of both directions use different spatial channels. In this manner, as mentioned above, the crosstalk between both directions is low because an SDM system is utilized [14–16]. Therefore, in this work, a MCF is employed to transport the optical signals of both directions.

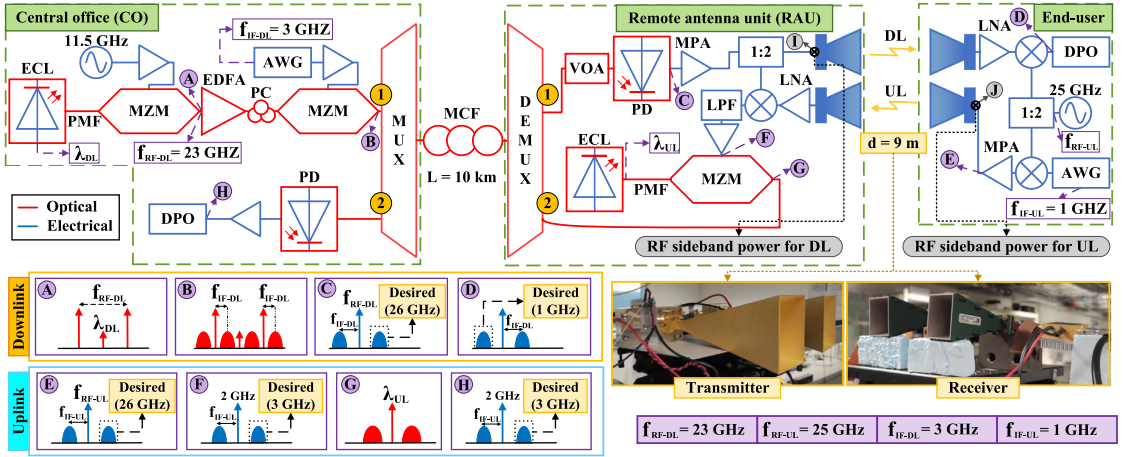


Fig. 2. Experimental setup of the proposed bidirectional AROF scheme based on MCF for the mm-wave 5G fronthaul.

3. Experimental demonstration

3.1. Experimental setup

This subsection describes the experimental setup employed to achieve bidirectional AROF fronthaul for mm-wave 5G communications. Fig. 2 shows the experimental schematic [21]. First, in the downlink part of the CO, an external cavity laser (ECL) generates an optical carrier at 1550 nm with 16 dBm of power. Next, the generated optical carrier is modulated using a Mach-Zehnder modulator (MZM), biased in the null point, with an RF sinusoid of 11.5 GHz. In this way, the MZM produces two optical tones with a separation twice larger than the frequency of the RF input sinusoid [22,23]. In this case, this separation is 23 GHz (spectrum of point A in Fig. 2). For this implementation, the optical carrier is suppressed, avoiding the RF power fading induced by the optical fiber transmission dispersion [24]. Next, the two-tone signal is boosted by an erbium-doped fiber amplifier (EDFA). Later, the boosted optical signal is modulated by a second MZM, biased in the quadrature point, with the OFDM signal. An arbitrary waveform generator (AWG) with 12 GSa/s of sampling rate generates the downlink OFDM signal with an intermediate frequency (IF) of 3 GHz. In such a manner, the optical spectrum at the output of the second MZM is as shown in the frequency domain representation of point B in Fig. 2. Since the MZMs are sensitive to input polarization, a polarization-maintaining fiber (PMF) and a polarization controller (PC) are located before the first and second MZM, respectively. This second MZM corresponds to the last element of the downlink for the CO.

After the downlink process in the CO, the modulated two-tone signal is launched and multiplexed into one core of a MCF with 10 km of length. This length emulates the distance between the CO and the RAU as illustrated in the scheme of Fig. 1. The employed MCF contains 7 cores, provides an attenuation of 0.21 dB/km, and its chromatic dispersion is equal to 18 ps/(nm.km). Then, in the RAU part of the downlink, the transmitted optical signal through the MCF is received, demultiplexed, and sent to a photodiode (PD). By beating the two optical tones in the PD, an electrical signal is produced with an RF carrier at 23 GHz and two OFDM sidebands located at 20 GHz and 26 GHz, respectively (spectrum of point C in Fig. 2). The OFDM sideband at 26 GHz is the desired signal for the wireless link, located in the 5G n258 band. Later, the resulting electrical signal is boosted by a 30 dB medium power amplifier (MPA). Next, the boosted signal goes through an RF power divider and consequently is launched into the wireless

link by a 24 dBi horn antenna. The distance of the wireless link is 9 m. The transmitter downlink antenna is the last device of the RAU in the downlink.

In the experimental results, the power of the EDFA is gradually changed to evaluate the performance of the proposed system by realizing a sweep in power, with 18 dBm being the maximum output power of the EDFA. Then, the RF sideband powers at 26 GHz are measured before the transmitter downlink antenna (point I of Fig. 2) in order to appraise the yields of the downlink communication. In the end-user side, the transmitted signal is captured by a 20 dBi horn antenna and amplified by a 40 dB low-noise amplifier (LNA). Next, the amplified electrical signal is mixed with a sinusoid of 25 GHz, shifting the desired OFDM sideband to 1 GHz of center frequency (spectrum of point D in Fig. 2). Finally, the resulting signal is sampled by a digital phosphor oscilloscope (DPO) with 12.5 GSa/s of sampling rate. In addition, as shown in the photographs of Fig. 2, the pair of antennas used in the RAU and in the end-user are the same, respectively. Furthermore, the pair of antennas for each direction are aligned in terms of height, altitude, and azimuth. Moreover, the separation between the RAU antennas is 8 cm meanwhile the end-user antennas are separated with a distance of 5.5 cm.

In the uplink direction, a second AWG, with the same features as the first one, creates an OFDM signal at 1 GHz of IF. This OFDM signal is mixed with a 25 GHz sinusoid which comes from the same RF synthesizer employed in the downlink downconversion. Hence, the OFDM signal is upconverted, resulting an RF carrier at 25 GHz and two OFDM sidebands at 24 GHz and 26 GHz, respectively (spectrum of point E in Fig. 2). The OFDM 26 GHz sideband is again the desired signal for the wireless uplink communication. To distribute both 25 GHz sinusoid signals in the end-user, an RF splitter, whose nominal insertion loss is 7 dB, is employed. After the uplink upconversion, a second 30 dB MPA is used to boost the electrical signal. Then, the boosted electrical signal is launched into the air by using a second 20 dBi horn antenna. This antenna forms the last element of the uplink direction in the end-user side. It is relevant to mention that the RF sideband power at 26 GHz is also measured for the uplink direction (point J of Fig. 2). In this case, the power is swept by modifying the output power of the RF synthesizer located in the end-user.

In the RAU side, a second 24 dBi horn antenna is employed to receive the transmitted uplink signal. Then, the captured uplink signal is amplified by a second 40 dB LNA and mixed with the 23 GHz tone of the downlink by using the second output of the power divider located in

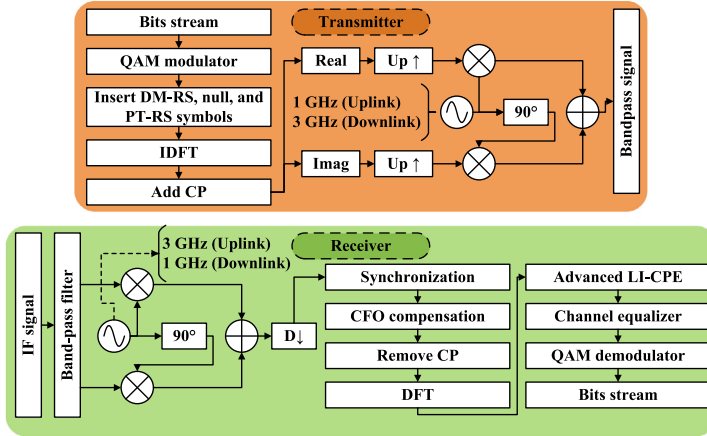


Fig. 3. DSP block diagrams for the transmitter and receiver part in both directions.

the RAU. Subsequent to the downconversion of the uplink, the desired OFDM sideband is transferred to a center frequency of 3 GHz (spectrum of point F in Fig. 2). Next, the undesired higher frequency components are suppressed by using a low-pass filter (LPF) with a cutoff frequency of 5.5 GHz. Later, the filtered signal is amplified and modulated into the optical domain by a third MZM, biased in the quadrature point (spectrum of point G in Fig. 2) and using an optical carrier at 1548 nm, generated by a second ECL with 16 dBm of optical power. The resulting optical signal is launched into a different core of the MCF than the one used in the downlink and, in this manner, the last process of the uplink RAU block is completed. The usage of independent optical channels for both directions instead of one single optical fiber results more efficient in term of yields due to the crosstalk reduction [14–16].

Regarding the processes realized in the CO for the uplink, the transmitted optical signal into the MCF is demultiplexed respecting the employed uplink core. Consequently, the demultiplexed signal beats at a second PD, converting the optical signal into the electrical domain (spectrum of point H in Fig. 2). Later, the resulting electrical signal is amplified and, finally, sampled by a second 12.5 GSa/s DPO. For both transmission directions, different OFDM signal traces are sent to the experimental testbed by using the two aforementioned AWGs. According to the DSP in the receiver part, an offline process is carried out in the sampled signals caught by the pair of used DPOs. Therefore, the performance of both directions can be studied, analyzed, and evaluated. More details about the DSP process is found in the next subsection.

TDD communication is performed in the experimental setup of Fig. 2, as the 5G standard determines for mm-wave communications [25]. Therefore, the downlink optical signal is unmodulated in the uplink time slot and vice versa. This fact allows the resulting 23 GHz tone from the downlink to be employed as local oscillator (LO) in the uplink downconversion process performed at the RAU, realizing effective reuse without causing signal interference. In such a manner, an extra RF synthesizer at the RAU can be avoided, reducing the volume, complexity, and power consumption. Furthermore, an RF synthesizer with an output power of 16 dBm is shared at the end-user for both directions, reducing hardware complexity. This type of reuse to simplify the system is highly desirable in mm-wave 5G communications since the number of expected RAUs is enormous. With the reusability of the RF carriers in two parts of the system and thus the avoidance of additional RF synthesizers, the proposed mm-wave AroF bidirectional scheme is highlighted as an efficient and low complexity solution.

3.2. DSP process

This subsection aims to explain the main key aspects of the used DSP to get the experimental results. Fig. 3 illustrates the utilized DSP process. The transmitter DSP block process is performed offline and the resulting signals are transmitted by the AWGs of both directions. This DSP process can be observed in the orange block of Fig. 3. First, the classical OFDM transmitter is realized consisting of the following blocks: M-QAM modulator where M specifies the modulation order; insertion process of reference symbols such as demodulation reference signal (DM-RS) and phase-tracking reference signal (PT-RS) for posterior channel and phase noise compensation [17]; injection of null symbols in the OFDM band edges to reduce the out-of-band (OOB) emissions and enable more guard band between technologies in the used mm-wave band; inverse discrete Fourier transform (IDFT) to move from frequency-domain to time-domain; and an adding cyclic prefix (CP) process [26]. After the OFDM transmitter blocks, an IF modulation is carried out. For that, the real and imaginary parts of the generated time-domain OFDM signal are separated in two branches. Subsequently, the signals of both branches are upsampled and multiplied by a sine and cosine, respectively for upconversion to the desired IF (3 GHz for downlink, 1 GHz for uplink).

The receiver DSP process is depicted in the green block diagram of Fig. 3 and is the same process for both directions. First, the captured IF signal by the DPO is filtered by a band-pass filter (BPF), eliminating the non-desired frequency components. Consequently, an IF demodulation process is executed to convert the received signal into the baseband domain. However, since the frequency downconversion is not performed in the experimental setup with the same frequency used in the upconversion process, the frequency values of the IF demodulation are different from the ones utilized in the IF modulation. In particular, the uplink and downlink signals must be demodulated with frequency values of 3 GHz and 1 GHz, respectively (spectrums of points H and D in Fig. 2). After the IF demodulation, the resulting baseband signal is downsampled and synchronized by using a preinserted preamble. Afterwards, a coarse carrier frequency offset (CFO) compensation is carried out. Then, the CP is removed in every OFDM symbol and a discrete Fourier transform (DFT) is realized to move into the frequency-domain. Later, a linear interpolation based intercarrier interference (ICI) estimation technique is executed by employing the PT-RS signals inserted in every OFDM symbol [27]. This method is also denominated LI-CPE and its function consists of compensating the common phase error (CPE) and ICI produced by phase noise and CFO [28]. Next,

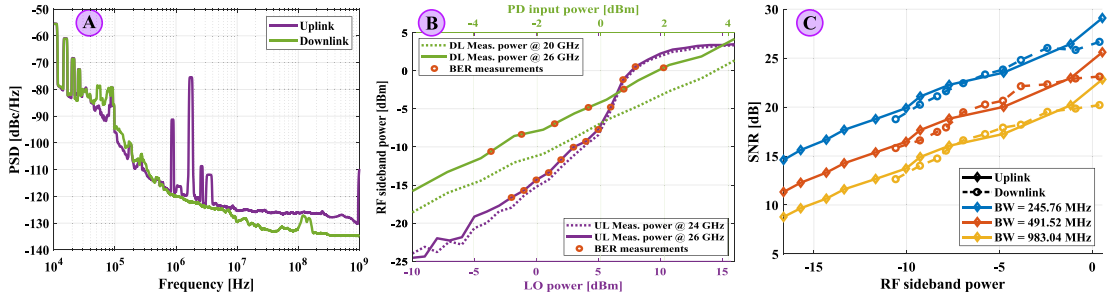


Fig. 4. Experimental measurements: phase noise measurements (A); power mapping conversion to RF sideband power (B); SNR as a function of the RF sideband power for both directions and the different bandwidth configurations (C).

Table 1
OFDM configuration parameters.

Config.	Sweep in subcarrier spacing [BW = 245.76 MHz]					
	1	2	3	4	5	6
Δf [kHz]	15	30	60	120	240	480
N	2^{14}	2^{13}	2^{12}	2^{11}	2^{10}	2^9
T_{cp} [μ s]	4.8	2.4	1.2	0.6	0.3	0.15

Config.	Sweep in bandwidth [$\Delta f = 240$ kHz]		
	A	B	C
BW [MHz]	245.76	491.52	983.04
N	2^{10}	2^{11}	2^{12}
T_{cp} [μ s]	0.3	0.3	0.3

the channel is equalized based on the DM-RS signals. Lastly, the QAM demodulator decodes the processed data symbols into bits.

Different OFDM configurations are generated and transmitted for both directions. In particular, two sweeps of one of the OFDM parameters are evaluated and compared. The first sweep is regarding the subcarrier spacing and the second one refers to the total bandwidth. The common OFDM parameters of these two sweeps are the following: 80% of the subcarriers are active, DM-RS signals on every 14th OFDM symbol or slot, and one subcarrier used as PT-RS on every 8th resource block (RB) [29]. Every RB is composed of 14 subcarriers [17]. The remaining parameters are detailed in Table 1 where Δf is the subcarrier spacing, N is the total number of subcarriers, T_{cp} is the CP duration, and BW is the transmitted bandwidth. Considering all the mentioned parameters, the transmitted spectral efficiency in term of baud rate is 0.683 Bd/Hz. Therefore, since the highest modulation order employed in the experimental testbed is 64-QAM and the largest used bandwidth is 983.04 MHz, the maximum achieved throughput is 4030 Mbps.

4. Transmission results

4.1. Experimental measures

The objective of this subsection consists of investigating and analyzing the main limiting factors of the proposed bidirectional transmission setup that is illustrated in Fig. 2. Phase noise is considered one of these main limiting factors in mm-wave ARoF systems, being more degrading in OFDM signals especially using the standardized 5G numerologies [28,30,31]. For this reason, the phase noise is measured in the experimental setup before the DPO of each direction. The resulting phase noise measures are shown in Fig. 4a. Since the carrier signals are shared and reused in both directions, the phase noise power spectral density (PSD) of the uplink and downlink are similar. Thus, the phase noise does not imply performance differences between both directions. In addition, the phase noise levels of Fig. 4a is relatively low and it

cannot be critical for high subcarrier spacing values such as 120 kHz or 240 kHz [28]. Hence, additional and complex phase noise compensation methods are not necessary to be employed for these subcarrier spacing configurations (Fig. 3).

Moreover, power shortage is another of the limiting factors in mm-wave wireless scenarios due to the high FSPL [5]. Then, power sweeps are realized in both direction to evaluate the performance of the proposed system in terms of SNR. As mentioned above, the power sweeps of the uplink and downlink are executed by modifying the power of the RF synthesizer located in the end-user and the EDFA, respectively. In order to properly compare the results of both directions, the experimental results must be represented on the same axis. Thus, the power sweeps of the uplink and downlink must be referred to the same parameter. The selected common parameter is the RF sideband power that is launched into the wireless link. This RF sideband power attributes to the power of the OFDM single-band signal located at 26 GHz in the spectrum, excluding the rest of transmitted signals such as the RF carrier. As mentioned above, the RF sideband powers are measured before the transmitter antennas of its respective direction (see points I and J of Fig. 2).

Fig. 4b represents the power map to get the desired RF sideband power of the two directions. Discrete points of the power sweeps are illustrated too with orange circles in these figures. These points are employed for the horizontal axis representation in the experimental results of the next subsection. The bottom x-axis of Fig. 4b concerns to the LO input power of the mixer located at the uplink path of the end-user. Meanwhile the top x-axis refers to the received optical power at the input of the PD located in downlink path. Furthermore, the powers related to the left OFDM side bands at 24 GHz and 20 GHz for the uplink and downlink, respectively, are also represented. The power of the left and right OFDM bands are very similar for the uplink direction (see Fig. 4b). However, examining the downlink measures of Fig. 4b, the power of the two OFDM sidebands are not symmetric in the downlink because several devices involved in the downlink path of the setup, such as the MPA, are less optimized at 20 GHz than at 26 GHz. Another important consideration regarding Fig. 4b is the linearity between the experimental power sweep values and the RF sideband power. By observing Fig. 4b, the uplink power map shows a saturation point at approximately 10 dBm of LO power due to the 1 dB compression loss of the end-user MPA. In addition, the uplink curves of Fig. 4b present two different slopes from -10 dBm to 10 dBm due to the non-linear transfer function of the RF mixer. For the downlink power map, the slope keeps constant with a value of ~ 2 dB/dB.

As mentioned before, different OFDM bandwidth configurations are evaluated in the experimental setup. The SNR is measured in the received signals for both directions and the different bandwidth configurations. These SNR measures are illustrated in Fig. 4c as a function of the RF sideband power at 26 GHz. The RF sideband power values are obtained from the power mapping exhibited in Fig. 4b.

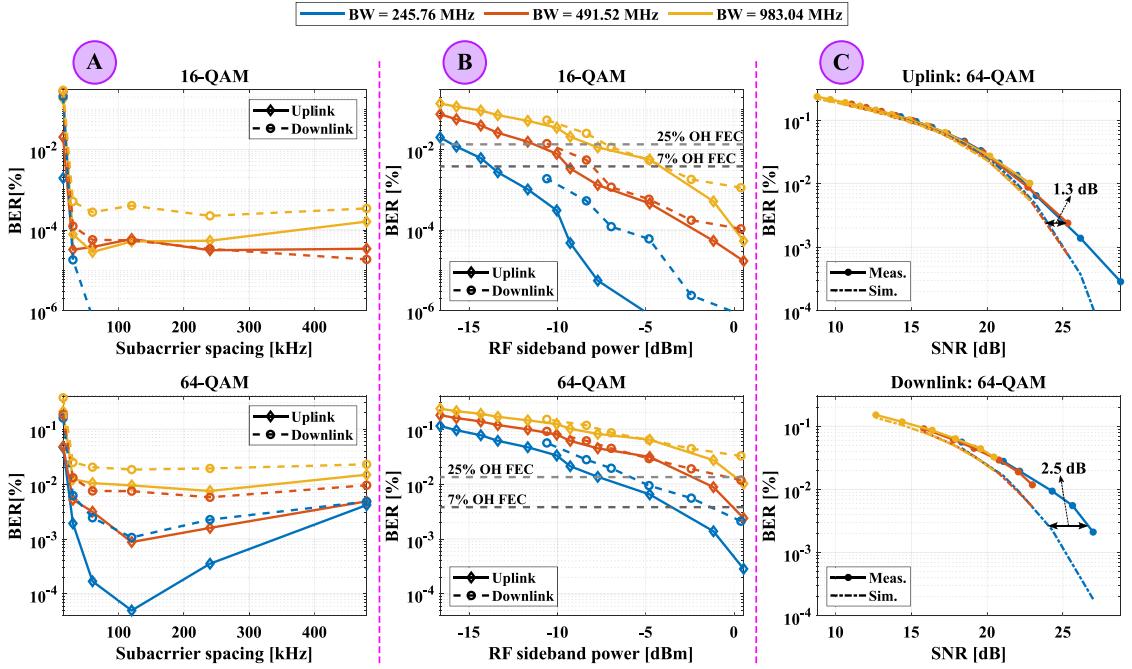


Fig. 5. Experimental results of both transmission directions for different bandwidth configurations and different modulation orders: BER as a function of the subcarrier spacing (A); BER as a function of the RF sideband power (B); and BER curves respecting the SNR comparing measured and simulated results (C).

By observing the SNR measures of Fig. 4c, it can be noticed that the downlink power sweep presents shorter range than in the uplink part. Moreover, SNR measures are quite similar for both directions in each bandwidth configuration. Hence, it can be determined that the SNR level is roughly the same for two directions at the same RF sideband power. This statement is relevant since the BER results of both directions will be compared by using the RF sideband power as the same x-axis parameter.

4.2. Experimental results

The experimental results of this work are shown, analyzed and discussed in this subsection. As commented in Section 3, the subcarrier spacing and bandwidth of the OFDM signal, and the wireless launched power are swept. Figs. 5a and 5b are obtained by processing the received signal of these sweeps for the uplink and downlink. Moreover, two different modulation orders are employed: 16-QAM (upper graphs) and 64-QAM (bottom graphs). Fig. 5a represents the BER results as a function of the subcarrier spacing for the different bandwidth configurations. The used OFDM parameters of these BER results are depicted in the sweep of subcarrier spacing section of Table 1. Examining the graphs of Fig. 5a, the BER presents an exponential decay as the subcarrier spacing increases for all the bandwidth configurations. This behavior is due to the fact that phase noise and the CFO introduce more distortion into the OFDM signal for lower subcarrier spacing values [28]. However, starting approximately at 120 kHz of subcarrier spacing, the BER shows a slight worsening for higher subcarrier spacing values. The reason of this BER behavior is because the subcarrier density is lower for higher subcarrier spacing values and, thus, the channel equalizer performs worse due to the shortage of DM-RS symbols (this behavior is easier perceived in the 64-QAM graph of Fig. 5a).

The results of Fig. 5a are obtained by setting the maximum power of the launched power sweep. Hence, by observing the BER results

of Fig. 5a, the best subcarrier spacing configuration can be selected. 120 kHz or 240 kHz of subcarrier spacing present the lowest BER for both directions, the evaluated modulation orders, and all the bandwidth configurations. It is relevant to highlight that the final phase noise of the experimental setup is not excessively high (Fig. 4a). Otherwise, the BER curves of Fig. 5a would tend to a continuous exponential decay [30]. Comparing the uplink and downlink BER results of Fig. 5a, it can be noticed that the uplink results show lower BER for all the cases. This BER difference between both directions appears more clearly in Fig. 5b. The BER results of Fig. 5b are plotted against the RF sideband power and for the three bandwidth configurations and a subcarrier spacing value of 240 kHz (see parameters of sweep in bandwidth of Table 1). The RF sideband power measurements of Section 4.1 are employed to plot these results. In addition, the 25% and 7% overhead (OH) FEC limits are illustrated in the graphs of Fig. 5b.

Inspecting the graphs of Fig. 5b, it can be observed that the BER decreases as the RF sideband power increments and the bandwidth decrements [21]. This BER dependence of the RF sideband power and the bandwidth are because these two parameters are directly related to the final SNR. Moreover, it is noticed a BER gap between the uplink and downlink results at the same RF sideband power. The reason of this gap is because the degradation of the signal in the downlink is higher than in the uplink. Another consideration to take into account is that the uplink achieves slightly higher RF sideband powers than in the opposite direction, accomplishing lower BER results. In the graphs of Fig. 5b, the BER value of all the cases is under the 25% OH FEC threshold at the maximum RF sideband power, except for the 64-QAM downlink case with 983.04 MHz of bandwidth. For the 16-QAM BER curves, all the cases are under the 7% OH FEC threshold at the maximum power. These BER yields under the OH FEC limits prove the validity of the proposed bidirectional AroF system as a strong candidate to be part of the future 5G mm-wave network.

In order to thoroughly analyze and understand the aforementioned experimental results, simulations are realized considering additive white Gaussian noise (AWGN), phase noise, and CFO. The AWGN is measured for the different configurations and all the RF sideband power points and, thus, the final SNR is obtained (see Fig. 4c). The phase noise is artificially simulated respecting the PSD curves of Fig. 4a. The achieved simulations and the experimental results are shown in Fig. 5c in terms of BER as a function of the measured SNR. The points of these BER results coincide sequentially with the RF sideband power points of Fig. 4c. In Fig. 5c, the 64-QAM modulation order is only considered and the uplink and downlink results are depicted in the upper and bottom graphs, respectively. Furthermore, it can be noticed in these two graphs that the different bandwidth configurations are overlapping because the selected x-axis parameter is the SNR instead of a power magnitude. The experimental and simulated BER curves of Fig. 5c exhibit a mismatch that increases as the SNR values increase. This fact provides a hint that the experimental results include non-linearity effects that are not considered in the simulations. For lower SNR values, the experimental and simulated BER curves are very similar because the AWGN is the dominant impairment. As the SNR increases, the non-linearity degradation becomes more degrading than the AWGN impairment.

Signal compression is one of the mentioned non-linearities in the experimental testbed of Fig. 2 and mainly comes from RF amplifiers and the signal modulation process in the MZM. In addition, the mismatch between the simulations and the experimental results is larger in the downlink than in the uplink and is numerically represented in Fig. 5c at 24 dB of SNR: 1.3 dB of SNR mismatch for the uplink and 2.5 dB for the downlink. The summary of conclusions regarding the results of Fig. 5c implies that the proposed bidirectional mm-wave AroF system presents more non-linearities in the downlink than in the uplink. The compression of the signal is measured for both directions at the different points of the power sweep. These compression results indicate that the downlink signals are more compressed than the uplink signals. The compression of the signal can be the main non-linearity factor of the received signal in the experimental setup and thus it determines the difference of non-linearity effects between both directions.

5. Conclusions

This article highlighted the importance of AroF to deploy, in a scalable way, future 5G mm-wave networks. To accomplish it, SDM and WDM were emphasized as suitable multiplexing techniques to enable a bidirectional AroF fronthaul with centralized beamforming. Consequently, an efficient and novel bidirectional AroF scheme based on the usage of MCF was experimentally demonstrated. The novelty of the proposed schematic resides in the utilization of MCF to enable an efficient AroF bidirectional link and the reuse of the carriers for the up and down-conversion processes of both transmission direction links. In this manner, the complexity, energy consumption, and cost are reduced. Moreover, the proposed schematic allows to transmit OFDM signals at the central frequency of n258 band (26 GHz, K-band) by employing the TDD multiplexing technique as the 5G standard determines.

To prove the validity of the proposed scheme for mm-wave 5G communications, a thorough measurement campaign was carried out by sweeping four different experimental parameters: the subcarrier spacing (covering all the 5G numerologies [15 kHz to 480 kHz]), the transmitted bandwidth, the modulation order (16-QAM and 64-QAM), and the launched wireless power. The transmitted OFDM signals in the experimental setup were in accordance with the 5G standard. Furthermore, experimental measurements such as phase noise and wireless power conversion were shown and discussed to evaluate the performance of the experimental setup. For reproducibility matters, the details of the employed DSP block of both transmitter and receiver parts

were also explained. Moreover, to optimize the overall performance, design considerations of the experimental testbed were described in detail.

The experimental results of both transmission directions were analyzed and compared in detail. The discussions of the results led to the conclusion that 120 kHz and 240 kHz of subcarrier spacing are the best configurations for the system under test. Another conclusion, achieved by comparing the experimental results and simulations, was that the downlink path performs worse in terms of non-linearity effect than the uplink. In addition, the experimental results exhibit acceptable pre-FEC BER values, proving the validity and efficiency of the proposed bidirectional AroF system as an excellent solution to play a significant role in beyond 5G mm-wave radio systems.

Declaration of competing interest

The authors declare the following financial interests/personal relationships which may be considered as potential competing interests: This work was partially financed by the 5G STEP FWD and blueSPACE projects (GA nos. 722429 and 762055).

Acknowledgments

This work was partially supported by the ITN 5G STEP-FWD and blueSPACE projects which have received funding from the European Union's Horizon 2020 research and innovation programme under grant agreements No. 722429 and 762055.

References

- [1] M. Jaber, M.A. Imran, R. Tafazolli, A. Tukmanov, 5G backhaul challenges and emerging research directions: A survey, *IEEE Access* 4 (2016) 1743–1766, <http://dx.doi.org/10.1109/ACCESS.2016.2556011>.
- [2] D. Konstantinou, T. Bressner, S. Rommel, U. Johannsen, M. Johansson, M. Ivashina, A.B. Smolders, I. Tafur Monroy, 5G RAN architecture based on analog radio-over-fiber fronthaul over UDWDM-PON and phased array fed reflector antennas, *Opt. Commun.* 454 (2020) 0030–4018, <http://dx.doi.org/10.1016/j.optcom.2019.124464>.
- [3] W.H. Chin, Z. Fan, R. Haines, Emerging technologies and research challenges for 5G wireless networks, *IEEE Wirel. Commun.* 21 (2) (2014) 106–112, <http://dx.doi.org/10.1109/MWC.2014.6812298>.
- [4] W. Jiang, B. Han, M.A. Habibi, H.D. Schotten, The road towards 6G: A comprehensive survey, *IEEE Open J. Commun. Soc.* 2 (2021) 334–366, <http://dx.doi.org/10.1109/OJCOMS.2021.3057679>.
- [5] I.A. Hemadeh, K. Satyanarayana, M. El-Hajjar, L. Hanzo, Millimeter-wave communications: Physical channel models, design considerations, antenna constructions, and link-budget, *IEEE Commun. Surv. Tutor.* 20 (2) (2018) 870–913, <http://dx.doi.org/10.1109/COMST.2017.2783541>.
- [6] S. Rommel, et al., Towards a scalable 5G fronthaul: Analog radio-over-fiber and space division multiplexing, *J. Lightwave Technol.* 38 (19) (2020) 5412–5422, <http://dx.doi.org/10.1109/JLT.2020.3004416>.
- [7] S. Rommel, et al., High-capacity 5G fronthaul networks based on optical space division multiplexing, *IEEE Trans. Broadcast.* 65 (2) (2019) 434–443, <http://dx.doi.org/10.1109/TBC.2019.2901412>.
- [8] A.H.M.R. Islam, M. Bakaul, A. Nirmalathas, G.E. Town, Simplified generation, transport, and data recovery of millimeter-wave signal in a full-duplex bidirectional fiber-wireless system, *IEEE Photon. Technol. Lett.* 24 (16) (2012) 1428–1430, <http://dx.doi.org/10.1109/LPT.2012.2205376>.
- [9] X. Pang, A. Lebedev, J.J. Vegas Olmos, I. Tafur Monroy, Multigigabit W-band (75–110 GHz) bidirectional hybrid fiber-wireless systems in access networks, *J. Lightwave Technol.* 32 (23) (2014) 4585–4592, <http://dx.doi.org/10.1109/JLT.2014.2361957>.
- [10] C. Ye, et al., A bidirectional multi-band 60-GHz wireless-over-fiber transmission system with compacted base station and mobile terminal using a robust mm-wave LO free technique, in: 2013 Optical Fiber Communication Conference and Exposition and the National Fiber Optic Engineers Conference, OFC/NFOEC, Anaheim, CA, USA, 2013, <http://dx.doi.org/10.1364/OFC.2013.OM3D.7>, OM3D.7.
- [11] C. Ye, et al., A bidirectional 60-GHz wireless-over-fiber transport system with centralized local oscillator service delivered to mobile terminals and base stations, *IEEE Photon. Technol. Lett.* 24 (22) (2012) 1984–1987, <http://dx.doi.org/10.1109/LPT.2012.2216257>.
- [12] P.T. Dat, A. Kanno, N. Yamamoto, T. Kawanishi, Full-duplex transmission of LTE-a carrier aggregation signal over a bidirectional seamless fiber-millimeter-wave system, *J. Lightwave Technol.* 34 (2) (2016) 691–700, <http://dx.doi.org/10.1109/JLT.2015.2466476>.

- [13] P.T. Dat, A. Kanno, N. Yamamoto, T. Kawanishi, Performance evaluation of full-duplex MIMO seamless fiber–wireless system in W-band, *IEEE Photon. Technol. Lett.* 30 (13) (2018) 1175–1178, <http://dx.doi.org/10.1109/LPT.2018.2837146>.
- [14] E. Ruggeri, et al., A 5G fiber wireless 4Gb/s WDM fronthaul for flexible 360° coverage in V-Band massive MIMO small cells, *J. Lightwave Technol.* 39 (4) (2021) 1081–1088, <http://dx.doi.org/10.1109/JLT.2020.3029608>.
- [15] Y. Liu, L. Ma, J. Xiong, C. Yang, M. Tang, W. Tong, Z. He, High-speed performance evaluation of graded-index multicore fiber compatible with multimode and quasi-single mode operation, *J. Lightwave Technol.* 38 (24) (2020) 6870–6878, <http://dx.doi.org/10.1109/JLT.2020.3019645>.
- [16] A. Kaszubowska-Anandarajah, A. Delmade, E. Martin, P. Anandarajah, L. Barry, C. Browning, Bidirectional fiber transmission of mmW signals using remote downconversion and wavelength reuse, in: *Conference on Lasers and Electro-Optics, CLEO, San Jose, CA, USA, 2019*, <http://dx.doi.org/10.1364/CLEO.SI.2019.SM4G.2>, SM4G.2.
- [17] 3GPP, FG IMT-2020: User equipment (UE) radio transmission and reception. 3GPP TR 38.101-2, version 16.5.0, 2020.
- [18] M. Fiorani, et al., Modeling energy performance of C-RAN with optical transport in 5G network scenarios, *IEEE J. Opt. Commun. Netw.* 8 (11) (2016) B21–B34, <http://dx.doi.org/10.1364/JOCN.8.000B21>.
- [19] R. Muñoz, et al., Experimental demonstration of dynamic optical beamforming for beyond 5G spatially multiplexed fronthaul networks, *IEEE J. Sel. Top. Quantum Electron.* 27 (6) (2021) 1–16, <http://dx.doi.org/10.1109/JSTQE.2021.3079726>.
- [20] J. He, et al., Experimental demonstration of bidirectional OFDM/OQAM-MIMO signal over a multicore fiber system, *IEEE Photon. J.* 8 (5) (2016) 1–8, <http://dx.doi.org/10.1109/JPHOT.2016.2607203>.
- [21] J.P. Santacruz, G. Nazarikov, S. Rommel, A. Jurado-Navas, I.T. Monroy, Bidirectional mm-Wave AroF fronthaul over multicore fiber for 5G and beyond, in: *2021 International Topical Meeting on Microwave Photonics, MWP, Pisa, Italy, 2021*, pp. 1–4, <http://dx.doi.org/10.1109/MWP53341.2021.9639425>.
- [22] S. Rommel, et al., Real-time high-bandwidth mm-wave 5G NR signal transmission with analog radio-over-fiber fronthaul over multi-core fiber, *EURASIP J. Wireless Commun. Networking* 43 (2021) 1–20, <http://dx.doi.org/10.1186/s13638-021-01914-6>.
- [23] J.P. Santacruz, et al., Experimental AroF system based on OPLL mm-wave generation for beyond 5G, in: *26th OptoElectronics and Communications Conference, Hong Kong, China, 2021*, <http://dx.doi.org/10.1364/OECC.2021.W2B.2>, W2B.2.
- [24] J. Yu, Z. Jia, L. Yi, Y. Su, G.-K. Chang, T. Wang, Optical millimeter-wave generation or up-conversion using external modulators, *IEEE Photon. Technol. Lett.* 18 (1) (2006) 265–267, <http://dx.doi.org/10.1109/LPT.2005.862006>.
- [25] 3GPP, FG IMT-2020: Study on new radio (NR) access technology. 3GPP TR 38.912, version 16.0.0, 2020.
- [26] B. Lim, Y.-C. Ko, SIR Analysis of OFDM and GFDM waveforms with timing offset, CFO, and phase noise, *IEEE Trans. Wirel. Commun.* 16 (10) (2017) 6979–6990, <http://dx.doi.org/10.1109/TWC.2017.2736998>.
- [27] Y. Ha, W. Chung, A feedforward partial phase noise mitigation in the time-domain using cyclic prefix for CO-OFDM systems, *J. Opt. Soc. Korea* 17 (6) (2013) 467–470, <http://opg.optica.org/josk/abstract.cfm?URI=josk-17-6-467>.
- [28] J.P. Santacruz, S. Rommel, U. Johannsen, A. Jurado-Navas, I.T. Monroy, Analysis and compensation of phase noise in mm-wave OFDM AroF systems for beyond 5G, *J. Lightwave Technol.* 39 (6) (2021) 1602–1610, <http://dx.doi.org/10.1109/JLT.2020.3041041>.
- [29] Y. Qi, M. Hunukumbure, H. Nam, H. Yoo, S. Amuru, On the phase tracking reference signal (PT-RS) design for 5G new radio (NR), in: *2018 IEEE 88th Vehicular Technology Conference, VTC-Fall, Chicago, IL, USA, 2018*, pp. 1–5, <http://dx.doi.org/10.1109/VTCFall.2018.8690852>.
- [30] A. Delmade, et al., OFDM baud rate limitations in an optical heterodyne analog fronthaul link using unlocked fibre lasers, in: *International Topical Meeting on Microwave Photonics, MWP, Ottawa, ON, Canada, 2019*, pp. 1–4, <http://dx.doi.org/10.1109/MWP.2019.8892190>.
- [31] J.P. Santacruz, et al., Probabilistically shaped OFDM for gradual capacity adaptation in 5G AroF systems, in: *26th OptoElectronics and Communications Conference, Hong Kong, China, 2021*, <http://dx.doi.org/10.1364/OECC.2021.W1B.4>, W1B.4.

Beamforming for mm-wave mobile communications

The goal of this chapter is to respond the research questions **RQ-6**, **RQ-7**, and **RQ-8**. As discussed in Section 2.4, the received power in mm-wave wireless channels is highly reduced by FSPL and material penetration, among other physical phenomena. Increasing the antenna gain is one of the most convenient ways to solve the power limitation in mm-wave wireless scenarios. By narrowing the beamwidth of the antenna, its radiation pattern is more directive and, thus, the gain increases in the angle of the antenna direction. Nonetheless, highly directive antennas suffer more from misalignment than omnidirectional ones, leading to severe power penalties, especially if the user is mobile. Therefore, in mobile communications, the main beam angle of the antenna requires to track the user in order to ensure adequate link power. Beam steering allows this tracking mechanism and can be simply implemented by using a mechanical system. However, mechanical beam steering systems are bulky, slow, power-hungry, and unreliable [165].

As a solution to the inefficient mechanical approach, electrical beam steering emerges as an excellent technique. Electrical beam steering is intrinsically linked to the realization of beamforming with a set of equidistributed antennas or AA. The beamwidth and maximum gain of an AA are inversely and directly proportional to the number of antenna elements involved in the AA, respectively. Moreover, for electrical beam steering, the same signal is sent to multiple antenna elements, but with shifted phase, causing positive interference between these signals only at some angles, while negative interference at others. This phase shifting process is usually realized with RF phase shifter blocks, which are attached to a specific antenna element. Hence, by correctly modifying the configuration of the phase shifters, the angle of the main beam, formed by the AA, changes. Electrical beam

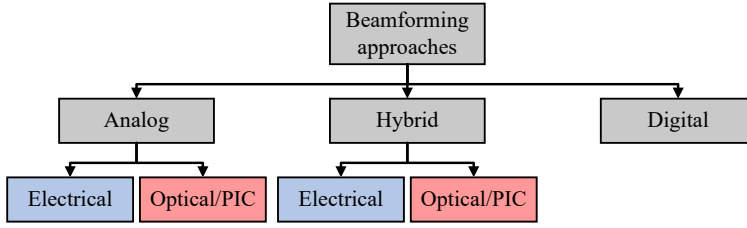


Figure 6.1: Types of beamforming approaches.

steering based on beamforming highlights for its low footprint, high reliability, low power consumption, and fast steering operation, compared to the mechanical approach. The structure of this chapter is organized as follows: Section 6.1 introduces a summary of the main categories of beamforming. Next, ARoF fronthaul architectures oriented towards mm-wave beamforming applications are presented in Section 6.2. Finally, Section 6.3 presents the two contribution works of this dissertation regarding experimental demonstration of beamforming for the mm-wave ARoF fronthaul: study, analysis, and characterization of an iOBFN PIC based on optical true time delay (TTD); and mm-wave outdoor experiment implementing an IFoF setup with phased array antennas.

6.1 Beamforming approaches

As mentioned above, beamforming is an essential technology for realizing reliable mm-wave mobile communications. There are three main categories of beamforming, as Fig. 6.1 illustrates: analog, digital, and hybrid. Hybrid beamforming combines analog and digital approaches. In low data rate communications, digital beamforming is widely employed because of its efficient digital calibration and multi-beam transmission [166]. However, the power consumption of digital beamforming realizations is proportional to the effective number of bits (ENoB) and sampling rate of the involved ADCs and DACs [29]. Therefore, for mm-wave broadband communications where high sampling rates are required, digital beamforming is unsustainable in terms of energy consumption and cost [29]. Hence, analog and hybrid beamforming approaches rise as suitable technologies for mm-wave mobile communications.

The scope of this dissertation focuses on the study, analysis, and experimental demonstration of analog beamforming for the mm-wave ARoF fronthaul. More specifically, analog beamforming can be implemented in two different domains (see Fig. 6.1): electrical or optical. Electrical beamforming has been well studied and investigated in the literature with respect to the optical approach. Electrical and optical beamforming approaches offer different advantages and disadvantages.

Table 6.1 qualitatively compares three different analog beamforming approaches:

Table 6.1: Qualitative comparison between three different analog beamforming approaches: electrical, optical, and PIC.

Approach → Characteristic ↓	Electrical beamforming	Optical beamforming	PIC beamforming
Bandwidth	Lower	Higher	Higher
Losses	Higher	Lower	Lower
Cross-talk	Higher	Lower	Lower
Complexity	Lower	Higher	Higher*
Maturity	High	Medium	Low

(*) → Integrated photonic circuits allow to miniaturize the complex systems linked to optical beamforming solutions.

electrical, optical, and PIC. As it can be observed, optical beamforming is a better solution than the electrical approach in terms of bandwidth of the transmitted signal, transmission losses, and cross-talk. However, compared to the electrical solution, optical beamforming includes E/O and O/E blocks, which increases the complexity of the system. Hence, PIC beamforming arises as a suitable solution for the optical approach since it reduces footprint and power consumption. Nonetheless, the technology maturity of PIC beamforming is still at the research stage. Therefore, further investigations are required to establish PIC beamforming as a mature technology for future mobile networks. Nevertheless, electrical, optical, and PIC beamforming approaches share the same theoretical foundations, which will be briefly introduced in the following paragraphs.

As discussed earlier at the beginning of this chapter, AA combined with phase shifters allows realizing beam steering in the formed beam. The array factor (AF) mathematically describes the beamforming and beam steering processes. The AF of a set of antennas equally distributed a round zero on the x-axis can be formulated as [167]:

$$AF_m(\theta) = \sum_{n=1}^{N_{ant}} w_{m,n} \cdot e^{-jnk\Delta d[\sin(\theta) - \sin(\alpha'_m)]}, \quad (6.1)$$

where N_{ant} is the number of antennas in the AA, Δd is the separation between antennas, θ is the azimuth angle, and k is the wavenumber. In Eq. (6.1), the term α'_m refers to the angle with the maximum AF value ($\theta_{max} = \alpha'$ for the beam m -th). Moreover, $w_{m,n}$ of Eq. (6.1) corresponds to the complex weight associated with the beam and antenna element with indexes m and n , respectively. This complex number is intrinsically related to the phase shift value of the phase shifter linked to its corresponding antenna element. At this point, it is important to mention that the analog realization of the w term in Eq. (6.1) can be performed by other building blocks such as optical/electrical waveguides or optical ring resonators (ORRs) [168], [169].

Figure 6.2 shows a representation of the explained AF equation. Figure 6.2(a)

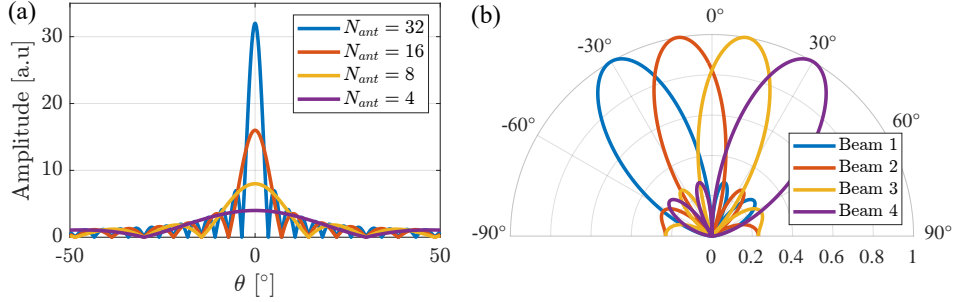


Figure 6.2: Array factor representation: (a) AF for different N_{ant} ; (b) Normalized AF for different beam angles ($N_{ant} = 4$).

depicts the absolute value of AF when all complex weights (w of Eq. (6.1)) are equal to 1 and $\alpha' = 0$. Furthermore, Fig. 6.2(a) illustrates the AF for different numbers of antennas (N_{ant}). By observing Fig. 6.2(a), it can be noticed that the beamwidth decreases as N_{ant} increases. Nevertheless, the maximum AF value (α') is proportional to the number of employed antennas. In addition, when the beamwidth of the AA is small, beam alignment and calibration becomes more complex [29]. In Fig. 6.2(b), the normalized AF for different beam angles (α'_m) is plotted in polar coordinates for four antenna elements ($N_{ant} = 4$). To achieve the beam angles illustrated in Fig. 6.2(b), the complex weight values of Eq. (6.1) must be correctly set. Taking into account the beam steering property of Eq. (6.1), multiple beams can be generated simultaneously on a single AA. To achieve this, the signal from each antenna element must be distributed along a phase shifter structure, commonly called as Blass matrix. The dimension of such Blass matrix is proportional to the number of antenna elements of the AA and the number of beams. **P11** presents an optical Blass matrix capable of generating four independent beams for an AA of four elements.

6.2 ARoF fronthaul architecture with beamforming implementation

This section aims to explain the key points to integrate beamforming applications in the mm-wave ARoF fronthaul. In Section 5, several RoF architectures for the mobile fronthaul were explained. In this section, the mm-wave ARoF and IFoF fronthauls of Figs. 5.2(b) and (c) are integrated with beamforming. Figure 6.3(a) shows a mm-wave ARoF fronthaul where multiple beams are generated from a single AA due to the use of an optical beamforming network (OBFN). First, in Fig. 6.3(a), the baseband signal for each user of the RAU is generated at the CO. In this case, the number of generated baseband signals is equal to the number of beams to be produced. In other words, for this implementation, each user

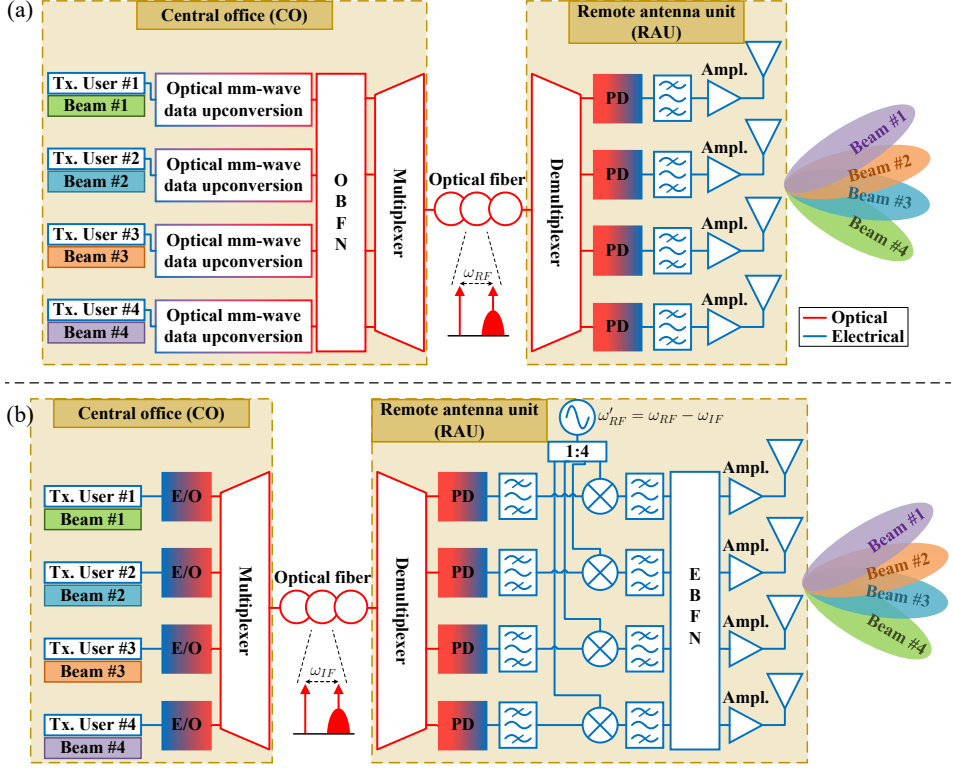


Figure 6.3: AROf fronthaul architectures for the generation of multiple beams: (a) mm-wave AROf fronthaul with optical beamforming network (OBFN); (b) IFoF fronthaul with electrical beamforming network (EBFN).

is independently associated with a beam. An alternative implementation of this multi-beam generation is to divide the area into small sectors. After the baseband blocks, the resulting electrical signals are converted to the optical domain by using two optical tones with a spectral separation of the desired mm-wave frequency. This conversion process is performed in the block denominated optical mm-wave data upconversion, which can be implemented by utilizing one of four systems depicted in Fig. 2.3. Next, the resulting optical signal passes through an OBFN block.

In the OBFN process, the N_{beam} optical signals are combined and delayed according to Eq. (6.1), obtaining N_{ant} optical signals. Each of the obtained N_{ant} optical signals is linked to a single antenna element of the AA. Subsequently, the N_{ant} optical signals, at the output of the OBFN, are multiplexed to be transported through the optical fiber [170]. For this multiplexing process, different technologies can be implemented: space division multiplexing (SDM) by using MCF and

WDM by utilizing SSMF. It is relevant to mention that in order to maintain the beamforming properties, the multiplexing, demultiplexing, and optical fiber transport procedures must preserve the relative delay between the different antenna signals. For this delay preservation, as discussed in Section 5.2, SDM by using MCF is a preferred option since the relative delays between the different MCF cores are negligible for mm-wave beamforming applications [159]. Because of this fact, SDM with MCF is the chosen multiplexing and transport technology in **P3**, **P9**, and **P10**. In the RAU, a demultiplexing process is carried out to recover the N_{ant} optical signals. Then, with a set of N_{ant} PDs, the data signal is directly upconverted to the mm-wave domain. After this, filtering and amplification blocks are performed to prepare the signal for the wireless transmission. Finally, in the AA, N_{beam} beams are formed whose angles are determined in the OBFN block of the CO. As it can be observed in Fig. 6.3(a), most of the processes are carried out in the CO, which allows the beamforming function to be managed in a centralized manner. Moreover, the simplicity of the RAU for this mm-wave ARoF fronthaul integrated with beamforming enables a scalable mm-wave 5G/6G deployment.

However, in the beamforming architecture of Fig. 6.3(a), the main challenge lies in preserving the relative delay between the antenna signals generated in the OBFN. This preservation remains more difficult when the OBFN is placed in the CO. One way to relax these delay preservation constraints consists of moving the OBFN block to the RAU, with the penalties of losing centralization and increasing the RAU complexity. Another alternative to reduce the delay preservation constraints lies in the realization of an electrical beamforming network (EBFN) in the RAU, harnessing the maturity of the electrical beamforming technology. At this point, it is worth mentioning that the location of the beamforming network (BFN) determines the number of optical signals transported in the optical fiber. By placing the BFN at the CO, N_{ant} signals are sent through the optical fiber while N_{beam} signals require to be transported when the BFN is at the RAU side.

Figure 6.3(b) illustrates a beamforming architecture for the mobile fronthaul based on IFoF transport where the EBFN is located in the RAU. First, in Fig. 6.3(b), the baseband signal of each user is generated in the CO and, subsequently, upconverted to the IF domain. Then, the resulting N_{beam} IF signals are converted to the optical domain with a set of E/O blocks. Next, for optical fiber transport, the N_{beam} optical signals are multiplexed. In this case, the selection of the multiplexing technology (SDM or WDM) is not limited by the delay preservation constraint, giving more flexibility for the deployment in this beamforming architecture.

After optical fiber transport in Fig. 6.3(b), the electrical IF signals are retrieved by using a set of N_{beam} PDs. Thus, after a previous filtering process, the electrical signals are upconverted to the mm-wave band by employing a set of RF mixers and an RF oscillator. Then, after another filtering process, the upconverted signals pass through an EBFN block. This EBFN block can be implemented with one of the different approaches explained in [171]. After boosting the RF signals with a set of amplifiers, multiple beams are formed at the AA.

Comparing the architectures of Figs. 6.3(a) and (b), it can be noted that the IFoF implementation contains more components in the RAU than the mm-wave ARoF one, making it less viable for the massive deployment of the expected number of mm-wave RAUs in future mobile networks. Nevertheless, the IFoF architecture of Fig. 6.3(b) stands out for its lower delay preservation requirements since this requirement only needs to be satisfied at the edge of the RAU. Therefore, there is a trade-off between delay preservation constraints along the mobile fronthaul and RAU complexity, as both architectures show in Fig. 6.3. In addition, the number of RF amplifiers and RF filters of both architectures scales with N_{ant} . On the other hand, the number of PDs scales with N_{ant} and N_{beam} for the architectures of Figs. 6.3(a) and (b), respectively.

6.3 Experimental demonstrations of mm-wave fronthaul with beamforming

The objective of this section is to explain the experimental demonstrations, that are included in the articles of this dissertation regarding beamforming implementations for the mobile fronthaul. As discussed above, optical beamforming is a promising technology for mm-wave beamforming applications. Nonetheless, there is a scarcity of studies in the literature concerning OBFN implementations for multi-beam transmission. Due to this fact, the work in [170] presents, for the first time to the best of the author's knowledge, an incoherent OBFN PIC based on optical waveguides capable to generate four beams at 27.5 GHz. At this point, it is necessary to differentiate between coherent and incoherent optical beamforming. Coherent optical beamforming is based on the usage of optical phase shifting. In contrast, incoherent optical beamforming does not use optical phase shifting, enabling the utilization of multiple wavelength sources.

P11 extends the work of [170] with an exhaustive theoretical study and analysis of the building blocks that compose the proposed OBFN. Moreover, **P11** qualitatively compares the electrical and optical beamforming approaches by using several KPIs. **P11** also performs a comprehensive characterization of all the building blocks involved in the presented OBFN structure, linking the measurement results with the theoretical formulations. The experimental measurements are in accordance with the expected values, which were decided during the design stage. Therefore, the experimental measurements validate the proposed OBFN as a suitable solution for mm-wave beamforming applications. More in-depth, the OBFN PIC, fully characterized in **P11**, is designed to be employed in a mm-wave ARoF fronthaul architecture as the one illustrated in Fig. 6.3(a). More specifically, this OBFN PIC is designed for the uplink direction. More details about this PIC can be found in **P11**. In conclusion, the work of **P11** validates the viability and feasibility of OBFNs based on optical waveguides to be part of the future architecture in the mm-wave 5G/6G fronthaul.

On the other hand, in **P12**, a throughout measurement campaign is carried out in a mm-wave outdoor scenario by using electrical beamforming. The experimental setup used in **P12** corresponds to an IFoF fronthaul as shown in Fig. 6.3(b). In particular, this experimental setup is performed to generate a single beam that serves one end-user. Furthermore, a pair of 64-element phased array antennas with analog RF beamforming are utilized to track the end-user. One phased array antenna is located at the RAU and end-user sites, respectively. The 64-element phased array antennas compose of an 8x8 matrix, enabling beam steering at both elevation and azimuth angles. Respecting the configuration of the transmitted waveform in **P12**, OFDM signals with 400 MHz of bandwidth and 240 kHz of subcarrier spacing, as the 5G standard determines [19], are sent through the experimental setup. These OFDM signals are transmitted at 27 GHz in the wireless link. In addition, the measurement campaign of **P12** covers the following wireless scenarios: diverse end-user locations with different angles and distances between transmitter and receiver antennas; LOS and NLOS links. In all these scenarios, a double sweep of the azimuth beam angle of both antennas is performed, allowing empirical assessments on the communication performance in case of misalignment errors. Moreover, two different antenna configurations are compared in a LOS scenario: low sidelobe level (SLL) and maximum main lobe level. For the low SLL antenna configuration, SLLs are minimized, diminishing the interference with other possible users, at the cost of decreasing the gain of the main lobe. As a conclusive remark, the experimental results of **P12** exhibit low error vector magnitude (EVM) values for 64-QAM modulation order, proving the feasibility of ARoF systems, in particular IFoF, as an excellent fronthaul technology combined with phased array antennas to be considered in future 5G/6G standards.

P11: Incoherent Optical Beamformer for ARoF Fronthaul in Mm-wave 5G/6G Networks

J. P. Santacruz, S. Rommel, C. G. H. Roeloffzen, *et al.*, “Incoherent Optical Beamformer for ARoF Fronthaul in Mm-wave 5G/6G Networks,” *Journal of Light-wave Technology*, 2022, [under review]

Incoherent Optical Beamformer for ARoF Fronthaul in Mm-Wave 5G/6G Networks

Javier Pérez Santacruz, Simon Rommel, *Member, IEEE, Member, Optica*, Chris G. H. Roeloffzen, Roelof Bernardus Tiemens, Paul W. L. van Dijk, Antonio Jurado-Navas, *Member, Optica*, and Idelfonso Tafur Monroy, *Senior Member, IEEE*,

Abstract—Analog beamforming is a key technology to enable millimeter-wave (mm-wave) mobile communications. Nonetheless, the most widespread beamforming solutions are based on electrical implementation, which is inefficient in terms of power consumption, signal bandwidth, and losses. Optical beamforming is a promising alternative for future mm-wave mobile communications due to its inherent benefits, such as large bandwidth, low cross-talk, and low losses. Optical beamforming networks (OBFN) are an outstanding technique to simultaneously generate and radiate multiple beams in an effective manner. True time delays (TTDs) based on optical waveguides are an attractive solution since they offer constant delay in the spectrum to avoid beam squint and allow highly scalable OBFN implementation. In this work, for the first time to the best of the authors' knowledge, an incoherent 4x4 OBFN based on optical waveguides and capable of simultaneously generating four beams is presented, including a thorough explanation of its operating principles and providing a detailed characterization. The presented OBFN is fabricated on Si₃N₄ photonic integrated circuit (PIC), and designed for transmission at 27.5 GHz, within the n257 5G band. Furthermore, the building blocks forming the OBFN PIC are deeply explained, providing their corresponding theoretical formulation and key design parameters. The fabricated PIC is exhaustively characterized through all its building blocks, showing in detail the realized measurement procedure. The experimental measures match the design parameters with minimal error, showing the feasibility of fabricating future OBFNs with the same technology and topology for larger antenna arrays. The experimental results corroborate the viability of the presented OBFN architecture as an excellent technology to consider in future mm-wave 5G/6G networks. The contribution of this work paves the road to turn optical beamforming into a mature, scalable, and efficient technology.

Index Terms—Optical Beamforming, OBFN, True time delay, 5G, 6G, ARoF, mm-wave, Fronthaul.

Manuscript received July ??, 2022; revised MMM DD, 2022, accepted MMM DD, YYYY. This work was partially supported by the ITN 5G STEP-FWD and blueSPACE projects which have received funding from the European Union's Horizon2020 research and innovation program under grant agreements No. 722429 and 762055.

J. Pérez Santacruz, S. Rommel and I. Tafur Monroy are with the Institute for Photonic Integration, Eindhoven University of Technology, 5600 MB Eindhoven, The Netherlands (e-mail: j.perez.santacruz@tue.nl; s.rommel@tue.nl; i.tafur.monroy@tue.nl).

Chris G. H. Roeloffzen, Roelof Bernardus Tiemens and Paul W. L. van Dijk are with Lionix International BV, 7521 AN Enschede, The Netherlands (e-mail: c.g.h.roeloffzen@lionix-int.com; r.b.tiemens@lionix-int.com; p.w.l.vandijk@lionix-int.com).

A. Jurado-Navas is with the Wireless Optical Lab, Instituto Universitario de Investigación en Telecomunicación (TELMA), University of Málaga, CEI Andalucía TECH E.T.S.I. Telecomunicación, 29010 Málaga, Spain (e-mail: navas@ic.uma.es).

Color versions of one or more of the figures in this paper are available online at <http://ieeexplore.ieee.org>.

Digital Object Identifier 10.1109/JLT.2022.XXXXXX

I. INTRODUCTION

MOBILE data traffic has followed an exponential trend in last years, requiring constant updating and enhancement of the mobile network. The fifth generation (5G) of mobile networks is the current solution to fulfill the demanding traffic requirements, with 6G being the next generation [1]. Since sub-7 GHz bands are highly congested, moving to higher frequency bands is seen as the obvious next step to increase the data bit rate in the mobile network. Millimeter-waves (mm-wave) are the next operating frequency range to exploit, offering large bandwidths available to use. However, compared to sub-7 GHz bands, the usage of mm-wave signals implies a substantial increase in free-space path loss (FSPL) [2].

Beamforming technique emerges as an excellent solution to alleviate the power limitations linked to wireless transmission of mm-wave signals [3]. In particular, digital implementation is one of the most widespread beamforming approaches [4]. However, digital beamforming requires a large number of digital-to-analog converters (DACs) and analog-to-digital converters (ADCs), especially in the case of massive multiple-input and multiple-output (MIMO) applications. Hence, the digital approach is infeasible in terms of cost, power consumption, and complexity to deploy beamforming with numerous antennas and beams. Consequently, analog and hybrid beamforming are alternative solutions to the digital approach where the number of required DACs and ADCs is reduced, enabling an efficient deployment of massive beamforming [5]. To perform analog beamforming, the utilization of RF phase shifters is the most studied solution [3]. Nonetheless, beamforming technology based on phase shifting is limited by beam squint, which is especially critical in broadband wireless scenarios such as in mm-wave 5G/6G communications [6]. True time delay (TTD) based beamforming is an alternative solution to the phase shifter approach. Optical TTD is more attractive than electrical implementations because of its low cross-talk and propagation losses, allowing to reduce power consumption [7], [8].

The optical ring resonator (ORR) and optical waveguide are the most common optical TTD devices in the literature [9], [10]. However, ORRs imply a finite delay bandwidth, limiting the operating bandwidth [9]. To clarify, a delay bandwidth of BW_x refers to the bandwidth range where the delay error remains below x , with x being a time unit. Moreover, the binary tree structure is linked to ORR based beamforming for single beam implementations. Thus, ORR based beamform-

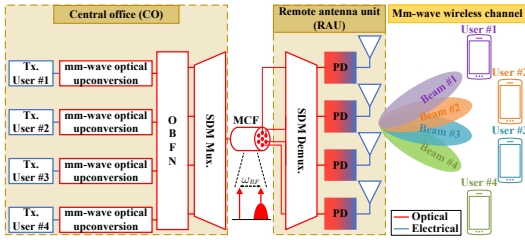


Figure 1. C-RAN scheme integrated with ARoF and OBFN technologies for the mm-wave 5G/6G fronthaul. Tx: transmitter. E/O: electrical to optical conversion. O/E: optical to electrical conversion.

ing does not extend well, in terms of scalability, to multi-beams implementations which are based on OBFN matrix realization [9]. As a consequence, OBFN based on optical waveguides arises a suitable solution in terms of scalability, power consumption, and signal bandwidth [11], [12]. Photonic integrated circuits (PICs) are a promising technology to perform optical processes in a miniaturized manner, reducing footprint, cost, and power consumption, especially on silicon nitride (Si_3N_4) platforms [13]. In addition, PIC brings other benefits such as high scalability, stability, and cost efficiency for volume production. Therefore, OBFN based on PIC optical waveguide implementation is a well-suited solution for high data rate communications in mm-wave 5G/6G networks.

In this work, for the first time to the author's knowledge, an incoherent OBFN PIC based on optical waveguides and fabricated in Si_3N_4 is presented and extensively discussed. In addition, to complement the work of this manuscript, an in-depth study and analysis of the principles of the proposed OBFN PIC are provided along with a full chip characterization. The organization of this manuscript is as follows: first, Section II gives an overview of the function and role of OBFN in the future mm-wave 5G/6G architecture; next, in Section III, the principles and fundamentals of the proposed incoherent OBFN PIC are thoroughly explained; then, in Section IV, the OBFN PIC is shown together with a comprehensive characterization of its components; finally, Section V summarizes the work and draws a number of conclusions.

II. OBFN IN THE MM-WAVE 5G/6G FRONTHAUL

Analog radio-over-fiber (ARoF) emerges as an excellent solution for mobile fronthaul since it brings attractive benefits such as low complex remote antenna unit (RAU), low latency, and high spectral efficiency [14]. These benefits make ARoF a suitable technology to deploy, in a scalable manner, the enormous quantity of mm-wave RAUs expected for the future 5G/6G network [14]. Moreover, ARoF allows efficient implementation of a centralized-radio access network (C-RAN) architecture, leading to a reduction in operation and maintenance cost, latency and energy consumption [15]. Therefore, C-RAN based on ARoF is considered one of the most prominent candidates to be part of the future mm-wave 5G/6G architecture [14].

Fig. 1 shows a general scheme of the ARoF C-RAN solution for the mm-wave 5G/6G fronthaul where several users are served by a single RAU. In the central office (CO) of Fig. 1, the transmitter block of each beam is realized and baseband signals are generated. These transmitter procedures can be carried out together in a baseband unit (BBU). For mm-wave transport in the optical fiber, the resulting electrical signal of each user is introduced into an mm-wave optical upconverter block. This block performs the optical two-tone generation and the optical modulation of the baseband data signal [16]. The frequency separation between the generated tones corresponds to the operating mm-wave frequency (f_{RF}). RF power fading induced by chromatic dispersion may be avoided by modulating only one of the optical tones with the data signal [17]. Next, the resulting optical modulated signals pass through an OBFN block. After the OBFN block beamforming process, the optical signals are individually transported through a multicore fiber (MCF). The main purpose of the OBFN block is to generate a multi-beam stream by effectively creating a mapping between the N_{beam} independent beam inputs and the N_{ant} antenna outputs. In the OBFN, every input is mapped to every output with a certain and progressive delay, generating multiple beams with independent angles [14].

At this point, it is important to mention that locating the OBFN in the CO results highly beneficial in terms of resource management, latency, and reducing the complexity of the RAUs. However, locating the OBFN block in the CO implies preserving the relative delay between the produced optical signals in order to maintain beamforming properties [18]. This delay conservation constraint is extremely challenging for multiplexing technologies such as wavelength division multiplexing (WDM). Nevertheless, MCF is an ideal solution for preserving the relative delay among optical signals, since the differential delays between the MCF cores are negligible for mm-wave beamforming applications [19]. Therefore, space division multiplexing (SDM) based on MCF is a preferred multiplexing technology for transporting the different antenna element signals of a specific RAU.

After the MCF transmission, an optical to electrical (O/E) conversion is performed in the RAU with a set of photodiodes (PDs), directly generating mm-wave signals by optical heterodyne. Then, each of the resulting mm-wave signals is filtered, boosted, and sent to its corresponding antenna element. Finally, the data signals at the OBFN output reach their corresponding antennas at the desired mm-wave frequency, generating multiple beams whose angles are determined by the delay matrix of the OBFN block. In this way, in Fig. 1, multiple users are served by different beams depending on their location. The generation of multiple beams results from the combination of the antenna array (AA) of the RAU together with the OBFN located in the CO. Furthermore, in Fig. 1, it can be noticed that most of the processes are performed in the CO, which reduces the complexity of the RAU and, then, enables a scalable deployment of the future mm-wave 5G/6G fronthaul [14]. As a last remark, Fig. 1 displays a downlink communication. Nonetheless, an uplink system can be implemented by performing an inverse procedure.

Electrical approach is the most studied analog beamform-

Table I
QUALITATIVE COMPARISON BETWEEN THE THREE DIFFERENT ANALOG
BEAMFORMING APPROACHES: ELECTRICAL, OPTICAL, AND PIC [7], [8],
[12].

Approach → Characteristic ↓	Electrical beamforming	Optical beamforming	PIC beamforming
Bandwidth	Lower	Higher	Higher
Losses	Higher	Lower	Lower
Cross-talk	Higher	Lower	Lower
Complexity	Lower	Higher	Higher*
Maturity	High	Medium	Low

(*) → Integrated photonic circuits enable miniaturizing of the complex systems attached to optical beamforming solutions.

ing technology [3]. However, as discussed above, electrical beamforming is not a preferred solution for broadband communications due to its beam squint problem, which limits the operating bandwidth [20]. There are other indicators that determine the suitability of a beamforming solution. Table I exhibits a qualitative comparison between three different beamforming approaches: electrical, optical, and PIC. This comparison is performed in terms of signal bandwidth, losses, cross-talk, system complexity, and technology maturity [7], [8], [12]. Optical and PIC beamforming approaches stand out for their wide operating bandwidth, respecting electrical solutions, highlighting their suitability for broadband mm-wave communications. Moreover, observing Table I, it can be noted that the main disadvantage of optical and PIC beamformings, compared to the electrical approach, is the system complexity. This fact is because optical and PIC beamformings require the usage of electrical to optical conversion blocks and vice versa, which augments the complexity of the system with respect to electrical solutions. Besides, for the optical beamforming approach, discrete components are needed, which implies bulky and low power efficiency systems [21], [22]. One of the main advantages of PIC beamforming is the reducing of footprint and power consumption, which lessens the impact of the system complexity drawback. However, the PIC beamforming technology is still at a recent stage, as can be seen in Table I. Fortunately, with the constant evolution of PIC technology in recent years, integrated optical beamforming is positioned as a promising candidate for future beamforming applications.

III. INCOHERENT OBFN PRINCIPLES

Coherent and incoherent implementations are the two main approaches to realize beamforming in the optical domain. Coherent optical beamforming relies on optical phase shifting. On the other hand, incoherent optical beamforming does not require optical phase shifting, which allows the use of multiple wavelength sources [18]. One of the most widespread methods for realizing optical coherent beamforming is based on the usage of phase shifters. To perform an OBFN with phase shifters, it is necessary to accomplish a carrier suppression and re-insertion process [20]. This process consists of filtering the optical carrier and re-inserting it before and after the phase shifter block, respectively. In this way, the resulting RF signal, after the optical heterodyne process in the PD, carries the desired phase shift [20]. However, this filtering and re-insertion process increases the system complexity, especially for OBFNs

with numerous inputs and outputs. As commented in Section I, the other drawback of optical beamforming methods based on phase shifter is its beam squint, limiting the bandwidth of data signal [20]. Additionally, the output power of the optical phase shifter varies with the phase shifting value [23]. This fact forces to use variable optical attenuators (VOAs) at the end of each phase shifter block in order to control the power level at the input of the PD array, further increasing the complexity of the system.

On the other hand, optical TTD is the most popular approach to perform incoherent optical beamforming. Optical TTD dispenses with the aforementioned carrier suppression and re-insertion process used in coherent optical beamforming, thus reducing the overall complexity of the system. As discussed before, two of the most popular devices for implementing optical TTD are as follows: ORR and optical waveguide [9], [18]. The optical waveguide solution does not provide high tunability to adjust the delay value. The tunability of this solution can be enhanced by incorporating multiple delay stages that can be turned on or off, hence offering a discrete delay tuning [24]. For the ORR case, the delay bandwidth is one of the major limiting factors [10], especially for mm-wave communications where broadband signals can be employed [25]. There are techniques, as proposed in [26], where the delay bandwidth of the ORR is increased. However, such techniques substantially increase the complexity and number of system components. Moreover, as mentioned in Section I, since ORR architecture for single beam implementations is intrinsically linked to binary tree structures, the scalability of the ORR solution is inefficient for multi-beam implementations which are based on matrix structures [9]. Thereby, TTD based on optical waveguides is an adequate solution for mm-wave 5G/6G communications due to its flat delay frequency response and high scalability to implement multi-beam OBFN.

This section explains the main principles of incoherent OBFN based on the optical waveguide implementation and is structured as follows: subsection III-A presents the theoretical formulation to demonstrate and show the functionality of optical waveguides as an OBFN delay block; subsections III-B and III-C exhibit the fundamentals of the optical tunable coupler and filter, respectively, which are the other two building blocks of the incoherent OBFN system; subsection III-D provides and explains a generic incoherent OBFN scheme based on the building blocks presented in the previous subsections.

A. Optical true time delay

Fig. 2 shows a basic schematic to perform certain relative delays in an RF signal by employing TTD with optical waveguides. In the upper branch of Fig. 2, a laser generates an optical carrier with a given wavelength (λ_1). Then, by using a Mach-Zehnder modulator (MZM) biased in the quadrature point, an RF sinusoid with an angular frequency of ω_{RF} is converted to the optical domain. Hence, the resulting optical signal at the output of the MZM can be expressed as follows [27];

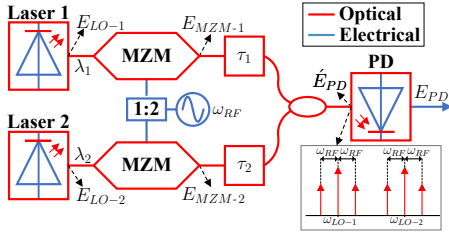


Figure 2. Basic scheme of an optical TTD based on the usage of optical waveguide.

$$E_{MZM}(t) = A_1 e^{j(\omega_{LO}t + \phi(t))} + A_2 [e^{j((\omega_{LO} + \omega_{RF})t + \phi(t) + \phi'(t))} - e^{j((\omega_{LO} - \omega_{RF})t + \phi(t) + \phi'(t))}] + \underbrace{\psi(\omega_{LO} \pm n\omega_{RF})}_{\text{Higher order harmonics}}, \quad (1)$$

where ω_{LO} is the angular frequency of the optical carrier, $\phi(t)$ refers to the laser phase, and $\phi'(t)$ corresponds to the RF source phase. Also, the first term of Eq. (1) indicates the optical carrier while the second term refers to the upper and lower optical bands. In addition, the last term of Eq. (1) (ψ) denotes the remaining harmonics components where $n > 1$, $n \in \mathbb{Z}$. As can be noticed, the signals E_{MZM-1} and E_{MZM-2} of Fig. 2 are formulated by Eq. (1) where ω_{LO} and $\phi(t)$ depend on the configuration of the employed laser. After the MZM block, the signal of each branch in Fig. 2 encounters a certain delay. This delay process is performed by an optical waveguide segment whose length determines the delay. Subsequently, the delayed optical signals from each branch are combined with a wavelength multiplexer. The spectral shape of the resulting combined signal is shown in Fig. 2. After the mixing process in the PD and without taking into account the high order harmonics of Eq. (1) (ignoring term $\psi(\omega_{LO} \pm n\omega_{RF})$), the obtained electrical signal can be formulated as follows:

$$E_{PD}(t) \propto DC + B_1 \cos(\omega_{RF}t + \omega_{RF}(\tau_1 + \tau'_1)) + B_2 \cos(\omega_{RF}t + \omega_{RF}(\tau_2 + \tau'_2)), \quad (2)$$

where τ'_1 and τ'_2 refer to the total delay, excluding the optical delay blocks, suffered by the RF signal of each branch of Fig. 2, respectively. Thus, assuming an ideal balance between the two branches of Fig. 2 ($\tau'_1 = \tau'_2$), the produced relative delay between the two input RF signals in Fig. 2 is equal to $\tau_2 - \tau_1$. Moreover, since the optical harmonics, at the output of each MZM, suffer from the same optical path and the two optical branches are fed with the same RF source, the laser and RF source phases (ϕ and ϕ') are canceled in the heterodyne process and does not appear at the PD output. Observing the spectral shape in Fig. 2, it can be noticed that the optical carrier separation of each laser must be sufficiently large to avoid spectral overlap in the RF domain between the frequency components of different branches. With this last mark, it is theoretically proven that the presented scheme enables the realization of optical TTD processes in parallel without interference.

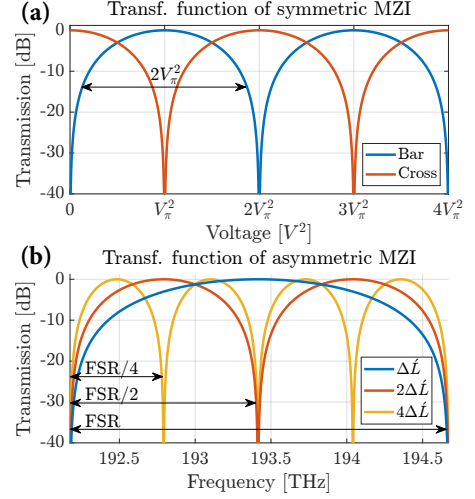


Figure 3. Transfer functions of two of the basic building blocks that compose the proposed incoherent OBFN: (a) transfer function of an SMZI used as an optical tunable coupler where the x-axis corresponds to applied squared voltage (V^2); (b) transfer function of an AMZI employed as an optical tunable filter where the x-axis refers to the frequency.

B. Optical tunable coupler

The transfer matrix of the symmetric Mach-Zehnder interferometer (MZI) can be formulated as follows [13]:

$$H_{MZI} = \begin{bmatrix} -s^2 + p^2 e^{-j\varphi} & -jsp(1 + e^{-j\varphi}) \\ -jsp(1 + e^{-j\varphi}) & -s^2 + p^2 e^{-j\varphi} \end{bmatrix} \quad (3)$$

where $p = \sqrt{1 - \kappa}$, $s = \sqrt{\kappa}$, and κ is the cross power coupling coefficient. In Eq. (3), φ indicates the phase shift that occurs in the phase shifter of the upper branch of the MZI and can be tuned by modifying the applied squared voltage according to $\varphi = (-\pi V^2)/(V_\pi^2)$. V_π refers to the half voltage of the MZI. When the second input of the symmetric MZI (SMZI) is null, the bar transfer function is equal to $-s^2 + p^2 e^{-j\varphi}$ while the cross one is $-jsp(1 + e^{-j\varphi})$. For an ideal SMZI, the κ coefficient is equal to 0.5 in order to have a constant group delay [13].

Fig. 3 (a) depicts the bar and cross transfer functions of an ideal SMZI ($\kappa = 0.5$). The x-axis of Fig. 3 (a) corresponds to the applied squared voltage of the SMZI phase shifter. By inspecting Fig. 3 (a), it can be observed that bar and cross output powers are complementary. Therefore, an SMZI can be used as an optical tunable coupler where the coupler factor depends on the applied squared voltage to the SMZI phase shifter.

C. Optical tunable filter

The spectral shape of the SMZI is similar to the curves in Fig. 3 (a) and is characterized by its frequency periodicity, also called free spectral range (FSR). Also, the spectrum of an SMZI can be shifted by applying different voltage values. Hence, the SMZI block can be used as an optical

filter to suppress a set of specific frequency components with a frequency separation multiple of the FSR value. However, the frequency separation between maximum and null power points is determined by the FSR. Then, the properties of the SMZI do not allow selecting the frequency values linked to the points of maximum and minimum power. In other words, the SMZI has a fixed FSR value that cannot be changed. One way to modify the FSR value of an SMZI consists of adding an extra segment of optical waveguide with length ΔL in the lower branch, obtaining an asymmetric MZI (AMZI) [13]. The transfer matrix of the AMZI is as follows [13]:

$$H_{AMZI} = \begin{bmatrix} -s^2\gamma_{\Delta L}z + p^2e^{-j\varphi} & -jsp(e^{-j\varphi} + \gamma_{\Delta L}z) \\ -jsp(e^{-j\varphi} + \gamma_{\Delta L}z) & -s^2\gamma_{\Delta L}z + p^2e^{-j\varphi} \end{bmatrix} \quad (4)$$

where $\gamma_{\Delta L}$ is the losses produced in the added segment of the AMZI. The term z of Eq. (4) is equal to $\exp(j\frac{\Delta L n_g}{\lambda})$ where n_g is the group index. Fig. 3 (b) illustrates the spectral shape of the bar transfer function of an ideal AMZI for different values of ΔL . For an ideal AMZI, the κ factor is equal to 0.5 and $\gamma_{\Delta L}$ is 0. As it can be observed in Fig. 3 (b), the length of the added segment (ΔL) allows the FSR value to be changed. Therefore, an optical tunable filter can be performed by using the AMZI block where the frequency values of the maximum and minimum power points are modified by changing the applied squared voltage V^2 and ΔL . It is important to mention that the ΔL length is fixed after manufacturing. Hence, AMZI enables to specify FSR during PIC design and the tunability relies on the frequency spectrum shift determined by the applied squared voltage. Thereby, by cascading a set of AMZIs with different ΔL values, the frequency value with maximum output power for all the used AMZIs can be fixed by shifting their spectra. This frequency value refers to the operating frequency of the system block in order to optimize the maximum output power. Then, the suppressed frequency points are determined by the ΔL length of each AMZI.

D. Optical Blass matrix

The array factor (AF) of a one-dimensional AA equidistributed round zero on the x-axis is expressed as follows [28]:

$$AF(\theta) = \sum_{n=1}^N w_{m,n} \cdot e^{-jnk\Delta d(\sin(\theta) - \sin(\alpha_m))}, \quad (5)$$

where N indicates the number of antenna elements, k is the wavenumber ($2\pi/\lambda$), Δd refers to the separation between consecutive antenna elements in m , θ corresponds to the azimuth angle, and $w_{m,n}$ is the amplitude weight related to each beam and antenna element with indexes m -th and n -th, respectively. In Eq. (5), the parameter α determines the angle θ with maximum AF amplitude or, in other words, the angle of the beam m -th ($\alpha_m = \theta_{\max}$). Hence, the delay associated with each antenna element for a specific beam of angle α can be calculated as follows:

$$\tau_{m,n} = (n-1) \cdot \underbrace{(\Delta d / c) \cdot \sin(\alpha_m)}_{\Delta\tau}, \quad (6)$$

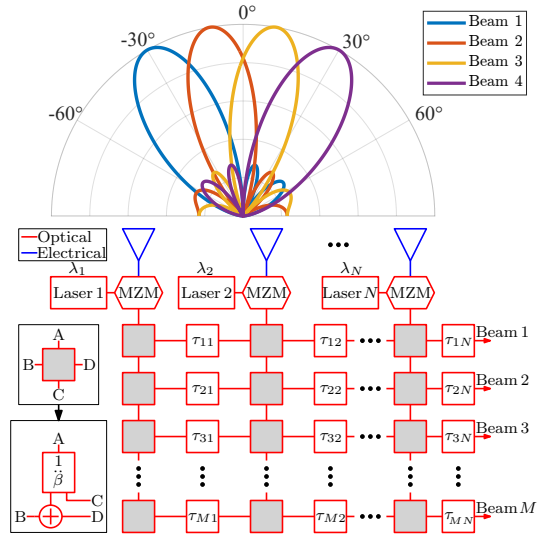


Figure 4. Blass matrix for performing OBFN based on TTD with optical waveguides.

where c is the speed of light in vacuum. As it can be observed in Eq. (6), the delay related to each antenna element increments proportionally to $\Delta\tau$. To realize simultaneous transmission of multiple beams from a single AA, signals must be distributed along a matrix architecture. Each row or column of this matrix architecture combines and delays the different AA signals according to Eq. 6 to form a specific beam m -th with angle α_m . In this way, a Blass matrix is created.

Fig. 4 illustrates an optical incoherent Blass matrix implementation by using TTD based on optical waveguides. In Fig. 4, gray blocks are used to distribute and combine the antenna input signals through the Blass matrix. These gray blocks are composed by a combiner and coupler (see lower left corner of Fig. 4). The optical tunable coupler architecture explained in subsection III-B can be employed to build each gray block of Fig. 4. The coupling factor β is adjusted by modifying the voltage applied to the SMZI block. In this manner, the amplitude weights w of the AF in Eq. (5) are fully programmable, enabling to vary the azimuth angle of the AF sidelobes [28]. Moreover, it is important to mention that the Blass matrix of Fig. 4 is designed for uplink communication since it is configured as a beamforming receiver.

To perform an optical Blass matrix, the electrical signal from each antenna element must be converted to the optical domain. For that, in Fig. 4, a set of MZMs is distributed along the AA. These MZMs use different optical wavelengths from an incoherent source ($\lambda_1, \lambda_2, \dots, \lambda_N$). Hence, each MZM is attached to a single laser. To ensure the correct operation of the OBFN block, an optical filtering process is performed after each MZM. In this filtering process, the non-desired wavelengths are suppressed, centering the filter spectrum on the operating wavelength for the corresponding input. This filtering process can be done by cascading AMZI blocks ex-

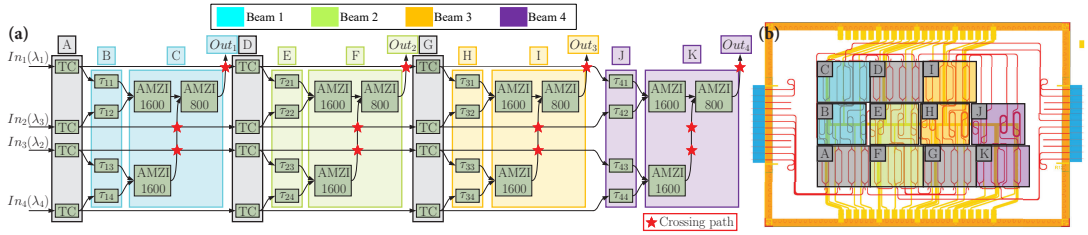


Figure 5. Integrated incoherent 4x4 OBFN PIC: (a) block diagram of the PIC; (b) PIC layout. TC: tunable coupler.

plained in the previous subsection. Therefore, with this AMZI cascade structure, the non-desired frequency components, that might be contained in the optical input signal, are suppressed and, thus, frequency interference is avoided for a correct optical TTD realization in the heterodyne process.

IV. PROPOSED INCOHERENT OBFN SOLUTION

In this section, an incoherent 4x4 OBFN PIC fabricated in Si_3N_4 is presented, explained, and characterized. The work published in [18] presents and introduces the OBFN concept from a system, network, and control point of view. This manuscript for the first time provides a thorough discussion of its operating principles and provides an exhaustive characterization of the presented OBFN, as well as theoretical formulation and design keys to accomplish a successful OBFN implementation based on optical waveguides. Fig. 5 (a) shows the block diagram of the proposed incoherent 4x4 OBFN based on TDD with optical waveguides. As it can be noticed, the block diagram in Fig. 5 (a) is a specific case of the optical Blass matrix in Fig. 4. Also, the presented OBFN is designed for uplink communication. The different block colors in Fig. 5 (a) indicate the beam to which it is related. Thereby, the outputs in Fig. 5 (a) refer to the four different beam signals extracted from the AA. As it can be seen in Fig. 5 (a), the block diagram structure for each beam are the same and are composed by the following components: a column of four tunable couplers (TCs), a column of four TTD blocks built with optical waveguides, and a cascade filter block. The TC columns are employed to distribute the input signals across the different beam blocks, while the delay columns determine the angle of each beam.

In Fig. 5 (a), there are two types of AMZI: AMZI 1600 whose FSR = 1600 GHz; and AMZI 800 whose FSR = 800 GHz. Moreover, in Fig. 5 (a), inputs 1 and 2 compose an input signal pair as inputs 3 and 4 do. Each of these input pairs passes through an AMZI 1600. These AMZI 1600 blocks are used to suppress at each input the wavelength associated with the other input. Then, for a proper filtering operation, the frequency separation between the wavelengths of inputs 1 and 2 must be a multiple of 800 GHz. The same condition occurs for the frequency separation between the wavelengths of inputs 3 and 4. Subsequently, the two outputs of these AMZI blocks are the inputs of an AMZI 800. The mission of this AMZI consists of suppressing at each input the wavelengths related to the other input signal pair. For instance, for the upper

Table II
DELAY MATRIX OF THE TARGET RELATIVE DELAYS DESIGNED FOR 27.5 GHz.

	Beam 1	Beam 2	Beam 3	Beam 4
Angle	0°	20°	40°	60°
Input 1	0.00 (τ_{11})	0.00 (τ_{21})	0.00 (τ_{31})	0.00 (τ_{41})
Input 2	0.00 (τ_{12})	6.22 (τ_{22})	11.69 (τ_{32})	15.75 (τ_{42})
Input 3	0.00 (τ_{13})	12.44 (τ_{23})	23.37 (τ_{33})	31.49 (τ_{43})
Input 4	0.00 (τ_{14})	18.66 (τ_{24})	35.06 (τ_{34})	47.24 (τ_{44})

*All the delay values are in ps.

input, the AMZI 800 block suppresses the wavelengths linked to inputs 3 and 4. Hence, the frequency separation between consecutive operating wavelengths must be 400 GHz. With these filtering cascade blocks, interference, produced by non-desired frequency components, is avoided.

Fig. 5 (b) illustrates the PIC layout of the presented incoherent 4x4 OBFN. As it can be observed, the blocks that compose the PIC are marked with the same labels in Figs. 5 (a) and (b). The presented OBFN PIC of this work is designed for an RF center frequency operation of 27.5 GHz and for beam angles of 0°, 20°, 40°, and 60°. Table II displays the relative delays between the four input signals of each beam for the target RF frequency. These relative delays can be calculated with Eq. (6), considering $\Delta d = \lambda/2$.

For a comprehensive analysis and study of the functional response of the proposed OBFN, a characterization of each of its components is carried out: optical tunable filters, optical tunable couplers, and optical TTDs. For proper OBFN operation, all the applied voltages to the 12 tunable couplers and 12 tunable filters must be set adequately. A set of 24 heaters are used to apply the mentioned voltages. For the optical filtering characterization, the employed measurement setup consists of a laser at each input of the PIC under test and an optical power meter at each output. Then, a frequency sweep is performed for each combination of input and output (16 combinations in total). The experimental measurements of this optical filter characterization are shown in Fig. 6 (a) and plotted in terms of insertion loss (IL). Moreover, graphs in Fig. 6 (a) illustrate the operating wavelengths of each input: Input 1 ($\lambda_1 \rightarrow 193.6$ THz); Input 2 ($\lambda_3 \rightarrow 192.8$ THz); Input 3 ($\lambda_2 \rightarrow 193.2$ THz); Input 4 ($\lambda_4 \rightarrow 192.4$ THz). As discussed above, the frequency separation between these wavelengths must be 400 GHz. Therefore, other frequency input combinations are possible by taking advantage in the FSR periodicity of the optical tunable filter. It can be seen from Fig. 6 (a) that for

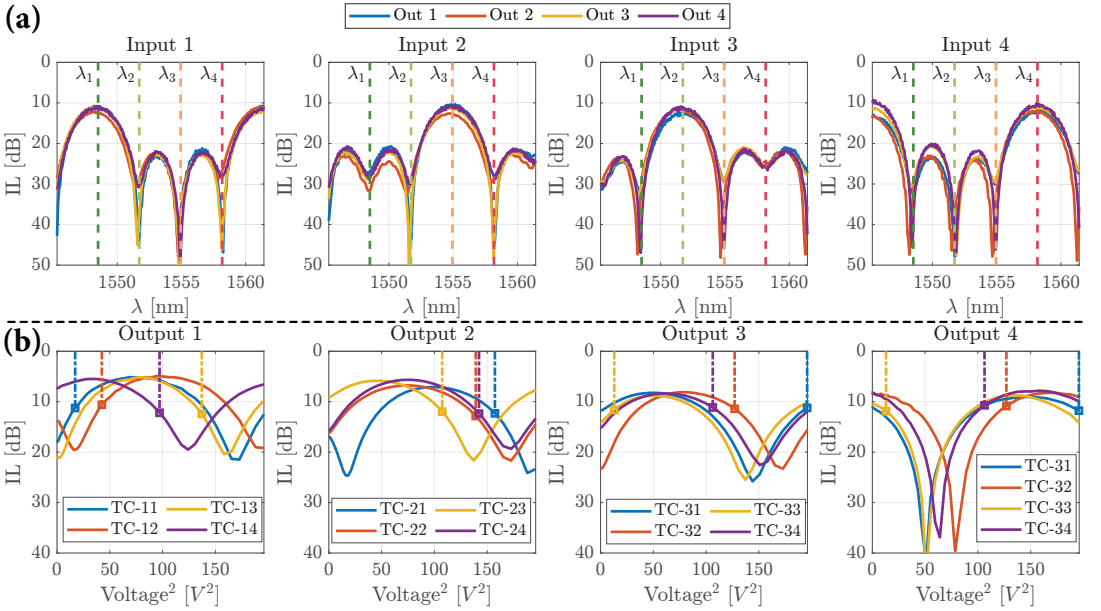


Figure 6. Incoherent 4x4 OBFN PIC measurements: (a) optical tunable filter characterization; (b) optical tunable coupler characterization.

each input, the wavelength with the maximum output power is the operating wavelength of the corresponding input, while the remaining operating wavelengths are suppressed by the cascaded AMZI blocks.

For the tunable coupler characterization, a measurement setup, equivalent to that of the filtering characterization, is employed. Nonetheless, in this case, the wavelength of each input is set to its operating frequency and a voltage sweep is performed for each tunable coupler. It is worth mentioning that the voltage settings of the 24 heaters remain the same for all the TC characterizations where the voltage of the TC under test is the only swept parameter. Fig. 6 (b) depicts the obtained experimental measures for the characterization of the 12 TCs that are part of the OBFN. The x-axis of the graphs in Fig. 6 (b) are in terms of the applied squared voltage. Furthermore, Fig. 6 (b) represents with vertical dotted lines the IL related to the squared voltage selected for each TC. Inspecting the vertical dotted lines of Fig. 6 (b), it can be noted that the ILs of the four inputs on each output are balanced, showing a maximum relative IL difference of 1.8 dB. These IL outputs are directly related to the amplitude weights w of Eq. (5), allowing the azimuth angle of the sidelobes to be adjusted [28].

Fig. 7 (a) illustrates the setup utilized to measure the delays of TTD blocks of the presented OBFN. In particular, the relative delays between the TTD blocks of each beam are measured with this setup. To perform the delay measurement, an RF carrier, produced by a vector signal generator (VSG), is employed and converted to the optical domain by employing a laser and MZM. Then, the resulting optical signal is boosted with an erbium-doped fiber amplifier (EDFA) and,

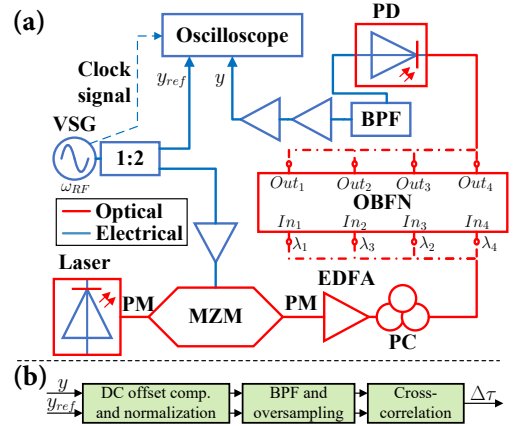


Figure 7. Employed technique to measure the relative delay between the TTD blocks of the manufactured incoherent 4x4 OBFN PIC: (a) experimental measurement setup; (b) digital signal processing (DSP) block diagram. PM: polarization maintaining fiber; PC: polarization controller.

subsequently, introduced to one of the OBFN inputs with its corresponding operating wavelength (λ_1 , λ_2 , λ_3 , or λ_4). Next, at each output of the OBFN, the signal is converted to the electrical domain with a PD. After the PD, the resulting electrical signal is filtered with a band-pass filter (BPF), amplified, and captured with an oscilloscope whose sampling rate is 100 GSa/s, giving an initial measurement resolution of 10 ps. The RF carrier, that passes through the OBFN block, is denoted as y . In order to measure the relative delays between

Table III
MEASURED RELATIVE DELAYS OF THE INCOHERENT 4X4 OBFN PIC.

	Beam 1	Beam 2	Beam 3	Beam 4
Input 1	0.0 [0.0]	0.0 [0.0]	0.0 [0.0]	0.0 [0.0]
Input 2	0.6 [0.6]	7.0 [0.8]	11.8 [0.1]	16.6 [0.9]
Input 3	0.4 [0.4]	12.8 [0.4]	24.4 [1.0]	31.8 [0.3]
Input 4	0.0 [0.0]	19.6 [0.9]	35.6 [0.5]	47.8 [0.6]

*All the delay values are in ps. The blue values correspond to the measured relative delays while the red values in brackets refer to the errors with respect to the target delay matrix of Table II.

the TTD blocks of each beam, a reference signal is required. The RF carrier at the output of the VSG is also utilized as the mentioned reference signal by employing an RF power splitter. Thus, this reference signal is sampled on another channel of the oscilloscope. To properly measure the delay between y and y_{ref} , both signals must be sampled at the same time.

Once y and y_{ref} traces are collected, digital signal processing (DSP) is carried out to calculate the delay $\Delta\tau$ between the two signals. This DSP process is represented in Fig. 7 (b). First, the amplitudes of y and y_{ref} are corrected with a DC offset compensation and normalization block. Next, a digital BPF, whose frequency center coincides with the RF carrier frequency (ω_{RF}) in Fig. 7 (a), is performed. Then, an oversampling process is realized, which allows increasing the delay resolution of the measurements since the initial measurement resolution of 10 ps, provided by the oscilloscope, is not sufficient to measure the target delays of Table II. Finally, a cross-correlation procedure is realized between the two oversampled signals. The location of the maximum point in the obtained cross-correlation signal is directly related to the delay between y and y_{ref} .

The aforementioned process for calculating the delay between y and y_{ref} is carried out for the 16 combinations of inputs and outputs of the under test OBFN PIC. The results of Table III show the measured relative delays for each TTD column of the OBFN. The measurement parameters used to get these results are the following: oversampling factor of 10, 5 GHz of RF carrier, and $1\mu s$ of time window for the cross-correlation process. Moreover, to reduce the impact of the noise, included in the y and y_{ref} signals, on the delay measurements, the relative delays of five different traces are averaged. These mean values correspond to those represented in Table III.

By ensuring that the relative delays between the TTD blocks of each OBFN column are in accordance with Table II, the beamforming properties are maintained. Thus, to obtain relative delays between the TTD blocks of a column, the measured delay of the first row in Table III (Input 1) is used as the reference delay. Hence, the measured delay column values are subtracted from the first column element to obtain the relative delay of each beam. In this manner, by subtracting two measured absolute values from the delay measurement setup, the delays produced by all the paths involved in the setup of Fig. 7 (a) are canceled, except the relative delay between the first TTD block in the column and the remaining TTD blocks in that column. For this reason, the first row of Table III contains only zeros, with the values of remaining rows being

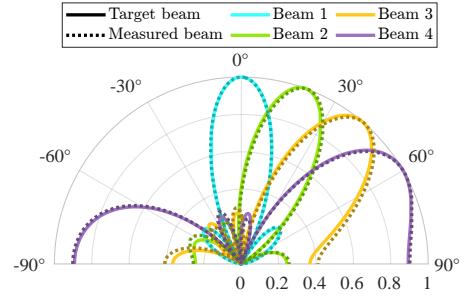


Figure 8. Multi-beam AF representation associated with the target and measured relative delays of Tables II and III, respectively.

the measured delays for inspection.

In addition, Table III displays the error of the measured relative delays with respect to the target delay values in Table II. As it can be observed, the mean relative error is not more than 1 ps for all cases, showing a global cumulative error of 6.5 ps. To quantify these delay measured errors for a communication scenario, the AFs related to the measured relative delays of Table III are illustrated with dotted lines in Fig. 8. The target AF beams corresponding to the relative delays of Table II are also plotted in Fig. 8. In this manner, the AF beam shapes attached to the measured relative delays can be compared with the expected AF beams. As it can be observed in Fig. 8, the shape deformation of the measured AF beams, with respect to the target ones, is slight since the delay errors of Table III are relatively low. To be more precise, the angle error of the measured AF beams regarding the target beam angles are the following: 0.06° , -0.81° , -1.05° , and -0.73° for measured beams 1, 2, 3, and 4, respectively. These angle errors of the measured AF beams signify a low impact on the performance in a communication scenario as the power loss is almost insignificant for an AA of four antennas.

Therefore, it has been proven that the behavior of the presented incoherent OBFN is in accordance with its design parameters, highlighting the potential of this structure to realize an accurate OBFN implementation. Also, it is important to emphasize that, in order to get these accurate delay measurements, the PIC layout paths that compose the branches of each beam block must be precisely equalized in terms of length. By ensuring this length balance constraint, the relative delay produced in the OBFN is determined by the TTD blocks.

It should be noted that the principles of the proposed OBFN implementation are applicable to other RF frequencies and especially for OBFNs with the presented architecture targeting higher frequency carriers (e.g., 60 GHz) the design may become easier and allow for reduced footprint since the required delay paths are shorter for higher frequencies (see PIC layout of Fig. 5 (b)). However, the bandwidth requirements for the remaining ARoF devices, such as PDs or MZMs, will scale with frequency, leading to a trade-off having to be found. As a solution to alleviate this bandwidth exigence, an IF signal can be used for the mm-wave ARoF transport, which requires an intermediate upconversion block in the RAU. Also, for multi-

frequency implementations, independent OBFNs designed for different carrier frequencies can be utilized, harnessing the small footprint of PIC technology or the possibility of implementing steep and narrow optical filters in the proposed PIC technology may be exploited for more involved designs handling multi-frequency transmission. Then, the optical outputs of these OBFN blocks can be transported through the optical link. Overall, the proposed OBFN architecture is a flexible and scalable solution for higher carrier frequencies and other types of applications such as multi-frequency systems.

V. CONCLUSIONS

First, in this manuscript, the need to use multi-beam beamforming for the future mm-wave 5G/6G mobile network based on AROF technology is highlighted. Subsequently, the relevance of optical beamforming based on PICs was emphasized, remarking it as a promising solution due to its small footprint, high production scalability, and low power consumption. Furthermore, TTD beamforming based on optical waveguides was highlighted as an excellent method to implement incoherent OBFNs with numerous inputs and outputs because of its simplicity, high scalability, and flat delay behavior over frequency. With these premises, a novel incoherent OBFN architecture based on optical waveguide TTDs was proposed. The foundation of this novel OBFN architecture was thoroughly explained with theoretical formulations of its building blocks, providing key designs for its successful implementation. The main advantages of the proposed OBFN architecture are its high scalability, low PIC occupation, and great flexibility, highlighting its use for an ample range of applications such as multi-frequency or multi-beam communication systems.

On the other hand, an incoherent 4x4 OBFN PIC fabricated in Si₃N₄ was presented, showing its functional block diagram and layout. The OBFN PIC of this work is designed for an RF frequency of 27.5 GHz and allows four beams to be formed with an angular separation of 20°. In addition, the proposed OBFN architecture is also suitable for higher carrier frequencies, such as in the V and W bands. A comprehensive characterization of all the functional blocks of the OBFN PIC was carried out. The experimental measurements of the components that are part of the OBFN were analyzed and discussed, matching the expected results based on the OBFN design. Thereby, the results of this work validate, for the first time, the correct operation of an integrated OBFN with simultaneous transmission of multiple beams based on optical TTD, paving the road for the efficient generation of massive multi-beam MIMO based on optical beamforming. The contribution of this work marks an important milestone to strengthen the maturity of PIC-based OBFN, speeding up its application and commercialization in future mobile networks.

REFERENCES

- [1] W. Jiang *et al.*, "The Road Towards 6G: A Comprehensive Survey," *IEEE Open J. Commun. Soc.*, vol. 2, pp. 334–366, Feb. 2021.
- [2] I. A. Hemadeh *et al.*, "Millimeter-Wave Communications: Physical Channel Models, Design Considerations, Antenna Constructions, and Link-Budget," *IEEE Commun. Surv. Tutor.*, vol. 20, no. 2, pp. 870–913, Dec. 2017.
- [3] S. Kuttu and D. Sen, "Beamforming for Millimeter Wave Communications: An Inclusive Survey," *IEEE Commun. Surv. Tutor.*, vol. 18, no. 2, pp. 949–973, Secondquarter 2016.
- [4] S. Dutta *et al.*, "A Case for Digital Beamforming at mmWave," *IEEE Trans. Wirel. Commun.*, vol. 19, no. 2, pp. 756–770, Feb. 2020.
- [5] A. F. Molisch *et al.*, "Hybrid Beamforming for Massive MIMO: A Survey," *IEEE Commun. Mag.*, vol. 55, no. 9, pp. 134–141, Sep. 2017.
- [6] S.-H. Park *et al.*, "Beam Squint in Ultra-wideband mmWave Systems: RF Lens Array vs. Phase-Shifter-Based Array," *IEEE Wirel. Commun.*, pp. 1–8, May 2022.
- [7] Y. Li *et al.*, "Analog Radio Over Fiber Aided C-RAN: Optical Aided Beamforming for Multi-User Adaptive MIMO Design," *Front. Commun. Net.*, vol. 2, Aug. 2021.
- [8] C. G. H. Roeloffzen *et al.*, "Integrated optical beamformers," in *2015 International Topical Meeting on Microwave Photonics (MWP)*, Paphos, Cyprus, Oct. 2015, pp. 1–3.
- [9] Y. Liu *et al.*, "Ultra-Low-Loss Silicon Nitride Optical Beamforming Network for Wideband Wireless Applications," *IEEE J. Sel. Top. Quantum Electron.*, vol. 24, no. 4, pp. 1–10, Apr. 2018.
- [10] A. B. Smolders *et al.*, "Building 5G Millimeter-Wave Wireless Infrastructure: Wide-Scan Focal-Plane Arrays With Broadband Optical Beamforming," *IEEE Antennas Propag. Mag.*, vol. 61, no. 2, pp. 53–62, Apr. 2019.
- [11] P. G. Sheehan and J. R. Forrest, "The Use Of Optical Techniques For Beamforming In Phased Arrays," in *Optical Technology for Microwave Applications I*, vol. 0477, Arlington, TX, USA, Nov. 1987, pp. 82–89.
- [12] X. Ye *et al.*, "Optical true time delay unit for multi-beamforming," *Opt. Express*, vol. 23, no. 8, pp. 10 002–10 008, Apr. 2015.
- [13] C. G. H. Roeloffzen *et al.*, "Silicon nitride microwave photonic circuits," *Opt. Express*, vol. 21, no. 19, pp. 22 937–22 961, Sep. 2013.
- [14] S. Rommel *et al.*, "Towards a Scalable 5G Fronthaul: Analog Radio-over-Fiber and Space Division Multiplexing," *J. Light. Technol.*, vol. 38, no. 19, pp. 5412–5422, Oct. 2020.
- [15] M. Fiorani *et al.*, "Modeling energy performance of C-RAN with optical transport in 5G network scenarios," *J. Opt. Commun. Netw.*, vol. 8, no. 11, pp. B21–B34, Nov. 2016.
- [16] I. Degli-Eredi *et al.*, "Millimeter-wave generation using hybrid silicon photonics," *J. Opt.*, vol. 23, no. 4, p. 043001, Mar. 2021.
- [17] G. Meslener, "Chromatic dispersion induced distortion of modulated monochromatic light employing direct detection," *IEEE J. Quantum Electron.*, vol. 20, no. 10, pp. 1208–1216, Oct. 1984.
- [18] R. Muñoz *et al.*, "Experimental Demonstration of Dynamic Optical Beamforming for Beyond 5G Spatially Multiplexed Fronthaul Networks," *IEEE J. Sel. Top. Quantum Electron.*, vol. 27, no. 6, pp. 1–16, May 2021.
- [19] F. Azendorf *et al.*, "Group Delay Measurements of Multicore Fibers with Correlation Optical Time Domain Reflectometry," in *2020 22nd International Conference on Transparent Optical Networks (ICTON)*, Bari, Italy, Jul. 2020, pp. 1–4.
- [20] C. Tsokos *et al.*, "Analysis of a Multibeam Optical Beamforming Network Based on Blass Matrix Architecture," *J. Light. Technol.*, vol. 36, no. 16, pp. 3354–3372, Aug. 2018.
- [21] B. Zhou *et al.*, "Optical Beamforming Networks Based on Broadband Optical Source and Chirped Fiber Grating," *IEEE Photon. Technol. Lett.*, vol. 20, no. 9, pp. 733–735, May 2008.
- [22] Álvaro Morales *et al.*, "50 GHz optical true time delay beamforming in hybrid optical/mm-wave access networks with multi-core optical fiber distribution," *Chin. Opt. Lett.*, vol. 16, no. 4, p. 040603, Apr. 2018.
- [23] G. Serafino *et al.*, "A Photonic Beamforming Network Based on Phase Shifters for Microwave Wide-Band Applications," in *2019 21st International Conference on Transparent Optical Networks (ICTON)*, Angers, France, Jul. 2019, pp. 1–4.
- [24] Q. Ma *et al.*, "Silicon-Based True-Time-Delay Phased-Array Front-Ends at Ka-Band," *IEEE Trans. Microw. Theory. Tech.*, vol. 63, no. 9, pp. 2942–2952, Sep. 2015.
- [25] Y. Liu *et al.*, "Ring Resonator Delay Elements for Integrated Optical Beamforming Networks: Group Delay Ripple Analysis," in *Advanced Photonics 2016 (IPR, NOMA, Sensors, Networks, SPPCom, SOF)*, Vancouver, Canada, Jul. 2016, p. IW1B.3.
- [26] M. Burla *et al.*, "Multiwavelength-Integrated Optical Beamformer Based on Wavelength Division Multiplexing for 2-D Phased Array Antennas," *J. Light. Technol.*, vol. 32, no. 20, pp. 3509–3520, Oct. 2014.
- [27] G. Meslener, "Chromatic dispersion induced distortion of modulated monochromatic light employing direct detection," *IEEE J. Quantum Electron.*, vol. 20, no. 10, pp. 1208–1216, Oct. 1984.
- [28] R. L. Haupt, "Lowering the Sidelobe Level of a Two-Way Array Factor for an Array With Uniform Transmit and Uniform Receive Arrays," *IEEE Trans. Antennas Propag.*, vol. 67, no. 6, pp. 4253–4256, Jun. 2019.

P12: Experimental outdoor IFoF fronthaul with adaptive analog beamforming for mm-wave 5G/6G networks

J. P. Santacruz, R. Budé, C. Stan, *et al.*, “Experimental outdoor IFoF fronthaul with adaptive analog beamforming for mm-wave 5G/6G networks,” *Scientific Reports*, 2022, [first draft]

Experimental outdoor IFOF fronthaul with adaptive analog beamforming for mm-wave 5G/6G networks

Javier Pérez Santacruz¹, Elmine Meyer^{*1,+}, Catalina Stan^{*1,+}, Roel X. F. Budé^{*1,+}, Antonio Jurado-Navas², Idelfonso Tafur Monroy¹, and Simon Rommel^{1,*}

¹Eindhoven University of Technology, Electrical Engineering Department, Eindhoven, 5600MB, The Netherlands

²Univeristy of Málaga, Department of Communications Engineering, Málaga, 29071, Spain

*corresponding author: s.rommel@tue.nl

+these authors contributed equally to this work

ABSTRACT

Intermediate frequency-over-fiber (IFoF) is a promising technology for the millimeter-wave (mm-wave) mobile fronthaul due to its low complexity, high optical spectrum efficiency, and low latency. On the other hand, adaptive analog beamforming is a key technology to enable mm-wave wireless technology, with phased array antenna (PAA) being a promising solution for future mobile networks. Therefore, the combination of IFoF together with PAA is crucial to implement mm-wave mobile communications in a scalable, centralized, efficient, and reliable manner. This work presents for the first time, to the best of the authors' knowledge, an extensive outdoor measurement campaign where an experimental IFoF mm-wave wireless setup is evaluated by using PAAs on the transmitter and receiver sides. The configuration of the experimental setup is according to 5G standards, transmitting signals wirelessly at 27 GHz central frequency. Different en-user locations, antenna configurations, and wireless scenarios are tested in the outdoor experiment, showing great error vector magnitude (EVM) results. Furthermore, this manuscript provides keynotes to efficiently implement mm-wave IFoF wireless systems based on PAA following the 5G standards. Moreover, the results of this work prove the viability and potential of IFoF combined with PAA to be part of the future 5G/6G structure.

Introduction

The dramatic growth of mobile data traffic in the last years requires a major upgrade and enhancement in the mobile network infrastructure, especially with the emergence of new applications and services such as augmented reality (AR), virtual reality (VR), 4K/8K video streaming, autonomous driving, industry 5.0, or Internet of Things (IoT)¹. The fifth-generation (5G) of mobile networks and its successor 6G aim to provide an adequate quality of experience (QoE) and quality of service (QoS) for such applications. To achieve this, 5G standards specify a set of requirements in terms of latency, number of connected devices, data rate, energy efficiency, mobility, and capacity². Increasing the data rate is one of the main objectives of future 5G/6G systems where exploiting the millimeter-wave (mm-wave) band is crucial to obtain a substantial improvement. Nonetheless, mm-wave wireless communications imply severe power limitations due to their high free-space path loss (FSPL), atmospheric attenuation, and penetration losses³. Hence, compared with the current sub-7 GHz network, the implementation of mm-wave cells signifies an important reduction in the coverage radio (≈ 200 m). In other words, respecting the current mobile network, the expected number of mm-wave cells for future 5G/6G scenarios is vast, greatly increasing the data traffic in the radio access network (RAN) domain⁴.

As a consequence of the RAN bottleneck issue in mm-wave mobile systems, radio-over-fiber (RoF) arises as an ideal technology to transport and distribute the mobile data between the core network and the remote antenna unit (RAU)^{5,6}. There are three main types of RoFs technologies⁷⁻⁹: mm-wave analog radio-over-fiber (ARoF), intermediate frequency-over-fiber (IFoF), and digital radio-over-fiber (DRoF). It is important to mention that IFoF is considered an ARoF solution as mm-wave ARoF. In contrast to the DRoF approach, ARoF solutions allow a great complexity reduction of the RAU, moving most of the functionalities to the central office (CO). This low-complexity RAU feature is essential to scalably and efficiently develop the large number of mm-wave cells for 5G/6G⁶. Moreover, mm-wave ARoF permits effective centralized radio access network (C-RAN) deployment, thereby reducing maintenance cost and latency¹⁰. However, compared to DRoF, mm-wave ARoF implies higher phase noise levels and higher signal degradation due to the non-ideal functionality of the components involved in RoF systems^{8,11}. Therefore, mm-wave ARoF and DRoF offer different advantages and disadvantages in terms of signal quality and system implementation. IFoF is a hybrid solution for these two RoF technologies. To be more specific, IFoF is a type of ARoF approach where the data signal is modulated at a specific intermediate frequency (IF) and transported through the optical fiber. Since IFoF dispenses with the optical two-tone generation in the CO, which is necessary for mm-wave

ARoF solutions, the phase noise level is reduced. In this manner, complex techniques to compensate for the phase noise can be dispensed with¹¹. However, IFoF brings the drawback of requiring a mm-wave oscillator at the RAU site, which increases the complexity, cost, and energy consumption at the RAU. Hence, IFoF brings intermediate features between the mm-wave ARoF and DRoF solutions, being a suitable choice to implement in many mobile scenarios⁹.

On the other hand, applying beamforming is one of the most appropriate ways to alleviate the power limitations intrinsically linked to mm-wave wireless communications¹². More specifically, digital implementation is one of the most extended beamforming solutions. However, digital beamforming scales with the number of analog-to-digital converters (ADCs) and digital-to-analog converters (DACs), not being the best solution in terms of power consumption, complexity, and cost, especially for massive multiple-input and multiple-output (MIMO) applications^{12,13}. As a consequence, analog and hybrid beamforming enable technologies for the deployment of mm-wave mobile communications in an effective and scalable manner, since they do not require numerous ADCs and DACs. In particular, the phased array antenna (PAA) is one of the most promising analog beamforming implementations, giving rapid and flexible beamsteering capabilities¹⁴. Thereby, IFoF combined with PAA-based beamforming is an outstanding solution for future mm-wave 5G/6G mobile networks.

To this end, the above-mentioned solutions, based on PAA and IFoF, aim to tackle the challenges associated with mm-wave mobile communications^{6,12}: congestion in the fronthaul due to the increased data rate and low received power, especially in scenarios with line-of-sight (LOS) blockage. In previous works, the IFoF technique has been extensively studied as a 5G fronthaul solution, validating its efficiency for 28 GHz mm-wave communications⁹, and V-band systems implementing various modulation formats (quadrature phase shift keying (QPSK), quadrature amplitude modulation (QAM)) and PAA-based beamsteering techniques^{15–17}. The coexistence of IFoF signal with passive optical network (PON) traffic was successfully demonstrated in the field environment and evaluated by using 16-QAM orthogonal frequency-division multiplexing (OFDM) signals¹⁸, while from a fronthaul capacity perspective, IFoF has been used to experimentally demonstrate an aggregate capacity up to 24 Gbit/s over 7 km fiber and 5 m V-band link¹⁹. An outdoor experiment using IFoF with 28 GHz mm-wave wireless transmission and 16-QAM and 64-QAM modulation orders has been demonstrated²⁰, with the terminal located at 10 m and 1 km LOS away from the remote radio head (RRH) in charge of beamforming using multiple fixed beams. Nevertheless, to the best of the authors' knowledge, there are no scientific reports in the research literature regarding experimental mm-wave wireless IFoF 5G setups with PAA-based beamsteering evaluated in outdoor scenarios. Aiming to fill this research gap, the work of this manuscript presents an experimental wireless IFoF testbed realized in different outdoor scenarios at a centre frequency of 27 GHz, within the n257 and n258 5G bands². The presented outdoor experiment is performed in a parking lot, serving as a measurement campaign for vehicle applications such as autonomous driving. In the experimental setup, a pair of PAA panels are employed on the transmitter and receiver sides, allowing for beamsteering capabilities. Furthermore, the experiment configuration is according to 5G standards, successfully transmitting 64-QAM OFDM signals with a subcarrier spacing of 240 kHz².

For a proper explanation and replication of the aforementioned experiment, this manuscript is structured as follows: the second section describes the overall concept of the used architecture and the different wireless scenarios where the experimental results are measured; the third section shows in detail the utilized PAA panels together with their characterization measurements, the configuration of the experimental setup, and the digital signal processing (DSP) processes carried out to obtain the final results; in the fourth section, the experimental results are presented, analysing, and interpreting; finally, the fifth section gives conclusive remarks concerning the contribution results of the presented work.

Wireless scenarios

Given the importance of high-speed communication in the future of the automotive industry, it is chosen to perform the outdoor experiment in the Flux building parking lot of the Eindhoven University of Technology campus. This location offers the opportunity to have an elevated transmitter, on the first-floor balcony of Flux, with a receiver at various locations in and around the parking lot, as shown in Fig. 1. The location consists of a complex environment, which includes pedestrians, vehicles, bicycles, vegetation, and buildings during the performance of the experiment. Both LOS and non-line-of-sight (NLOS) conditions can be tested, since the adjacent buildings have been proven to function well as reflectors²¹.

The transmitter and receiver are placed on carts, as can be seen in Figs. 1 (i)–(j). The transmitter cart contains the CO and RAU, while the receiver cart includes the end-user equipment. The transmitter remains in one geographical location during the entirety of the outdoor measurement campaign; however, the main beam direction is moved manually for different scenarios as can be seen in Figs. 1 (a)–(c). Table 1 indicates the angle to which the transmitter antenna is manually rotated with reference to the receiver antenna. The beam direction and scanning range of the transmitter is indicated by the red circle sector, while the receiver's is indicated by the yellow circle sector. The dashed red lines show ray-tracing of the main beam's centre at the extremities of the scanning range of the transmitter PAA. The solid lines in Figs. 1 (a)–(c) indicate the expected LOS and NLOS ray traces.

In Fig. 1 (a) and (b), the beamsteering capability of the transmitter is tested. From ray-tracing it is determined that these are

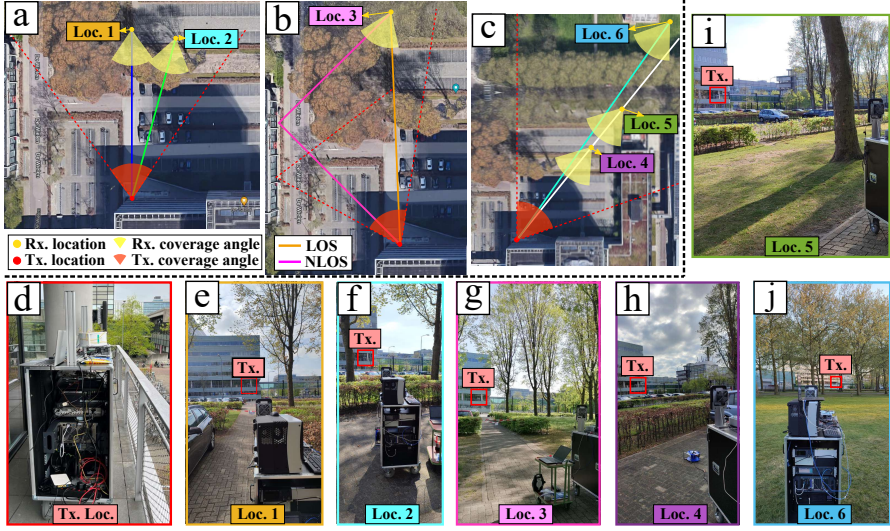


Figure 1. Locations and configurations of the different wireless scenarios utilized in the outdoor measurement campaign: (a, b, c) 2D map representing the different measurement locations with their respective antenna orientations; (d) photo of the transmitter cart located on the first floor of Flux building; (e, f, g, h, i, j) photos of the different locations of the end-user cart where the transmitter cart can be visualized.

Table 1. Wireless scenarios parameters.

Location	Distance	Angle	Location	Distance	Angle
1	59.0 m	0°	4	74.2 m	4°
2	58.5 m	13°	5	107.3 m	4°
3	83.5 m	50°	6	165.5 m	0°

mainly LOS-only scenarios. It is clear from Fig. 1 (a) that the left most beam direction misses the adjacent building. Though it is possible that a side-lobe from the TX antenna causes signal to be received at location 1 (Loc. 1) and possibly also Loc. 2. Location 3 is chosen as a test point for a combined LOS and NLOS scenario, as can be seen from the main traces in Fig. 1 (b). Location 3 also provides some additional challenges given the location of the tree trunks, shown in Fig. 1 (g). The ray-tracing shown by the orange line of Fig. 1 (b) indicates LOS is expected for beamscanning angles of 25° and -25° in transmitter and receiver PAAs, respectively. For the NLOS case, shown by the solid pink line, the transmitter PAA should be set to -18° and the receiver PAA to 22° . For locations 4-6, the environment is expected to yield LOS-only scenarios. Location 5 is located right next to the De Zaaie road, on a pedestrian pathway. Location 6 tests the performance at a longer distance of 165.5 m. For all locations and measurements, the transmitter PAA elevation is set to -5° and the receiver PAA is set to 5° . Therefore, only azimuth scanning is performed for each scenario.

Demonstration setup

This section explains the presented mm-wave IFoF setup at the device, system, and DSP levels. The first subsection exhibits the pair of PAAs employed to realize beamsteering on the experimental testbed. Secondly, the utilized mm-wave IFoF wireless scheme is presented and explained, highlighting the 5G entities that are involved in the test bench. Finally, the key aspects of the used transmitter and receiver DSP block diagrams are shown together with the used OFDM configuration.

Phased array antenna description and characterization

The PAAs used in the setup are 8-by-8 arrays of dual-polarized circular patch antennas. The antenna elements are separated by 5.8 mm, and each element is connected to an integrated power amplifier (PA) and phase shifter. The panel has a total of 128

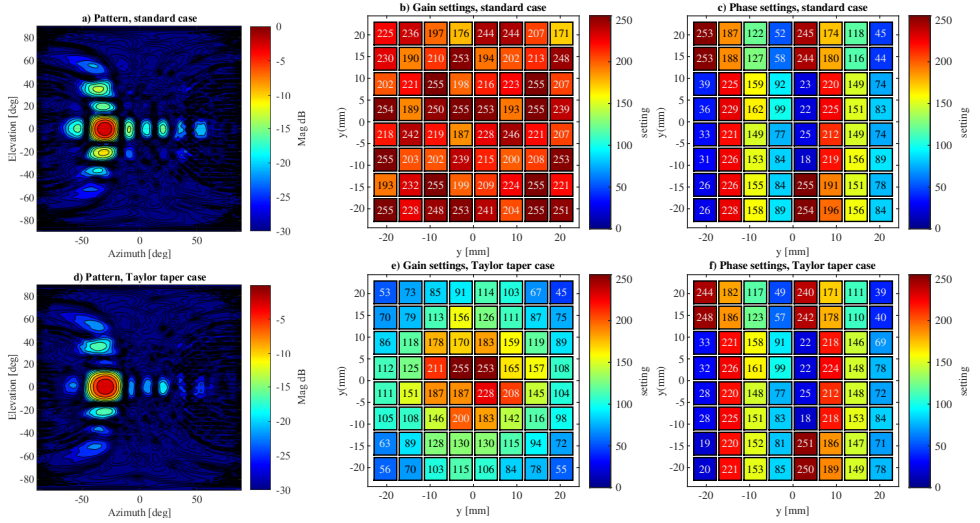


Figure 2. Measured radiation pattern in the standard case when scanning to -30° in azimuth, normalized to the peak amplitude in a), and the gain and phase settings used to excite the array in b) and c). In d) the pattern is shown when an additional Taylor taper is applied, and the gain and phase settings are shown in e) and f) for this situation.

Table 2. Measured array parameters.

Array type	Highest scan loss	Average peak SLL	HPBW of center beam
Tx mode standard	0.94 dB	-10.6 dB	12.6°
Rx mode standard	0.55 dB	-10.9 dB	11.9°
Tx mode Taylor	1.07 dB	-15.7 dB	13.7°
Rx mode Taylor	0.72 dB	-15.9 dB	13.3°

channels with independent phase and gain control with a resolution of 8 bits. This allows beamsteering in the intended direction and manipulation of the beam shape. The array has two ports, one for the horizontal and one for the vertical polarization, which can operate independently. For optimal performance, it is required that the array is calibrated. This entails measuring the gain and phase responses of each channel for each gain and phase setting and creating a map that shows the actual response for any of the 8-bit weights.

This calibration is performed in the anechoic chamber facility in a near-field setup, where an open-ended waveguide probe is placed at 5λ distance from the panel. For each channel, the probe is moved directly in front of the associated antenna element, and the gain and phase are swept. By measuring the S_{21} parameter the map is obtained. In this setup only the channel under test is turned on, all other channels are disabled. This process is sped up by only measuring 8 gain settings and 16 phase settings out of all 256^2 possible combinations, and interpolating the resulting map.

With the resulting maps, some issues with the PAA can be addressed. Firstly, the gain and phase responses of each channel differ. Furthermore, changing the phase on a channel can lead to an unintended change in gain on that channel and vice-versa. This gain-phase coupling can be addressed by using the interpolated map as a lookup table, and selecting the setting that matches the intended response most closely. This method is also used to address the phase offsets between the channels. The gain offsets can only be addressed by scaling the most powerful elements to lower power, such that all elements radiate the same amount of power. This increases the side-lobe level (SLL) at the cost of radiated power and gain. Here, we opt not to scale the element powers, in order to optimize the link budget, at the cost of increased SLL.

Taking this calibration into account, the phase and gain settings are determined for the transmitter and receiver arrays to steer the beam between $\pm 35^\circ$ in azimuth in 2.5° steps and $\pm 5^\circ$ in elevation in 5° steps. This is done in the standard phased array case and for an additional case where a 20 dB Taylor taper is applied to the weights resulting in reduced an SLL. These

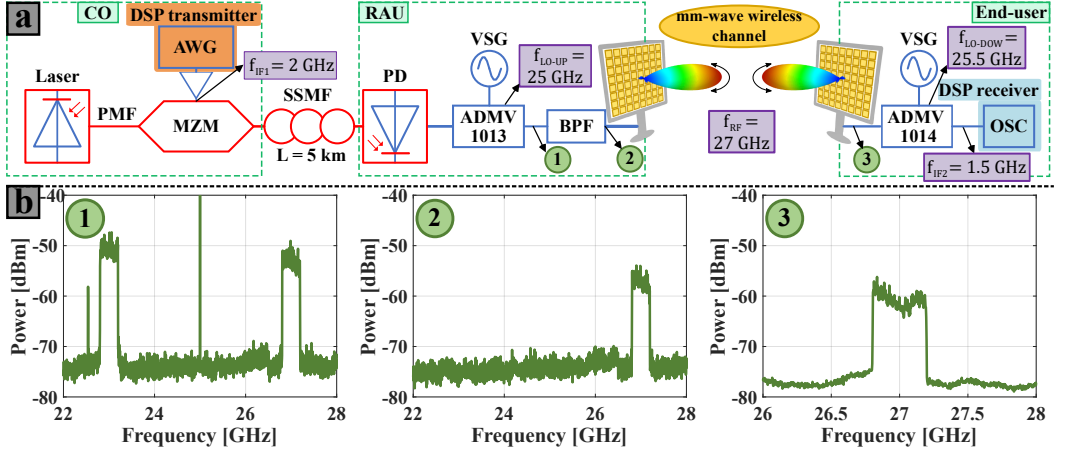


Figure 3. Experimental IFoF wireless setup for the mm-wave 5G/6G fronthaul: (a) schematic of the setup; (b) graphs of the signal spectra at different points of the experimental setup. OSC: oscilloscope.

cases will be compared in terms of error vector magnitude (EVM) and bit error rate (BER) in the outdoor setup. The low-SLL case will have a reduced gain of about 4 dB both in transmitter and receiver, resulting in an 8 dB link budget reduction. The radiation patterns generated and the array setting used to generate them using our method are shown in Fig. 2. Here an example is shown for the transmitter case, scanning towards -30° in azimuth and 0° in elevation. The patterns are similar in the receiver case. The peak SLL averaged across the measured beams for these configurations, as well as the highest scan loss compared to the center beams are given in Table 2. The scan loss is 0.13 dB to 0.35 dB higher in transmitter than in receiver mode, and the Taylor Taper reduces the SLL by 5.0 dB to 5.1 dB and increases the half power beamwidth (HPBW) with 1.1° to 1.4° . The SLL in the transmitter PAA is almost the same as in the receiver one, and the beamwidths are also equivalent. In general, the transmitter and receiver mode arrays perform similarly and their patterns are equivalent.

Experimental setup

Figure 3 (a) depicts the proposed IFoF wireless setup for mm-wave 5G/6G communications. As it can be seen in Fig. 3 (a), the schematic of the experimental setup is divided into three different segments that are enclosed in dotted cyan blocks. These segments correspond to the different entities of the 5G/6G fronthaul²²: CO, RAU, and end-user. The CO function consists of generating and preparing the data signal for the optical link transport. For achieving this, a distributed-feedback (DFB) laser emits an optical carrier at 1550 nm with 16 dBm of output power. The generated optical carrier is then used to convert the electrical data signal into the optical domain by using a Mach-Zehnder modulator (MZM). For proper optical data modulation, the MZM is biased in the quadrature point. The electrical data signal, that is introduced into the MZM, is produced with a Si6.4GSa/s arbitrary waveform generator (AWG). The IF upconversion of the baseband data signal is digitally performed in the AWG at 2 GHz and will be explained in the next subsection. After the optical data modulation, the resulting IF optical data signal is sent through a 5 km long standard single-mode fiber (SSMF). The SSMF length emulates the distance between the CO and the RAU.

In the RAU site, the optical signal at the output of the SSMF beats in a photodiode (PD), generating an electrical baseband signal at 2 GHz. Then, the resulting electrical signal is upconverted to 27 GHz of center frequency. For this mm-wave upconversion, a vector signal generator (VSG) and the ADMV1013 evaluation board from Analog Devices are utilized. The ADMV1013 board integrates a carrier quadrupler, RF mixer, and amplification controlled by voltage variable attenuators (VVA's). Hence, the VSG frequency requirements are reduced due to the use of the carrier quadrupler. More specifically, the VSG generates a sinusoid of 6.25 GHz. Since the IF mode is the selected configuration on the ADMV1013 board, the upconverted electrical signal is a double-sideband (DSB) with a carrier at 25 GHz (see the spectrum of Fig. 3 (b1)). Moreover, the maximum VVA gain is set in the used ADMV1013 configuration. To adequate the output signal for the wireless transmission, a band-pass filter (BPF) is used with a 27 GHz center frequency and ≈ 600 MHz of bandwidth²³. The spectrum of the signal obtained after this filtering process is illustrated in Fig. 3 (b2). Next, the filtered signal is fed into the transmitter PAA panel, where amplification, splitting, and phase shifting processes are carried out. Consequently, the data signal is sent to the wireless domain

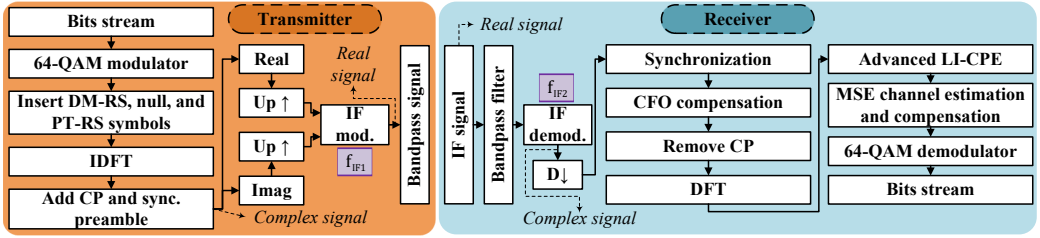


Figure 4. DSP block diagrams for transmitter (left) and receiver (right) sides.

at 27 GHz, within the n257 and n258 5G bands.

After wireless transmission, the PAA panel of the end-user catches the signal, and subsequently, phase shifting, amplification, and coupling procedures are performed. The spectrum of the signal at the output of the receiver PAA can be seen in Fig. 3 (b3). After the end-user PAA, the mm-wave signal is downconverted to a second IF whose value is 1.5 GHz. For this downconversion process, another evaluation board from Analog Devices is employed. In this case, the ADMV1014 evaluation board is the selected model for the mm-wave downconversion. A carrier quadrupler, RF mixer, and RF amplifiers are also integrated on the ADMV1014 board, which is the complementary downconverted model of the ADMV1013 board used in the RAU. In addition, for this downconversion procedure, a second VSG is required, which produces an RF carrier at 6.375 GHz. Finally, the resulting IF signal is sampled and captured by an oscilloscope with a sampling rate of 10 GSa/s.

DSP configuration

The same OFDM configuration is employed for all the different types of measurements carried out in this work. These OFDM configurations are according to 5G standards and are as follows²: 14 OFDM symbols per slot; 12 subcarriers per resource block (RB); 240 kHz of subcarrier spacing; every OFDM symbol contains 2048 subcarriers of which 416 are null, getting a total bandwidth of 391.68 MHz; one OFDM symbol per slot for channel estimation with all active subcarriers serving as demodulation reference signals (DM-RSs); one phase tracking reference signal (PT-RS) subcarrier every 8 RBs for phase noise compensation²⁴; 0.2976 μ s of cyclic prefix (CP); and 64-QAM as modulation order on the data subcarriers. With these parameters, the spectral efficiency of the OFDM signal is 0.86 Baud/Hz. Hence, the final throughput is 2015.5 Mbps for 64-QAM data modulation and 391.68 MHz of bandwidth.

The DSP block diagram used on the transmitter side is represented on the left side of Fig. 4. This DSP process is carried out in the AWG of the RAU (see Fig. 3 (a)). First, in the DSP transmitter block diagram, the input bits are mapped to 64-QAM symbols. The resulting 64-QAM symbols refer to the data subcarriers. Later, null, PT-RS, and DM-RS subcarriers are inserted respecting the OFDM configuration discussed in the previous paragraph. After this subcarrier insertion, an inverse discrete Fourier transform (IDFT) is performed, moving from the frequency to the time domain. Then, the CP is added to each OFDM symbol. All the aforementioned DSP blocks compose the OFDM transmitter. A preamble is also added at the beginning of the 5G slot frame for fine synchronization on the receiver side. Subsequently, the real and imaginary parts are separated and upsampled for a 2 GHz IF upconversion in the digital domain. As a result, an OFDM bandpass signal with an IF of 2 GHz is generated.

On the other hand, the block diagram on the right of Fig. 4 corresponds to the DSP processes performed on the receiver side in order to properly demodulate the captured signal by the oscilloscope. For that, the received signal is filtered with a digital BPF, suppressing undesired frequency components. Then, an IF demodulation procedure is realized, moving to the baseband domain. In this case, the IF value is 1.5 GHz as explained in the previous subsection. Later, the obtained baseband signal is downsampled. By using the preamble previously inserted on the transmitter side, fine synchronization is performed to find the starting time sample of the received signal. Subsequently, a rough carrier frequency offset (CFO) compensation is executed because of the frequency drift of some devices, such as VSGs and AWG, involved in the experimental setup. At this point, the OFDM receiver block starts by removing the CP. For more accurate CFO compensation, the advanced linear interpolation based ICI estimation (LI-CPE) method of article²⁵ is used by harnessing the inserted PT-RS symbols. Furthermore, this LI-CPE method allows efficient mitigation of the common phase error (CPE) that equally affects all the subcarriers of each OFDM symbol²⁵. After the LI-CPE method, a mean squared error (MSE) channel estimation is carried out by using the DM-RS OFDM symbol containing in every slot²⁶. Thus, the MSE detection is utilized to compensate for the channel on the data subcarriers. Finally, a 64-QAM demodulator is employed to extract the bits from the processed data subcarriers.

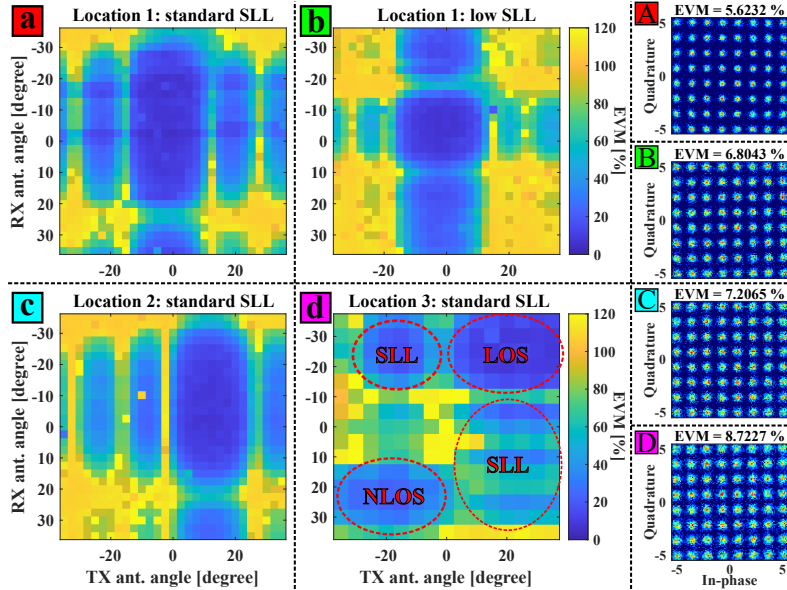


Figure 5. Experimental 2D EVM map results by realizing a double sweep in the transmitter and receiver antenna beam angles for different en-user locations and system configurations: (a) location 1 with standard SLL configuration in the PAAs; (b) location 1 with low-SLL configuration; (c) location 2 with standard SLL; (d) location 3 with standard SLL. Constellation representations of the minimum EVM points in the different EVM 2D results are also illustrated on the right side.

Measurement results and discussions

This section aims to present and explain the results obtained in the outdoor measurement campaign by using the IFoF wireless experimental setup of Fig. 3 (a). It is important to mention that all the results are collected employing the same DSP, OFDM, and device configurations specified in the previous section. Also, all the measurements in this manuscript are taken with the same PAA elevation settings: -5° and 5° elevation angles on the transmitter and receiver sides, respectively. In this way, the results of the different measurement locations can be fairly compared and examined. Figures 5 (a)-(d) exhibit the results of the measurements caught from locations 1 to 3 of Figs. 1 (e)-(g), respectively. The graphs of Figs. 5 (a)-(d) are obtained by realizing a double sweep at the beam angles of the transmitter and receiver PAAs. In other words, the x-axis indicates the transmitter beam angle while the y-axis that of the receiver. For both antennas, the range of the beam angle sweep is -35° to 35° as can be noted in Figs. 5 (a)-(d). In addition, the color of these graphs denotes the EVM value in percentage of the processed 64-QAM data symbols at the input of the QAM demodulator (see DSP receiver block diagram in Fig. 4). Cooler color signifies lower EVM as the color bar indicates. In contrast, warmer colors are associated with higher EVM values, with yellow color indicating an EVM of 100 % or superior.

Results of Figs. 5 (a) and (b) refer to the same location. However, the antenna configuration utilized at the transmitter and receiver sides is different: EVM values of Fig. 5 (a) are obtained with standard SLL configuration, while Fig. 5 (b) is obtained with a low SLL setting (see Table 2). The remaining results in this section are related to measurements captured with standard SLL antenna configurations. Moreover, on the right side of Fig. 5, in-phase and quadrature (IQ) constellations of the received 64-QAM symbols are illustrated. These IQ constellations refer to the minimum EVM of the graphs in Figs. 5 (a)-(d) where the EVM value is displayed at the top of the constellation. It is worth mentioning that Figs. 5 (a)-(c) have a beam angle step of 2.5° while 5° of beam angle step is used for the EVM results of Fig. 5 (d). For this reason Figs. 5 (a)-(c) have higher resolution than Fig. 5 (d).

Observing Fig. 5 (a), it can be noted that the minimum EVM area corresponds to the main lobe of the transmitter and receiver PAA beams. Therefore the surface of this area should be proportional to the beamwidth of the PAAs. In other words, the width and height of this area correspond to the beamwidths of the transmitter and receiver PAAs, respectively. Furthermore, examining Fig. 5 (a), other low EVM areas are noticed. These EVM spots exhibit higher EVM values and are associated with

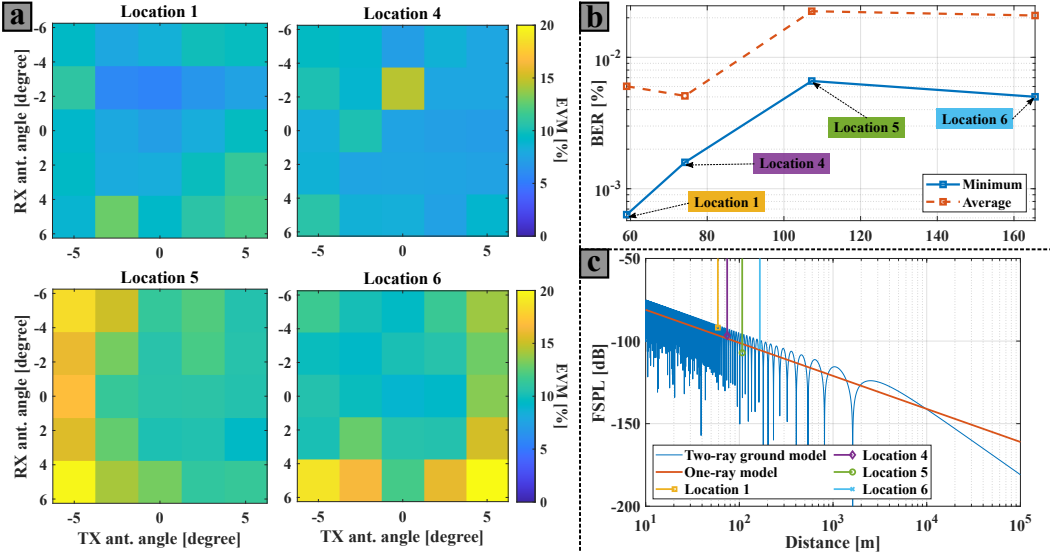


Figure 6. Experimental results in terms of distance: (a) 2D EVM map results for different locations where x-axis and y-axis are the transmitter and receiver antenna beam angles, respectively; (b) BER as a function of the distance; (c) FSPL as a function of the distance by using different ray models where the distances of the under-test locations are also represented.

the SLLs of the employed PAA panels. In order to reduce the interference induced by SLLs for a multi-user scenario case, low SLL configuration is set at location 1 of Fig. 1 (e), obtaining the EVM results of Fig. 5 (a). Comparing Figs. 5 (a) and (b), it can be seen that the blue EVM areas related to the SLLs are less intense in Fig. 5 (b) than in Fig. 5 (a). This SLL reduction occurs primarily on the transmitter antenna angle axis, while secondary blue EVM spots caused by SLLs still remain in the receiver antenna angle axis. Nonetheless, this interference reduction when using the low SLL configuration leads to a decrease in the maximum received power. For this reason, the minimum EVM value in the results of Fig. 5 (a) are lower than in Fig. 5 (b) (see constellation diagrams for these two type of measurements in Fig. 5 (A) and (B)).

As commented above, the results in Fig. 5 (c) correspond to the measurements realized in location 2 of Fig. 1 (f). The EVM results of Figs. 5 (a) and (c) exhibit a similar shape with a shifting in the x-axis. This shifting phenomenon is because the transmitter PAA is not pointing to the end-user angle (see Fig. 1 (a)). Thus, the transmitter antenna angle of minimum EVM value Fig. 5 (c) is approximately equal to the dimensional angle between both PAAs (angle value of location 2 in Table 1). Figure 5 (d) exhibits the EVM results of the measurements carried out in location 3 of Fig. 1 (b). The main purpose of these measurements dwells on quantitatively comparing LOS and NLOS communications with the same end-user location. For this reason, Fig. 5 (d) shows EVM blue spots respecting LOS and NLOS links, respectively. It is obvious that the EVM values concerning the NLOS communication are higher than in the LOS case: 20.39 % of minimum EVM for the NLOS link and 8.72 % for the LOS case. These EVM values indicate that the LOS link in this wireless scenario of location 3 permit 64-QAM modulation order while the NLOS link conditions are suitable for QPSK as modulation for the data subcarriers. These results experimental prove that NLOS communication can be found by properly by scanning with the beamsteering capabilities provided by the employed PAAs. Then, this NLOS link can be used a secondary channel in case of a blockage of the LOS communication, strengthening the robustness of the mm-wave mobile system. In Fig. 5 (d), there are also low EVM areas caused by the SLLs of the used PAAs. Additionally, the transmitter and receiver antenna angles related to the minimum EVM value of the NLOS are -15° and 25° degree, respectively. These angle values are related to the NLOS link angles of Fig. 1 (b) previously commented. Thus, the EVM results are according to the wireless scenario considerations, discussed above.

Figure 6 shows the results obtained from the measurements of locations 1, 4, 5, and 6 (see Fig. 1). The aim of Fig. 6 is to represent the performance of the IFoF wireless setup in terms of distance. For that, Fig. 6 (a) depicts 2D EVM color maps referring the aforementioned locations. In this case, the sweep range of the transmitter and receiver antenna beam angles is -5° to 5° . Moreover, in Fig. 6 (b) the BER results are shown as a function of the distance of each location. In this graph, the continuous blue lines are concerned with the minimum value of the BER plots of Fig. 6 (a), while the dotted orange lines refer to

Table 3. Summary of the experimental results for the different wireless locations and system configurations. Forward error correction (FEC) thresholds: $3.8e^{-3}$ % and $1.34e^{-2}$ % for 7 % and 25 % overhead (OH), respectively²⁸.

Loc.	low SLL	min(BER)	min(EVM)	α_{tx} [°]	α_{rx} [°]	OH FEC	Throughput
1	No	$6e^{-4}$ %	5.6 %	0	-2.5	7 %	1.88 Gbps
1	Yes	$1.5e^{-3}$ %	6.8 %	-2.5	-5	7 %	1.88 Gbps
2	No	$1.2e^{-3}$ %	7.2 %	12.5	-2.5	7 %	1.88 Gbps
3	No	$2.7e^{-3}$ %	8.7 %	20	-20	7 %	1.88 Gbps
4	No	$1.6e^{-3}$ %	7.2 %	5	0	7 %	1.88 Gbps
5	No	$6.6e^{-3}$ %	9.4 %	5	2.5	25 %	1.61 Gbps
6	No	$5.0e^{-3}$ %	9.0 %	0	0	25 %	1.61 Gbps

the average of all the BER values in each antenna beam angle combinations. Examining Fig. 6 (b), it is noticeable that location 4 presents the lowest gap value between the average and minimum BER results. This gap is related to the impact of the antenna misalignment that can occur in the communication. Thereby, location 4 exhibits more robustness to antenna misalignment than location 1 as the average BER values are lower. The reason for this phenomenon could be that fewer obstacles are involved in the wireless scenario of location 4, respecting location 1 (compare Figs. 1 (e) and (h)). Also, it is important to notice that the BER results of location 6 are lower than in location 5, even though the link distance is greater in the location 6 case. One of the possible causes of this decrease of BER for larger communication distances is the impact of the ray reflected by the ground is more significant at these distances²⁷.

Figure 6 (c) illustrates the theoretical FSPL values of the under-test wireless scenarios, considering the one-ray (Friis transmission equation) and two-ray ground-reflection models. Both models are set for 27 GHz of carrier frequency. The blue line of Fig. 6 (c) is obtained assuming a perfect ground reflection ($\Gamma = 1$)²⁷. The remaining parameters to get this curve are the following: the transmitter and receiver heights (h_{tx} and H_{rx}) are 6 m and 1.5 m, respectively. Furthermore, the FSPL values of the two-ray ground model for the distances of locations 1, 4, 5, and 6 are disclosed also in Fig. 6 (c). The FSPL value of location 6 presents a drop larger than the rest of the locations. This FSPL drop induced by the ground reflected ray might justify the BER/BER decay respecting the link distance. However, as it can be observed in Fig. 6 (c), the periodicity of the fading pattern in the two-ray ground-reflection model is high, where a small error in the distance calculation originates a large FSPL variation.

Lastly, Table 1 shows the minimum BER/EVM results for each type of measurement realized with the presented IFoF wireless experimental setup. The transmitter and receiver antenna beam angles (α_x and α_{rx}) related to these BER/EVM values are also illustrated in Table 1. All these angle values are approximately 0, except for the results of locations 2 and 3 because in these scenarios the antennas are not aligned (Figs. 1 (a) and (b)). Moreover, the BER results in Table 1 are linked to the minimum OH FEC percentage that allow a final BER after coding of $1e^{-9}$ ²⁸. Therefore, regarding the throughput value calculated in the previous section, the throughput values considering channel coding are 1.88 Gbps and 1.61 Gbps for 7 % and 25 % of OH FEC, respectively.

Conclusions

First, in this manuscript, the relevance of ARoF technology is highlighted as key technology for the future mm-wave 5G/6G fronthaul, with IFoF being interesting because of its attractive benefits. Beam steering based on PAA is also remarked as an essential solution for enabling mm-wave mobile communications. Hence, an experimental IFoF fronthaul setup for mm-wave wireless transmission at 27 GHz is presented and deeply explained. In the proposed experimental setup, 8-by-8 PAA panels with integrated amplification are employed for the transmitter and receiver front-ends, allowing beamsteering capabilities in the azimuth and elevation dimensions. For proper comprehension of the setup, the used PAAs are described and measured. Furthermore, the configuration of the experimental setup is according to the 5G standards transmitting 64-QAM OFDM signals with ≈ 400 MHz of bandwidth at 27 GHz of center frequency, within the n257 and n258 bands.

An exhaustive measurement campaign is carried out in different outdoor wireless scenarios, positioning the end-user receiver at different locations. For all these measurements, a double sweep in the azimuth angle of both PAAs is performed in order to evaluate the performance of the experimental setup in different wireless scenarios. Moreover, two different PAA configurations are testing: standard SLL and low SLL. Standard SLL results show lower EVM values while low SLL reduces the user interference. Therefore, there is a clear trade-off between user interference and final performance in terms of BER and EVM. In addition, LOS and NLOS communications are compared under the same end-user location, permitting a fair comparison between both types of links. The obtained EVM values determine that LOS link conditions can support 64-QAM

modulation order while the NLOS link is capable of successfully transmit QPSK OFDM signals. Thus, in case of a blockage in the LOS communication, it is proven that beamsteering based on PAAs is able to scan a possible NLOS link, increasing the reliability of mm-wave mobile communications.

A comparison of the performance between different end-user locations in terms of link distance is also realized. In this comparison, it is seen that the two-ray reflected by the ground might affect the system performance in the under-test distances since the obtained BER curve as a function of the distance is not gradually increasing. Overall, great EVM and BER results are obtained in all the realized measurement locations, achieving a maximum distance of 165.5 m with a BER under the 25 % OH FEC limit and with a final throughput of 1.61 Gbps. With the proposed IFoF wireless system and the experimental results, keynotes are provided to suitably realize a robust mm-wave wireless fronthaul based on IFoF and PAA technologies. Also, the excellent BER/EVM results obtained in the measurement campaign strengthen wireless IFoF combined with PAA as an excellent solution to transport and transmit mm-wave signals in the future 5G/6G networks.

References

1. Jiang, W., Han, B., Habibi, M. A. & Schotten, H. D. The Road Towards 6G: A Comprehensive Survey. *IEEE Open J. Commun. Soc.* **2**, 334–366, DOI: [10.1109/OJCOMS.2021.3057679](https://doi.org/10.1109/OJCOMS.2021.3057679) (2021).
2. 3GPP. *FG IMT-2020: User Equipment (UE) radio transmission and reception*. 3GPP TR 38.101-2, version 16.5.0 (2020).
3. Hemadeh, I. A., Satyanarayana, K., El-Hajjar, M. & Hanzo, L. Millimeter-Wave Communications: Physical Channel Models, Design Considerations, Antenna Constructions, and Link-Budget. *IEEE Commun. Surv. & Tutorials* **20**, 870–913, DOI: [10.1109/COMST.2017.2783541](https://doi.org/10.1109/COMST.2017.2783541) (2018).
4. Ranaweera, C., Wong, E., Nirmalathas, A., Jayasundara, C. & Lim, C. 5G C-RAN With Optical Fronthaul: An Analysis From a Deployment Perspective. *J. Light. Technol.* **36**, 2059–2068, DOI: <https://doi.org/10.1109/JLT.2017.2782822> (2018).
5. Browning, C., Dass, D., Townsend, P. & Ouyang, X. Orthogonal Chirp-Division Multiplexing for Future Converged Optical/Millimeter-Wave Radio Access Networks. *IEEE Access* **10**, 3571–3579, DOI: [10.1109/ACCESS.2021.3137716](https://doi.org/10.1109/ACCESS.2021.3137716) (2022).
6. Rommel, S. *et al.* Towards a Scaleable 5G Fronthaul: Analog Radio-over-Fiber and Space Division Multiplexing. *J. Light. Technol.* **38**, 5412–5422, DOI: [10.1109/JLT.2020.3004416](https://doi.org/10.1109/JLT.2020.3004416) (2020).
7. Thomas, V. A., El-Hajjar, M. & Hanzo, L. Millimeter-Wave Radio Over Fiber Optical Upconversion Techniques Relying on Link Nonlinearity. *IEEE Commun. Surv. & Tutorials* **18**, 29–53, DOI: [10.1109/COMST.2015.2409154](https://doi.org/10.1109/COMST.2015.2409154) (2016).
8. Che, D. Analog vs Digital Radio-Over-Fiber: A Spectral Efficiency Debate From the SNR Perspective. *J. Light. Technol.* **39**, 5325–5335, DOI: [10.1109/JLT.2021.3102220](https://doi.org/10.1109/JLT.2021.3102220) (2021).
9. Sung, M. *et al.* Demonstration of IFoF-Based Mobile Fronthaul in 5G Prototype With 28-GHz Millimeter wave. *J. Light. Technol.* **36**, 601–609, DOI: <https://doi.org/10.1109/JLT.2017.2763156> (2018).
10. Fiorani, M. *et al.* Modeling energy performance of C-RAN with optical transport in 5G network scenarios. *J. Opt. Commun. Netw.* **8**, B21–B34, DOI: [10.1364/JOCN.8.000B21](https://doi.org/10.1364/JOCN.8.000B21) (2016).
11. Santacruz, J. P., Rommel, S., Johannsen, U., Jurado-Navas, A. & Monroy, I. T. Analysis and Compensation of Phase Noise in Mm-Wave OFDM ARoF Systems for Beyond 5G. *J. Light. Technol.* **39**, 1602–1610, DOI: [10.1109/JLT.2020.3041041](https://doi.org/10.1109/JLT.2020.3041041) (2021).
12. Kutty, S. & Sen, D. Beamforming for Millimeter Wave Communications: An Inclusive Survey. *IEEE Commun. Surv. & Tutorials* **18**, 949–973, DOI: [10.1109/COMST.2015.2504600](https://doi.org/10.1109/COMST.2015.2504600) (2016).
13. Roth, K., Pirzadeh, H., Swindlehurst, A. L. & Nossek, J. A. A Comparison of Hybrid Beamforming and Digital Beamforming With Low-Resolution ADCs for Multiple Users and Imperfect CSI. *IEEE J. Sel. Top. Signal Process.* **12**, 484–498, DOI: [10.1109/JSTSP.2018.2813973](https://doi.org/10.1109/JSTSP.2018.2813973) (2018).
14. Omam, Z. R. *et al.* Ka-Band Passive Phased-Array Antenna With Substrate Integrated Waveguide Tunable Phase Shifter. *IEEE Transactions on Antennas Propag.* **68**, 6039–6048, DOI: [10.1109/TAP.2020.2983838](https://doi.org/10.1109/TAP.2020.2983838) (2020).
15. Ruggeri, E. *et al.* A 5G Fiber Wireless 4Gb/s WDM Fronthaul for Flexible 360° Coverage in V-Band massive MIMO Small Cells. *J. Light. Technol.* **39**, 1081–1088, DOI: <https://doi.org/10.1109/JLT.2020.3029608> (2021).
16. Vagionas, C. *et al.* Linearity Measurements on a 5G mmWave Fiber Wireless IFoF Fronthaul Link With Analog RF Beamforming and 120° Degrees Steering. *IEEE Commun. Lett.* **24**, 2839–2843, DOI: <https://doi.org/10.1109/LCOMM.2020.3019733> (2020).

17. Ruggeri, E. *et al.* Multi-User V-Band Uplink Using a Massive MIMO Antenna and a Fiber-Wireless IFoF Fronthaul for 5G mmWave Small-Cells. *J. Light. Technol.* **38**, 5368–5374, DOI: <https://doi.org/10.1109/JLT.2020.2984374> (2020).
18. Kanta, K. *et al.* Analog fiber-wireless downlink transmission of IFoF/mmWave over in-field deployed legacy PON infrastructure for 5G fronthauling. *J. Opt. Commun. Netw.* **12**, D57–D65, DOI: <https://doi.org/10.1364/JOCN.391803> (2020).
19. Argyris, N. *et al.* A 5G mmWave Fiber-Wireless IFoF Analog Mobile Fronthaul Link With up to 24-Gb/s Multiband Wireless Capacity. *J. Light. Technol.* **37**, 2883–2891, DOI: <https://doi.org/10.1109/JLT.2019.2897109> (2019).
20. Sung, M. *et al.* RoF-Based Radio Access Network for 5G Mobile Communication Systems in 28 GHz Millimeter-Wave. *J. Light. Technol.* **38**, 409–420, DOI: <https://doi.org/10.1109/JLT.2019.2942636> (2020).
21. Schulpen, R., Bronckers, L. A., Smolders, A. B. & Johannsen, U. 5g millimeter-wave nlos coverage using specular building reflections. In *2020 14th European Conference on Antennas and Propagation (EuCAP)*, 1–5, DOI: [10.23919/EuCAP48036.2020.9136044](https://doi.org/10.23919/EuCAP48036.2020.9136044) (2020).
22. Santacruz, J. P., Nazarikov, G., Rommel, S., Jurado-Navas, A. & Tafur Monroy, I. Bidirectional ARoF fronthaul over multicore fiber for beyond 5G mm-wave communications. *Opt. Commun.* **521**, 128591, DOI: <https://doi.org/10.1016/j.optcom.2022.128591> (2022).
23. Meyer, E., Bressner, T. A. H., Bart Smolders, A. B. & Johannsen, U. Miniaturized Conical Waveguide Filtenna for 5G Millimeter Wave Base Stations. In *2021 15th European Conference on Antennas and Propagation (EuCAP)*, 1–5, DOI: [10.23919/EuCAP51087.2021.9411045](https://doi.org/10.23919/EuCAP51087.2021.9411045) (Dusseldorf, Germany, 2021).
24. Qi, Y., Hunukumbure, M., Nam, H., Yoo, H. & Amuru, S. On the Phase Tracking Reference Signal (PT-RS) Design for 5G New Radio (NR). In *2018 IEEE 88th Vehicular Technology Conference (VTC-Fall)*, 1–5, DOI: [10.1109/VTCTFall.2018.8690852](https://doi.org/10.1109/VTCTFall.2018.8690852) (Chicago, IL, USA, 2018).
25. Ha, Y. & Chung, W. A Feedforward Partial Phase Noise Mitigation in the Time-Domain using Cyclic Prefix for CO-OFDM Systems. *J. Opt. Soc. Korea* **17**, 467–470 (2013).
26. Xiong, X., Jiang, B., Gao, X. & You, X. DFT-Based Channel Estimator for OFDM Systems with Leakage Estimation. *IEEE Commun. Lett.* **17**, 1592–1595, DOI: [10.1109/LCOMM.2013.060513.130891](https://doi.org/10.1109/LCOMM.2013.060513.130891) (2013).
27. Weiler, R. J., Peter, M., Keusgen, W., Kortke, A. & Wisotzki, M. Millimeter-wave channel sounding of outdoor ground reflections. In *2015 IEEE Radio and Wireless Symposium (RWS)*, 95–97, DOI: [10.1109/RWS.2015.7129712](https://doi.org/10.1109/RWS.2015.7129712) (San Diego, CA, USA, 2015).
28. G.975.1, I-T. *Forward error correction for high bit-rate DWDM submarine systems* (2004).

Funding

This work was supported and partially funded by 5G-MOBIX (GA no. 825496), 5G STEP FWD (GA no. 722429), and IoTalentum (GA no. 953442) projects which have received funding from the European Union's Horizon2020 research and innovation programme. Additionally, this work was also supported by the research program FREEPOWER with project number 17094, which is financed by the Dutch Research Council (NWO).

Additional information

To include, in this order: **Accession codes** (where applicable); **Competing interests** (mandatory statement).

The corresponding author is responsible for submitting a [competing interests statement](#) on behalf of all authors of the paper. This statement must be included in the submitted article file.

Conclusions and future outlook

7.1 Summary and conclusions

This section aims to give a summary and concluding remarks regarding this dissertation. The work presented in this thesis expands the SOTA with regard the study, analysis, design, and selection of technologies to be implemented in the future mm-wave fronthaul based on ARoF. Hence, the work of this dissertation facilitates the selection of these technologies for future 5G/6G standards. The summary and conclusions of each of the chapters presented throughout this thesis are the following:

- In **Chapter 2**, the theoretical foundations of ARoF for the mm-wave fronthaul has been provided, segmenting the system under study into different blocks. In particular, the optical two-tone generation block has been proven to be a key building block for the mm-wave ARoF fronthaul. Different optical two-tone generation techniques have been qualitatively compared, offering a trade-off between power efficiency, complexity, and phase noise, making their appropriate selection based on the configuration and requirements of the system. Moreover, since mm-wave ARoF wireless systems combine multiple channels, their complexity is high, leading to a set of multiple combined impairments: non-linearities, AWGN noise, dynamic range, and phase noise. Therefore, in order to mitigate these ARoF impairments, in the future mm-wave fronthaul, the utilized waveform, DSP techniques, building blocks, devices, and system design must be properly studied, realized and implemented.
- **Chapter 3** focuses on the most suitable waveforms and modulation schemes for the future mm-wave fronthaul based on ARoF. More specifically, **P1** qualitatively compares the main waveform candidates for 5G in terms of several

KPIs that indicate the adequacy to the mm-wave ARoF wireless channel. One of the results from **P1** is that the waveform selection based on a qualitative comparison is not conclusive and depends on the channel conditions. For a waveform selection based on empirical assessments, **P2** experimentally compares different waveforms in a static mm-wave ARoF setup. The results of **P2** show that the standardized OFDM modulation format is not the best waveform for the system under test, with SC-FDM and Multi-CAP being better solutions in terms of BER. According to the optimization of the channel capacity usage in the ARoF based mm-wave fronthaul, **P3** proposes and experimentally validates PAS-OFDM as an excellent modulation scheme as it allows to gradually decrease the impact, caused by the mm-wave ARoF impairments, on the OFDM subcarriers. Furthermore, the empirical results of **P3** remark OFDM-PAS as a better solution than traditional methods such as the bit-loading technique. As Table 3.1 shows, **P3** fills a research gap related to the first PAS-OFDM based on ESS transmission in an experimental mm-wave ARoF wireless setup, following 5G standards.

- In **Chapter 4**, first, the phase noise channel model and its impact on the OFDM subcarriers have been explained. Then, different DSP techniques to mitigate the phase noise in OFDM signals have been presented and explained. Most of these presented DSP techniques have been proposed in the contribution papers of this dissertation. Next, **Chapter 4** realizes a qualitative comparison between the presented phase noise mitigation techniques, concluding that the most convenient technique depends on the phase noise level and requirements of the system. Finally, all the explained DSP techniques to mitigate the phase noise have been evaluated in experimental mm-wave ARoF setups where the phase noise is the main drawback of the channel. With the contribution works of **P4**, **P5**, **P6**, **P7**, and **P8** included in **Chapter 4**, the SOTA on the investigation of techniques to reduce the phase noise impact in mm-wave ARoF systems oriented towards the 5G standard has been significantly extended, as shown in Table 4.3.
- In **Chapter 5**, the main RoF solutions for the mm-wave fronthaul have been introduced, presented, and compared, highlighting ARoF technology as a preferred transport solution due to the large number of mm-wave cells expected for future mobile networks. **P9** and **P10** provide several key system design choices for implementing a bidirectional mm-wave fronthaul based on ARoF and MCF. As Table 5.2 shows, the work of **P9** and **P10** covers a research gap linked to the experimental and efficient implementation of a bidirectional ARoF fronthaul following 5G standards. With the experimental results of **P9** and **P10**, empirical assessments are given, facilitating the selection of the best OFDM configurations and system settings for future investigations and upcoming 5G/6G standards.
- The importance of beamforming and beam steering techniques for mm-wave

mobile communications has been remarked in **Chapter 6**. In addition, **Chapter 6** qualitatively compares three different analog beamforming approaches: electrical, optical, and PIC. Besides, experimental validation of electrical and PIC approaches has been successfully accomplished: **P11** fully characterizes and theoretically explains an OBFN PIC designed to generate four beams at 27.5 GHz; **P12** realizes an extensive measurement campaign for an experimental mm-wave outdoor demonstration based on IFoF combined with RF beamforming and phased array antennas. The work presented in **P11** validates and proves for the first time, to the best of the author's knowledge, the correct operation of an OBFN PIC based on optical waveguides and capable of simultaneously generating multiple beams, paving the road to make PIC based beamforming a mature technology for future mobile communications. In parallel, the contribution of **P12** allows to provide quantified communication performance in a realistic mm-wave mobile scenario based on IFoF transport and phased array antennas.

7.2 Future outlook and recommendations

This section lists and explains the future research lines and recommendations regarding the work realized in this dissertation. For the mm-wave ARoF implementation in the fronthaul, optical two-tone generation techniques need to be further investigated in order to reach a proper balance between phase noise, power efficiency, and system complexity. In this way, the future mm-wave fronthaul will be less expensive, more energy efficient, and will dispense with complex phase noise mitigation techniques. In other words, alternative solutions to the techniques presented in Table 2.1 must be found, analyzed, and evaluated.

Concerning waveforms for mm-wave ARoF systems, future 6G standards should consider other modulation formats, apart from OFDM and SC-FDM. The inclusion of new waveforms in future mobile standards is crucial for the case of high mobility mm-wave scenarios where the OFDM subcarriers suffer from high degradation due to the Doppler effect, which is intensified in the mm-wave domain with respect to sub-7 GHz bands. Doppler effect is not a concern in all the experimental setups of this dissertation since the end-user is not mobile. As a consequence, new waveforms, such as orthogonal time frequency space (OTFS), have emerged as great solution for high mobility scenarios where the Doppler spread is one of the main impairments [172]. Therefore, new waveforms, such as the mentioned OTFS, should be experimentally evaluated and compared with already standardized solutions in a mm-wave ARoF wireless scenario, as **P2** does. Also, it is relevant to investigate linearization techniques to reduce OOB emissions, increasing the suitability of the wireless signal for multiband transmission. Regarding the PAS-OFDM modulation scheme, different ESS configurations shall be designed and compared in an experimental mm-wave fronthaul based on ARoF in order to

assess the best ESS configuration, providing a proper ESS dictionary for future 5G/6G standards.

For a proper standardization of ARoF technology for the mobile fronthaul, as done for DRoF in CPRI, eCPRI and NGFI, more experimental investigation of ARoF solutions by transporting 5G NR signals should be accomplished, yielding empirical results. More explicitly, schemes and techniques to increase the dynamic range in the downlink and uplink of ARoF systems should be further researched. In such a manner, ARoF technology can be consolidated as a mature technology to be standardized for future mm-wave mobile networks.

The reduction of power consumption is one of the main requirements in mobile network standards. Integrating the ARoF transmitter and receiver on a single-chip will greatly reduce the volume, cost, and power consumption in the COs and RAUs. For the case of multi-chip integration, the optical and electrical components are wire bonded and packaged together [173], [174]. For example, the RAU based on mm-wave ARoF transport, is composed of a PD, an RF filter, an RF amplifier, and an antenna. These four components can be designed, integrated, and packaged in a single-chip. In this manner, by optimizing the production of this chip, the mm-wave 5G deployment would be miniaturized and optimized in terms of cost and energy with a low environmental and infrastructural impact. The same integration and package concept can be applied to the ARoF transmitter of the CO. In other words, one of the schematics of Fig. 2.3 can be integrated into a single-chip. Moreover, for a bidirectional scenario, the mentioned integrated chips shall be designed as transceivers.

The DSP processes of the experiments in **P2**, **P3**, **P9**, **P10**, and **P12** are performed offline. For a more realistic scenario, these DSP processes should be realized in real-time by using a BBU composed of a field programmable gate array (FPGA) or an application-specific integrated circuit (ASIC). Therefore, the work realized in **P2**, **P3**, **P9**, **P10**, and **P12** can be extended to a system closer to a final commercial mm-wave ARoF fronthaul for 5G/6G networks. In the case of a bidirectional mobile fronthaul, a transceiver to process the baseband signals is placed at the CO and end-user sites, respectively. Hence, the RF switches of the RAU and end-user shall be controlled, allowing an adequate TDD communication [175]. After doing this, protocols of the radio stack can be implemented in a central processing unit (CPU) that interfaces with the DSP process of the FPGA. In addition, for this BBU realization, DACs and ADCs must be interconnected to the FPGA [176]. A co-integration of CPU, FPGA, DACs, and ADCs devices corresponds to a system-on-chip (SoC) solution, which is currently accessible on the market. After the implementation of the necessary protocols in the BBU of the CO, SDN can be applied on top in order to optimize the network resources by orchestration [170].

Depending on the phase noise conditions of the mm-wave ARoF system, one of the phase noise compensation algorithms presented in **Chapter 4** can also be implemented in the BBU discussed above. Thereby, the computational complexity of these algorithms can be translated into a more tangible parameters, such as the

power consumption and the number of look-up-tables (LUTs), flip-flops, configurable logic blocks (CLBs), and multipliers embedded in FPGAs. Regarding the IDF algorithm with adaptive LPF proposed in **P4**, an advanced version of this method can be performed by discarding the less reliable demodulated QAM symbols for the phase noise estimate. Thus, better performance can be obtained by using this advanced phase noise compensation algorithm. Another possible enhancement of the algorithm proposed in **P4** consists of utilizing a specific percentage of the demodulated data subcarriers for the phase noise estimate, allowing granular adjustment of the computational complexity of each iteration. By applying this additional feature, the complexity of the IDF algorithm with adaptive LPF can be efficiently adjusted to different phase noise levels, optimizing the DSP process.

The ESS algorithm utilized in **P3** can also be implemented in the mentioned BBU to perform PAS-OFDM, assessing its integrability in an FPGA. Additionally, in order to improve the presented soft ESS demapping algorithm in **P3**, a similar detection and correction strategy to the Viterbi decoder can be applied. Thereby, the number of successful corrections of this soft demapping process could be increased. Furthermore, this Viterbi decoder strategy can also be applied to other PAS approaches such as CCDFM or SM. For improving the performance in PAS-OFDM systems, a soft PAS demapping block assigns to each PAM symbol a value, that indicates its reliability, such as the Hamming distance. Hence, this reliable indicator is introduced in the channel decoding block, attempting to enhance the correction rate. In such a manner, the soft ESS demapping algorithm can be efficiently integrated with the channel decoding.

To perform reliable mm-wave mobile communications, in addition to beam steering, reconfigurable intelligent surface (RIS) is a promising candidate to be part of future mobile networks [177]. In mm-wave wireless scenarios, an obstacle in the LOS link significantly deteriorates the communication link. Therefore, RIS combined with beam steering permits to find a secondary LOS link, avoiding the possible blockage produced by obstacles in the wireless scenario. Figure 7.1 shows a perspective of future mm-wave outdoor mobile communications where the beam steering mechanism of the RAU is connected to a nearby RIS, enabling a secondary LOS path. In Fig. 7.1, cell-free massive MIMO is also considered since it brings attractive benefits such as low complexity signal processing, augmented cell coverage area, high energy efficiency, and low deployment cost, compared to traditional mobile networks [178]. By observing Fig. 7.1, the mobile phone of the user is capable of generating three independent beams for having high connectivity. Furthermore, the mobile phone performs baseband, downconversion, upconversion, filtering, and amplification processes for mm-wave communication. Integrating of all these mm-wave and baseband functionalities into a mobile phone is quite challenging, especially to minimize power consumption in order to get an acceptable battery life [179]. mm-wave ARoF fronthaul co-integrated with beam steering, RIS, and cell-free massive MIMO shall be validated in experimental demonstrations to appraise the performance of these combined techniques and the

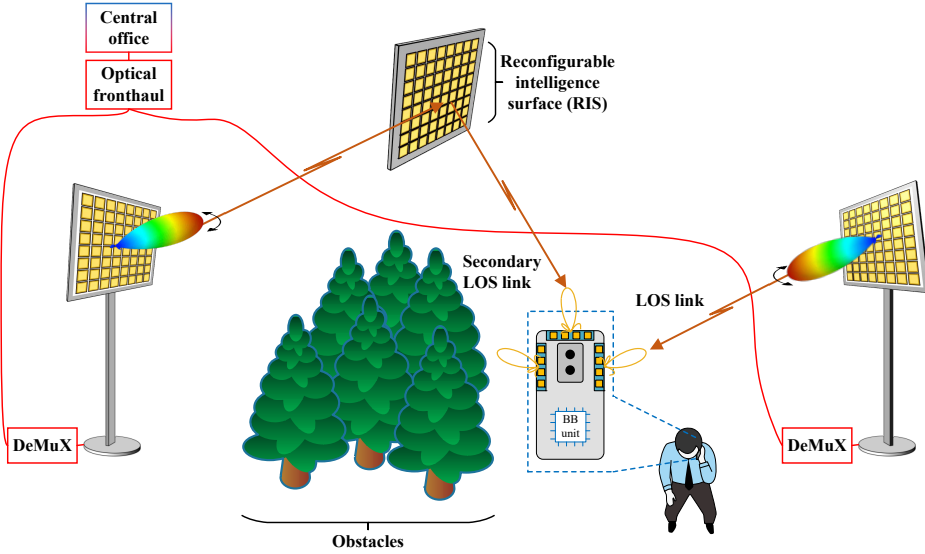


Figure 7.1: The perspective of future mm-wave outdoor scenarios based on ARoF fronthaul, beam steering, RIS, and cell-free massive MIMO.

potential challenges that this co-integration could face.

Regarding the optical beamforming research realized in **P11**, the proposed OBFN PIC would be fully validated in a realistic mm-wave ARoF wireless setup, as Fig. 6.3(a) shows, by successfully transmitting 5G NR signals. To be more precise, the experimental setup for the OBFN PIC validation shall be the uplink version of the scheme in Fig. 6.3(b). In addition, the proposed OBFN PIC of **P11** should be extended to an advanced version. This advanced PIC version shall be designed, manufactured, and characterized. In this advanced version, the number of output antennas that the OBFN allows shall be in the order of 64 or even more, for a more realistic scenario according to 5G standards [180]. Moreover, to implement beam steering functionalities in the proposed OBFN of **P11**, a more advanced version shall incorporate multiple delay stages that can be switched on or off, offering discrete delay tuning.

In **P12**, an outdoor mm-wave demonstration is performed by using an IFoF setup. For a more realistic mm-wave scenario, one of the next steps of the work in **P12** is to include multiple end-users. Therefore, the interference between users can be empirically evaluated, analyzed, and quantified. Also, different phased array antennas codebooks can be tested with the goal of minimizing the overall user interference in the communication system. In addition, non-orthogonal multiple access (NOMA) technologies can be implemented in this multi-user outdoor experiment to balance and optimize the average data rate of each user [181]. Furthermore, at higher protocol layers, algorithms should be implemented to control

beam angles for proper user tracking.

Finally, since the maturity of artificial intelligence (AI) has been consolidated in recent years, AI could be applied to most of algorithms and technologies involved in mm-wave AroF wireless systems [182]–[184]: SDN orchestrator, antenna beam alignment, codebook selection, QAM demapping, selection of the best waveform configuration depending on the channel conditions, search for secondary LOS path in case of blockage, power allocation in NOMA scenarios, selection of the best PAS-OFDM setting according to the channel stage, automatic configuration of the heaters that control the different components of OBFN based on PIC, management of heterogeneous systems, etc. However, the integration of AI algorithms in these communication blocks must be realized with a deep understanding of the problem to solve and reasonable criteria, since AI is not always the best solution to apply. As a final comment, the contributions from the work presented in this dissertation set the foundations and are necessary pre-requirements for much of the future work and lines of research discussed above.

Bibliography

- [1] R. Wenzlhuemer, “The dematerialization of telecommunication: communication centres and peripheries in Europe and the world, 1850–1920,” *Journal of Global History*, vol. 2, no. 3, pp. 345–372, Nov. 2007. DOI: 10.1017/S174002280700232X.
- [2] G. Madden and S. J. Savage, “Telecommunications and Economic Growth,” *International Journal of Social Economics*, vol. 27, no. 7/8/9/10, pp. 893–906, Jul. 2000. DOI: 10.1108/03068290010336397.
- [3] W. Brinkman, D. Haggan, and W. Troutman, “A history of the invention of the transistor and where it will lead us,” *IEEE Journal of Solid-State Circuits*, vol. 32, no. 12, pp. 1858–1865, Dec. 1997. DOI: 10.1109/4.643644.
- [4] T. Dunnewijk and S. Hultén, “A brief history of mobile communication in Europe,” *Telematics and Informatics*, vol. 24, no. 3, pp. 164–179, Aug. 2007. DOI: <https://doi.org/10.1016/j.tele.2007.01.013>.
- [5] R. Ling and R. McEwen, “Mobile communication and ethics: implications of everyday actions on social order,” *Etikk i praksis - Nordic Journal of Applied Ethics*, vol. 4, no. 2, pp. 11–26, Jul. 2010. DOI: 10.5324/eip.v4i2.1760.
- [6] A. Fehske, G. Fettweis, J. Malmudin, and G. Biczok, “The global footprint of mobile communications: The ecological and economic perspective,” *IEEE Communications Magazine*, vol. 49, no. 8, pp. 55–62, Aug. 2011. DOI: 10.1109/MCOM.2011.5978416.
- [7] Cisco, “Cisco Annual Internet Report (2018–2023),” Tech. Rep., Mar. 2020.
- [8] Ericsson, “Ericsson Mobility Report,” Tech. Rep., Nov. 2021, Available: <https://www.ericsson.com/en/reports-and-papers/mobility-report>.
- [9] S. Mattisson, “An Overview of 5G Requirements and Future Wireless Networks: Accommodating Scaling Technology,” *IEEE Solid-State Circuits Magazine*, vol. 10, no. 3, pp. 54–60, Aug. 2018. DOI: 10.1109/MSSC.2018.2844606.
- [10] W. Jiang, B. Han, M. A. Habibi, and H. D. Schotten, “The Road Towards 6G: A Comprehensive Survey,” *IEEE Open Journal of the Communications Society*, vol. 2, pp. 334–366, Feb. 2021. DOI: 10.1109/OJCOMS.2021.3057679.

- [11] A. F. M. S. Shah, A. N. Qasim, M. A. Karabulut, H. Ilhan, and M. B. Islam, "Survey and Performance Evaluation of Multiple Access Schemes for Next-Generation Wireless Communication Systems," *IEEE Access*, vol. 9, pp. 113 428–113 442, Aug. 2021. DOI: 10.1109/ACCESS.2021.3104509.
- [12] Y. Siriwardhana, P. Porambage, M. Liyanage, and M. Ylianttila, "A Survey on Mobile Augmented Reality With 5G Mobile Edge Computing: Architectures, Applications, and Technical Aspects," *IEEE Communications Surveys & Tutorials*, vol. 23, no. 2, pp. 1160–1192, Feb. 2021. DOI: 10.1109/COMST.2021.3061981.
- [13] P. Popovski, K. F. Trillingsgaard, O. Simeone, and G. Durisi, "5G Wireless Network Slicing for eMBB, URLLC, and mMTC: A Communication-Theoretic View," *IEEE Access*, vol. 6, pp. 55 765–55 779, Sep. 2018. DOI: 10.1109/ACCESS.2018.2872781.
- [14] M. Gerasimenko, D. Moltchanov, R. Florea, *et al.*, "Cooperative Radio Resource Management in Heterogeneous Cloud Radio Access Networks," *IEEE Access*, vol. 3, pp. 397–406, Apr. 2015. DOI: 10.1109/ACCESS.2015.2422266.
- [15] H. Alshaer and H. Haas, "Software-Defined Networking-Enabled Heterogeneous Wireless Networks and Applications Convergence," *IEEE Access*, vol. 8, pp. 66 672–66 692, Apr. 2020. DOI: 10.1109/ACCESS.2020.2986132.
- [16] I. Afolabi, T. Taleb, K. Samdanis, A. Ksentini, and H. Flinck, "Network Slicing and Softwarization: A Survey on Principles, Enabling Technologies, and Solutions," *IEEE Communications Surveys Tutorials*, vol. 20, no. 3, pp. 2429–2453, Mar. 2018. DOI: 10.1109/COMST.2018.2815638.
- [17] C. E. Shannon, "Communication in the presence of noise," *Proceedings of the IRE*, vol. 37, no. 1, pp. 10–21, Jan. 1949. DOI: 10.1109/JRPROC.1949.232969.
- [18] M. Agiwal, A. Roy, and N. Saxena, "Next Generation 5G Wireless Networks: A Comprehensive Survey," *IEEE Communications Surveys Tutorials*, vol. 18, no. 3, pp. 1617–1655, Feb. 2016. DOI: 10.1109/COMST.2016.2532458.
- [19] 3GPP TS 38.101-2, *User Equipment (UE) radio transmission and reception; Part 2: Range 2 Standalone*, version 17.4.0, Dec. 2021.
- [20] "IEEE Standard Letter Designations for Radar-Frequency Bands," *IEEE Std 521-2019 (Revision of IEEE Std 521-2002)*, pp. 1–15, Feb. 2020. DOI: 10.1109/IEEESTD.2020.8999849.
- [21] I. A. Hemadeh, K. Satyanarayana, M. El-Hajjar, and L. Hanzo, "Millimeter-Wave Communications: Physical Channel Models, Design Considerations, Antenna Constructions, and Link-Budget," *IEEE Communications Surveys Tutorials*, vol. 20, no. 2, pp. 870–913, Dec. 2017. DOI: 10.1109/COMST.2017.2783541.
- [22] A. Checko, H. L. Christiansen, Y. Yan, *et al.*, "Cloud RAN for Mobile Networks—A Technology Overview," *IEEE Communications Surveys Tutorials*, vol. 17, no. 1, pp. 405–426, Sep. 2014. DOI: 10.1109/COMST.2014.2355255.
- [23] R. Wang, H. Hu, and X. Yang, "Potentials and Challenges of C-RAN Supporting Multi-RATs Toward 5G Mobile Networks," *IEEE Access*, vol. 2, pp. 1187–1195, Oct. 2014. DOI: 10.1109/ACCESS.2014.2360555.

- [24] M. Fiorani, S. Tombaz, J. Martensson, B. Skubic, L. Wosinska, and P. Monti, "Modeling energy performance of C-RAN with optical transport in 5G network scenarios," *Journal of Optical Communications and Networking*, vol. 8, no. 11, B21–B34, Nov. 2016. DOI: 10.1364/JOCN.8.000B21.
- [25] G. Agrawal, *Fiber-Optic Communication Systems: Fourth Edition (Chapter 2)*. WILEY, Jan. 2012. DOI: 10.1002/9780470918524.
- [26] D. Chitimala, K. Kondepudi, L. Valcarenghi, M. Tornatore, and B. Mukherjee, "5G fronthaul-latency and jitter studies of CPRI over ethernet," *Journal of Optical Communications and Networking*, vol. 9, no. 2, pp. 172–182, Feb. 2017. DOI: 10.1364/JOCN.9.000172.
- [27] S. Rommel, D. Dodane, E. Grivas, *et al.*, "Towards a Scaleable 5G Fronthaul: Analog Radio-over-Fiber and Space Division Multiplexing," *Journal of Lightwave Technology*, vol. 38, no. 19, pp. 5412–5422, Oct. 2020. DOI: 10.1109/JLT.2020.3004416.
- [28] D. Che, "Analog vs Digital Radio-Over-Fiber: A Spectral Efficiency Debate From the SNR Perspective," *Journal of Lightwave Technology*, vol. 39, no. 16, pp. 5325–5335, Aug. 2021. DOI: 10.1109/JLT.2021.3102220.
- [29] K. Roth, H. Pirzadeh, A. L. Swindlehurst, and J. A. Nossek, "A Comparison of Hybrid Beamforming and Digital Beamforming With Low-Resolution ADCs for Multiple Users and Imperfect CSI," *IEEE Journal of Selected Topics in Signal Processing*, vol. 12, no. 3, pp. 484–498, Jun. 2018. DOI: 10.1109/JSTSP.2018.2813973.
- [30] L. Breynne, G. Torfs, X. Yin, P. Demeester, and J. Bauwelinck, "Comparison Between Analog Radio-Over-Fiber and Sigma Delta Modulated Radio-Over-Fiber," *IEEE Photonics Technology Letters*, vol. 29, no. 21, pp. 1808–1811, Nov. 2017. DOI: 10.1109/LPT.2017.2752284.
- [31] I. Degli-Eredi, P. An, J. Drasbæk, *et al.*, "Millimeter-wave generation using hybrid silicon photonics," *Journal of Optics*, vol. 23, no. 4, p. 043001, Mar. 2021. DOI: 10.1088/2040-8986/abc312.
- [32] T. Shao, F. Paresys, G. Maury, Y. L. Guennec, and B. Cabon, "Investigation on the Phase Noise and EVM of Digitally Modulated Millimeter Wave Signal in WDM Optical Heterodyning System," *Journal of Lightwave Technology*, vol. 30, no. 6, pp. 876–885, Mar. 2012. DOI: 10.1109/JLT.2012.2183340.
- [33] U. Gliese, S. Norskov, and T. Nielsen, "Chromatic dispersion in fiber-optic microwave and millimeter-wave links," *IEEE Transactions on Microwave Theory and Techniques*, vol. 44, no. 10, pp. 1716–1724, Oct. 1996. DOI: 10.1109/22.538964.
- [34] 5G STEP FWD, "5G System Technological Enhancements Provided by Fiber Wireless Deployments (5G STEP FWD)," This project has received funding from the European Union's Horizon 2020 research and innovation programme under the Marie Skłodowska Curie grant agreement No: 722429". (2017), [Online]. Available: <https://www.5gstepfwd.eu/>.

- [35] M. R. Akdeniz, Y. Liu, M. K. Samimi, *et al.*, “Millimeter Wave Channel Modeling and Cellular Capacity Evaluation,” *IEEE Journal on Selected Areas in Communications*, vol. 32, no. 6, pp. 1164–1179, Jun. 2014. DOI: 10.1109/JSAC.2014.2328154.
- [36] B. A. Khawaja and M. J. Cryan, “Study of Millimeter Wave Phase Shift in 40 GHz Hybrid Mode Locked Lasers,” vol. 19, no. 3, pp. 182–184, Mar. 2009. DOI: 10.1109/LMWC.2009.2013747.
- [37] M. Schiemangk, S. Spießberger, A. Wicht, G. Erbert, G. Tränkle, and A. Peters, “Accurate frequency noise measurement of free-running lasers,” *Applied Optics*, vol. 53, no. 30, pp. 7138–7143, Oct. 2014. DOI: 10.1364/AO.53.007138.
- [38] S. Rommel, S. Rodríguez, L. Chorchos, *et al.*, “Outdoor W-Band Hybrid Photonic Wireless Link Based on an Optical SFP+ Module,” *IEEE Photonics Technology Letters*, vol. 28, no. 21, pp. 2303–2306, Nov. 2016. DOI: 10.1109/LPT.2016.2592326.
- [39] L. Cheng, S. Aditya, and A. Nirmalathas, “An exact analytical model for dispersive transmission in microwave fiber-optic links using Mach-Zehnder external modulator,” *IEEE Photonics Technology Letters*, vol. 17, no. 7, pp. 1525–1527, Jul. 2005. DOI: 10.1109/LPT.2005.848563.
- [40] J. Yu, Z. Jia, L. Yi, Y. Su, G.-K. Chang, and T. Wang, “Optical millimeter-wave generation or up-conversion using external modulators,” *IEEE Photonics Technology Letters*, vol. 18, no. 1, pp. 265–267, Jan. 2006. DOI: 10.1109/LPT.2005.862006.
- [41] A. Bordonalli, C. Walton, and A. Seeds, “High-performance phase locking of wide linewidth semiconductor lasers by combined use of optical injection locking and optical phase-lock loop,” *Journal of Lightwave Technology*, vol. 17, no. 2, pp. 328–342, Feb. 1999. DOI: 10.1109/50.744252.
- [42] S. Fukushima, C. Silva, Y. Muramoto, and A. Seeds, “Optoelectronic millimeter-wave synthesis using an optical frequency comb Generator, optically injection locked lasers, and a unitraveling-carrier photodiode,” *Journal of Lightwave Technology*, vol. 21, no. 12, pp. 3043–3051, Dec. 2003. DOI: 10.1109/JLT.2003.822250.
- [43] G. Nazarikov, S. Rommel, W. Yao, and I. Tafur Monroy, “Optical Injection Locking for Generation of Tunable Low-Noise Millimeter Wave and THz Signals,” *Applied Sciences*, vol. 11, no. 21, Oct. 2021. DOI: 10.3390/app112110185.
- [44] G. Nazarikov, S. Rommel, W. Yao, and I. Tafur Monroy, “Optical Injection Locking for Generation of Tunable Low-Noise Millimeter Wave and THz Signals,” *Applied Sciences*, vol. 11, no. 21, Oct. 2021. DOI: 10.3390/app112110185.
- [45] K. Kikuchi, “Fundamentals of Coherent Optical Fiber Communications,” *Journal of Lightwave Technology*, vol. 34, no. 1, pp. 157–179, Jan. 2016. DOI: 10.1109/JLT.2015.2463719.
- [46] U. Gliese, T. Nielsen, M. Bruun, *et al.*, “A wideband heterodyne optical phase-locked loop for generation of 3-18 GHz microwave carriers,” *IEEE Photonics Technology Letters*, vol. 4, no. 8, pp. 936–938, Aug. 1992. DOI: 10.1109/68.149915.

- [47] F. Ashtiani, P. Sanjari, M. H. Idjadi, and F. Aflatouni, "High-Resolution Optical Frequency Synthesis Using an Integrated Electro-Optical Phase-Locked Loop," *IEEE Transactions on Microwave Theory and Techniques*, vol. 66, no. 12, pp. 5922–5932, Dec. 2018. DOI: 10.1109/TMTT.2018.2878567.
- [48] T. Kuri and K. Kitayama, "Optical heterodyne detection technique for densely multiplexed millimeter-wave-band radio-on-fiber systems," *Journal of Lightwave Technology*, vol. 21, no. 12, pp. 3167–3179, Dec. 2003. DOI: 10.1109/JLT.2003.821729.
- [49] V. A. Thomas, M. El-Hajjar, and L. Hanzo, "Millimeter-Wave Radio Over Fiber Optical Upconversion Techniques Relying on Link Nonlinearity," *IEEE Communications Surveys Tutorials*, vol. 18, no. 1, pp. 29–53, Mar. 2015. DOI: 10.1109/COMST.2015.2409154.
- [50] C.-T. Lin, J. Chen, P.-T. Shih, W.-J. Jiang, and S. Chi, "Ultra-High Data-Rate 60 GHz Radio-Over-Fiber Systems Employing Optical Frequency Multiplication and OFDM Formats," *Journal of Lightwave Technology*, vol. 28, no. 16, pp. 2296–2306, Aug. 2010. DOI: 10.1109/JLT.2010.2047712.
- [51] X. Ruan, K. Li, D. J. Thomson, *et al.*, "Experimental comparison of direct detection Nyquist SSB transmission based on silicon dual-drive and IQ Mach-Zehnder modulators with electrical packaging," *Optics Express*, vol. 25, no. 16, pp. 19 332–19 342, Aug. 2017. DOI: 10.1364/OE.25.019332.
- [52] R. Qu, H. Zhao, Z. Fang, E. Marin, and J. Meunier, "Configurable wavelength-selective switch based on fiber grating and fiber loop mirror," *IEEE Photonics Technology Letters*, vol. 12, no. 10, pp. 1343–1345, Oct. 2000. DOI: 10.1109/68.883824.
- [53] S. Xiao and A. Weiner, "Optical carrier-suppressed single sideband (O-CS-SSB) Modulation using a hyperfine blocking filter based on a virtually imaged phased-array (VIPA)," *IEEE Photonics Technology Letters*, vol. 17, no. 7, pp. 1522–1524, Jul. 2005. DOI: 10.1109/LPT.2005.848564.
- [54] J. Ballato and P. Dragic, "Glass: The Carrier of Light - A Brief History of Optical Fiber," *International Journal of Applied Glass Science*, vol. 7, no. 4, pp. 413–422, Oct. 2016. DOI: <https://doi.org/10.1111/ijag.12239>.
- [55] Y. Yamamoto, Y. Kawaguchi, and M. Hirano, "Low-Loss and Low-Nonlinearity Pure-Silica-Core Fiber for C- and L-band Broadband Transmission," *Journal of Lightwave Technology*, vol. 34, no. 2, pp. 321–326, Jan. 2016. DOI: 10.1109/JLT.2015.2476837.
- [56] A. Ghazi, S. Aljunid, S. Z. S. Idrus, *et al.*, "A Systematic review of Multi-Mode Fiber based on Dimensional Code in Optical-CDMA," *Journal of Physics: Conference Series*, vol. 1860, no. 1, p. 012016, Mar. 2021. DOI: 10.1088/1742-6596/1860/1/012016.
- [57] K.-i. Kitayama and N.-P. Diamantopoulos, "Few-Mode Optical Fibers: Original Motivation and Recent Progress," *IEEE Communications Magazine*, vol. 55, no. 8, pp. 163–169, Aug. 2017. DOI: 10.1109/MCOM.2017.1600876.

- [58] B. Auguie, A. Mussot, A. Boucon, E. Lantz, and T. Sylvestre, "Ultralow chromatic dispersion measurement of optical fibers with a tunable fiber laser," *IEEE Photonics Technology Letters*, vol. 18, no. 17, pp. 1825–1827, Sep. 2006. DOI: 10.1109/LPT.2006.881148.
- [59] J. P. Gordon and H. Kogelnik, "PMD fundamentals: Polarization mode dispersion in optical fibers," *Proceedings of the National Academy of Sciences*, vol. 97, no. 9, pp. 4541–4550, Apr. 2000. DOI: 10.1073/pnas.97.9.4541.
- [60] C. Madsen, G. Lenz, A. Bruce, M. Cappuzzo, L. Gomez, and R. Scotti, "Integrated all-pass filters for tunable dispersion and dispersion slope compensation," *IEEE Photonics Technology Letters*, vol. 11, no. 12, pp. 1623–1625, Dec. 1999. DOI: 10.1109/68.806867.
- [61] V. Bogatyrev, M. Bubnov, E. Dianov, *et al.*, "A single-mode fiber with chromatic dispersion varying along the length," *Journal of Lightwave Technology*, vol. 9, no. 5, pp. 561–566, May 1991. DOI: 10.1109/50.79530.
- [62] U. Gliese, S. Norskov, and T. Nielsen, "Chromatic dispersion in fiber-optic microwave and millimeter-wave links," *IEEE Transactions on Microwave Theory and Techniques*, vol. 44, no. 10, pp. 1716–1724, Oct. 1996. DOI: 10.1109/22.538964.
- [63] G. Meslener, "Chromatic dispersion induced distortion of modulated monochromatic light employing direct detection," *IEEE Journal of Quantum Electronics*, vol. 20, no. 10, pp. 1208–1216, Oct. 1984. DOI: 10.1109/JQE.1984.1072286.
- [64] S. Havstad, A. Sahin, O. Adamczyk, Y. Xie, and A. Willner, "Distance-independent microwave and millimeter-wave power fading compensation using a phase diversity configuration," *IEEE Photonics Technology Letters*, vol. 12, no. 8, pp. 1052–1054, Aug. 2000. DOI: 10.1109/68.868005.
- [65] T. Zhang, W. Pan, X. Zou, *et al.*, "High-Spectral-Efficiency Photonic Frequency Down-Conversion Using Optical Frequency Comb and SSB Modulation," *IEEE Photonics Journal*, vol. 5, no. 2, pp. 7 200 307–7 200 307, Apr. 2013. DOI: 10.1109/JPHOT.2013.2247035.
- [66] M. J. Potasek, G. P. Agrawal, and S. C. Pinault, "Analytic and numerical study of pulse broadening in nonlinear dispersive optical fibers," *Journal of the Optical Society of America B*, vol. 3, no. 2, pp. 205–211, Feb. 1986. DOI: 10.1364/JOSAB.3.000205.
- [67] F. Devaux, Y. Sorel, and J. Kerdiles, "Simple measurement of fiber dispersion and of chirp parameter of intensity modulated light emitter," *Journal of Lightwave Technology*, vol. 11, no. 12, pp. 1937–1940, Dec. 1993. DOI: 10.1109/50.257953.
- [68] W.-J. Jiang, C.-T. Lin, A. Ng'oma, *et al.*, "Simple 14-Gb/s Short-Range Radio-Over-Fiber System Employing a Single-Electrode MZM for 60-GHz Wireless Applications," *Journal of Lightwave Technology*, vol. 28, no. 16, pp. 2238–2246, Aug. 2010. DOI: 10.1109/JLT.2010.2045341.
- [69] L. Shen, W.-P. Huang, G. Chen, and S. Jian, "Design and optimization of photonic crystal fibers for broad-band dispersion compensation," *IEEE Photonics Technology Letters*, vol. 15, no. 4, pp. 540–542, Apr. 2003. DOI: 10.1109/LPT.2003.809322.

- [70] T. Xu, G. Jacobsen, S. Popov, *et al.*, “Chromatic dispersion compensation in coherent transmission system using digital filters,” *Optics Express*, vol. 18, no. 15, pp. 16 243–16 257, Jul. 2010. DOI: 10.1364/OE.18.016243.
- [71] V. A. Vardanyan, “Effect of self-phase modulation and cross-phase modulation on OFDM signals in fibre-optic access networks,” *Quantum Electronics*, vol. 48, no. 4, pp. 395–400, Apr. 2018. DOI: 10.1070/qe116608.
- [72] S. C. Pinault and M. J. Potasek, “Frequency broadening by self-phase modulation in optical fibers,” *Journal of the Optical Society of America B*, vol. 2, no. 8, pp. 1318–1319, Aug. 1985. DOI: 10.1364/JOSAB.2.001318.
- [73] V. Sleiffer, D. van den Borne, M. Kuschnerov, *et al.*, “A comparison between SSMF and large-Aeff Pure-Silica core fiber for ultra long-haul 100G transmission,” in *2011 37th European Conference and Exhibition on Optical Communication*, Geneva, Switzerland, Sep. 2011, pp. 1–3. DOI: 10.1364/OE.19.00B710.
- [74] R. R. Alfano, P. L. Baldeck, P. P. Ho, and G. P. Agrawal, “Cross-phase modulation and induced focusing due to optical nonlinearities in optical fibers and bulk materials,” *Journal of the Optical Society of America B*, vol. 6, no. 4, pp. 824–829, Apr. 1989. DOI: 10.1364/JOSAB.6.000824.
- [75] V. R. Supradeepa, “Stimulated Brillouin scattering thresholds in optical fibers for lasers linewidth broadened with noise,” *Optics Express*, vol. 21, no. 4, pp. 4677–4687, Feb. 2013. DOI: 10.1364/OE.21.004677.
- [76] A. Kobayakov, M. Sauer, and D. Chowdhury, “Stimulated Brillouin scattering in optical fibers,” *Advances in Optics and Photonics*, vol. 2, no. 1, pp. 1–59, Mar. 2010. DOI: 10.1364/AOP.2.000001.
- [77] F. Forghieri, R. Tkach, and A. Chraplyvy, “Effect of modulation statistics on Raman crosstalk in WDM systems,” *IEEE Photonics Technology Letters*, vol. 7, no. 1, pp. 101–103, Jan. 1995. DOI: 10.1109/68.363362.
- [78] K. Inoue, “Four-wave mixing in an optical fiber in the zero-dispersion wavelength region,” *Journal of Lightwave Technology*, vol. 10, no. 11, pp. 1553–1561, Nov. 1992. DOI: 10.1109/50.184893.
- [79] J. Yao, “Microwave Photonics,” *Journal of Lightwave Technology*, vol. 27, no. 3, pp. 314–335, Feb. 2009. DOI: 10.1109/JLT.2008.2009551.
- [80] H. Shams, P. M. Anandarajah, P. Perry, and L. P. Barry, “Optical Generation of Modulated Millimeter Waves Based on a Gain-Switched Laser,” *IEEE Transactions on Microwave Theory and Techniques*, vol. 58, no. 11, pp. 3372–3380, Nov. 2010. DOI: 10.1109/TMTT.2010.2076930.
- [81] A. Delmade, C. Browning, T. Verolet, *et al.*, “Optical Heterodyne Analog Radio-Over-Fiber Link for Millimeter-Wave Wireless Systems,” *Journal of Lightwave Technology*, vol. 39, no. 2, pp. 465–474, Jan. 2021. DOI: 10.1109/JLT.2020.3032923.
- [82] A. Stohr, R. Heinzelmann, A. Malcoci, and D. Jager, “Optical heterodyne millimeter-wave generation using 1.55- μm traveling-wave photodetectors,” *IEEE Transactions on Microwave Theory and Techniques*, vol. 49, no. 10, pp. 1926–1933, Oct. 2001. DOI: 10.1109/22.954809.

- [83] J. de Graaf, X. Zhao, D. Konstantinou, *et al.*, “Beyond 110 GHz Uni-Travelling Carrier Photodiodes on an InP-Membrane-on-Silicon Platform,” *IEEE Journal of Selected Topics in Quantum Electronics*, vol. 28, no. 2, pp. 1–10, Mar. 2022. doi: 10.1109/JSTQE.2021.3110411.
- [84] O. Franek, “Phasor Alternatives to Friis’ Transmission Equation,” *IEEE Antennas and Wireless Propagation Letters*, vol. 17, no. 1, pp. 90–93, Jan. 2018. doi: 10.1109/LAWP.2017.2776523.
- [85] F. Fouquet, “Friis Formula,” in *Noise in Radio-Frequency Electronics and its Measurement*. 2020, pp. 23–35. doi: 10.1002/9781119706656.ch2.
- [86] 3GPP TR 38.901, *Study on channel model for frequencies from 0.5 to 100 GHz*, version 17.0.0, Mar. 2022.
- [87] D. B. Leeson, “Oscillator Phase Noise: A 50-Year Review,” *IEEE Transactions on Ultrasonics, Ferroelectrics, and Frequency Control*, vol. 63, no. 8, pp. 1208–1225, Aug. 2016. doi: 10.1109/TUFFC.2016.2562663.
- [88] G. Zhang, K. Saito, W. Fan, *et al.*, “Experimental Characterization of Millimeter-Wave Indoor Propagation Channels at 28 GHz,” *IEEE Access*, vol. 6, pp. 76 516–76 526, Nov. 2018. doi: 10.1109/ACCESS.2018.2882644.
- [89] J. Wang, C. Gentile, P. B. Papazian, J.-K. Choi, and J. Senic, “Quasi-Deterministic Model for Doppler Spread in Millimeter-Wave Communication Systems,” *IEEE Antennas and Wireless Propagation Letters*, vol. 16, pp. 2195–2198, May 2017. doi: 10.1109/LAWP.2017.2705578.
- [90] L. Ma, H. Jia, S. Liu, and I. U. Khan, “Low-Complexity Doppler Compensation Algorithm for Underwater Acoustic OFDM Systems With Nonuniform Doppler Shifts,” *IEEE Communications Letters*, vol. 24, no. 9, pp. 2051–2054, Sep. 2020. doi: 10.1109/LCOMM.2020.2998293.
- [91] C. Svec and T. Shay, “Wide dynamic range Doppler-shift compensation for spaceborne optical communications,” *IEEE Photonics Technology Letters*, vol. 16, no. 1, pp. 260–262, Jan. 2004. doi: 10.1109/LPT.2003.818931.
- [92] X. Li and J. Yu, “Generation and Heterodyne Detection of gt;100-Gb/s Q -Band PDM-64QAM mm-Wave Signal,” *IEEE Photonics Technology Letters*, vol. 29, no. 1, pp. 27–30, Jan. 2017. doi: 10.1109/LPT.2016.2625042.
- [93] S. Bronckers, A. Roc’h, and B. Smolders, “Wireless Receiver Architectures Towards 5G: Where Are We?” *IEEE Circuits and Systems Magazine*, vol. 17, no. 3, pp. 6–16, Aug. 2017. doi: 10.1109/MCAS.2017.2713306.
- [94] B. Razavi, “Challenges in portable RF transceiver design,” *IEEE Circuits and Devices Magazine*, vol. 12, no. 5, pp. 12–25, Sep. 1996. doi: 10.1109/101.537352.
- [95] S. Rommel, L. C. P. Cavalcante, A. G. Quintero, A. K. Mishra, J. J. V. Olmos, and I. T. Monroy, “W-band photonic-wireless link with a Schottky diode envelope detector and bend insensitive fiber,” *Optics Express*, vol. 24, no. 11, pp. 11 312–11 322, May 2016. doi: 10.1364/OE.24.011312.
- [96] Z. Li, M. Erkilinç, K. Shi, *et al.*, “Joint Optimisation of Resampling Rate and Carrier-to-Signal Power Ratio in Direct-Detection Kramers-Kronig Receivers,” in *2017 European Conference on Optical Communication (ECOC)*, Gothenburg, Sweden, Sep. 2017, pp. 1–3. doi: 10.1109/ECOC.2017.8346206.

- [97] C. Ye, L. Zhang, M. Zhu, J. Yu, S. He, and G.-K. Chang, "A Bidirectional 60-GHz Wireless-Over-Fiber Transport System With Centralized Local Oscillator Service Delivered to Mobile Terminals and Base Stations," *IEEE Photonics Technology Letters*, vol. 24, no. 22, pp. 1984–1987, Nov. 2012. DOI: 10.1109/LPT.2012.2216257.
- [98] S. Mirabbasi and K. Martin, "Classical and modern receiver architectures," *IEEE Communications Magazine*, vol. 38, no. 11, pp. 132–139, Nov. 2000. DOI: 10.1109/35.883502.
- [99] H. Landau, "Sampling, data transmission, and the Nyquist rate," *Proceedings of the IEEE*, vol. 55, no. 10, pp. 1701–1706, Oct. 1967. DOI: 10.1109/PROC.1967.5962.
- [100] K.-I. Kitayana and R. Griffin, "Optical downconversion from millimeter-wave to IF-band over 50 km-long optical fiber link using an electroabsorption modulator," *IEEE Photonics Technology Letters*, vol. 11, no. 2, pp. 287–289, Feb. 1999. DOI: 10.1109/68.740732.
- [101] A. Morales, D. Konstantinou, S. Rommel, *et al.*, "Bidirectional K-Band Photonic/Wireless Link for 5G Communications," in *2019 44th International Conference on Infrared, Millimeter, and Terahertz Waves (IRMMW-THz)*, Paris, France, Sep. 2019, pp. 1–2. DOI: 10.1109/IRMMW-THz.2019.8874031.
- [102] C.-T. Lin, J. Chen, S.-P. Dai, P.-C. Peng, and S. Chi, "Impact of Nonlinear Transfer Function and Imperfect Splitting Ratio of MZM on Optical Up-Conversion Employing Double Sideband With Carrier Suppression Modulation," *Journal of Lightwave Technology*, vol. 26, no. 15, pp. 2449–2459, Aug. 2008. DOI: 10.1109/JLT.2008.927160.
- [103] Y. Ogiso, Y. Tsuchiya, S. Shinada, S. Nakajima, T. Kawanishi, and H. Nakajima, "High Extinction-Ratio Integrated Mach-Zehnder Modulator With Active Y-Branch for Optical SSB Signal Generation," *IEEE Photonics Technology Letters*, vol. 22, no. 12, pp. 941–943, Jun. 2010. DOI: 10.1109/LPT.2010.2047854.
- [104] A. E. Jayati and M. Sipan, "Impact of Nonlinear Distortion with the Rapp Model on the GFDM System," in *2020 Third International Conference on Vocational Education and Electrical Engineering (ICVEE)*, Surabaya, Indonesia, Oct. 2020, pp. 1–5. DOI: 10.1109/ICVEE50212.2020.9243295.
- [105] J.-C. Chen and C.-K. Wen, "PAPR Reduction of OFDM Signals Using Cross-Entropy-Based Tone Injection Schemes," *IEEE Signal Processing Letters*, vol. 17, no. 8, pp. 727–730, Aug. 2010. DOI: 10.1109/LSP.2010.2051617.
- [106] Y. London and D. Sadot, "Nonlinear Effects Mitigation in Coherent Optical OFDM System in Presence of High Peak Power," *Journal of Lightwave Technology*, vol. 29, no. 21, pp. 3275–3281, Nov. 2011. DOI: 10.1109/JLT.2011.2167715.
- [107] D.-h. Park and H.-k. Song, "A New PAPR Reduction Technique of OFDM System with Nonlinear High Power Amplifier," *IEEE Transactions on Consumer Electronics*, vol. 53, no. 2, pp. 327–332, May 2007. DOI: 10.1109/TCE.2007.381696.

- [108] S. Deligiannidis, A. Bogris, C. Mesaritakis, and Y. Kopsinis, “Compensation of Fiber Nonlinearities in Digital Coherent Systems Leveraging Long Short-Term Memory Neural Networks,” *Journal of Lightwave Technology*, vol. 38, no. 21, pp. 5991–5999, Nov. 2020. DOI: 10.1109/JLT.2020.3007919.
- [109] R. Gerzaguët, N. Bartzoudis, L. G. Baltar, *et al.*, “The 5G candidate waveform race: a comparison of complexity and performance,” *EURASIP Journal on Wireless Communications and Networking*, vol. 2017, no. 13, Jan. 2017. DOI: 10.1186/s13638-016-0792-0.
- [110] N. Maziar, W. Yue, T. Milos, W. Shangbin, Q. Yinan, and A.-I. Mohammed, “Overview of 5G modulation and waveforms candidates,” *Journal of Communications and Information Networks*, vol. 1, no. 1, pp. 44–60, Jun. 2016. DOI: 10.1007/BF03391545.
- [111] J. Cho and P. J. Winzer, “Probabilistic Constellation Shaping for Optical Fiber Communications,” *Journal of Lightwave Technology*, vol. 37, no. 6, pp. 1590–1607, Mar. 2019. DOI: 10.1109/JLT.2019.2898855.
- [112] T. Fehenberger, A. Alvarado, G. Böcherer, and N. Hanik, “On Probabilistic Shaping of Quadrature Amplitude Modulation for the Nonlinear Fiber Channel,” *Journal of Lightwave Technology*, vol. 34, no. 21, pp. 5063–5073, Nov. 2016. DOI: 10.1109/JLT.2016.2594271.
- [113] M. M. Wang, A. Agrawal, A. Khandekar, and S. Aedudodla, “Preamble design, system acquisition, and determination in modern OFDMA cellular communications: an overview,” *IEEE Communications Magazine*, vol. 49, no. 7, pp. 164–175, Jul. 2011. DOI: 10.1109/MCOM.2011.5936170.
- [114] H. Yang, J. Li, B. Lin, *et al.*, “DSP-Based Evolution From Conventional TDM-PON to TDM-OFDM-PON,” *Journal of Lightwave Technology*, vol. 31, no. 16, pp. 2735–2741, Aug. 2013. DOI: 10.1109/JLT.2013.2271909.
- [115] M. Bohge, J. Gross, A. Wolisz, and M. Meyer, “Dynamic resource allocation in OFDM systems: an overview of cross-layer optimization principles and techniques,” *IEEE Network*, vol. 21, no. 1, pp. 53–59, Jan. 2007. DOI: 10.1109/MNET.2007.314539.
- [116] H. Tataria, M. Shafi, A. F. Molisch, M. Dohler, H. Sjöland, and F. Tufvesson, “6G Wireless Systems: Vision, Requirements, Challenges, Insights, and Opportunities,” *Proceedings of the IEEE*, vol. 109, no. 7, pp. 1166–1199, Jul. 2021. DOI: 10.1109/JPROC.2021.3061701.
- [117] S. Rommel, R. Puerta, J. J. V. Olmos, and I. T. Monroy, “Capacity enhancement for hybrid fiber-wireless channels with 46.8Gbit/s wireless multi-CAP transmission over 50m at W-band,” in *2017 Optical Fiber Communications Conference and Exhibition (OFC)*, Los Angeles, CA, USA, Mar. 2017, pp. 1–3. DOI: 10.1364/OFC.2017.M3E.5.
- [118] D. Wulich, “Definition of efficient PAPR in OFDM,” *IEEE Communications Letters*, vol. 9, no. 9, pp. 832–834, Sep. 2005. DOI: 10.1109/LCOMM.2005.1506718.

- [119] T. Jiang, M. Guizani, H.-H. Chen, W. Xiang, and Y. Wu, "Derivation of PAPR Distribution for OFDM Wireless Systems Based on Extreme Value Theory," *IEEE Transactions on Wireless Communications*, vol. 7, no. 4, pp. 1298–1305, Apr. 2008. DOI: 10.1109/TWC.2008.060862.
- [120] Y. Liu, Z. Tan, H. Hu, L. J. Cimini, and G. Y. Li, "Channel Estimation for OFDM," *IEEE Communications Surveys Tutorials*, vol. 16, no. 4, pp. 1891–1908, May 2014. DOI: 10.1109/COMST.2014.2320074.
- [121] A. Armada and M. Calvo, "Phase noise and sub-carrier spacing effects on the performance of an OFDM communication system," *IEEE Communications Letters*, vol. 2, no. 1, pp. 11–13, Jan. 1998. DOI: 10.1109/4234.658613.
- [122] Y. Rahmatallah and S. Mohan, "Peak-To-Average Power Ratio Reduction in OFDM Systems: A Survey And Taxonomy," *IEEE Communications Surveys Tutorials*, vol. 15, no. 4, pp. 1567–1592, Mar. 2013. DOI: 10.1109/SURV.2013.021313.00164.
- [123] Y. C. Gültekin, T. Fehenberger, A. Alvarado, and F. M. J. Willems, "Probabilistic Shaping for Finite Blocklengths: Distribution Matching and Sphere Shaping," *Entropy*, vol. 22, no. 5, May 2020. DOI: 10.3390/e22050581.
- [124] S. Goossens, S. Van der Heide, M. Van den Hout, *et al.*, "First Experimental Demonstration of Probabilistic Enumerative Sphere Shaping in Optical Fiber Communications," in *2019 24th OptoElectronics and Communications Conference (OECC) and 2019 International Conference on Photonics in Switching and Computing (PSC)*, Fukuoka, Japan, Jul. 2019, pp. 1–3. DOI: 10.23919/PS.2019.8818086.
- [125] Y. C. Gültekin, W. J. van Houtum, A. G. C. Koppelaar, F. M. J. Willems, and W. J. van Houtum, "Enumerative Sphere Shaping for Wireless Communications With Short Packets," *IEEE Transactions on Wireless Communications*, vol. 19, no. 2, pp. 1098–1112, Feb. 2020. DOI: 10.1109/TWC.2019.2951139.
- [126] K. Wu, J. He, Z. Zhou, J. He, and J. Shi, "Probabilistic Amplitude Shaping for a 64-QAM OFDM W-Band RoF System," *IEEE Photonics Technology Letters*, vol. 31, no. 13, pp. 1076–1079, Jul. 2019. DOI: 10.1109/LPT.2019.2917925.
- [127] J. Ma, J. He, M. Chen, K. Wu, and J. He, "Performance Enhancement of Probabilistically Shaped OFDM Enabled by Precoding Technique in an IM-DD System," *Journal of Lightwave Technology*, vol. 37, no. 24, pp. 6063–6071, Dec. 2019. DOI: 10.1109/JLT.2019.2946294.
- [128] R. Zhang, Y.-W. Chen, S. Shen, *et al.*, "Joint Optimization of Processing Complexity and Rate Allocation through Entropy Tunability for 64-/256-QAM Based Radio Fronthauling with LDPC and PAS-OFDM," in *2020 Optical Fiber Communications Conference and Exhibition (OFC)*, Mar. 2020, pp. 1–3. DOI: 10.1364/OFC.2020.M2F.2.
- [129] A. Delmade, C. Browning, A. Farhang, R. D. Koilpillai, D. Venkitesh, and L. P. Barry, "OFDM Baud Rate Limitations in an Optical Heterodyne Analog Fronthaul Link using Unlocked Fibre Lasers," in *2019 International Topical Meeting on Microwave Photonics (MWP)*, Ottawa, ON, Canada, Oct. 2019, pp. 1–4. DOI: 10.1109/MWP.2019.8892190.

- [130] H. Ghozlan and G. Kramer, "On Wiener phase noise channels at high Signal-to-Noise Ratio," in *2013 IEEE International Symposium on Information Theory*, Istanbul, Turkey, Jul. 2013, pp. 2279–2283. DOI: 10.1109/ISIT.2013.6620632.
- [131] 3GPP TR 38.803, *Study on new radio access technology: Radio Frequency (RF) and co-existence aspects*, version 14.3.0, Mar. 2022.
- [132] H.-G. Ryu and Y.-S. Lee, "Phase noise analysis of the OFDM communication system by the standard frequency deviation," *IEEE Transactions on Consumer Electronics*, vol. 49, no. 1, pp. 41–47, Feb. 2003. DOI: 10.1109/TCE.2003.1205454.
- [133] S. Wu and Y. Bar-Ness, "OFDM systems in the presence of phase noise: consequences and solutions," *IEEE Transactions on Communications*, vol. 52, no. 11, pp. 1988–1996, Nov. 2004. DOI: 10.1109/TCOMM.2004.836441.
- [134] M. E. Mousa-Pasandi and D. V. Plant, "Noniterative Interpolation-Based Partial Phase Noise ICI Mitigation for CO-OFDM Transport Systems," *IEEE Photonics Technology Letters*, vol. 23, no. 21, pp. 1594–1596, Nov. 2011. DOI: 10.1109/LPT.2011.2164785.
- [135] 3GPP TS 38.214, *Physical layer procedures for data*, version 17.1.0, Mar. 2022.
- [136] Y. Qi, M. Hunukumbure, H. Nam, H. Yoo, and S. Amuru, "On the Phase Tracking Reference Signal (PT-RS) Design for 5G New Radio (NR)," in *2018 IEEE 88th Vehicular Technology Conference (VTC-Fall)*, Chicago, IL, USA, Aug. 2018, pp. 1–5. DOI: 10.1109/VTCFall.2018.8690852.
- [137] P. Mathecken, T. Riihonen, S. Werner, and R. Wichman, "Constrained Phase Noise Estimation in OFDM Using Scattered Pilots Without Decision Feedback," *IEEE Transactions on Signal Processing*, vol. 65, no. 9, pp. 2348–2362, May 2017. DOI: 10.1109/TSP.2017.2655481.
- [138] Y. Ha and W. Chung, "A Feedforward Partial Phase Noise Mitigation in the Time-Domain using Cyclic Prefix for CO-OFDM Systems," *Journal of the Optical Society of Korea*, vol. 17, no. 6, pp. 467–470, Dec. 2013. DOI: 10.3807/JOSK.2013.17.6.467.
- [139] V. Syrjälä and M. Valkama, "Flexible adjacent channel interference and phase noise suppression in energy-efficient OFDMA receivers," in *2012 IEEE 17th International Workshop on Computer Aided Modeling and Design of Communication Links and Networks (CAMAD)*, Barcelona, Spain, Sep. 2012, pp. 221–225. DOI: 10.1109/CAMAD.2012.6335338.
- [140] R. Casas, S. Biracree, and A. Youtz, "Time domain phase noise correction for OFDM signals," *IEEE Transactions on Broadcasting*, vol. 48, no. 3, pp. 230–236, Sep. 2002. DOI: 10.1109/TBC.2002.803711.
- [141] T. Schmidl and D. Cox, "Robust frequency and timing synchronization for OFDM," *IEEE Transactions on Communications*, vol. 45, no. 12, pp. 1613–1621, Dec. 1997. DOI: 10.1109/26.650240.
- [142] C.-T. Lin, C.-C. Wei, and M.-I. Chao, "Phase noise suppression of optical OFDM signals in 60-GHz RoF transmission system," *Optics Express*, vol. 19, no. 11, pp. 10 423–10 428, May 2011. DOI: 10.1364/OE.19.010423.

- [143] T. Shao, E. Martin, P. M. Anandarajah, *et al.*, “Chromatic Dispersion-Induced Optical Phase Decorrelation in a 60 GHz OFDM-RoF System,” *IEEE Photonics Technology Letters*, vol. 26, no. 20, pp. 2016–2019, Oct. 2014. DOI: 10.1109/LPT.2014.2344314.
- [144] C.-C. Wei, C.-T. Lin, H.-T. Huang, W.-L. Liang, and S. Chi, “Estimation and Suppression of Dispersion-Induced Phase Noise in W-band Direct-Detection OFDM Radio-Over-Fiber Systems,” *Journal of Lightwave Technology*, vol. 32, no. 20, pp. 3874–3884, Oct. 2014. DOI: 10.1109/JLT.2014.2322601.
- [145] E. P. Martin, T. Shao, V. Vujicic, *et al.*, “25-Gb/s OFDM 60-GHz Radio Over Fiber System Based on a Gain Switched Laser,” *Journal of Lightwave Technology*, vol. 33, no. 8, pp. 1635–1643, Apr. 2015. DOI: 10.1109/JLT.2015.2391994.
- [146] C. Browning, E. P. Martin, A. Farhang, and L. P. Barry, “60 GHz 5G Radio-Over-Fiber Using UF-OFDM With Optical Heterodyning,” *IEEE Photonics Technology Letters*, vol. 29, no. 23, pp. 2059–2062, Dec. 2017. DOI: 10.1109/LPT.2017.2763680.
- [147] C. Browning, H. H. Elwan, E. P. Martin, *et al.*, “Gain-Switched Optical Frequency Combs for Future Mobile Radio-Over-Fiber Millimeter-Wave Systems,” *Journal of Lightwave Technology*, vol. 36, no. 19, pp. 4602–4610, Oct. 2018. DOI: 10.1109/JLT.2018.2841365.
- [148] A. Delmade, C. Browning, T. Verolet, *et al.*, “Optical Heterodyne Analog Radio-Over-Fiber Link for Millimeter-Wave Wireless Systems,” *Journal of Lightwave Technology*, vol. 39, no. 2, pp. 465–474, Jan. 2021. DOI: 10.1109/JLT.2020.3032923.
- [149] K. Zeb, Z. Lu, J. Liu, *et al.*, “A quantum dash mode-locked laser-based photonic aided broadband multi-Gb/s wireless signal delivery system at 5G NR,” in *Broadband Access Communication Technologies XV*, vol. 11711, Mar. 2021, pp. 65–70. DOI: 10.1117/12.2583066.
- [150] A. Delmade, E. Martin, C. Browning, and L. P. Barry, “5G Millimeter-Wave Analog RoF System employing Optical Injection Locking and Direct Modulation of DFB Laser,” in *2022 Optical Fiber Communications Conference and Exhibition (OFC)*, San Diego, CA, USA, Mar. 2022, W4C.7. DOI: 10.1364/OFC.2022.W4C.7.
- [151] A. Haddad and M. Gagnaire, “Radio-over-Fiber (RoF) for mobile backhauling: A technical and economic comparison between analog and digitized RoF,” in *2014 International Conference on Optical Network Design and Modeling*, Stockholm, Sweden, Jul. 2014, pp. 132–137.
- [152] A. Udalcovs, M. Levantesi, P. Urban, *et al.*, “Total Cost of Ownership of Digital vs. Analog Radio-Over-Fiber Architectures for 5G Fronthauling,” *IEEE Access*, vol. 8, pp. 223 562–223 573, Dec. 2020. DOI: 10.1109/ACCESS.2020.3044396.
- [153] A. de la Oliva, J. A. Hernandez, D. Larrabeiti, and A. Azcorra, “An overview of the CPRI specification and its application to C-RAN-based LTE scenarios,” *IEEE Communications Magazine*, vol. 54, no. 2, pp. 152–159, Feb. 2016. DOI: 10.1109/MCOM.2016.7402275.
- [154] 3GPP TR 38.912, *Study on New Radio (NR) access technology*, version 17.0.0, Mar. 2022.

- [155] S. Jang, G. Jo, J. Jung, B. Park, and S. Hong, "A Digitized IF-Over-Fiber Transmission Based on Low-Pass Delta-Sigma Modulation," *IEEE Photonics Technology Letters*, vol. 26, no. 24, pp. 2484–2487, Dec. 2014. doi: 10.1109/LPT.2014.2361753.
- [156] S. Ishimura, H.-Y. Kao, K. Tanaka, K. Nishimura, and M. Suzuki, "SSBI-Free Direct-Detection System Employing Phase Modulation for Analog Optical Links," *Journal of Lightwave Technology*, vol. 38, no. 9, pp. 2719–2725, May 2020. doi: 10.1109/JLT.2020.2971134.
- [157] Y. Liu, L. Ma, J. Xiong, *et al.*, "High-Speed Performance Evaluation of Graded-Index Multicore Fiber Compatible With Multimode and Quasi-single Mode Operation," *Journal of Lightwave Technology*, vol. 38, no. 24, pp. 6870–6878, Dec. 2020. doi: 10.1109/JLT.2020.3019645.
- [158] E. Ruggeri, A. Tsakyridis, C. Vagionas, *et al.*, "A 5G Fiber Wireless 4Gb/s WDM Fronthaul for Flexible 360° Coverage in V-Band massive MIMO Small Cells," *Journal of Lightwave Technology*, vol. 39, no. 4, pp. 1081–1088, Feb. 2021. doi: 10.1109/JLT.2020.3029608.
- [159] F. Azendorf, A. Dochhan, F. Spinty, M. Lawin, B. Schmauss, and M. Eiselt, "Group Delay Measurements of Multicore Fibers with Correlation Optical Time Domain Reflectometry," in *2020 22nd International Conference on Transparent Optical Networks (ICTON)*, Bari, Italy, Jul. 2020, pp. 1–4. doi: 10.1109/ICTON51198.2020.9203412.
- [160] A. H. M. R. Islam, M. Bakaul, A. Nirmalathas, and G. E. Town, "Simplified Generation, Transport, and Data Recovery of Millimeter-Wave Signal in a Full-Duplex Bidirectional Fiber-Wireless System," *IEEE Photonics Technology Letters*, vol. 24, no. 16, pp. 1428–1430, Aug. 2012. doi: 10.1109/LPT.2012.2205376.
- [161] P. T. Dat, A. Kanno, N. Yamamoto, and T. Kawanishi, "Full-Duplex Transmission of LTE-A Carrier Aggregation Signal Over a Bidirectional Seamless Fiber-Millimeter-Wave System," *Journal of Lightwave Technology*, vol. 34, no. 2, pp. 691–700, Jan. 2016. doi: 10.1109/JLT.2015.2466476.
- [162] J. He, B. Li, L. Deng, *et al.*, "Experimental Demonstration of Bidirectional OFDM/OQAM-MIMO Signal Over a Multicore Fiber System," *IEEE Photonics Journal*, vol. 8, no. 5, pp. 1–8, Oct. 2016. doi: 10.1109/JPHOT.2016.2607203.
- [163] P. T. Dat, A. Kanno, N. Yamamoto, and T. Kawanishi, "Performance Evaluation of Full-Duplex MIMO Seamless Fiber-Wireless System in W-Band," *IEEE Photonics Technology Letters*, vol. 30, no. 13, pp. 1175–1178, Jul. 2018. doi: 10.1109/LPT.2018.2837146.
- [164] P. T. Dat, A. Kanno, N. Yamamoto, N. V. Dien, N. T. Hung, and T. Kawanishi, "Full-Duplex Transmission of Nyquist-SCM Signal over a Seamless Bidirectional Fiber-Wireless System in W-Band," in *Optical Fiber Communication Conference (OFC) 2019*, San Diego, CA, USA, Mar. 2019, W1I.5. doi: 10.1364/OFC.2019.W1I.5.
- [165] J. A. Frantz, J. D. Myers, R. Y. Bekele, *et al.*, "Non-mechanical beam steering in the mid-wave infrared," in *Advanced Optics for Defense Applications: UV through LWIR II*, vol. 10181, Anaheim, California, United States, Jun. 2017, pp. 206–212. doi: 10.1117/12.2271898.

- [166] M. Younis, C. Fischer, and W. Wiesbeck, "Digital beamforming in SAR systems," *IEEE Transactions on Geoscience and Remote Sensing*, vol. 41, no. 7, pp. 1735–1739, Jul. 2003. DOI: 10.1109/TGRS.2003.815662.
- [167] R. L. Haupt, "Lowering the Sidelobe Level of a Two-Way Array Factor for an Array With Uniform Transmit and Uniform Receive Arrays," *IEEE Transactions on Antennas and Propagation*, vol. 67, no. 6, pp. 4253–4256, Jun. 2019. DOI: 10.1109/TAP.2019.2905932.
- [168] Y. Liu, A. R. Wichman, B. Isaac, *et al.*, "Ultra-Low-Loss Silicon Nitride Optical Beamforming Network for Wideband Wireless Applications," *IEEE Journal of Selected Topics in Quantum Electronics*, vol. 24, no. 4, pp. 1–10, May 2018. DOI: 10.1109/JSTQE.2018.2827786.
- [169] Q. Ma, D. M. W. Leenaerts, and P. G. M. Baltus, "Silicon-Based True-Time-Delay Phased-Array Front-Ends at Ka-Band," *IEEE Transactions on Microwave Theory and Techniques*, vol. 63, no. 9, pp. 2942–2952, Sep. 2015. DOI: 10.1109/TMTT.2015.2458326.
- [170] R. Muñoz, S. Rommel, P. van Dijk, *et al.*, "Experimental Demonstration of Dynamic Optical Beamforming for Beyond 5G Spatially Multiplexed Fronthaul Networks," *IEEE Journal of Selected Topics in Quantum Electronics*, vol. 27, no. 6, pp. 1–16, May 2021. DOI: 10.1109/JSTQE.2021.3079726.
- [171] W. Hong, Z. H. Jiang, C. Yu, *et al.*, "Multibeam Antenna Technologies for 5G Wireless Communications," *IEEE Transactions on Antennas and Propagation*, vol. 65, no. 12, pp. 6231–6249, Dec. 2017. DOI: 10.1109/TAP.2017.2712819.
- [172] P. Singh, K. Yadav, H. B. Mishra, and R. Budhiraja, "BER Analysis for OTFS Zero Forcing Receiver," *IEEE Transactions on Communications*, vol. 70, no. 4, pp. 2281–2297, Apr. 2022. DOI: 10.1109/TCOMM.2022.3148363.
- [173] D. Konstantinou, C. Caillaud, T. Shivan, *et al.*, "Simulation of an Integrated UTC-Photodiode with a High-Speed TIA for 5G mm-Wave Generation," in *2020 International Conference on Numerical Simulation of Optoelectronic Devices (NUSOD)*, Turin, Italy, Sep. 2020, pp. 1–2. DOI: 10.1109/NUSOD49422.2020.9217642.
- [174] D. Konstantinou, J. de Graaf, S. Rommel, U. Johannsen, Y. Jiao, and I. T. Monroy, "V-Band Vivaldi Antenna for Beyond-5G Integrated Photonic-Wireless Millimetre Wave Transmitter," in *2022 16th European Conference on Antennas and Propagation (EuCAP)*, Madrid, Spain, Mar. 2022, pp. 1–5. DOI: 10.23919/EuCAP53622.2022.9768943.
- [175] K. Nishimori, K. Cho, Y. Takatori, and T. Hori, "Automatic calibration method using transmitting signals of an adaptive array for TDD systems," *IEEE Transactions on Vehicular Technology*, vol. 50, no. 6, pp. 1636–1640, Nov. 2001. DOI: 10.1109/25.966592.
- [176] S. Rommel, B. Cimoli, E. Grivas, *et al.*, "Real-Time Demonstration of ARoF Fronthaul for High-Bandwidth mm-Wave 5G NR Signal Transmission over Multi-Core Fiber," in *2020 European Conference on Networks and Communications (EuCNC)*, Dubrovnik, Croatia, Jun. 2020, pp. 205–208. DOI: 10.1109/EuCNC48522.2020.9200921.

- [177] M. A. ElMossallamy, H. Zhang, L. Song, K. G. Seddik, Z. Han, and G. Y. Li, “Reconfigurable Intelligent Surfaces for Wireless Communications: Principles, Challenges, and Opportunities,” *IEEE Transactions on Cognitive Communications and Networking*, vol. 6, no. 3, pp. 990–1002, Sep. 2020. DOI: 10.1109/TCCN.2020.2992604.
- [178] J. Zhang, S. Chen, Y. Lin, J. Zheng, B. Ai, and L. Hanzo, “Cell-free massive mimo: A new next-generation paradigm,” *IEEE Access*, vol. 7, pp. 99 878–99 888, Jul. 2019. DOI: 10.1109/ACCESS.2019.2930208.
- [179] A. M. Niknejad, S. Thyagarajan, E. Alon, Y. Wang, and C. Hull, “A circuit designer’s guide to 5G mm-wave,” in *2015 IEEE Custom Integrated Circuits Conference (CICC)*, San Jose, CA, USA, Sep. 2015, pp. 1–8. DOI: 10.1109/CICC.2015.7338410.
- [180] 3GPP TR 37.910, *Study on self evaluation towards IMT-2020 submission*, version 17.0.0, May 2022.
- [181] J. A. Altabas, S. Rommel, R. Puerta, *et al.*, “Nonorthogonal Multiple Access and Carrierless Amplitude Phase Modulation for Flexible Multiuser Provisioning in 5G Mobile Networks,” *Journal of Lightwave Technology*, vol. 35, no. 24, pp. 5456–5463, Dec. 2017. DOI: 10.1109/JLT.2017.2761541.
- [182] K. B. Letaief, Y. Shi, J. Lu, and J. Lu, “Edge Artificial Intelligence for 6G: Vision, Enabling Technologies, and Applications,” *IEEE Journal on Selected Areas in Communications*, vol. 40, no. 1, pp. 5–36, Jan. 2022. DOI: 10.1109/JSAC.2021.3126076.
- [183] L. Zhang, Y.-C. Liang, and D. Niyato, “6G Visions: Mobile ultra-broadband, super internet-of-things, and artificial intelligence,” *China Communications*, vol. 16, no. 8, pp. 1–14, Aug. 2019. DOI: 10.23919/JCC.2019.08.001.
- [184] H. Yang, A. Alphones, Z. Xiong, D. Niyato, J. Zhao, and K. Wu, “Artificial-Intelligence-Enabled Intelligent 6G Networks,” *IEEE Network*, vol. 34, no. 6, pp. 272–280, Dec. 2020. DOI: 10.1109/MNET.011.2000195.
- [185] P. Schulte and G. Böcherer, “Constant Composition Distribution Matching,” *IEEE Transactions on Information Theory*, vol. 62, no. 1, pp. 430–434, Jan. 2016. DOI: 10.1109/TIT.2015.2499181.

List of Acronyms

1G	First-generation of mobile networks
2G	Second-generation of mobile networks
3G	Third-generation of mobile networks
3GPP	3rd Generation Partnership Project
4G	Fourth-generation of mobile networks
5G	Fifth-generation of mobile networks
5G NR	Fifth-generation new radio
6G	Sixth-generation of mobile networks
AA	Antenna array
ADC	Analog-to-digital converter
AF	Array factor
AI	Artificial intelligence
AIR	Achievable information rate
AM	Amplitude
ARoF	Analog radio-over-fiber
ASIC	Application-specific integrated circuit
ASK	Amplitude-shift keying
AWGN	Additive white Gaussian noise
BB	Baseband
BBU	Baseband unit
BER	Bit error rate
BFN	Beamforming network
BMD	Bit-metric decoding
BTB	Back-to-back
CAGR	Compound annual growth rate
CAPEX	Capital expenditure
CCDM	Constant composition distribution matching
CCF	Coupled-core fiber

CDF	Cumulative distribution function
CFO	Carrier frequency offset
CLB	Configurable logic block
CO	Central office
CP	Cyclic prefix
CPE	Common phase error
CPRI	Common public radio interface
CPU	Central processing unit
C-RAN	Centralized radio access network
DAC	Digital-to-analog converter
DA-PNS	Decision-aided phase noise suppression
DC	Direct current
DCF	Dispersion compensation fiber
DD-LMS	Decision directed least mean square
DES	Deserializer
DFB	Distributed feedback
DFT	Discrete Fourier transform
DL	Downlink
DM	Distribution matching
D-RAN	Distributed radio access network
DRoF	Digital radio-over-fiber
DSB	Double-sideband
DSP	Digital signal processing
E/O	Electrical-to-Optical
EBFN	Electrical beamforming network
eCPRI	Enhanced common public radio interface
EIGS	External injected gain switched
eMBB	Enhanced mobile broadband
ENoB	Effective number of bits
ER	Extinction ratio
ESS	Enumerative sphere shaping
EVM	Error vector magnitude
FBMC	Filter bank multi-carrier
FDD	Frequency division duplex
FEC	Forward error correction
FMF	Few-mode fiber
FPGA	Field programmable gate array
FR	Frequency range
FSPL	Free-space path loss
FWHM	Full-width at half-maximum

GFDM	Generalized frequency division multiplexing
HD	High-definition
ICI	Inter-carrier interference
IDF	Iterative decision feedback
IDFT	Inverse discrete Fourier transform
IEEE	Institute of Electrical and Electronics Engineers
IF	Intermediate frequency
IFoF	Intermediate frequency-over-fiber
IM-DD	Intensity-modulation and direct-detection
iOBFN	Incoherent optical beamforming network
IoT	Internet of Things
IQ	In-phase and quadrature
KPI	Key performance indicator
LI-CPE	Linear interpolation based ICI estimation
LLR	Log-likelihood ratio
LO	Local oscillator
LOS	Line-of-sight
LPF	Low-pass filter
LSB	Left sideband
LTE	Long-Term Evolution
LTE-A	Long-Term Evolution-Advanced
LTI	Linear time-invariant
LUT	Look-up-table
MAR	Mobile augmented reality
MC	Multi-carrier
MCF	Multi-core fiber
MIMO	Multiple-input multiple-output
MLLs	Mode-locked lasers
MMF	Multi-mode fiber
mMTC	Massive machine-type communications
mm-wave	Millimeter-wave
Multi-CAP	Multi-band carrierless amplitude and phase modulation
MZM	Mach-Zehnder modulator
NF	Noise figure
NFV	Network function virtualization
NGFI	Next generation fronthaul interface
NLOS	Non-line-of-sight
NOMA	Non-orthogonal multiple access
NRZ	Non-return-to-zero

O/E	Optical-to-Electrical
OBFN	optical beamforming network
OCS	Optical carrier suppression
OFCG	Optical frequency comb generator
OFDM	Orthogonal frequency-division multiplexing
OH	Overhead
OIL	Optical-injection-locking
OOB	Out-of-band
OOK	On-off keying
OPEX	Operating expenditure
OPLL	Optical phase-locked loop
OQAM	Offset quadrature amplitude modulation
ORR	Optical ring resonator
OTFS	Orthogonal time frequency space
PAM	Pulse-amplitude modulation
PA-PNS	Pilot-aided phase noise suppression
PAPR	Peak-to-average power ratio
PAS	Probabilistic amplitude shaping
PCF	Photonic crystal fiber
PD	Photodiode
PDM	Polarization-division multiplexing
PIC	Photonic integrated circuit
PMD	Polarization mode dispersion
PN	Phase noise
PON	Passive optical network
PSD	Power spectral density
PT-RS	Phase-tracking reference signal
QAM	Quadrature amplitude modulation
QPSK	Quadrature phase-shift keying
RAN	Radio access network
RAU	Remote antenna unit
RB	Resource block
RF	Radio frequency
RIS	Reconfigurable intelligent surface
RoF	Radio-over-fiber
RQ	Research question
RSB	Right sideband
SBS	Stimulated Brillouin scattering
SBST	Stimulated Brillouin scattering threshold
SC	Single-carrier

SC-FDM	Single-carrier frequency-division multiplexing
SCM	Subcarrier modulation
SC-QAM	Single-carrier quadrature amplitude modulation
SDM	Space division multiplexing
SDN	Software-defined networking
SER	Serializer
SI	International System of Units
SISO	Single-input single-output
SLL	Sidelobe level
SM	Shell mapping
SMF	Single-mode fiber
SNR	Signal-to-noise ratio
SoC	System-on-chip
SOTA	State-of-the-art
SPDF	Scattered pilots with decision feedback
SPM	Self-phase modulation
SRS	Stimulated Raman scattering
SSB	Single-sideband
SSBI	Signal-signal beat interference
SSMF	Standard single-mode fiber
TBD	To be defined
TDD	Time-division duplexing
TDHM	Time-division hybrid modulation
TDL	Tapped delay line
TTD	True time delay
UFMC	Universal filtered multi-carrier
UF-OFDM	Universally filtered orthogonal frequency-division multiplexing
UL	Uplink
ULS	Unconstrained least-squares
UMa	Urban macro
UMi	Urban micro
URLLC	Ultra-reliable and low latency communication
VSG	Vector signal generator
WDM	Wavelength-division multiplexing
WSS	Wavelength selective switch
XPM	Cross-phase modulation

List of Publications

Summary of original work

- [P1] **J. P. Santacruz**, S. Rommel, U. Johannsen, A. Jurado-Navas, and I. Tafur Monroy, “Candidate Waveforms for ARoF in Beyond 5G,” *Applied Sciences*, vol. 10, no. 11, Jun. 2020. DOI: 10.3390/app10113891.
- [P2] **J. P. Santacruz**, A. Morales, S. Rommel, U. Johannsen, A. Jurado-Navas, and I. Tafur Monroy, “Experimental Assessment of Modulation Formats for Beyond 5G mm-Wave ARoF Systems,” in *2020 European Conference on Networks and Communications (EuCNC)*, Dubrovnik, Croatia: IEEE, Jun. 2020, pp. 300–304. DOI: 10.1109/EuCNC48522.2020.9200955.
- [P3] **J. P. Santacruz**, S. Rommel, A. Jurado-Navas, and I. Tafur Monroy, “Probabilistic Amplitude Shaping to Enhance ARoF Fronthaul for Mm-Wave 5G/6G Systems,” in *2022 European Conference on Networks and Communications (EuCNC)*, Grenoble, France: IEEE, Jun. 2022, pp. 1–6. DOI: 10.1109/EuCNC/6GSummit54941.2022.9815694.
- [P4] **J. P. Santacruz**, S. Rommel, U. Johannsen, A. Jurado-Navas, and I. Tafur Monroy, “Analysis and Compensation of Phase Noise in Mm-Wave OFDM ARoF Systems for Beyond 5G,” *Journal of Lightwave Technology*, vol. 39, pp. 1602–1610, 6 Mar. 2021. DOI: 10.1109/JLT.2020.3041041.
- [P5] **J. P. Santacruz**, S. Rommel, A. Jurado-Navas, U. Johannsen, and I. Tafur Monroy, “Experimental Study of the Phase Noise in K-band ARoF systems for Low Complexity 5G receivers,” in *2020 National Symposium of the International Scientific Radio Union (URSI)*, Málaga, Spain: arXiv, Sep. 2020, pp. 1–4. arXiv: 2109.07392 [eess.SP].
- [P6] **J. P. Santacruz**, D. Dodane, J. Bourderionnet, *et al.*, “Experimental ARoF System Based on OPLL Mm-Wave Generation for Beyond 5G,” in *26th Optoelectronics and Communications Conference (OECC)*, Hong Kong, China: Optica Publishing Group, Jul. 2021, W2B.2. DOI: 10.1364/OECC.2021.W2B.2.
- [P7] D. Dodane, **J. P. Santacruz**, J. Bourderionnet, *et al.*, “Optical Phase-Locked Loop Phase Noise in 5G mm-Wave OFDM ARoF Systems,” *Optics Communications*, vol. 526, p. 128 872, Aug. 2022, [under review, format in preliminary version for review]. DOI: 10.1016/j.optcom.2022.128872.

- [P8] **J. P. Santacruz**, S. Rommel, A. Jurado-Navas, U. Johannsen, and I. Tafur Monroy, “Probabilistically Shaped OFDM for Gradual Capacity Adaptation in 5G ARoF Systems,” in *26th Optoelectronics and Communications Conference (OECC)*, Hong Kong, China: Optica Publishing Group, Jul. 2021, W1B.4. doi: 10.1364/OECC.2021.W1B.4.
- [P9] **J. P. Santacruz**, G. Nazarikov, S. Rommel, A. Jurado-Navas, and I. Tafur Monroy, “Bidirectional mm-Wave ARoF Fronthaul over Multicore Fiber for 5G and Beyond,” in *2021 International Topical Meeting on Microwave Photonics (MWP)*, Pisa, Italy: IEEE, Nov. 2021, pp. 1–4. doi: 10.1109/MWP53341.2021.9639425.
- [P10] **J. P. Santacruz**, G. Nazarikov, S. Rommel, A. Jurado-Navas, and I. Tafur Monroy, “Bidirectional ARoF Fronthaul over Multicore Fiber for Beyond 5G Mm-Wave Communications,” *Optics Communications*, vol. 521, p. 128 591, Jun. 2022. doi: 10.1016/j.optcom.2022.128591.
- [P11] **J. P. Santacruz**, S. Rommel, C. G. H. Roeloffzen, *et al.*, “Incoherent Optical Beamformer for ARoF Fronthaul in Mm-wave 5G/6G Networks,” *Journal of Lightwave Technology*, 2022, [under review].
- [P12] **J. P. Santacruz**, R. Budé, C. Stan, *et al.*, “Experimental outdoor IFoF fronthaul with adaptive analog beamforming for mm-wave 5G/6G networks,” *Scientific Reports*, 2022, [first draft].

Other scientific publications

- [O1] **J. P. Santacruz**, U. Farooq, K. T. Atra, *et al.*, “Modulation and Equalization Techniques for mmWave ARoF,” in *Enabling 6G Mobile Networks*, J. Rodriguez, C. Verikoukis, J. S. Vardakas, and N. Passas, Eds. Springer International Publishing, 2022, pp. 259–292. doi: 10.1007/978-3-030-74648-3_8.
- [O2] T. R. Raddo, **J. P. Santacruz**, U. Johannsen, *et al.*, “FSO-CDMA Systems Supporting end-to-end Network Slicing,” in *Imaging and Applied Optics Congress*, Washington, DC United States: Optica Publishing Group, 2020, JW2A.38. doi: 10.1364/3D.2020.JW2A.38.

Curriculum Vitae



Javier Pérez Santacruz was born on 10-12-1994 in Vélez-Málaga, Spain. In 2016, he received his BSc degree in Telecommunications Engineering from the University of Málaga (Spain). In 2018, he obtained his double MSc degree in Telecommunications Engineering and Telematic and Telecommunication Networks while working as a research assistant in the Communications Engineering Department of the University of Málaga. In the same year, he continued his academic career as a Ph.D. student at the Terahertz Photonic Systems Group within the Electrical Engineering Department of the Eindhoven University of Technology (TU/e). His Ph.D. research was part of the framework of the ITN 5G STEP FWD project of the European Union's Horizon

2020 Marie Skłodowska Curie Action. The results obtained during his Ph.D. project are presented in this dissertation and have led to several scientific journal publications and conference contributions. His main expertise is in the areas of digital signal processing (DSP), radio-over-fiber systems, photonic circuit integration, and millimeter-wave wireless communications.

During his PhD project he has been involved in academic-industry collaboration with Lionix International, Thales Research and Technology, and ADVA Optical Networking and contributed to European projects such as 5G PPP blueSPACE, 5G-MOBIX, and PICaboo. Moreover, he has supervised several students carrying out their bachelor's and master's thesis projects. In addition, he acts as a peer-reviewer of research articles submitted for publication to technical journals and conferences in the field.